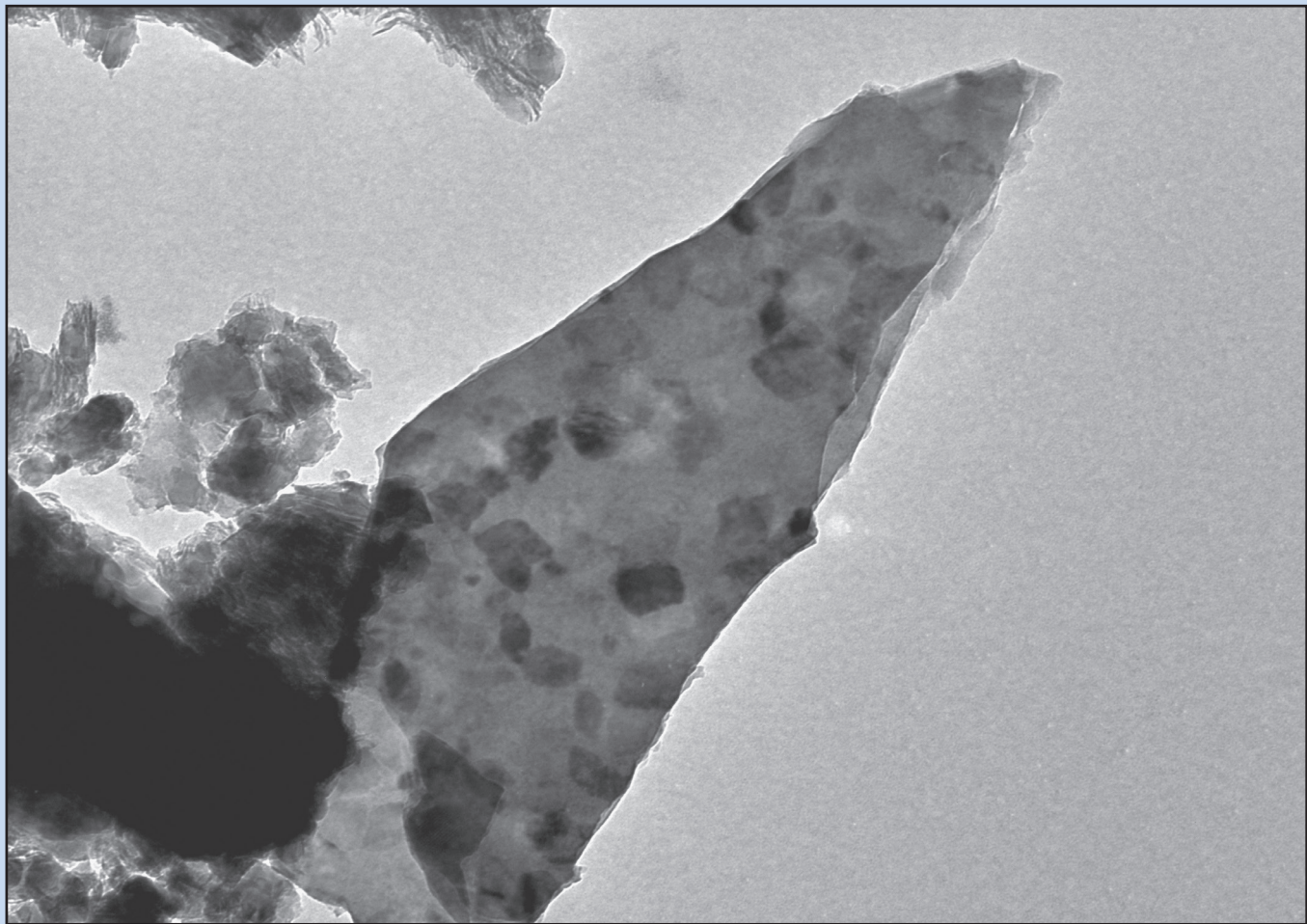


**Roy TRITTSCHACK**

## **Dehydroxylation kinetics of the serpentine group minerals**



## Already published:

- Vol. 11 **FREUDIGER-BONZON, Jeanne** (2005) Archaeometrical study (petrography, mineralogy and chemistry) of Neolithic Ceramics from Arbon Bleiche 3 (Canton of Thurgau, Switzerland) (187 pp.).
- Vol. 12 **STOFFEL, Markus** (2005) Spatio-temporal variations of rockfall activity into forests - results from tree-ring and tree analysis (188 pp.).
- Vol. 13 **RAMEIL, Niels** (2005) Carbonate sedimentology, sequence stratigraphy, and cyclostratigraphy of the Tithonian in the Swiss and French Jura Mountains - a high-resolution record of changes in sea level and climate (246 pp.).
- Vol. 14 **BRAILLARD, Luc** (2006) Morphogenèse des vallées sèches du Jura tabulaire d'Ajoie (Suisse): rôle de la fracturation et étude des remplissages quaternaires (224 pp.).
- Vol. 15 **GOYETTE-PERNOT, Joëlle** (2006) L'Ambroisie: analyse statistique et modélisation numérique de sa trajectoire aérobiologique (274 pp.).
- Vol. 16 **TRESCH, Jonas** (2007) History of a Middle Berriasian transgression (Switzerland, France, and southern England) (271 pp.).
- Vol. 17 **BONNET, Cécile** (2007) Interactions between tectonics and surface processes in the Alpine foreland: Insights from analogue model and analysis of recent faulting (189 pp.).
- Vol. 18 **VONLANTHEN, Pierre** (2007) EBSD-based investigations of upper mantle xenoliths, snowball garnets and advanced ceramics (114 pp.).
- Vol. 19 **VÉDRINE, Stéphanie** (2007) High-frequency palaeoenvironmental changes in mixed carbonate-siliciclastic sedimentary systems (Late Oxfordian, Switzerland, France, and southern Germany) (216 pp.).
- Vol. 20 **BOLLSCHWEILER, Michelle** (2008) Spatial and temporal occurrence of past debris flows in the Valais Alps - results from tree-ring analysis (182 pp.).
- Vol. 21 **MARTY, Daniel** (2008) Sedimentology, taphonomy, and ichnology of Late Jurassic dinosaur tracks from the Jura carbonate platform (Chevenez-Combe Ronde tracksite, NW Switzerland): insights into the tidal-flat palaeoenvironment and dinosaur diversity, locomotion, and palaeoecology (278 pp.).
- Vol. 22 **STIENNE, Noémie** (2010) Paléoécologie et taphonomie comparative en milieux carbonatés peu profonds (Oxfordien du Jura Suisse et Holocène du Belize) (248 pp.).
- Vol. 23 **WAITE, Richard** (2010) The palaeoecology of high-spired gastropods and the lost palaeosols: depositional reconstructions on a shallow carbonate platform (Late Kimmeridgian, Swiss Jura Mountains) (149 pp.).
- Vol. 24 **MARGRET, Stephan** (2010) Benthic foraminifera associated to cold-water coral ecosystems (248 pp.).
- Vol. 25 **VON ALLMEN, Katja** (2010) Variations of calcium and barium isotopes and elemental contents in biogenic and abiogenic geological archives (97 pp.).
- Vol. 26 **VOUILLAMOZ, Naomi / SAUDAN, Corinne / MOSAR, Jon** (2010) Microzonage sismique du canton de Fribourg - Cartographie au 1:25'000 des sols de fondation selon la norme SIA 261 (57 pp.).
- Vol. 27 **IBELE, Tobias**, (2011) Tectonics of the Western Swiss Molasse Basin during Cenozoic Time (166 pp.).
- Vol. 28 **GENNARI, Giordana**, (2011) The Mediterranean - Black Sea connections: The fundamental role of foraminifera as a multifaceted tool for the geological reconstruction of the last 10 ky (171 pp.).
- Vol. 29 **MORARD, Sébastien**, (2011) Effets de la circulation d'air par effet de cheminée dans l'évolution du régime thermique des éboulis froids de basse et moyenne altitude (220 pp.).
- Vol. 30 **BOCHUD, Martin**, (2011) Tectonics of the Eastern Greater Caucasus in Azerbaijan (201 pp.).
- Vol. 31 **MATZENAUER, Eva**, (2012) Tectonics of the Préalpes Klippen and the Subalpine Molasse (Canton Fribourg, Switzerland) (207 pp.).
- Vol. 32 **MENNECART, Bastien**, (2012) The Ruminantia (Mammalia, Cetartiodactyla) from the Oligocene to the Early Miocene of Western Europe: systematics, palaeoecology and palaeobiogeography (263 pp.).
- Vol. 33 **JARAMILLO-VOGEL, David**, (2013) Shallow-marine sedimentary records of the Eocene-Oligocene greenhouse-icehouse transition (Italy, Switzerland and France) (182 pp.).

Already published:

- Vol. 1 **HILLGÄRTNER, Heiko** (1999) The evolution of the French Jura platform during the Late Berriasian to Early Valanginian: controlling factors and timing (203 pp.).
- Vol. 2 **DUPRAZ, Christophe** (1999) Paléontologie, paléoécologie et évolution des faciès récifaux de l'Oxfordien Moyen-Supérieur (Jura suisse et français) (247 pp.).
- Vol. 3 **BASSANT, Philip** (1999) The high-resolution stratigraphic architecture and evolution of the Burdigalian carbonate-siliciclastic sedimentary systems of the Mut Basin, Turkey (278 pp.).
- Vol. 4 **COLOMBIÉ, Claude** (2002) Sédimentologie, stratigraphie séquentielle et cyclostratigraphie du Kimmériidgien du Jura suisse et du Bassin vocontien (France): relations plate-forme - bassin et facteurs déterminants (198 pp.).
- Vol. 5 **PICOT, Laurent** (2002) Le Paléogène des synclinaux du Jura et de la bordure sud-rhénane: paléontologie (Ostracodes), paléoécologie, biostratigraphie et paléogéographie (240 pp.).
- Vol. 6 **DAPPLES, Florence** (2002) Instabilités de terrain dans les Préalpes fribourgeoises (Suisse) au cours du Tardiglaciaire et de l'Holocène: influence des changements climatiques, des fluctuations de la végétation et de l'activité humaine (158 pp.).
- Vol. 7 **HUG, Wolfgang Alexander** (2003) Sequenzielle Faziesentwicklung der Karbonatplattform des Schweizer Jura im Späten Oxford und frühesten Kimmeridge (156 pp.).
- Vol. 8 **OSWALD, Daniel** (2003) Analyse de l'activité de glissements de terrain et relation avec les conditions climatiques: Exemples dans les Préalpes fribourgeoises (Suisse) (147 pp.).
- Vol. 9 **BECKER, Damien** (2003) Paléoécologie et paléoclimats de la Molasse du Jura (Oligo-Miocène): apport des Rhinocerotidea (Mammalia) et des minéraux argileux (327 pp.).
- Vol. 10 **DELALOYE, Reynald** (2005) Contribution à l'étude du pergélisol de montagne en zone marginale (240 pp.).

**GeoFocus** is the publication series of the Department of Geosciences, University of Fribourg, Switzerland, and can be ordered at:  
Department of Geosciences - Earth Sciences - University of Fribourg - 1700 Fribourg, Switzerland - <http://www.unifr.ch/geoscience/geology>

Aus dem Departement für Geowissenschaften  
Universität Freiburg (Schweiz)

*Dehydroxylation kinetics of the serpentine group minerals*

**INAUGURAL-DISSERTATION**

zur Erlangung der Würde eines *Doctor rerum naturalium*  
der Mathematisch-Naturwissenschaftlichen Fakultät  
der Universität Freiburg in der Schweiz

vorgelegt von  
Roy Trittschack  
aus  
Allendorf/ Thüringen, Deutschland

These N° 1795

2013

Multiprint SA, Fribourg, 2013



Von der Mathematisch-Naturwissenschaftlichen Fakultät der Universität Freiburg in der Schweiz  
angenommen, auf Antrag von

Prof. Dr. Bernard Grobéty	Universität Freiburg/ Schweiz	Dissertationsleiter
Prof. Dr. Eugen Libowitzky	Universität Wien/ Österreich	Gutachter
Prof. Dr. Pierre Brodard	Hochschule für Technik und Architektur Freiburg/ Schweiz	Gutachter
Prof. Dr. Vincent Serneels	Universität Freiburg/ Schweiz	Präsident der Prüfungskommission

Freiburg i. Ü., den 05. Juni 2013

Dissertationsleiter



.....  
Prof. Dr. Bernard Grobéty

Dekan der Fakultät



.....  
Prof. Dr. Fritz Müller

# CONTENTS

ABSTRACT .....	1
ZUSAMMENFASSUNG .....	3
ACKNOWLEDGMENTS .....	5
ABBREVIATION LIST .....	6
<b>1. INTRODUCTION</b> .....	<b>8</b>
1.1. RESEARCH BACKGROUND .....	8
1.2. GOALS .....	9
1.3. SERPENTINITES AND SERPENTINE MINERALS: A BRIEF OVERVIEW .....	9
1.3.1. Serpentine bearing rocks .....	9
1.3.2. Mineralogy and Crystallography of serpentine minerals .....	11
<b>2. REACTION KINETICS OF DECOMPOSITION EXPERIMENTS: A BRIEF OVERVIEW</b> .....	<b>13</b>
2.1. INTRODUCTION .....	13
2.2. ISOTHERMAL APPROACH .....	16
2.3. NON-ISOTHERMAL APPROACH .....	17
2.4. HOW TO DEAL WITH VARIABLE APPARENT ACTIVATION ENERGIES? .....	19
<b>3. EXPERIMENTAL METHODS</b> .....	<b>22</b>
3.1. FTIR AND RAMAN SPECTROSCOPY .....	22
3.1.1. Reasons for the chosen methods .....	22
3.1.2. Brief historical background .....	22
3.1.3. Micro-FTIR spectroscopy (at non-ambient temperatures) .....	23
3.1.4. Conventional FTIR spectroscopy .....	24
3.1.5. Micro-Raman spectroscopy (at non-ambient temperatures) .....	24
3.2. X-RAY DIFFRACTION .....	24
3.3. HIGH-TEMPERATURE X-RAY DIFFRACTION .....	25
3.4. IR SPECTROMETRY (LECO IR SPECTROMETER) .....	26
3.5. THERMOGRAVIMETRIC ANALYSES (TGA) .....	27
3.6. TRANSMISSION ELECTRON MICROSCOPY (TEM) .....	27
3.7. SCANNING ELECTRON MICROSCOPY (SEM) .....	27

#### 4. DEHYDROXYLATION KINETICS OF LIZARDITE 28

ABSTRACT .....	28
4.1. INTRODUCTION .....	28
4.2. EXPERIMENTAL METHODS .....	29
4.3. DATA EXTRACTION .....	31
4.4. RESULTS .....	32
4.4.1. Characteristics of the sample material .....	32
4.4.2. Decomposition of lizardite .....	33
4.4.3. Reaction kinetics .....	34
4.5. DISCUSSION .....	37
4.6. CONCLUDING REMARKS .....	39

#### 5. *IN SITU* HIGH-TEMPERATURE RAMAN AND FTIR SPECTROSCOPY OF THE PHASE TRANSFORMATION OF LIZARDITE 40

ABSTRACT .....	40
5.1. INTRODUCTION .....	40
5.2. EXPERIMENTAL METHODS .....	41
5.2.1. Sample material .....	41
5.2.2. FTIR and Raman spectroscopy .....	41
5.2.3. Fitting procedure .....	42
5.3. RESULTS .....	42
5.3.1. Raman and FTIR spectra at ambient conditions .....	42
5.3.2. Temperature-dependent Raman-spectra in the low-frequency region .....	43
5.3.3. Temperature-dependent Raman- and FTIR spectra in the OH stretching region .....	44
5.4. DISCUSSION .....	47
5.4.1. OH bands and their assignments .....	47
5.4.2. The lizardite dehydroxylation I: Comparison between FTIR, Raman, and TGA data .....	49
5.4.3. The lizardite dehydroxylation II: Kinetic aspects and their spectroscopic indications .....	50
5.4.4. Dehydroxylation products: a talc-like intermediate and forsterite .....	52

#### 6. THE DEHYDROXYLATION OF CHRYSOTILE: A COMBINED *IN SITU* MICRO-RAMAN AND MICRO-FTIR STUDY 55

ABSTRACT .....	55
6.1. INTRODUCTION .....	55
6.2. EXPERIMENTAL METHODS .....	56
6.2.1. Sample material .....	56
6.2.2. FTIR and Raman spectroscopy .....	57
6.2.3. Fitting procedure .....	58
6.3. RESULTS .....	58
6.3.1. Raman and FTIR spectra at ambient conditions .....	58
6.3.2. High-temperature FTIR and Raman spectroscopy of the dehydroxylation of chrysotile .....	59
6.3.3. FTIR and Raman spectroscopy of quenched samples .....	64

6.4. DISCUSSION.....	64
6.4.1. Raman and FTIR spectra at ambient conditions .....	64
6.4.2. The chrysotile phase transformation as seen in the OH stretching band range .....	68
6.4.3. The chrysotile phase transformation as seen in the low-frequency range (100-1200 cm <sup>-1</sup> ) ....	70
 7. KINETICS OF THE CHRYSOTILE AND BRUCITE DEHYDROXYLATION REACTION: A COMBINED NON-ISOTHERMAL/ ISOTHERMAL THERMOGRAVIMETRIC ANALYSIS AND HIGH-TEMPERATURE X-RAY DIFFRACTION STUDY	74
ABSTRACT.....	74
7.1. INTRODUCTION.....	74
7.2. EXPERIMENTAL METHODS.....	76
7.2.1. Sample materials .....	76
7.2.2. X-ray fluorescence .....	76
7.2.3. X-ray powder diffraction.....	76
7.2.4. Thermogravimetric analysis.....	76
7.3. KINETIC APPROACH.....	77
7.3.1. Avrami-Erofe'ev method.....	77
7.3.2. Time to a given fraction method .....	78
7.3.3. Friedman method.....	78
7.3.4. ASTM E 698 .....	78
7.3.5. Master plots .....	78
7.4. RESULTS AND DISCUSSION .....	80
7.4.1. The dehydroxylation reaction as seen from thermogravimetry .....	80
7.4.2. The course of the apparent activation energies .....	82
7.4.3. Towards a mechanistic interpretation.....	86
7.4.3.1. <i>Brucite</i> .....	86
7.4.3.2. <i>Chrysotile</i> .....	88
7.5. CONCLUDING REMARKS .....	92
 8. CONCLUSIONS AND PERSPECTIVES	94
APPENDIX I.....	95
APPENDIX II.....	99
APPENDIX III .....	108
APPENDIX IV .....	111
REFERENCES .....	113
CURRICULUM VITAE.....	125



## ABSTRACT

Chemical reactions in general and solid-state reactions in particular are controlled by thermodynamics and kinetics. Whereas thermodynamic rules are used to state whether a phase is stable under a specific set of intensive and extensive parameters or not, kinetics applied to an underlain reaction of interest decipher the time-scale of such a reaction by offering the chance to determine associated rate constants and rate-limiting steps. But, contrary to thermodynamics, kinetic studies require knowledge about reaction intermediates. Resulting information of kinetic investigations, e.g., the apparent activation energy  $E_a$ , must not be confused with the enthalpy of the reaction. This thesis deals with phase transformation reactions and underlain dehydroxylation kinetics of two geoscientifically important members of the serpentine mineral group, lizardite and chrysotile respectively, which are main constituents of serpentinite rocks.

A kinetics chapter briefly summarising modern concepts and mathematical treatments introduces the main part of this thesis as there are multiple ways to extract kinetic information from a dehydroxylation/ decomposition reaction and different theories how to interpret kinetic information.

The first peer-reviewed article (Chapter 4) studies the dehydroxylation kinetics of flat lying lizardite by using and comparing non-isothermal and isothermal data derived from thermogravimetry (TG) and high-temperature X-ray diffraction (HT-XRD) analysis. Apart from the classical Avrami-Erofe'ev approach, isoconversional treatments, which allow a reaction progress-resolved calculation of the apparent  $E_a$ , are used. The latter indicate a

dynamic evolution, which can be shown independently in TG and HT-XRD derived data. This behaviour contradicts former findings of model-fitting methods which suggest a single 'rate-determining' reaction mechanism and a constant  $E_a$  over the entire reaction progress. These results clearly stress the limitations of the Avrami-Erofe'ev approach. Instead, a scenario with changing rate-limiting steps is proposed. The results are compared with *ab initio* DFT calculations of phyllosilicate dehydroxylation reactions. A multi-step reaction sequence is supported by *ex situ* FTIR data, which also suggest a formation of an intermediate phase influencing the rate. The paper highlights the influence of a steadily changing crystal structure on the overall reactions kinetics.

The second peer-reviewed article (Chapter 5) focuses on the dehydroxylation of lizardite and its transformation to forsterite by applying *in situ* high-temperature (HT) micro-Raman and micro-FTIR techniques. A weak expansion of the O3-H3...O2 interlayer distance during heat treatment can be shown and a slight change in ditrigonal distortion was evidenced. OH band deconvolution suggests the occurrence of extra band(s) during dehydroxylation, especially in Raman data. Multiple reasons such as longitudinal optic-transverse optic splitting, non-structural OH groups and effects related to structural heterogeneities (e.g., different polytypes, chrysotile-like impurities) are discussed. Potential influences of non-structural OH groups on the outlined reaction mechanisms suggested in Chapter 4 are discussed. There are obvious differences between spectroscopic and thermogravimetric data with respect to the onset, maximum and offset of the dehydroxylation signal. These differences are linked to different



processes studied, i.e., primary liberation of OH at specific crystal sites (spectroscopy) *versus* the H<sub>2</sub>O release from the reactant grain and the powder (TG).

The formation and the presence of a reaction intermediate has been proven and confirmed in the temperature range of around 640 °C to around 690 °C. The spectroscopic signature of this intermediate phase provides evidence for a talc-like character.

The third peer-reviewed article (Chapter 6) examines the phase transformation behaviour of chrysotile at ambient pressure and non-ambient temperature conditions by using *in situ* HT micro-Raman and micro-FTIR spectroscopy. Aims of this study are devoted to unresolved questions arising when comparing IR and Raman spectra of both polymorphs. A special attention lies on the influence of the chrysotile structure on the phase transformation in comparison to lizardite (Chapter 5).

Before dealing with the phase transformation itself, the paper critically discusses the number, wavenumber position and band assignments of chrysotile-related frequency modes at ambient conditions as there are ambiguous results in literature. The high- and low-frequency ranges are discussed separately for clarity. Similar to lizardite, the spectroscopically determined temperature range during which chrysotile dehydroxylates, is much narrower than the range observed in TG studies. The decrease of the OH Raman band intensity starts at much lower temperatures than the onset visible in infrared data of chrysotile. This discrepancy is attributed to differences in OH group orientations in response to temperature changes, i.e., reorientation of fibre bundles and/or ordering effects.

Compared to lizardite, main differences in the dehydroxylation behaviour of chrysotile are a much broader temperature range characterised by

the coexistence of primary chrysotile, ‘disordered chrysotile’, a talc-like intermediate phase and forsterite. Similarities between the dehydroxylation of lizardite and chrysotile are a minor change in the ditrigonal distortion with increasing temperature and the appearance of new bands whose frequencies are compatible with a talc-like intermediate.

The fourth article (Chapter 7) is a case study of two comprehensively studied dehydroxylation reactions, i.e., the decomposition of chrysotile under N<sub>2</sub> atmosphere and brucite under N<sub>2</sub> and CO<sub>2</sub> atmosphere. Compared to former studies, non-isothermal data acquired by TG and isothermal data taken from HT-XRD are treated by isoconversional techniques to check the nature of the reaction kinetics, i.e., single versus multiple rate-limiting steps. The DTG signals point towards a rather complex reaction in case of chrysotile, whereas DTG curves for brucite decomposition under N<sub>2</sub> and CO<sub>2</sub> are characterised by a single peak without shoulders and, suggesting, therefore, a simple rate limiting mechanism. This fact is in contradiction to literature data presenting clear evidence for a multi-step reaction mechanism scenario. To decipher the underlain reaction mechanisms, two independent ‘master plot’ techniques are used, one requiring an almost constant value of the apparent  $E_a$  ( $z(\alpha)$  master plot) and one allowing a dynamic course (generalised time master plot). As all reactions studied are characterised by a dynamic evolution of the apparent  $E_a$ , the  $z(\alpha)$  master plot technique resting on almost constant apparent  $E_a$  reveal their limitations. The generalised time master plot is much better suited to gather reaction progress-resolved mechanistic information. Chrysotile shows a progressively more complex reaction mechanism which can be explained by structural properties deduced from spectroscopic data presented in Chapter 6. In a similar way, reaction mechanisms of the brucite decomposition derived from the generalised time master plot approach are in accordance to structural studies presented in literature.

## ZUSAMMENFASSUNG

Chemische Reaktionen von denen Festphasenreaktionen eine besondere Stellung innerhalb der Geowissenschaften einnehmen, werden im Wesentlichen von thermodynamischen und kinetischen Faktoren kontrolliert. Werden thermodynamische Regeln genutzt um Aussagen über die Stabilität einer Phase unter festgelegten intensiven und extensiven Parametern zu treffen, so gestattet die Kinetik eine zeitliche Beschreibung der Reaktion. Darüber hinaus gewährt sie einen Einblick in ablaufende Reaktionsmechanismen und ermöglicht die Bestimmung der zugehörigen Reaktionsgeschwindigkeiten. Im Gegensatz zur Thermodynamik setzt eine kinetische Betrachtung der Reaktion ein allgemeines Verständnis für die Reaktion voraus, d.h. sämtliche Zwischenprodukte sollten bekannt sein. Ermittelte Kenngrößen der Kinetik sollten nicht mit thermodynamischen Größen wie der Reaktionsenthalpie verwechselt werden. Die Dissertation beschäftigt sich mit Phasenumwandlungsreaktionen und der zugehörigen Dehydroxylationskinetik zweier geowissenschaftlich bedeutender Vertreter der Serpentinegruppe, Lizardit und Chrysotil.

Ein kinetisches Kapitel, welches heutige Konzepte und gebräuchliche mathematische Verfahren beschreibt, wurde dem Hauptteil vorangestellt, um die vielseitigen Methoden des Extrahierens kinetischer Informationen aus Dehydroxylations-/ Zersetzungsreaktionen und deren Interpretation überblicksweise darzustellen.

Die erste Publikation beschäftigt sich mit der Dehydroxylationskinetik von Lizardit unter Ausnutzung nicht-isothermaler und isothermaler Datenreihen die mittels Thermogravimetrie und Hochtemperatur-Röntgendiffraktometrie erhoben wurden. Neben dem klassischen Avrami-Erofe'ev Verfahren, kommen Isokonversions-

methoden zum Einsatz, die eine Reaktionsfortschritt aufgelöste Bestimmung der Aktivierungsenergie gestatten. Letztere zeigen in voneinander unabhängigen Daten einen dynamischen Verlauf der scheinbaren Aktivierungsenergie. Die Ergebnisse widersprechen früheren modelbasierten Methoden, die einen einzigen Reaktionsmechanismus und eine konstante  $E_a$  anzeigen. Die Ergebnisse unterstreichen die eingeschränkte Anwendbarkeit der Avrami-Erofe'ev Methode. Stattdessen wird eine Reaktionsabfolge bestehend aus mehreren Teilschritten vorgeschlagen, die auf eine präferenzielle Abspaltung von Hydroxylgruppen abzielt. Die Erkenntnisse werden mit *ab initio* Daten der Dehydroxylation anderer Schichtsilikate verglichen. Ein mehrstufiger Reaktionsmechanismus wird von *ex situ* FTIR Daten untermauert, da es Hinweise für die Bildung einer Zwischenphase gibt. Der Artikel hebt den Einfluss einer sich ständig verändernden Primärstruktur auf die Gesamtkinetik hervor.

Der zweite Artikel setzt sich mit der thermisch induzierten Phasenumwandlung von Lizardit zu Forsterit auseinander, wobei *in situ* Hochtemperatur mikro-Raman und mikro-FTIR Spektroskopie genutzt wurde. Mit Hilfe der spektroskopischen Methoden war es möglich, eine leichte Expansion des O3-H3...O2 Abstandes und eine geringe Veränderung der ditrigonalen Verzerrung nachzuweisen. Die Dekonvolution von OH Raman Banden verweist auf eine Bandenaufspaltung. Verschiedene Gründe wie longitudinal optische-transversal optische Aufspaltung, nicht-strukturelle OH Gruppen und die Auswirkungen struktureller Heterogenitäten (verschiedene Polytype, chrysotilähnliche Verunreinigungen) werden erörtert. Die möglichen Effekte des Vorhandenseins von nicht strukturellen Hydroxylgruppen auf die vorgeschlagenen

Reaktionsmechanismen im Kapitel 4 werden diskutiert. Es bestehen konkrete Unterschiede zwischen spektroskopischen und thermogravimetrischen Daten in Bezug auf den Beginn, das Maximum und das Ende der Dehydroxylation. Diese Abweichungen werden als Folge verschiedenartiger Prozesse aufgefasst. Ermöglicht die Spektroskopie die Erfassung primärer Reaktionsschritte wie die Abspaltung von OH Gruppen, so erfasst die Thermogravimetrie eine Freisetzung von Wasser aus dem reagierenden Partikel respektive Pulver.

Das Vorhandensein eines Zwischenproduktes wurde geprüft und konnte für das Temperaturintervall von rund 640 °C bis 690 °C nachgewiesen werden. Es handelt sich um eine talkähnliche Phase ohne diagnostische OH Bande.

Die dritte Publikation untersucht die Phasenumwandlung von Chrysotil bei Normaldruck und erhöhter Temperatur mittels *in situ* Hochtemperatur mikro-Raman und mikro-FTIR Spektroskopie. Die Studie widmet sich offenen Fragen die beim Vergleich von IR und Raman Spektren bei der Polymorphe aufkommen. Ein Hauptaugenmerk liegt auf dem Einfluss der Chrysotilstruktur auf die Phasenumwandlung. Die vorangestellte Lizarditstudie (Kapitel 5) dient hierbei als Referenz.

Die Studie setzt sich aufgrund widersprüchlicher Literaturdaten vorab kritisch mit der Anzahl, der Position der Wellenzahl und Bandenzuordnung entsprechender Chrysotil-Ramanfrequenzen bei Normalbedingungen auseinander. Hoch- und Tieffrequenzbereich werden gesondert behandelt. Ähnlich wie beim Lizardit, liefern spektroskopische Untersuchungen an Chrysotil ein engeres Dehydroxylationsintervall im Vergleich zu TG Daten. Intensitätsschwankungen der OH Ramanbanden vor Einsatz des mit Hilfe der FTIR ermittelten Dehydroxylationsbereiches werden als Auswirkung einer temperaturbedingten Hydroxylreorientierung verstanden, die als Folge von Faserreorientierung und/ oder Ordnungseffekten auftreten.

Das Temperaturintervall der Chrysotildehydroxylierung ist wesentlich breiter als das von Lizardit und durch die Koexistenz von primärem Chrysotil, fehlgeordnetem Chrysotil, einer talkähnlichen Zwischenphase und Forsterit gekennzeichnet. Dies wird als Auswirkung der Chrysotilstruktur auf die Entwässerungsreaktion verstanden. Gemeinsamkeiten zwischen beiden Polymorphen sind die geringe Veränderung der ditrigonalen Verzerrung und kompatible Frequenzen der Zwischenphase.

Der vierte Artikel ist eine Fallstudie zweier bereits gut untersuchter Dehydroxylationsreaktionen, der von Chrysotil unter N<sub>2</sub> und der von Brucit unter N<sub>2</sub> und CO<sub>2</sub> Atmosphäre. Im Vergleich zu früheren Studien werden nicht isothermale TG Daten und isothermale HT-RPD Daten mit Hilfe von Isokonversionsmethoden untersucht, um die Komplexität der Reaktionen zu bewerten. DTG Signale der Reaktionen deuten auf verschiedene Grade der Komplexität hin. Chrysotil zeigt im Vergleich zu der Zerfallsreaktion von Brucit (N<sub>2</sub>, CO<sub>2</sub>) ein multiples DTG Signal. Die scheinbar simple Zersetzung von Brucit steht im Widerspruch zu Literaturdaten, die eindeutige Beweise für eine mehrstufige Reaktion zeigen. Um die zu Grunde liegenden Reaktionsmechanismen zu entschlüsseln, werden zwei unabhängige „Master Plot“ Verfahren genutzt, die einen konstanten ( $z(\alpha)$  Master Plot) bzw. dynamischen Verlauf der  $E_a$  (Verallgemeinerter Master Plot) berücksichtigen. Da alle untersuchten Reaktionen einen dynamischen Kurs der  $E_a$  aufweisen, werden die Grenzen des  $z(\alpha)$  Master Plots aufgezeigt. Der Verallgemeinerte Master Plot weist deutliche Vorteile im Bereich Reaktionsfortschritt aufgelöster mechanistischer Interpretationen auf. Die Chrysotilreaktion ist durch einen zunehmend komplexer werdenden Reaktionsmechanismus gekennzeichnet. Dieser erklärt sich aus den strukturellen Veränderungen, die mittels Spektroskopie erfasst werden können (Kapitel 6). Reaktionsmechanismen der Brucitzersetzung können in ähnlicher Weise ermittelt werden und stehen im Einklang mit früheren strukturellen Studien.

## ACKNOWLEDGMENTS

---

This PhD thesis benefited from many collaborations and personal efforts of various people in, around and far away from Fribourg.

First of all, I would like to thank Prof. Bernard Grobéty who gave a geologist the chance to work in a highly exciting field of mineralogy which bridges the gap between Earth Sciences and physical chemistry and allowed me to work with an extensive set of analytical techniques. Bernard offered me the possibility to visit workshops and conferences all over Europe in order to ‘sell’ my scientific results and broaden my horizon. I guess all the lively discussions regarding the thesis and beyond have been fruitful for both of us. Thank you for having been my ‘Doktorvater’/ supervisor!

Further on, I am very grateful to Prof. Monika Koch-Müller and Dr. Sergio Speziale (Geoforschungszentrum Potsdam/ Germany) who gave me the chance to realise my *in situ* FTIR and Raman spectroscopy studies. I would like to thank them also for their personal commitment during my stay in the laboratories of the GFZ. In this context, I am indebted to Prof. Eugen Libowitzky (University of Vienna/ Austria) for previous discussions regarding such spectroscopical experiments prior to the realised studies in Potsdam.

My grateful thanks go to Prof. Jean-Nicolas Aebischer, Prof. Pierre Brodard and Sophie Gomez-von Allmen who enabled me to use the thermoanalytical facilities at the College of Engineering and Architecture in Fribourg, helped me during various troubles with analytical devices and encouraged me to get a deeper insight into reaction kinetics.

Many thanks go to Christoph Neururer for his competent support and efforts in case of troubles and questions concerning X-ray devices and the SEM. I would like to thank Nicole Bruegger for her pleasant way to help me in administrative issues.

I wish to thank Dr. Martin Robyr for his support with the electron microprobe at the University of Bern.

Although not directly involved in my thesis, I would like to thank Prof. Jon Mosar for the opportunity to join his mapping courses which brought me back to my roots – geology.

Thanks to all my friends and colleagues at the Department of Geosciences in Fribourg, you made the last four years to a delightful and pleasant experience: André, Andres, Anna, Anneleen, Bastien, Cédric, Claudio, Claudius, Daniel, David, Eva, Florent, Giordana, Gisela, Ildiko, Jean-Paul, Jean-Pierre, Juanita, Luc, Maëlle, Marino Maggetti, Mario, Marius, Martin, Martinus, Monica, Naomi, Patrick, Raphaëlle, Silvia, Thibault, Tobias and Vincent.

A special thank to the SNF for funding this thesis!

Ein ganz herzlicher Dank gilt meinen Eltern und Großeltern in Allendorf und Leipzig, ohne deren Unterstützung die Voraussetzung für die Promotion (das Geologiestudium), nicht gegeben gewesen wäre.

My dearly thanks are dedicated to my wife Daniela and my son Leonard Richard. You make my life full of joy, encourage and support me on rainy days full of dark clouds.

## ABBREVIATION LIST

Ø	average	EDS	energy dispersive X-Ray spectroscopy
°C	degree Celsius	et al.	et alii/ and others
$\alpha$	reaction progress	etc.	et cetera/ and more
Å	Ångström	ETH	Eidgenössische Technische Hochschule
AKTS	Advanced Kinetics and Technology Solutions	FEG	field emission gun
Ar	argon	FTIR	Fourier transform infrared spectroscopy
BSE	backscattered electron(s)	FWHM	full width at half maximum
CCD	charge-coupled device	GFZ	Geoforschungszentrum
CL	cathodoluminescence	H <sup>+</sup>	proton(s)
cm <sup>-1</sup>	wavenumber units	H <sub>2</sub> O	water, water vapor, (supercritical) H <sub>2</sub> O fluid
CO <sub>2</sub>	carbon dioxide	HRTEM	high-resolution transmission electron microscopy
CRTA	Controlled Rate Thermal Analysis	HT	high-temperature
CSEM	Centre Suisse d'Electronique et de Microtechnique	HTK	Hochtemperatur-Kamera/ high-temperature camera
DAC	diamond anvil cell	HT-XRD	high-temperature X-ray diffraction
DFT	density functional theory	i.e.	id est/ that means
DTA	differential thermal analysis	ICDD	International Centre for Diffraction Data
DTG	differential thermogravimetric	ICTAC	International Confederation for Thermal Analysis and Calorimetry
DSC	differential scanning calorimetry	IR	infrared
e.g.	exempli gratia/ for example	K	Kelvin
E <sub>a</sub>	(apparent) activation energy		
E <sub>aa</sub>	reaction progress-resolved (apparent) activation energy		
EBSD	electron backscatter diffraction		

KBr	potassium bromide	SE	secondary electron(s)
kJ	kilojoule	sec	second(s)
kV	kilovolt	SEM	scanning electron microscop(e/y)
LO	longitudinal optical	t	time
ln	natural logarithm	T	temperature
mA	milliampere	T <sub>m</sub>	temperature of the melting point
mg	milligram(s)	TA	thermal analysis
min	minute(s)	TEM	transmission electron microscop(e/y)
ml	millilitre(s)	TG	thermogravimetry
mm	millimetre(s)	TGA	thermogravimetric analysis
MSH	MgO-SiO <sub>2</sub> -H <sub>2</sub> O grid	TGF	time to a given fraction
mW	milliwatt	TO	transversal optical
µm	mikrometre(s)	v <sub>as</sub>	antisymmetric stretching vibrations
N <sub>2</sub>	nitrogen	v <sub>s</sub>	symmetric stretching vibrations
nm	nanometer(s)	XRD	X-ray diffraction analysis
NMR	nuclear magnetic resonance	XRF	X-ray fluorescence analysis
N.N.	nomen nescio/ unknown autorship	XRPD	X-ray powder diffraction analysis
O <sup>-</sup>	Oxygen ion vacancy	WDS	wavelength dispersive X-ray spectroscopy
OH	hydroxyl (group)	wt%	weigth percent
OIM	orientation imaging microscopy	Further/ special characters and abbreviations are indicated in the respective chapters of this PhD thesis.	
PDF	powder diffraction file of the ICDD		
pH	activity of the hydrogen ion		
PhD	Doctor of Philosophy		
RPD	Röntgenpulverdiffraktometrie		
RRUFF	international database of Raman spectra as part of the RRUFF project		
RT	room temperature		
SAED	selected area electron diffraction		



## 1 - INTRODUCTION

---

### 1.1 RESEARCH BACKGROUND

The dehydration behaviour of the main polymorphs of the serpentine group, i.e., chrysotile, antigorite and lizardite, in general and the dehydroxylation mechanisms and kinetics in particular have drawn much attention since the first investigations of serpentine structures in the 1950s and 60s (e.g., Zussman 1954; Whittaker and Zussman 1956; Brindley and Zussman 1957; Kalousek and Muttart 1957; Zussman *et al.* 1957; Ball and Taylor 1963; Brindley and Hayami 1963a and b; Weber and Greer 1965; Naumann and Dresher 1966). This interest is related to the widespread occurrence of serpentine minerals in key geodynamic locations such as subduction and suture zones. The particular structure of chrysotile and the related thermal and mechanical properties made it a material of choice in heat protection and insulating applications. Great efforts have been made to determine their stability fields and petrological grid for the MgO-SiO<sub>2</sub>-H<sub>2</sub>O system. However, since the first attempts devoted to the identification of the stability window of each of the three polymorphs, problems are arising from the serpentine properties itself. One has to overcome following problems to achieve experimentally representative data:

#### *1. Chemical purity and mineralogical homogeneity of the sample material*

Substitution in octahedral and tetrahedral sites and metastable persistence far beyond the stability field is common for all three polymorphs. It is, therefore, difficult to find natural samples with end-member stoichiometry and containing only one polymorph. Chrysotile impurities are ubiquitous in both antigorite and lizardite

serpentinites. The peculiar crystal structures of both chrysotile and antigorite make it more difficult to define a homogenous sample. The physico-chemical properties depend on curvature for chrysotile and wavelength for antigorite, respectively. From a thermodynamic perspective, almost every serpentine mineral sample has to be considered a multiphase assemblage.

#### *2. Reconstruction of dehydroxylation mechanisms and identification of H<sub>2</sub>O bearing intermediates*

The determination of kinetic data often rests on thermoanalytical measurements, e.g., DTA, DSC, etc. Their interpretation depends on certain assumptions concerning the respective reaction equation and of the knowledge of all reaction steps/ intermediate (metastable) phase occurring during the dehydroxylation reaction. The latter, however, are poorly known and have often unknown crystal structures and/ or stoichiometry.

Resulting from these problems there are following aspects of the serpentine dehydroxylation reactions, which are unresolved or disputed in literature:

- Presence and nature of potential intermediate phase(s) during the dehydroxylation reaction, which are important to refine the MSH system especially under ambient pressure and low-pressure conditions.
- Large differences of published apparent activation energies of the serpentine breakdown reaction.
- Nature of all reaction steps occurring during the dehydroxylation reaction.

These aspects are relevant in a series of socio-economic and geoscientific issues, in which serpentine minerals play an important role:

- CO<sub>2</sub> capture and storage through simultaneous dehydroxylation and carbonation of serpentine-bearing mafites and ultramafites to reduce the global green house gases output which is of major relevance for the Earth's climate and global biochemical cycles.
- Inertisation of asbestos waste (fireproof clothing, roofing tars and shingles, thermal pipe insulation, filters, caulks, etc.) through dehydroxylation of chrysotile and transformation into harmless amorphous or crystalline phases.
- Understanding and modelling of subduction related fluid-release due to the breakdown of serpentine minerals, which is related to deep-seated earthquakes, melt-production and isotope fractionation (e.g., Ulmer and Trommsdorff 1995; Kerrick 2002; Hacker *et al.* 2003; Rüpke *et al.* 2004).

## 1.2 GOALS

The goals of this PhD thesis are directly linked to the outlined series of unresolved questions in this matter, although it is evident that not all of these problems are resolvable within the frame of a single thesis. However, this study is committed to improve the knowledge about the decomposition/phase transformation of the serpentine polymorphs lizardite and chrysotile under ambient pressure. The thesis is therefore subdivided into two parts, which include four scientific peer-review articles dealing with:

- Determination of dehydroxylation kinetics of lizardite and chrysotile by using HT-XRD and TA techniques. Here, individual aims are the application of isothermal and non-isothermal kinetics to unravel incremental reaction steps and demonstrate the limitations of such treatments.

- *In situ* Raman and FTIR investigations of the dehydroxylation and subsequent phase transformation of both polymorphs.

These spectroscopic investigations are devoted to shed light onto the single phase transformation steps by monitoring individual molecule groups (e.g., hydroxyl groups) in order to study the stability of the tetrahedral and octahedral sheet. Both spectroscopic techniques enable a much better identification of less crystalline or even amorphous intermediate phases than X-ray based techniques.

## 1.3 SERPENTINES AND SERPENTINITES: A BRIEF OVERVIEW

### 1.3.1 Serpentine bearing rocks

Serpentinites and serpentine bearing rocks in general often result from the hydration of ultramafic and mafic rocks and are therefore of secondary nature. Most serpentinites are associated with recent or ancient ocean floor sequences (Fig. 1-1), although ultramafic dykes or layered intrusions are also a preferred host (Wiebe 1988; Kerrick 2002). Ocean-floor linked serpentinisation of peridotites (dunites and harzburgites) already starts along the spreading centres of mid-ocean ridges and continues during cooling of the oceanic lithosphere (Kerrick 2002; Rüpke *et al.* 2004). Hydration is very intense along the forearc mantle wedge above the subducting lithosphere (Hyndman and Peacock 2003).

Serpentinites play a significant role in the global geochemical cycle owing to buffering and liberation effects which are associated with the serpentinisation of the ocean floor and the lithospheric mantle (Früh-Green *et al.* 2004; Agranier *et al.* 2007; Wunder *et al.* 2010). Serpentinisation causes reduced, high pH fluids with a high concentration of H<sub>2</sub> and CH<sub>4</sub>, which directly influence the rock and water chemistry and give rise to a series of further alterations and particular features such as the production

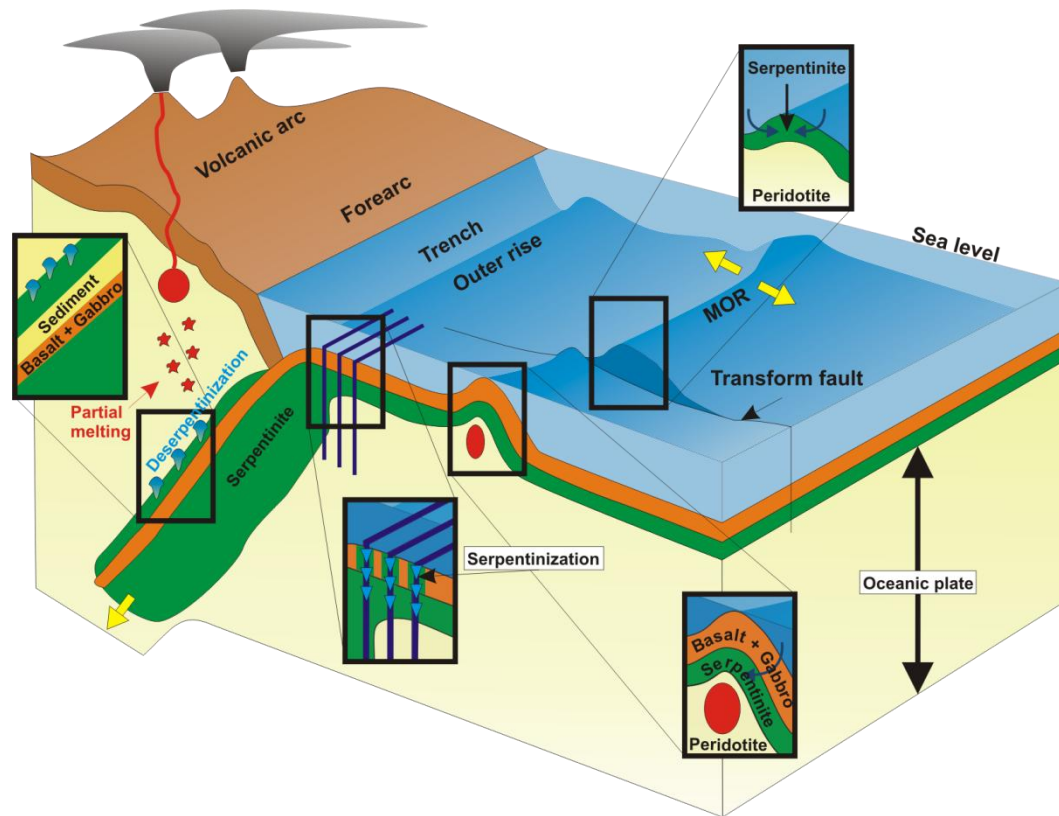


**Figure 1-1.** Geodynamic sketch of major serpentinization and deserpentinization areas along the oceanic-continental transition including divergent and convergent plate margins (modified after Kerrick 2002).

of magnetite, iron-nickel alloys and other native metals which catalyse the formation of abiogenic methane (Früh-Green *et al.* 2004). Such gaseous serpentinisation products played an important role during the evolution of life on Earth and are also responsible for specialist ecosystem on the ocean floor (Guillot and Hattori 2012). Deserpentinization processes, i.e., dehydration of serpentinites and serpentine bearing rocks, are not of minor importance as mantle melting and deep seated earthquakes which might be related to fluid release and subsequent phase transitions along subduction zones (e.g., Peacock 2001; Hacker *et al.* 2003; Padrón-Navarta *et al.* 2010).

Serpentinites in general can be distinguished into low-grade metamorphic rocks, characterised by a dominance of the lizardite and chrysotile polymorph, and high-grade metamorphic rocks, characterised by a dominance of antigorite (Wicks and O'Hanley 1988). Sluggish transformation

rates, multiple retrograde-prograde cycles as well as surficial weathering affect the nature of serpentine members present. Thus, (metastable) mixtures of various serpentine minerals within one serpentinite are common.

Industrial applications of serpentinites are manifold, but changed considerably during the last two decades. Mining and use of asbestos ceased almost completely in Europe due to the cancerogenic nature of asbestos fibres, but the extraction of nickel from obducted serpentinites is of major importance as more than 50 % of the world's reserves are hosted in such serpentinite deposits (Guillot and Hattori 2012). Sequestration and storage of carbon dioxide within serpentine bearing rocks is another application which became attractive during the last two decades (e.g., Goff and Lackner 1998).

### 1.3.2 Mineralogy and Crystallography of serpentine minerals

The serpentine group is composed of the rock-forming members called lizardite, chrysotile and antigorite, and additional rarer species like polygonal and polyhedral serpentine (Whittaker and Zussman 1956; Cressey *et al.* 2008). This group has a common chemistry of  $\text{Mg}_3\text{Si}_2\text{O}_5(\text{OH})_4$  with a variable affinity to substitute other cations for magnesium and silicon (Viti and Mellini 1997). Serpentes are trioctahedral 1:1 phyllosilicates with a hexagonal arrangement of tetrahedrally coordinated silicon in the T-sheet linked by sharing apical oxygens with octahedrally coordinated magnesium in a brucite-like O-sheet (Figs. 1-2 and 1-3). There is a mismatch along the *b* direction of an ideal Mg-occupied octahedral sheet ( $b = 9.43 \text{ \AA}$ ) and a Si-occupied tetrahedral sheet ( $b = 9.1 \text{ \AA}$ ) (Wicks and O'Hanley 1988). This mismatch can be alleviated by a series of chemical and crystallographic modifications, which give rise to the various polymorphs of the serpentine group (Wicks and O'Hanley 1988).

The reduction of the misfit within the flat lying lizardite structures (Figs. 1-2 and 1-3) is mainly achieved by  $^{\text{tet}}\text{Si}_{-1}^{\text{tet}}\text{Al}$ ,  $^{\text{oct}}\text{Mg}_{-1}^{\text{oct}}\text{Al}$  and  $^{\text{oct}}\text{Mg}_{-1}^{\text{oct}}\text{Fe}$  substitutions (Caruso and Chernosky 1979; Mellini 1982; Viti and Mellini 1997; Evans 2004; Deer *et al.* 2009), although the natural amount of substitution is much smaller than the necessary amount calculated for a full reduction of the misfit. A part of the remaining misfit is reduced by the coupled rotation of  $\text{SiO}_4$  tetrahedra resulting in ditrigonal symmetry which stabilises the lizardite structure (Mellini and Viti 1994; Mellini 1982; Evans 2004). Residual stresses are probably responsible for the limited growth of lizardite and the fine grained crystal size (Deer *et al.* 2009). In chrysotile (Fig. 1-4), the misfit is overcome by a tube-like structure with cylindrical, spiral, helical and conical wrapping schemes (Yada 1971; Yada 1979; Wicks and O'Hanley 1988; Deer *et al.* 2009). Here, the octahedral sheet forms the outer,

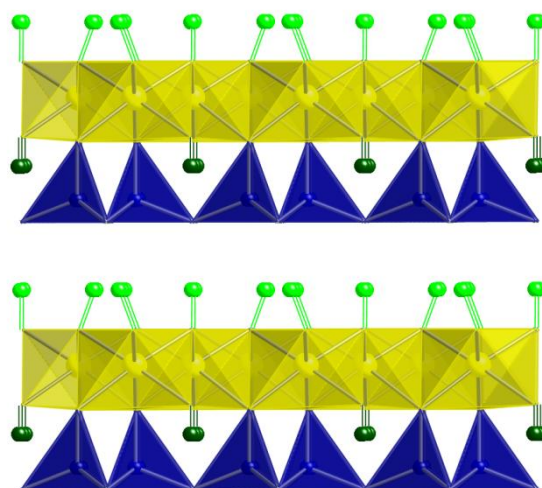


**Figure 1-2.** Crystal structure of lizardite-1T as seen along the *b* axis (modified after Mellini 1982); blue polyhedra =  $\text{SiO}_4$  tetrahedra/ T-sheet, yellow polyhedra =  $\text{Mg}(\text{O},\text{OH})_6$  octahedra/ O-sheet, dark green = inner OH, light green = inner surface/ outer OH.

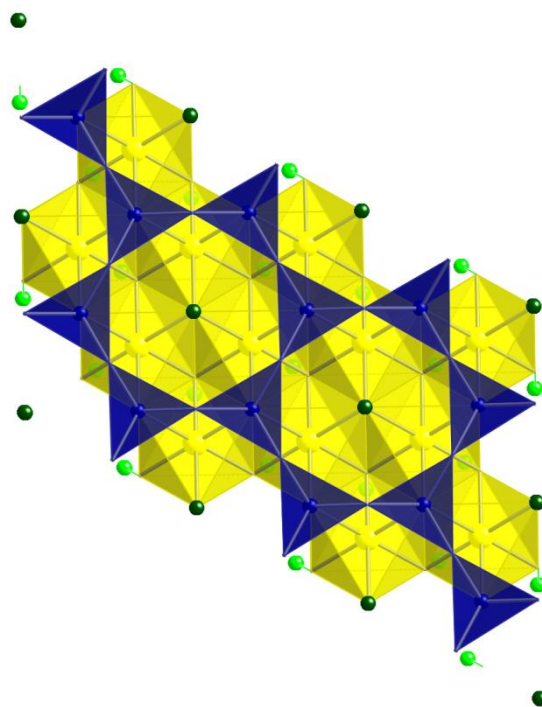


**Figure 1-3.** Crystal structure of lizardite-1T as seen along the *c* axis (modified after Mellini 1982) illustrating the trioctahedral nature and the pseudohexagonal arrangement of the  $\text{SiO}_4$  tetrahedra; structural elements are colour-coded as specified in Fig. 1-2.

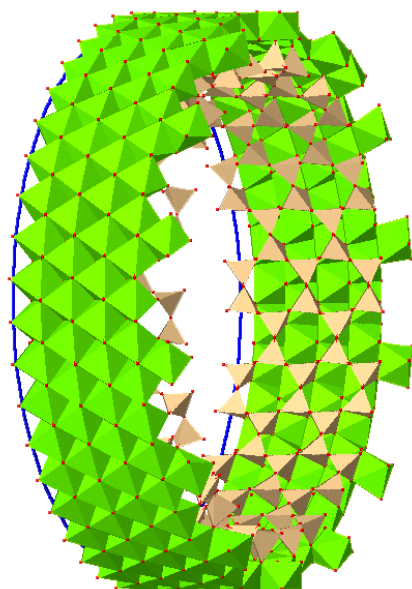


**Figure 1-4.** TO monolayer of chrysotile showing the bending of tetrahedral (yellow-red) and octahedral (light green) sheets around the *b* axis (parachrysotile) of a lizardite-like unit cell (modified after D'Arco *et al.* 2009).

convex part of the layer, as the brucite-like sheet has a larger *b* dimension than the tetrahedral sheet (Deer *et al.* 2009). Antigorite, the modification of serpentine stable in amphibolite and eclogite facies, is characterised by a wave-like corrugation of the TO-layers (Fig. 1-5) with a change of the sense of bending at inversion points. The antigorite wavelength *m* is pressure- and temperature-dependent (Grobéty 2003; Wunder *et al.* 2010). Because each second inversion is Mg-deficient, the stoichiometry of antigorite changes with the wavelength, i.e., antigorite is not a real polymorph of the serpentine mineral group and forms a polysomatic series. The stoichiometry of this polysomatic series is expressed as  $M_{3m-3}T_{2m}O_{5m}(OH)_{4m-6}$  with *M* = Mg, Fe, Cr, Ni, Al and

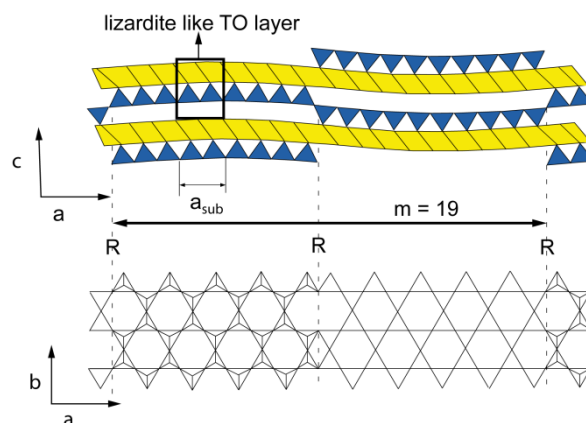


**Figure 1-5.** Corrugated structure of a *m*=19 antigorite polysome illustrating the effect of reversals (*R*) on lizardite-like building blocks as viewed along [010] (top) and [001] (bottom). Taken from Grobéty (2003) and modified after Kunze (1961) and Mellini *et al.* (1987).

Li, T = Si, Al and B, and *m* = number of tetrahedra in a wave along *a* (Kunze 1961).

Different formation conditions and the often secondary nature of serpentine minerals give rise to a variety of serpentine textures. Hourglass, mesh textures and bastite are the most prominent textures and often have a pseudomorphic character as they replace primary Mg-silicates such as olivine, pyroxene, amphibole, etc. (Dungan 1979; Wicks and O'Hanley 1988). These textures are also causal for mineralogical heterogeneities as they consist of a mixture of different polymorphs including chemical variations which also reflect a complex growth (Wicks and O'Hanley 1988; Evans 2004). Natural chrysotile samples are additionally characterised by heterogeneities related to fibre intergrowth, intergrowth of polytypes, crystallite bending, etc. (Mellini and Viti 1994).

## 2 - REACTION KINETICS OF DECOMPOSITION EXPERIMENTS: A BRIEF OVERVIEW

### 2.1 INTRODUCTION

Many reactions relevant to Earth Sciences are solid-state reactions with or without the participation of a gaseous (supercritical) phase. They are often initiated by a change in intensive parameters (e.g., temperature, pressure) or, in open systems, of extensive parameters, such as fluid composition. Typical reactions are (de)carbonisation, (de)hydration, (de)-hydroxylation, polymorphic transformations, etc. All these processes commonly occur in the frame of metamorphic and magmatic processes in general. It has to be noted, that diffusion driven processes such as order-disorder and metasomatism are also summarised under the term solid-state reactions for which local changes in concentration are often responsible.

This thesis focuses on the reaction mechanisms and kinetics of the thermally activated breakdown of the serpentine polymorphs lizardite and chrysotile. The reaction itself is triggered by the dehydroxylation of the octahedral sheet. The overall reaction can generally be described as  $\text{Mg}_3\text{Si}_2\text{O}_5(\text{OH})_{4(s)} \rightarrow \text{I}_{(s)} + \text{H}_2\text{O}_{(g)} \rightarrow \text{B}_{(s)}$ . The intermediate phases  $\text{I}_{(s)}$  have not been identified with certainty, so far. The final products  $\text{B}_{(s)}$  are forsterite followed by enstatite. The rate of the reaction has been investigated by TG. The reaction progress  $\alpha$  of this generalised equation is monitored by the mass loss of serpentine due to dehydroxylation and is expressed as:

$$\alpha = \frac{m_0 - m_t}{m_0 - m_f} \quad (2.1)$$

with  $0 \leq \alpha \leq 1$ . In case of non-isothermal experiments equation 2.1 has to be written as:

$$\alpha = \frac{m_0 - m_T}{m_0 - m_f} \quad (2.2)$$

where  $m_0$ ,  $m_t$ ,  $m_T$  and  $m_f$  are initial, time, temperature and final mass of the sample. Thus, the weight loss indicates only the rate by which volatile product(s) leave the solid reactant (Vyazovkin and Wight 1997).

The same reaction progress was studied by using *in situ* high-temperature XRPD. Here,  $\alpha$  is often expressed as:

$$\alpha = 1 - \frac{I_t}{I_0} \quad (2.3)$$

where  $I_t$  is the integral peak intensity of an individual peak at time  $t$  and  $I_0$  the initial peak intensity. Some studies use the peak amplitude only instead of the integral intensity to define  $\alpha$ . Care must be taken when defining the initial intensity  $I_0$ . Strictly speaking  $I_0$  corresponds to the peak intensity before dehydroxylation starts. As XRPD peak intensities are also a function of temperature, it is necessary to measure  $I_0$  immediately before the onset of the decomposition reaction. Isothermal experiments have one major disadvantage, namely that for all temperature above the equilibrium temperature, it is impossible to determine  $I_0$  exactly (because of finite heating rates). The dehydroxylation starts already before the actual temperature of interest is reached. Here,  $I_0$  was defined as the first measured integral intensity at the isothermal temperature of interest. Thus, one has to bear in mind, that, despite the fastest possible heating rates were used, the activation energies calculated for small reaction progress at high temperatures are seriously influenced by this artefact.



With the reaction progress  $\alpha$  defined as the fraction of serpentine phase converted, the rate of the reaction can be parameterised as function of temperature  $T$  and  $\alpha$ :

$$\frac{d\alpha}{dt} = k(T)f(\alpha) \quad (2.4)$$

where  $k(T)$  is the temperature-dependent rate constant and  $f(\alpha)$  is the function describing the rate-determining reaction step, i.e., a certain reaction model. There is a large number of reaction models  $f(\alpha)$ , which have been used to describe solid state reactions like 1-dimensional, 2-dimensional, 3-dimensional diffusion, nucleation and growth models, etc. For a rate limiting step, which can be described by a first order reaction, the above rate equation is given as:

$$\text{Rate} = \frac{d\alpha}{dt} = k(1 - \alpha) \quad (2.5)$$

or in integrated form

$$-\ln(1 - \alpha) = kt \quad (2.6)$$

The rate constant  $k$  is usually given by the Arrhenius equation:

$$k(T) = Ae^{-\frac{E_a}{RT}} \quad (2.7)$$

with the pre-exponential factor  $A$ , the activation energy  $E_a$ , the gas constant  $R$  and the absolute temperature  $T$ . Replacing  $k(T)$  in equation (2.4) by equation (2.7) gives

$$\frac{d\alpha}{dt} = Ae^{-\frac{E_a}{RT}} f(\alpha) \quad (2.8)$$

Alternatively, one can use the integral form which gives

$$g(\alpha) = \int_0^\alpha [f(\alpha)]^{-1} d(\alpha) = k(T)t \quad (2.9)$$

Reactions are usually subdivided into two different categories, namely homogeneous and heterogeneous ones. Whereas homogeneous reactions refer to ongoing reactions within a single macroscopic phase or a gas, heterogeneous

reactions comprise any kind of interface controlled reaction (Lasaga 1998). Thus, almost all solid-state reactions are thought to be heterogeneous, except of some polymorphic and order-disorder reactions. One main difference between both reaction types is the ability of freely moving and identical reactants in case of homogeneous reactions and a fixed position of reactants within a crystal lattice in case of heterogeneous reactions (Galwey 2003; Khawam 2007). Reacting molecule groups, e.g., hydroxyls groups within crystals are sometimes characterised by a non-equivalent surrounding. For instance, differing distances to adjacent OH groups which can result in a preferential loss during dehydroxylation reactions (see Chapter 4). Thus, combinations with different neighbours result in divergent activation energies for different kinds of reacting OH pairs. They are therefore considered as different elementary steps. An *ab initio* model showing such behaviour is given by Molina-Montes *et al.* (2008a and b). All reactions including at least two of such elementary steps with their own activation energies are considered as complex (Steinfeld *et al.* 1999).

There are multiple ongoing elementary steps in a solid-state reaction. This elementary steps cause either consecutive/ sequential or parallel reaction mechanisms. However, parallel and sequential mechanisms are often acting simultaneously during dehydroxylation reactions, i.e., they are itself dependent on a reaction progress. Nevertheless, it is virtually possible to define a rate-determining step as known from homogeneous reactions. The latter corresponds to the slowest step determining the reaction rate in case of a sequential reaction. In a series of parallel reactions the fastest rate is rate-determining (Lasaga 1998). This general statement holds only in case of large differences between the ‘velocity’ of individual reaction steps, i.e., only if one step is much faster than another, the overall rate will be determined by the slowest step (Vyazovkin 2008). A simple model representing a simplified sequential reaction mechanism is illustrated in Fig. 2-1. There, the water flow from left to right will be determined by the tube with the smallest diameter which is between box B and C.



**Figure 2-1.** Water flow scheme illustrating a reaction controlled by sequential reaction mechanisms ( $A \rightarrow B \rightarrow C \rightarrow D$ ); the water flow from  $A \rightarrow D$  will be limited/ determined by the narrowest tube diameter which is between B and C.

A parallel reaction model is illustrated in Fig. 2-2 with a water flow from a reservoir at the top to a basin at the bottom. As more water can pass the tube on the right hand side of the scheme, the overall process is mainly determined by the tube with the largest diameter.

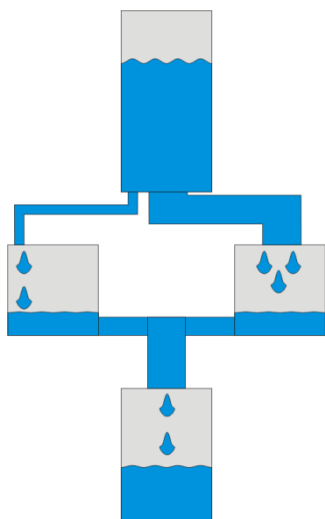


**Figure 2-2.** Water flow scheme illustrating a reaction controlled by parallel reaction mechanisms; in such a case the fastest step, i.e., the larger tube diameter on the right-hand side of the scheme, will be the rate-determining step for the overall reaction.

Independent of the rate-determining step, the overall reaction is characterised by a contribution of each elementary step. In the case that the rate of a reaction is determined by  $i$  parallel elementary reaction steps, the general rate equation (2.8) has to be extended by introducing weights  $w_i$  of individual reaction steps (modified after Vyazovkin 2008):

$$\frac{d\alpha}{dt} = w_1 k_1 f_1(\alpha) + \dots + w_i k_i f_i(\alpha) \quad (2.10)$$

By taking the logarithmic derivative of the above reaction rate at a constant  $\alpha$ , it is possible to determine the apparent  $E_a$  at each  $\alpha$  as follows:

$$E_{a\alpha} = -R \left[ \frac{d \ln \left( \frac{d\alpha}{dt} \right)}{dT^{-1}} \right]_{\alpha} \\ = \frac{w_1 E_1 k_1 f_1(\alpha) + \dots + w_i E_i k_i f_i(\alpha)}{w_1 k_1 f_1(\alpha) + \dots + w_i k_i f_i(\alpha)} \quad (2.11)$$

Thus, it is obvious that the apparent  $E_a$  is a function of  $\alpha$  and  $T$ . This dependency is valid for all apparent  $E_a$  estimated by isoconversional methods. By doing so, it is possible to consider the relative contribution of single steps to the overall reaction rate, but there is no chance to extract the  $E_a$  of a single reaction step (Vyazovkin 2000b).

The ‘variable activation energy’ provoked lively and persistent discussions between traditionalists and vanguards in the field of thermoanalysis culminating in a publication of Galwey (2003) and an immediate reply by Vyazovkin (2003). The term ‘variable activation energy’ refers to a variable course of the effective or more often labelled ‘apparent activation energy’. This term accentuates that the experimentally determined ‘activation energy’ is a function of the rates of several simultaneously occurring single step reactions, each of which with a unique energy barrier (Vyazovkin 2003). It is, thus, not equal to the enthalpy of the reaction activation (Vyazovkin 2003).

## 2.2 ISOTHERMAL APPROACH

Isothermal data usually contain useful kinetic information only over a small temperature range. This is due to the fact that experiments at temperature close to the equilibrium temperature for the given reaction are often too time-consuming, while experiments at high-temperatures often yield just a small number of sustainable data points. Nevertheless, such data allow the determination of both the overall apparent activation energy as well as a reaction progress,  $\alpha$ , resolved apparent activation energies with respect to the examined temperature range. Elementary rate-limiting steps are often ‘determined’ by force-fitting experimental data to given theoretical reaction models  $f(\alpha)$  of which some important ones are shown in Table 2-1. A popular way to extract a mechanistic model from an  $\alpha$ - $t$  plot is the classical Avrami-Erofe’ev treatment (Bamford and Tipper 1980) like follows:

$$\alpha = 1 - e^{-(kt)^n} \quad (2.12)$$

Thus, the rate-determining step is obtained by extracting  $n$  from the best fit, which is usually done by linearising the function by taking the logarithm two times:

$$\ln(-\ln(1-\alpha)) = n \ln k + n \ln t \quad (2.13)$$

plotting  $\alpha$ - $t$  pairs into a  $\ln(-\ln(1-\alpha))$  versus  $\ln(t)$  graph and performing a linear regression (Hancock and Sharp 1972). The parameter  $n$  corresponds to the slope of the corresponding lines. In a similar way, the rate constant  $k$  can be extracted from the intercept on the y axis which corresponds to  $n \ln k$ . The extraction of these parameters is only valid if the Avrami-Erofe’ev equation is the appropriate function to describe the rate-determining step over the range of reaction progress considered. Varying values of  $n$  and non-parallel straight lines in the double logarithmic plot, respectively, indicate a temperature dependent change in the rate-limiting step(s).

Afterwards, the Arrhenius plot of  $\ln k_T$  against  $1/T_i$  is used to determine the apparent  $E_a$  after

performing a series of isothermal runs  $T_1, \dots, T_i$ . This method gives a single apparent  $E_a$ . In literature, this value is sometimes used to state whether the reaction is diffusion-controlled or not (e.g., Tokiwai and Nakashima 2010). The apparent  $E_a$  deduced from this sometimes called ‘rate constant’ method is biased by the empirical selection of the differential reaction model  $f(\alpha)$  (Putnis 1992). Moreover, that value is only meaningful when the rate is controlled by the same reaction step(s) over the entire reaction progress. An elegant method to circumvent these problems is the application of isoconversional methods. The base of these methods is the isoconversional principle saying that the reaction rate is a function of temperature and conversion alone, and that the temperature dependence obeys the Arrhenius equation (Šimon 2004). The starting point of the ‘time to a given fraction’ (TGF) method resting on an isothermal dataset is, that the integral in equation (2.15) for a given  $\alpha$  range is constant over the studied temperature range (Burke 1965; Putnis 1992). In doing so, one can rearrange equation (2.4) as follows:

$$dt = k^{-1} f^{-1}(\alpha) d\alpha \quad (2.14)$$

Thus, the time  $t_\alpha$ , i.e., time  $t$  necessary for reaching certain  $\alpha$  at a respective temperature  $T$ , is given by:

$$t_{\alpha_i} = k^{-1} \int_{\alpha=0}^{\alpha=\alpha_i} f^{-1}(\alpha) d\alpha \quad (2.15)$$

The integral has a constant value only if the reaction model  $f(\alpha)$  does not change over the temperature range studied. The corresponding apparent  $E_a$  of an arbitrary chosen value of  $0 \leq \alpha \leq 1$  can thus be calculated from the slope  $E_a/R$  of the graph in a plot of  $\ln t_\alpha$  against  $1/T$ . It has to be noted that the apparent  $E_a$  calculated for a given  $\alpha$  by this method is the mean value from  $\alpha = 0$  to an  $\alpha$  of interest or two  $\alpha$  of interest defining a certain range of the reaction progress. If this average value does not change with  $\alpha$ , the rate-determining step or combination of steps and their contributions to the overall reaction are the same over the entire temperature range studied and independent of  $\alpha$ .

Mechanistic model	Symbol	$f(\alpha)$	$g(\alpha)$
<i>Nucleation models</i>			
(Random nucleation and growth of nuclei through different nucleation and nucleus growth)			
Avrami-Erofeev eq., $n=2$	A2	$2(1-\alpha)[- \ln(1-\alpha)]^{1/2}$	$[- \ln(1-\alpha)]^{1/2}$
Avrami-Erofeev eq., $n=2.5$	A2.5	$2.5(1-\alpha)[- \ln(1-\alpha)]^{3/5}$	$[- \ln(1-\alpha)]^{1/2.5}$
Avrami-Erofeev eq., $n=3$	A3	$3(1-\alpha)[- \ln(1-\alpha)]^{2/3}$	$[- \ln(1-\alpha)]^{1/3}$
Avrami-Erofeev eq., $n=4$	A4	$4(1-\alpha)[- \ln(1-\alpha)]^{3/4}$	$[- \ln(1-\alpha)]^{1/4}$
<i>Geometrical contraction models</i>			
Phase boundary controlled reaction (contracting area)	R2	$2(1-\alpha)^{1/2}$	$[1 - (1-\alpha)^{1/2}]$
Phase boundary controlled reaction (contracting volume)	R3	$3(1-\alpha)^{2/3}$	$[1 - (1-\alpha)^{1/3}]$
<i>Diffusion models</i>			
One-dimensional diffusion (Parabola law)	D1	$1/(2\alpha)$	$\alpha^2$
Two-dimensional diffusion (Valensi equation)	D2	$[- \ln(1-\alpha)]^{-1}$	$(1-\alpha)\ln(1-\alpha) + \alpha$
Three-dimensional diffusion (Jander equation)	D3	$\frac{[3(1-\alpha)^{2/3}]}{[2(1-(1-\alpha)^{1/3})]}$	$[1 - (1-\alpha)^{1/3}]^2$
<i>Reaction order model</i>			
First order (Mampel) (Random nucleation followed by instantaneous growth of nuclei) Avrami-Erofeev eq., $n=1$	F1, A1	$(1-\alpha)$	$-\ln(1-\alpha)$

<sup>a</sup>Vyazovkin *et al.* (2011), <sup>b</sup>Sánchez-Jiménez *et al.* (2013)

**Table 2-1.** Differential  $f(\alpha)$  and integral  $g(\alpha)$  functions of some widely used kinetic models in the solid-state kinetics<sup>a,b</sup>.

In order to obtain absolute activation energies as function of  $\alpha$ , it is better to perform a series of non-isothermal experiments and treat the data with isoconversional methods.

### 2.3 NON-ISOTHERMAL APPROACH

Although non-isothermal approaches have already been used in early times of solid-state reaction research, dynamic temperature programs and isoconversional methods to analyse solid-state processes have rarely been applied in Earth Sciences. Reasons for this absence are unknown. Most solid-state reactions in Earth Science

literature such as dehydroxylation, dehydration or decarbonisation reactions are treated as single rate-determining-step processes. Such behaviour is rather unlikely. Although the physical properties measured by thermal analysis cannot be linked directly to specific elementary reaction steps of molecules, the overall transformation can generally involve more than a single reaction step (Vyazovkin *et al.* 2011). It has to be mentioned that diffusion which is often considered as the rate-determining step, adds an extra reaction step to primary occurring chemical reaction steps. Thus, the overall process rate, including the resulting apparent  $E_a$ , becomes dependent on the chemical reaction rate and the transport rate of reactants and

products in the reaction medium (Vyazovkin 2008).

Non-isothermal isoconversional calculations were made by using the differential method offered by Friedman (1964) and the integral approach proposed by Vyazovkin (2008). The latter differ in the treatment of the temperature integral in order to refine the reaction progress resolved determination of  $E_a$ . All of these methods allow the extraction of the activation energy for a given  $\alpha$ . A main advantage of the methods provided by Vyazovkin is the integration over small increments of  $\alpha$  rather than integration over a large range of  $\alpha$ . Friedman's method follows directly the general rate equation by taking the logarithm:

$$\ln\left(\frac{d\alpha}{dt}\right)_{\alpha,i} = \ln(A_\alpha f(\alpha)) - \frac{E_a}{RT_{\alpha,i}} \quad (2.16)$$

The subscript  $i$  denotes a series of different linear heating rates. The slope ( $\sim E_a/R$ ) of corresponding plots of  $\ln(d\alpha/dt)_{\alpha,i}$  against  $1/T$  delivers the apparent  $E_a$  for a given  $\alpha$ . However, this method is very sensitive to experimental noise, especially in case of deviations from a linear heating rate (Vyazovkin 2001). Such problems can be circumvented by using integral methods. Following relationship holds for non-isothermal experiments:

$$\frac{d\alpha}{dT} = \frac{d\alpha}{dt} \cdot \frac{dt}{dT} \quad (2.17)$$

with  $d\alpha/dT$  the non-isothermal reaction rate and  $d\alpha/dt$  the isothermal reaction rate. Introducing equation (2.17) into equation (2.8) and defining the heating rate  $\beta = dT/dt$  results in the differential non-isothermal rate law:

$$\frac{d\alpha}{dT} = \frac{A}{\beta} e^{-\frac{E_a}{RT}} f(\alpha) \quad (2.18)$$

Integration gives:

$$g(\alpha) = \frac{A}{\beta} \int_0^T e^{-\frac{E_a}{RT}} dT \quad (2.19)$$

The obtained equation contains the temperature integral for which there is no analytical solution. Nowadays, the temperature integral is mostly approximated by the Senum-Yang approximation (Senum and Yang 1977). Several methods have been proposed by Vyazovkin (Vyazovkin 1996, 1997 and 2001) to increase the accuracy of the numerical integration and to apply the method for any variation of the temperature. Generalising of Equation (2.19) gives:

$$g(\alpha) = \frac{AE_a}{\beta R} I(E_a, T) \quad (2.20)$$

where  $I(E_a, T)$  corresponds to a general expression of the numerical approximation of the temperature integral. A comprehensive overview including single substitution steps to approximate the integral as proposed by Vyazovkin (1996, 1997) is given in Khawam (2007).

The proposed methods of Vyazovkin are based on the general assumption that the reaction model  $g(\alpha)$  is independent of the chosen heating rate. Such an assumption leads to following expression for a particular degree of conversion  $\alpha$ :

$$\begin{aligned} g(\alpha) &= \frac{A_\alpha E_{a\alpha}}{\beta_1 R} I(E_{a\alpha}, T_{\alpha 1}) \\ &= \frac{A_\alpha E_{a\alpha}}{\beta_2 R} I(E_{a\alpha}, T_{\alpha 2}) \quad (2.21) \end{aligned}$$

Here,  $\beta_1$  denotes the first heating rate,  $\beta_2$  denotes the second heating rate,  $T_{\alpha 1}$  and  $T_{\alpha 2}$  are the temperatures for which a given  $\alpha$  is reached using the first and second heating rate, respectively,  $E_{a\alpha}$  the apparent  $E_a$  at the chosen  $\alpha$  of interest and  $A_\alpha$  the pre-exponential factor at that  $\alpha$ . Equation (2.21) can be reduced to:

$$\begin{aligned} \frac{I(E_{a\alpha}, T_{\alpha 1})}{\beta_1} &= \frac{I(E_{a\alpha}, T_{\alpha 2})}{\beta_2} = \dots = \frac{I(E_{a\alpha}, T_{\alpha i})}{\beta_i} \\ &= \sigma \quad (2.22) \end{aligned}$$

where,  $\sigma$  is a constant. In case of three different heating rates ( $\beta_1$ ,  $\beta_2$  and  $\beta_3$ ) and division of each corresponding heating rate term by each other, we get:

$$\begin{aligned} \frac{\beta_1 I(E_{a\alpha}, T_{\alpha 2})}{\beta_2 I(E_{a\alpha}, T_{\alpha 1})} &= \frac{\beta_2 I(E_{a\alpha}, T_{\alpha 3})}{\beta_3 I(E_{a\alpha}, T_{\alpha 2})} = \frac{\beta_3 I(E_{a\alpha}, T_{\alpha 1})}{\beta_1 I(E_{a\alpha}, T_{\alpha 3})} \\ &= \frac{\beta_1 I(E_{a\alpha}, T_{\alpha 3})}{\beta_3 I(E_{a\alpha}, T_{\alpha 1})} = \frac{\beta_2 I(E_{a\alpha}, T_{\alpha 2})}{\beta_1 I(E_{a\alpha}, T_{\alpha 2})} \\ &= 6 \quad (2.22) \end{aligned}$$

For a series of runs, i.e.,  $i$  heating rates,  $E_{a\alpha}$  can then be calculated by minimising:

$$\Omega = \left| n(n-1) - \sum_{i=1}^n \sum_{j \neq i}^n \frac{\beta_j I(E_{a\alpha}, T_{\alpha i})}{\beta_i I(E_{a\alpha}, T_{\alpha j})} \right| \quad (2.23)$$

This approach, often referred as the Vyazovkin method, is only valid for constant heating rates, which is often not real considering the temperature evolution of the sample. Thus, Vyazovkin (2001) introduced an advanced isoconversional method valid for any temperature program and for instantaneous changes of  $E_{a\alpha}$ . The temperature integral is substituted by a time-dependent temperature integral, where an arbitrary number of small and equidistant time intervals are chosen to subdivide the overall reaction. Thus, the integral is written as:

$$g(\alpha)_\alpha = A_\alpha \int_{t_{\alpha-\Delta\alpha}}^{t_\alpha} e^{-\frac{E_a}{RT(t)}} dt \quad (2.24)$$

where  $\Delta\alpha = 1/m$  and  $m$  is the arbitrary chosen number of intervals. Generalising equation (2.24) for a series of runs,  $E_{a\alpha}$  can be determined by minimising:

$$\Omega = \left| \sum_{i=1}^n \sum_{j \neq i}^n \frac{J(E_{a\alpha}, T_i(t_\alpha))}{J(E_{a\alpha}, T_j(t_\alpha))} \right| \quad (2.25)$$

## 2.4 HOW TO DEAL WITH VARIABLE APPARENT ACTIVATION ENERGIES?

After the calculation of  $E_{a\alpha}$  by either a differential or an integral method it is necessary to evaluate if a change in  $E_a$  with  $\alpha$  is real or just due to errors of the calculation procedure or the chosen analytical technique (e.g., DSC, TGA, FTIR, XRD,

etc.). This evaluation is not straightforward as reactions, which are believed to be controlled by a single step are also characterised by a certain extent of variation in  $E_{a\alpha}$  (Vyazovkin and Wight 1997). Apparently simple examples are dehydroxylation or decarbonization reactions. For  $\text{CaCO}_3$ , and  $\text{Mg}(\text{OH})_2$ , the general reaction can be described as  $\text{MCO}_{3(s)} \text{ or } -\text{M}(\text{OH})_{n(s)} \rightarrow \text{MO}_{n(s)} + \text{H}_2\text{O}_{(g)} \text{ or } \text{CO}_{2(g)}$ . Following reaction steps may be distinguished: debonding of hydroxyl and carbonate groups, respectively, transport of the gaseous products, nucleation and growth of the solid product phase. A common theory (Taylor 1962; Guggenheim *et al.* 1987; Mazzucato *et al.* 1999) on the formation of water by dehydroxylation is the reaction of two adjacent hydroxyl groups, i.e.,  $\text{OH}^- + \text{OH}^- \rightarrow \text{H}_2\text{O} + \text{O}^-$ . Prior to mineralogical applications using high-resolution electron microscopy techniques, most of such decomposition reactions were described as reactions forming one solid product phase and an associated gaseous product. Therefore, they have often been described to be homogeneous in nature (see Taylor 1962 for references). But, the nucleation and growth of a product structure within a host phase have a major impact on the overall reaction kinetics, which should shortly be demonstrated in two case examples.

Two mineralogical important phases, i.e.,  $\text{CaCO}_3$  and  $\text{Mg}(\text{OH})_2$ , are chosen to give a brief overview about the complexity in interpreting variable activation energies and their controversies in literature. The reaction kinetics of the calcite  $\text{CaCO}_3$  decomposition were comprehensively studied by the ICTAC project (Brown *et al.* 2000) using a multi-analytical approach. Model-dependent non-isothermal and isothermal as well as model-free approaches under nitrogen and vacuum conditions were used to decipher the decomposition kinetics. The varying nature of calculated activation energies of the calcite decomposition for different experimental conditions and a varying reaction progress are summarised in Table 2-2.

atmosphere	non-isothermal [kJ/mol]	isothermal [kJ/mol]
Vacuum	low $\alpha$ : 105-204	low $\alpha$ : 227-262
	high $\alpha$ : 89-187	high $\alpha$ : 120-221
	Ø 102-138	Ø 220-224
Nitrogen	low $\alpha$ : 163-223	low $\alpha$ : 156
	high $\alpha$ : 131-211	high $\alpha$ : 183
	Ø 197	Ø 175-191

**Table 2-2.** Overview about the range of apparent activation energies derived from isothermal and non-isothermal model-fitting and model-free techniques of the decarbonization reaction of  $\text{CaCO}_3$  presented in the frame of the ICTAC Kinetics Project 2000 (Brown *et al.* 2000).

Maciejewski (2000) stresses the influence of the calculation routine and the chosen atmosphere when determining kinetic data of the  $\text{CaCO}_3$  decomposition. This point is often neglected especially in literature comparing experimental data of one study with kinetic data published elsewhere without giving explicit information regarding the atmosphere. It is important to note that even similar  $E_a$ - $\alpha$  dependencies of the overall decomposition reaction cause diverging interpretations of elementary reaction steps. Such differing interpretations are obvious between the studies of Farjas and Roura (2011), Rodriguez-Navarro *et al.* (2009) and Maciejewski (1992). Their published evolution of  $E_a$  versus  $\alpha$  is similar, i.e., all three datasets are characterised by a decreasing trend starting in the range of 200 kJ/mol for low  $\alpha$  and going down to around 170-180 kJ/mol for high  $\alpha$ . In addition, Rodriguez-Navarro *et al.* (2009) document a slight increase in  $E_a$  up to  $\alpha = 0.2$ . Farjas and Roura (2011) propose a single-step reaction model based on the only weakly decreasing  $E_a$  versus  $\alpha$  dependency. They consolidate their single-step model by the low variation amplitude  $\Delta E_a/E_a$ , which is less than 4 % for the range  $0.2 \leq \alpha \leq 0.8$ . However, they obtained no further analytical data on the decomposition reaction in their study. Rodriguez-Navarro *et al.* (2009) realised a comprehensive study of the thermal decomposition of calcite by using XRD,

electron microscopy and TGA from which they calculated kinetic parameters. They interpret there  $E_a$  versus  $\alpha$  dependency as resulting from a complex reaction mechanism including multiple reaction steps owing to a reaction progress towards the core of the particles. They suggest two possible rate-limiting steps from the course of  $E_a$ , i.e., a diffusion-controlled reaction in the range  $\alpha \leq 0.2$  and a first-order chemical reaction at  $\alpha \geq 0.2$ . These suggestions are supported by the model-fitting procedure which delivers D1 (1D diffusion) and F1 (first-order reaction) as best fit. The 1D diffusion model as early rate-limiting step is explained by the growing product layer of CaO along the edges of the primary calcite particles inhibiting a fast diffusion of  $\text{CO}_2$  out of the particles. They interpret the F1 model as related to a simple decarbonisation reaction with a topotactic or shear-type growth of the product phase. However, although they support their diffusion model with literature and structural data, the increasing  $E_a$  versus  $\alpha$  dependency is in contradiction with the general assumption made for diffusion reactions given by Vyazovkin and Wight (1997). They latter deduce a decreasing  $E_a$  versus  $\alpha$  dependency for solid  $\rightarrow$  solid + gas reaction, in which the solid product grows on top of the remaining reactant. This forces the gaseous product to diffuse through this layer and diffusion becomes the rate-limiting step of the decomposition. It has to be stated that Rodriguez-Navarro *et al.* (2009) used the integral method developed by Ozawa (1965) and Flynn-Wall (1966). A major drawback of this method is the crude approximation of the temperature interval which results in inaccurate values of the apparent  $E_a$  (Vyazovkin *et al.* 2011). Therefore, the suggestion of Rodriguez-Navarro *et al.* (2009) that their calculated minimum  $E_a$  is close to the reaction enthalpy of calcite reported by Fuller and Yoss (1987) is improbable considering the interpretational value of data derived from their indicated techniques (Maciejewski 2000).

In literature, the mechanistic interpretation of different dehydroxylation experiments of brucite  $\text{Mg}(\text{OH})_2$  are similar. Published values of the

apparent  $E_a$ , either determined by isothermal or non-isothermal techniques, lie in the range of around 150 kJ/mol to around 190 kJ/mol (Gordon and Kingery 1967; Butt *et al.* 1996; L'vov and Ugolkov 2004; Yue *et al.* 2005; Nahdi *et al.* 2009), although these authors used different approaches, different sample weights and different gas atmospheres. Isoconversional calculations of the  $E_a$  versus  $\alpha$  dependency yield a flat, slightly decreasing curve in the range  $0.2 \leq \alpha \leq 0.8$  (see Fig. 7-6 in Chapter 7). Although differing in detail, proposed mechanisms derived from model-fitting approaches favour a nucleation and growth mechanism as the rate-limiting step (Yue *et al.* 2005; Nahdi *et al.* 2009). These findings are also in agreement with isothermal studies done by Halikia *et al.* (1998) and non-isothermal studies of Halikia and Economacou (1993), although the published  $E_a$  are smaller than those of the other authors.

McKelvy *et al.* (2006) decipher the brucite decomposition reaction and successfully illustrate the dehydroxylation progress by HRTEM techniques. Their results point to a lamellar nucleation and growth mechanism forming regions

of lamellar oxyhydroxide. Yue *et al.* (2005) point out that the water pressure has a major influence on the dehydroxylation reaction of  $\text{Mg}(\text{OH})_2$ , i.e., on the reaction mechanism itself, which, in the opinion of the authors, changes from A2 to A1.5. Well, this point has to be considered in any kind of dehydroxylation reaction, or, generally speaking, for all reactions sensitive to a change in the concentration of the gaseous product (Maciejewski 1992). A comprehensive summary of extrinsic parameters effecting solid state reactions producing gaseous products are given by Roduit *et al.* (1996) and Maciejewski (1992).

This short literature appraisal may illuminate the ambiguous aspects of dealing with reaction kinetics and the difficulties arising when trying to find supporting data/ information for own kinetic studies. A more detailed discussion on the brucite decomposition kinetics and the application of master plots for defining reaction mechanisms follows in Chapter 7.



## 3 - EXPERIMENTAL METHODS

---

### 3.1 FTIR AND RAMAN SPECTROSCOPY

#### 3.1.1 Reasons for the chosen methods

The use of spectroscopic techniques, i.e., micro-FTIR and micro-Raman spectroscopy, in the framework of the present PhD thesis is related to the versatility of such methods regarding the identification of less crystalline or amorphous phases when compared to XRD studies. The latter are also not suited to unravel a temperature induced change in the short range order whereas spectroscopic techniques provide a sufficient insight in such scales. Reasons for gathering this knowledge are related to questions arising from measured properties of the reaction kinetics in general, i.e., empirical values such as the apparent activation energy  $E_{aa}$ . A comprehensive kinetic interpretation focussing on mechanistic issues is not possible without data derived from accompanied techniques offering results from the overall phase change. Thus, the spectroscopic detection of an OH containing talc-like phase as one intermediate of the temperature-induced phase transformation of lizardite and chrysotile is an essential result of this work and helps to refine the interpretation of the reaction kinetics (see Chapters 5 and 6). The possibility to measure changes in the short range order enables an almost immediate detection of site specific changes, e.g., distortion of the ditrigonal  $\text{SiO}_4$  arrangement, release of OH, formation of non-structural OH, etc.

Microscope-based spectroscopy systems were chosen in order to avoid a complex sample preparation especially with chrysotile fibres. These techniques are also suited to perform *in situ* dehydroxylation experiments, which cannot be realised with conventional non-microscope coupled Raman and FTIR spectrometers.

#### 3.1.2 Brief historical background

The application of Raman spectroscopy goes back to the 1920s as Smekal (1923) made first theoretical predictions on the interaction of matter and light (Nasdala *et al.* 2004). Later on, the predictions of Smekal (1923) were practically verified by Raman and Krishnan (1928) on liquids and by Landsberg and Mandelstam (1928) in crystals. Disadvantages over infrared spectroscopy, e.g., the use of mercury arcs instead of lasers used in Raman spectrometers or the properties of natural samples in general (impurities, structural defects, micro-inclusions), prevent a widespread application of Raman spectroscopy in Earth Sciences until the 1980s/ 90s (Nasdala *et al.* 2004). However, the fast developments of laser systems, fibre optics, the use of CCD detectors and the combination with appropriate microscope systems have gained growing interest in this field (Pelletier 1999).

Infrared spectrometers were developed based on the discovery of infrared radiation by Herschel 1800. However, the first commercial infrared spectrometer became available in the 1940s, although the first infrared spectra were already published in 1905 (Farmer 1974b). The development of the Fourier transform technique and the use of Michelson interferometer in the 1960s, a crucial part of modern infrared spectrometers, offered the possibility for more use after 1965 (Thomas 11<sup>th</sup> March 2013).

Both techniques are nowadays an easy-to-use and a mostly destruction free technique in Earth Sciences. Especially the use of Raman spectrometers increased rapidly during the last two decades. The combination with heating stages and diamond anvil cells placed onto Raman/ FTIR microscopes offers additional applications for

studying phase transition and/ or phase transformation reactions at non-ambient conditions to get a better insight into ongoing reactions in the Earth's interior. Moreover, the use of microscopes enables two-dimensional projections of the measured Raman/ infrared signals from a surface of interest (Raman/ IR mapping).

### 3.1.3 Micro-FTIR spectroscopy (at non-ambient temperatures)

Infrared spectroscopy based *in situ* dehydroxylation experiments were realised by using a Bruker VERTEX 80v FTIR spectrometer attached to a Hyperion1000 infrared microscope equipped with a software-controlled Linkam TS1000 heating stage at the GeoForschungsZentrum Potsdam/ Germany. Spectral measurements were limited to the 2500-4000  $\text{cm}^{-1}$  range owing to the defect of the low-frequency detector at the measurement interval in June/ July 2011. These circumstances prevent comparative studies between FTIR and Raman investigations in the low-frequency range indicative for lattice vibrations such as Si-O and Mg-O modes.

Spectra were collected by using a Globar light source, a KBr beamsplitter and a liquid nitrogen (LN) cooled InSb D413 detector for the 2500-4000  $\text{cm}^{-1}$  range. Single spectra were acquired with a resolution of 2  $\text{cm}^{-1}$  and averaged over 60 individual scans resulting in a measurement interval of about 64 s. This measurement procedure was chosen to achieve a compromise between resolution and a linear heating rate of 1 K/min. A transparent lizardite film was generated by gently pressing loose lizardite powder in a diamond-anvil cell (DAC) without gasket of which single pieces were afterwards used to select 20x20  $\mu\text{m}$  sized areas of interest without visible cracks to conduct spectral measurements (Fig. 3-1). Chrysotile dehydroxylation experiments were realised by using sub-parallel fibre bundles (Fig. 3-2). The samples of interest were placed into a heat-



**Figure 3-1.** Transparent lizardite flake generated by gently pressing loose lizardite powder. Single pieces without cracks were used for the FTIR analysis. The indicated scale corresponds to the  $\mu\text{m}$  range.

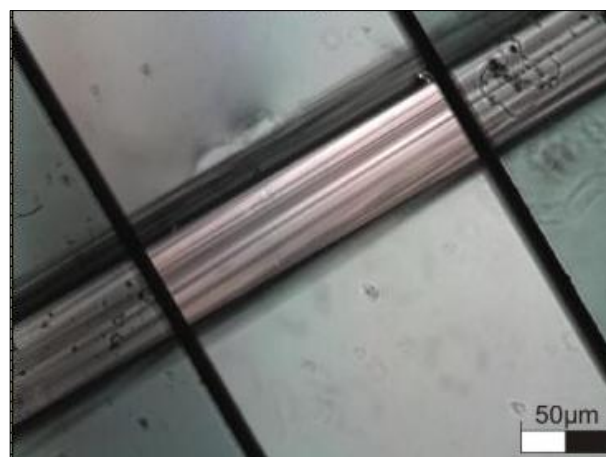


**Figure 3-2.** An exemplary chrysotile fibre bundle used for FTIR analysis. The indicated scale corresponds to the  $\mu\text{m}$  range.

resistant sapphire crucible deposited within the Linkam TS1000 heating stage (Fig. 3-3).

Individual temperature programs are documented in the experimental sections of Chapter 5 and 6.

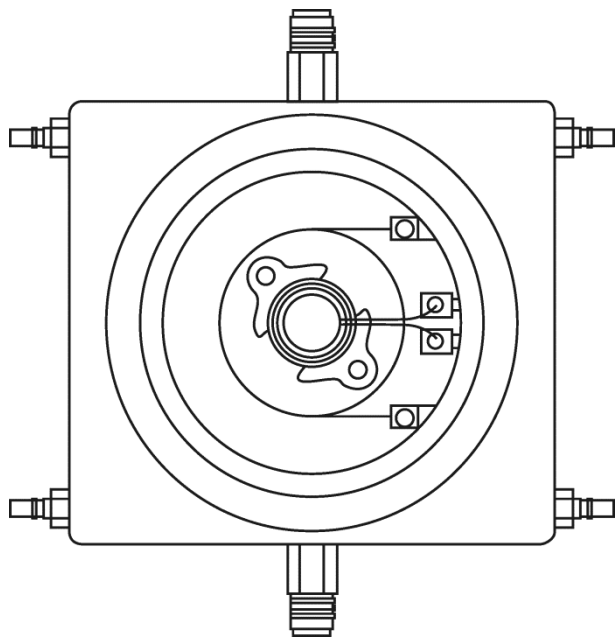


**Figure 3-3.** Scheme representing the Linkam TS1000 heating stage. Connections on the left- and right-hand side are for cooling purposes, the thermocouple is illustrated within the inner circle of the stage, purging gas in- and outlets are shown on the top and the bottom of the sketch, modified after images shown on the [linkam.co.uk](http://linkam.co.uk) website.

### 3.1.4 Conventional FTIR spectroscopy

A pre-investigation studying the phase transformation behaviour of lizardite were realised by using a Bomem-Hartmann & Braun MB155 FTIR spectroscope at the College of Engineering and Architecture of Fribourg. Infrared data were acquired in the spectral range of 400-4000  $\text{cm}^{-1}$  using a resolution of 4  $\text{cm}^{-1}$  and a stacking of 30 individual scans. Thermally pre-treated lizardite powder were dispersed in KBr and pressed to conventional KBr pellets. The pellets were afterwards dried at 130 °C for at least 2 h to reduce the influence of adsorbed  $\text{H}_2\text{O}$ . Background measurements were done by using sample free KBr pellets which were also dried at 130 °C for at least 2 h.

### 3.1.5 Micro-Raman spectroscopy (at non-ambient temperatures)

All Raman experiments were performed with a HORIBA HR 800 UV Raman spectrometer (grating 1800 grooves/mm, focal length 800 mm, 1024x256 pixel CCD detector) connected to an Olympus BX41 (20x objective, backscattering configuration) and equipped with a XY adjustable stage. The Raman device uses a confocal setup with a pinhole diameter of 100  $\mu\text{m}$ . All Raman spectra were acquired by using an argon laser with  $\lambda = 488 \text{ nm}$  at a power of 300 mW. The resulting illuminated diameter on the sample surface reaches 4.4  $\mu\text{m}$  considering the chosen Raman setup. A calibration against the emission bands of a neon lamp was done to guarantee a high precision of the wavenumber positions (Fig. 3-4). Chrysotile and lizardite spectra were measured in the 100-1200  $\text{cm}^{-1}$  and 3500-3800  $\text{cm}^{-1}$  spectral range with a spectral acquisition time of 40 sec and a cumulation of 3 stacks to improve the signal-to-noise ratio. Temperature-dependent dehydroxylation experiments were realised by using the same heating stage system as described for *in situ* FTIR runs. The heating stage was calibrated using the melting points of different salts:  $\text{NaNO}_3$  ( $T_M = 306 \text{ }^\circ\text{C}$ ),  $\text{NaI}$  ( $T_M = 651 \text{ }^\circ\text{C}$ ), and  $\text{NaCl}$  ( $T_M = 801 \text{ }^\circ\text{C}$ ). The 0 °C point was included in the calibration line (Fig. 3-5).

## 3.2. X-ray diffraction

Qualitative phase analyses of the sample material were realised by using a Philips PW1800 diffractometer with a conventional Bragg-Brentano geometry and a  $\text{Cu K}\alpha$  tube operating at 40 kV-40 mA conditions. The system was run with a variable divergence slit and a receiving slit size of 0.1 mm. In general, diffraction patterns were recorded in step scan mode with a step size of 0.02  $^\circ 2\theta$  and a scanning rate of 1 sec/step. However, varying sample properties and overlapping peak conditions caused an individual adaption of step size and scanning rate. Specific conditions are indicated in the scientific articles.

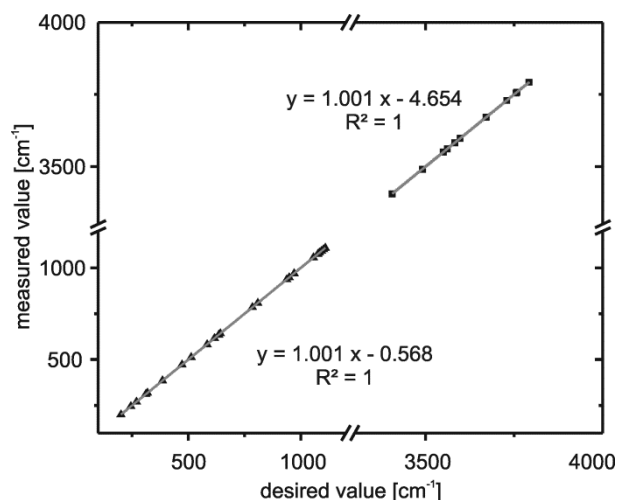


**Figure 3-4.** Raman wavenumber calibration using a 488 nm laser and neon emission line positions as provided by the NIST.

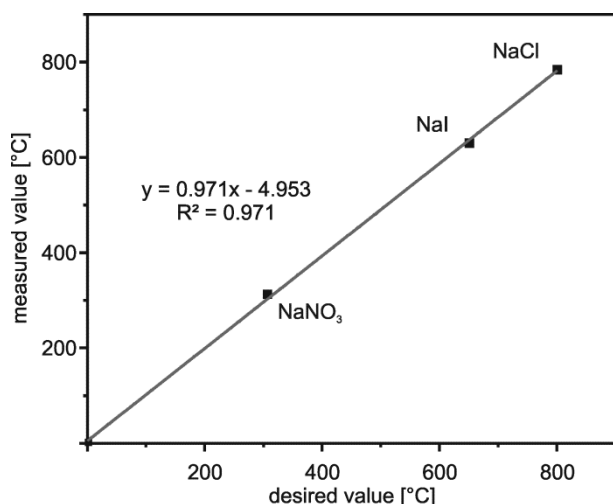


**Figure 3-5.** Temperature calibration of the Linkam TS1000 heating stage using the melting points of  $\text{NaNO}_3$ ,  $\text{NaI}$  and  $\text{NaCl}$ .

### 3.3 HIGH-TEMPERATURE X-RAY DIFFRACTION

The phase transformation of lizardite and chrysotile as well as brucite in general and kinetic data of this reactions in particular were studied by a Philips PW1830 X-ray diffractometer equipped with a water-cooled high-temperature HTK 10 X-ray camera by Anton Paar/ Austria and controlled

by a temperature control unit (TCM 2000, Anton Paar/ Austria). The PW1830 diffractometer uses a Bragg-Brentano geometry and was run with a Cu tube at a voltage of 40 kV and a current of 40 mA. All data were collected using a fixed divergence slit of  $1^\circ$  and a receiving slit of 0.2 mm. Standard measurements for gathering kinetic data were run with a step size of  $0.02^\circ 2\theta$  and a scanning rate of 5 sec/step. The long scanning rate is related to the sensitivity of the scintillation detector. The HTK 10 is equipped with two X-ray transparent kapton windows and two gas-ports for experiments at low vacuum or gas flow conditions (Fig. 3-6). X-ray patterns were collected in air and under controlled  $\text{N}_2$  atmosphere (200 ml/min) to guarantee a rapid removal of released water during the experimental runs.

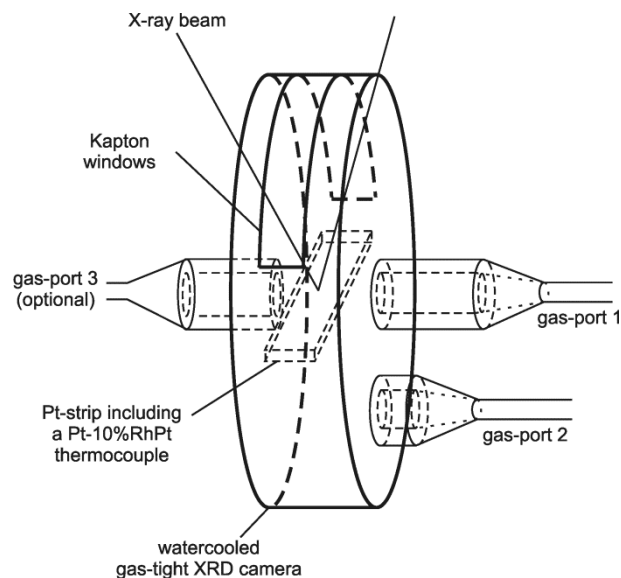


**Figure 3-6.** Scheme illustrating the main components of the Anton Paar HTK 10 attached to the PW1830 including three optional gas-ports of which gas-port 1 and 2 were used for the dehydroxylation experiments (modified after Lepora 2002).

Powdered samples were dispersed in ethanol and dropwise deposited on the surface of 1737F (PGO GmbH Iserlohn/ Germany) low alkali glass holders (6 x 12 x 0.7 mm) by using a pipette. After the

release of ethanol, this procedure was repeated several times to guarantee a homogeneous thin film on the surface of the glass platelets. Then, the sample holder was placed onto a platinum strip with an attached Pt-10%RhPt thermocouple positioned in the centre of the HTK 10 (Fig. 3-6). The thermocouple was regularly calibrated by using the melting points of  $\text{NaNO}_3$  ( $T_M = 306\text{ }^\circ\text{C}$ ),  $\text{Ba}(\text{NO}_3)_2$  ( $T_M = 592\text{ }^\circ\text{C}$ ),  $\text{KCl}$  ( $T_M = 790\text{ }^\circ\text{C}$ ) and  $\text{NaCl}$  ( $T_M = 801\text{ }^\circ\text{C}$ ). A summary of the temperature calibration is listed in Appendix I.

There are some main disadvantages of the diffraction system used:

1. The low sensitivity of the scintillation detector prevents a fast scan of individual peaks used for kinetic analyses, i.e., the peak shape is biased by the long scanning interval especially at high reaction rates. By using the indicated measurement parameters, one peak measurement lasts around 5 min, which result in just a few data points at isothermal runs with high reaction rates.
2. The high temperature gradient of the thermocouple and the positioning of the glass holder including the sample can cause major deviations from the programmed temperature. As illustrated in Appendix II, there are certain overlaps in experimental data of one isothermal sequence, although measured at different temperatures with a standard increment size of 10 K.
3. The sample preparation technique is susceptible to cause variations in the film thickness at the glass holder surface. This will also influence the duration of a dehydroxylation experiment and therefore the kinetics, i.e., thicker films cause longer dehydroxylation runs at the same temperature studied as there are longer diffusion trajectories.

### 3.4 IR SPECTROMETRY (LECO IR SPECTROMETER)

Experiments were done with a LECO infrared RC-412 multiphase carbon/ hydrogen/ moisture determinator/ spectrometer in order to get an overview about the dehydroxylation behaviour and to produce a reliable amount of (partly) dehydroxylated sample material for further analyses (e.g., conventional FTIR spectroscopy, XRPD). The LECO spectrometer uses three infrared detector cells, two for the measurement of  $\text{CO}_2$  and one independent cell for the measurement of  $\text{H}_2\text{O}$ . The spectral range of the detector cells are adjusted for the absorption bands of  $\text{CO}_2$  and  $\text{H}_2\text{O}$  by using a precise wavelength filter for the respective infrared cells (LECO user manual).

Prior to use,  $\text{Al}_2\text{O}_3$  sample holders have been annealed at temperatures higher than  $1000\text{ }^\circ\text{C}$  to avoid possible sample contaminations. Afterwards they have been stored in a desiccator placed in a furnace at a temperature of  $130\text{ }^\circ\text{C}$ . Before starting a measurement, a  $\text{H}_2\text{O}$  calibration routine has to be initiated by using a  $\text{H}_2\text{O}$  containing calcium oxalate standard (LECO Reference 502-091). The calibration has been done with 250 mg calcium oxalate at  $200\text{ }^\circ\text{C}$  for 600 sec. The measurements were repeated at least three times. A calibration factor extracted from the calibration runs has to be inserted in the installed software program for all following calculations of the  $\text{H}_2\text{O}$  content. All sample and standard measurements are done under a constant flow of oxygen. A detection limit of 0.1 wt% is indicated for  $\text{H}_2\text{O}$  measurement. The relative error during the standard calibration accounts for 5 %, whereas sample measurements show much higher values. It has to be noted, that some measurements were characterised by impossible values such as negative  $\text{H}_2\text{O}$  contents.

The negative aspects concerning precision and accuracy in measured  $\text{H}_2\text{O}$  concentrations prevent the application of this technique for kinetic analysis.

### 3.5 THERMOGRAVIMETRIC ANALYSES (TGA)

Standard thermogravimetric analyses were realised by a Mettler-Toledo TGA/SDTA 851e device including a 801RO sample robot and a Mettler-Toledo TSO800GC1 gas controller at the College of engineering and architecture in Fribourg/Switzerland. More advanced analyses, i.e., extracting of kinetic data using a method proposed by Drita (2012) were realised with a Mettler-Toledo TGA/DSC 1 device including an automated sample robot and a Mettler-Toledo GC10 gas controller. All analyses were run with a constant flux of 100 ml/min N<sub>2</sub>. All samples have been deposited in 70 µl sized Al<sub>2</sub>O<sub>3</sub> crucibles.

### 3.6 TRANSMISSION ELECTRON MICROSCOPY (TEM)

Structural analyses, high resolution imaging, phase analyses by selected area electron diffraction (SAED) and chemical analyses (TEM-EDS) were done with a Philips CM200 TEM equipped with an EDAX energy-dispersive X-ray spectrometer at the CSEM Neuchâtel/ Switzerland. Additional imaging analyses were realised with a Philips CM10 TEM operating at 100 kV at the University of Fribourg. For this, some milligrams of powdered sample material were dispersed in

ethanol and afterwards deposited on a 300 mesh copper grid Lacey-Carbon Film (S166-3 by Plano GmbH Wetzlar/ Germany). A carbon-coated ion-milled lizardite sample prepared from a conventional thin-section was produced with the help of a BAL-TEC Res100 ion mill (Ar, 4kV).

### 3.7 SCANNING ELECTRON MICROSCOPY (SEM)

Scanning Electron microscopy was done with a Philips FEI XL30 SFEG Sirius equipped with an EDAX energy-dispersive X-Ray spectrometer (EDS), a secondary electron detector (SE), a backscatter electron detector (BSE), a cathodoluminescence detector (CL) and an OIM electron backscatter diffraction system (EBSD) of which the EDS, the SE and BSE detectors were used. The FEG system offers a possibility to work in high resolution as well as ultra high resolution mode which is useful to detect and analyse existing chrysotile fiber bundles within lizardite samples. The attached EDS system was used for semi-quantitative chemical analyses to check the homogeneity of the serpentine samples used. Powdered chrysotile and lizardite samples were placed on sticky carbon patches or directly measured on the copper grid Lacey-carbon films prepared for TEM analyses.

## 4 - DEHYDROXYLATION KINETICS OF LIZARDITE

*Trittschack R, Grobéty B*

*published in European Journal of Mineralogy 24:47-57 (2012)*

---

### ABSTRACT

The thermally-induced dehydroxylation of lizardite and its phase transformation to forsterite were studied by high-temperature X-ray diffraction (HT-XRD), thermogravimetry (TGA) and Fourier-transformed infrared spectroscopy (FTIR). Primary sample characteristics like chemical composition and crystallographical structure were determined by combined (HR)TEM-EDX, electron-microprobe analyses (EMPA) as well as conventional X-ray diffraction (XRD). Isothermal HT-XRD and non-isothermal TGA data were treated with the classical Avrami-Erofe'ev method and more advanced isoconversional methods in order to obtain kinetic data of a multi-step decomposition reaction. A highly precise activation energy  $E_a$  versus reaction progress ( $\alpha$ ) dependency based on non-isothermal TGA data of lizardite are provided and associated mechanisms are discussed. Here, the main focus lays on recently-published *ab initio* calculations from the phase transformation of other phyllosilicates. Moreover, a comparison and discussion of the calculated overall apparent activation energy with diverging data from the literature is given. Especially, the usability of overall activation energies of multi-step decomposition reactions is critically discussed. The presented and discussed reaction steps of water formation from different hydroxyl species in lizardite can be used to improve *ab initio* calculations, especially the pre-selection of reacting hydroxyl species in hydrous sheet like minerals.

### 4.1 INTRODUCTION

Lizardite  $\text{Mg}_3\text{Si}_2\text{O}_5(\text{OH})_4$  is a trioctahedral 1:1 phyllosilicate and together with chrysotile and antigorite is the most prominent representative of the serpentine mineral group. The general building blocks of these trioctahedral serpentine minerals are tetrahedrally-coordinated silicate sheets (T) and octahedrally-coordinated brucite-like sheets (O), which are connected to TO layers. In the case of lizardite, these TO layers are flat and stacked along the *c* axis. Crystal structure refinements on suitable crystals by Brigatti *et al.* (1997), Mellini (1982) and Mellini and Zanazzi (1987) revealed three polytypes  $2H_2$ ,  $1T$  and  $2H_1$ . However, natural samples often consist of an inseparable mixture of these polytypes and some minor amounts of chrysotile and/ or antigorite.

Serpentinites are important water-bearing rocks of the oceanic lithosphere and underlying mantle. Their dehydration is responsible for fractional melting in the overlying mantle wedge and may be the trigger for deep-seated Earthquakes (Ulmer and Trommsdorff 1995). Dehydration has also been proposed for the disposal of chrysotile asbestos (Gualtieri and Tartaglia 2000). Astonishingly, the mechanisms of these dehydration reactions are only poorly understood. The structural diversity of the serpentine minerals i.e., flat layers in lizardite, but bent layers in antigorite and chrysotile, are ideally suited to explore the influence of mesoscale structure on dehydration. The cylindrical structure of chrysotile may be an ideal example to study basic aspects of reactions in non-translational multiwall nanotube phases.

Dehydroxylation kinetics of serpentine minerals have been extensively studied by thermogravimetric analysis (e.g., Brindley and Hayami 1963a and b; Weber and Greer 1965) and in recent times by X-ray powder diffraction (XRPD) techniques (Cattaneo *et al.* 2003). In these investigations, kinetic and mechanistic data were derived from experiments done under isothermal conditions and treated by classical kinetic methods developed by Avrami (1939, 1940, 1941), Erofe'ev (1946) and Johnson and Mehl (1939) or by the 'time to a given fraction' (TGF) method (Burke 1965). Hancock and Sharp (1972) used these principles to extract physical interpretation from a single reaction dependent constant ('reaction order') alone. A comprehensive overview of these methods including various case studies is given by Bamford and Tipper (1980). A critical appraisal discussing the limitations and shortcomings in the classic treatment of solid state kinetics has been given by Galwey (2004).

Isothermal experiments have some major disadvantages (Vyazovkin and Wight 1997). It is not possible to determine time resolved (reaction progress,  $\alpha$ ) activation energies by such methods, but only values averaged over a certain reaction duration. It is, therefore, almost impossible to extract mechanistic information from such data, except for reactions for which the same reaction step is rate-determining for the entire duration of the reaction (Vyazovkin and Wight 1997). The difficulties in the interpretation of isothermal experiments begin with the heating up of the sample, which inevitably leads to an inaccurate determination of the zero time  $t_{\alpha=0}$  of an experiment. This might explain the large spread in reported activation energy determined by the isothermal method. The TGF method has the advantage to indicate a change of the activation energy with time. But the activation energies are always integrated over time and volume of the sample. Non-isothermal methods give reaction progress resolved activation energies. The value, however, is still integrated over the entire reaction volume. Each change indicates that

either the contribution of an individual parallel step changes or that a new reaction step contributes to the overall rate. In the case where several parallel and/ or sequential reaction steps are rate-determining, the value again represents an average of the activation energies of the individual steps.

This study presents kinetic data for the dehydroxylation of lizardite derived from non-isothermal isoconversional measurements obtained from thermogravimetry (Friedman 1964; Vyazovkin 2000a) and compares them with data from conventional isothermal results obtained from *in situ* high temperature X-ray powder diffraction. The highly resolved datasets will be discussed in terms of mechanisms and compared with recent *ab initio* calculations of dehydroxylation induced phase-transformations in pyrophyllite (Molina-Montes *et al.* 2008a and b) and kaolinite (White *et al.* 2010). These data serve as starting point for future dehydration experiments on chrysotile and antigorite.

## 4.2 EXPERIMENTAL METHODS

The sample under study was a pale-green, in parts translucent, lizardite from the collection of the ETH Zurich without any details of composition or locality. It was crushed by hand and translucent pieces were then manually separated to exclude magnetite inclusions present in the sample. The fragments were subsequently milled with a vibratory disk mill for 45 s. Part of the powder was sieved to obtain a fraction  $\leq 63$   $\mu\text{m}$ . A qualitative phase analysis was performed by X-ray powder diffraction using a Philips PW1800 diffractometer with conventional Bragg-Brentano geometry, operated with a Cu  $K\alpha$  tube (40 kV-40 mA) and equipped with a variable divergence slit. The diffraction patterns were recorded in step scan mode (0.02  $^{\circ}2\Theta$ /step, 5 sec/step) in the range of 5-100  $^{\circ}2\Theta$ .

The samples were structurally characterised by Transmission Electron Microscopy (TEM)



with a Philips CM200 TEM (200 kV, CSEM Neuchâtel). HRTEM imaging and selected area electron diffraction (SAED) were carried out on powdered samples deposited on carbon-coated copper grids and a carbon-coated ion-milled lizardite sample prepared from a conventional thin section (BAL-TEC Res100 ion mill, Ar, 4 kV).

The chemical composition was determined using a JEOL JXA-8200 electron microprobe (15 kV, beam current: 20 nA, beam diameter: 10  $\mu\text{m}$ ) at the University of Bern. Calibration was done using forsterite (Mg), anorthite (Al, Ca), wollastonite (Si), ilmenite (Ti), eskolaite (Cr), tephroite (Mn), almandine (Fe) and bunsenite (Ni). Primary data were corrected by the PhiRhoZ-method.

Reaction rates were determined from *in situ* high temperature X-ray powder diffraction patterns, which were recorded in air and under controlled  $\text{N}_2$  atmosphere (200 ml/min) with a Philips PW1830 diffractometer (Bragg-Brentano geometry, Cu  $K\alpha$  radiation, 40 kV-40 mA) equipped with a high temperature vacuum camera (Paar Physica HTK 10). The powdered sample was deposited on a 0.7 mm thick 1737F low alkali glass holder, which itself was placed onto a platinum strip with an attached Pt-10%RhPt thermocouple in the centre of the camera. Temperature calibration was performed using the melting points of  $\text{NaNO}_3$  ( $T_M = 306^\circ\text{C}$ ),  $\text{Ba}(\text{NO}_3)_2$  ( $T_M = 592^\circ\text{C}$ ), KCl ( $T_M = 790^\circ\text{C}$ ) and NaCl ( $T_M = 801^\circ\text{C}$ ). During data collection a divergence slit of  $1^\circ$  and a receiving slit of 0.2 mm were used. The sample was heated at  $550^\circ\text{C}/\text{min}$  to keep the impact of the heating up cycle as small as possible. Because of peak overlap between lizardite and newly-formed olivine peaks, only the decrease of (001) lizardite reflections was analysed. The range between  $12.25\text{--}14.00^\circ 2\theta$  was measured in step scan mode ( $0.02^\circ 2\theta/\text{step}$ , 5 sec/step). Data were collected between  $600^\circ\text{C}$  and  $660^\circ\text{C}$  ( $10^\circ\text{C}$  increments). The chosen temperatures are directly related to analytical requirements, i.e., acceptable

measurement duration and a necessary (minimum) number of individual data points. The experiments lasted two hours to three days and between 20 and 200 diffractograms were recorded for each temperature increment. A profile fitting function implemented in the Philips APD V3.6h software was used to fit measured peaks. The same data were also fitted with the automated *Fit Single Peak* (GaussAmp model) function of the OriginPro8® software package to verify the relative integral intensity decrease.

Particle size distributions (0.40 to  $2000\ \mu\text{m}$ ) were determined with a LS230 laser diffraction particle size analyser by Beckman-Coulter at the EMPA Duebendorf/ Switzerland.

Fourier transformed infrared powder spectra were recorded with a Bomem Hartmann and Braun MB155 FTIR spectrometer (College of engineering and architecture, Fribourg) in the spectral range between 400 and  $4000\ \text{cm}^{-1}$  with a resolution of  $4\ \text{cm}^{-1}$ . Noise reduction was achieved by stacking 30 scans. Measurements of thermally pre-treated samples were carried out on conventional KBr pellets, which were dried for at least two hours at  $130^\circ\text{C}$  to avoid additional  $\text{H}_2\text{O}$  bands caused by sample moisture. Background spectra were acquired from sample-free KBr pellets.

Non-isothermal thermogravimetric analyses (TGA) using a Mettler-Toledo TGA/SDTA 851e device (College of engineering and architecture, Fribourg) were carried out under a constant  $\text{N}_2$  flux of 100 ml/min. The AKTS Thermogravimetric software package was used for kinetic calculations (Friedman method). Powdered samples were placed in conventional corundum sample holders and heated at 1, 2, 4, 8, 12, 16 and  $32^\circ\text{C}/\text{min}$  from  $25\text{--}800^\circ\text{C}$ . For all experiments sample weights between 10 and 13 mg were used to avoid heat-transfer effects within the sample material. The weight variation between individual samples of one experimental run (seven samples) was less than 0.5 mg.

### 4.3 DATA EXTRACTION

Integral peak intensities extracted from isothermal *in situ* high-temperature X-ray powder diffraction patterns (HT-XRD) were converted to relative intensities ( $I/I_0$ ) and plotted as reaction progress ( $\alpha$  in %) *versus* time ( $t$ ) curves. The first integral peak intensity measured immediately after reaching the temperature of interest was taken as zero time intensity ( $I_0$ ). The classical Avrami-Erofe'ev (Bamford and Tipper 1980) equation:

$$\alpha = 1 - e^{-(kt)^n} \quad (4.1)$$

allows, after linearization

$$\ln(-\ln(1-\alpha)) = n \ln k + n \ln t \quad (4.2)$$

to extract the exponent  $n$  from the slope, which for homogeneous reactions is indicative for the reaction mechanism, and the reaction rate  $k$  from the intercept  $n \ln k$  in corresponding  $\ln(-\ln(1-\alpha))$  *versus*  $\ln t$  plots. A series of isothermal experiments deliver temperature-dependent reaction rates  $k$ , which are used to calculate the apparent activation energy  $E_a$  on the base of the Arrhenius equation:

$$k = A e^{-\frac{E_a}{RT}} \quad (4.3)$$

with the pre-exponential factor  $A$ , the gas constant  $R$  and the absolute temperature  $T$ . The activation energy then can be extracted from  $\ln k$  *versus*  $1/T$  [ $K^{-1}$ ] plots, but the results only provide an average value over the entire reaction duration. Reaction order and activation energies for reactions involving solids can only be connected to specific reaction mechanisms, if there is only one rate-determining step over the entire reaction duration.

The so-called 'time to a given fraction' method (Burke 1965) was used to calculate activation energies in dependency of the reaction progress, which may partly overcome the problem of averaged activation energy values of multi-step processes. This method follows the isoconversional principle (Friedman 1964) under

isothermal conditions, i.e., the calculation of  $E_a$  is, in contrast to the Avrami approach, independent of empirical rate functions. Instead the general differentiated rate equation serves as starting point:

$$\frac{d\alpha}{dt} = k f(\alpha) \quad (4.4)$$

$$dt = k^{-1} f^{-1}(\alpha) d\alpha \quad (4.5)$$

The time,  $t_{\alpha}$  required for a certain reaction progress  $\alpha = \alpha_1$  can be obtained by integrating Eq. 5 as follows

$$t_{\alpha} = k^{-1} \int_{\alpha=0}^{\alpha=1} f^{-1}(\alpha) d\alpha \quad (4.6)$$

Under the assumption of a constant  $f(\alpha)$  within the investigated temperature interval, it is possible to calculate the activation energy for a certain reaction progress  $E_{a\alpha}$  from the slopes of a set of plots  $\ln t_{\alpha}$  *versus*  $1/T$  [ $K^{-1}$ ]. This method contains a major advantage compared to the Avrami treatment, namely changes of the activation energy as function of  $\alpha$ , i.e., changes in the rate-determining step, can be recognised. The equation makes only sense if the function describing the rate  $f(\alpha)$  is the same over the entire reaction duration, which is usually not the case for solid state reactions (Vyazovkin 2008).

Non-isothermal data from TG analyses were treated with the differential isoconversional method (Friedman 1964), starting with the customised general rate equation known from the isothermal case

$$\frac{d\alpha}{dt} = A e^{-\frac{E_a}{RT}} f(\alpha) \quad (4.7)$$

with

$$\alpha = \frac{W_0 - W_t}{W_0 - W_f} \quad (4.8)$$

where  $W_0$ ,  $W_f$  and  $W_t$  are initial, final and time weights of the sample. Replacing the constant temperature term by the heating rate  $\beta = dT/dt$  lead to

$$\frac{d\alpha}{dt} = \frac{A}{\beta} e^{-\frac{E_a\alpha}{RT(t)}} f(\alpha) \quad (4.9)$$

The slopes  $m$  in a plot  $\ln(d\alpha/dt)$  versus  $1/T$  [K<sup>-1</sup>] for a given reaction progress  $\alpha$  gives the activation energy. A significant difference to the TGF method is that the derivation of the activation energy does not require a constant rate-determining function over the entire reaction duration. This procedure has to be done for a series of different heating rates to guarantee to accuracy of the estimated  $E_a$ - $\alpha$  dependency (Vyazovkin 2000a). For the theoretical case that the rate-determining step changes simultaneously within the whole reaction volume, the activation energy of an individual step could be determined. Such a case would result in a step wise evolution of  $E_a$  with  $\alpha$ . But for solid-state reactions it is rather improbable. However, recently published data about the kinetics of Fe-oxidation/deprotonation in iron rich phlogopites suggest a single rate-determining step for a narrow temperature range (Zema *et al.* 2010).

## 4.4 RESULTS

### 4.4.1 Characteristics of the sample material

The X-ray diffraction patterns are close to the PDF reference pattern for lizardite-1T (No 18-0779) which fit all observed peaks (Fig. 4-1). The broad and strongly asymmetric peaks indicate small coherently scattering domains due to small grain size and the presence of defects such as turbostratic stacking. Electron optical investigations have shown that the powdered sample consists of crystallites ranging from 40 nm to 1  $\mu$ m in size. The crushed powders used in the experiments consist of polycrystalline grains composed of such crystallites (Fig. 4-2). HRTEM studies on ion-thinned sections reveal a complex pattern of ordered lizardite intergrown with a minor amount of curled TO-layers (Fig. 4-3) as already reported from other localities (Dódony and Buseck 2004). Stacking defects and

intercalation of 1T and 2H polytypes are common (Fig. 4-4).

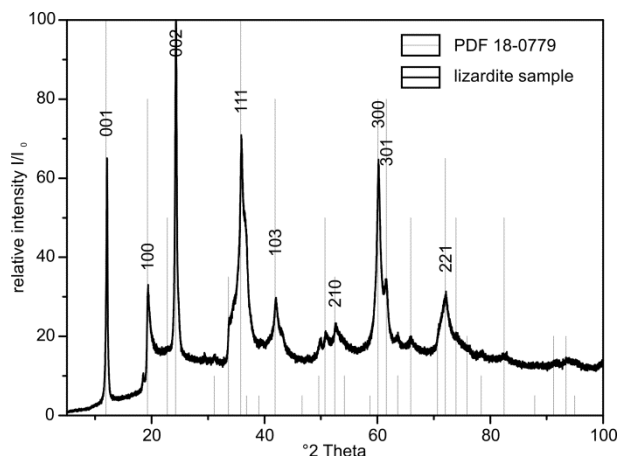


**Figure 4-1.** XRD pattern of the LizZH1 sample fitting all peaks of the 18-0779 entry of the ICDD database.

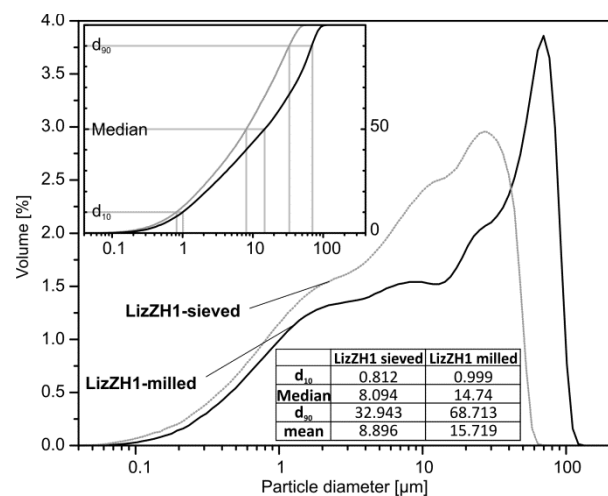


**Figure 4-2.** Particle size distribution of the two investigated LizZH1 samples including  $d_{10}$ ,  $d_{90}$ , mean and median parameters.

The average of 50 individual electron microprobe analyses gave the following stoichiometric formula:  $(\text{Mg}_{2.84}\text{Fe}_{0.04}\text{Al}_{0.03})(\text{Si}_{2.02})\text{O}_5(\text{OH})_{4.09}$  normalising on 9 (O, OH) and calculating the hydroxyl content by difference. The water content obtained this way

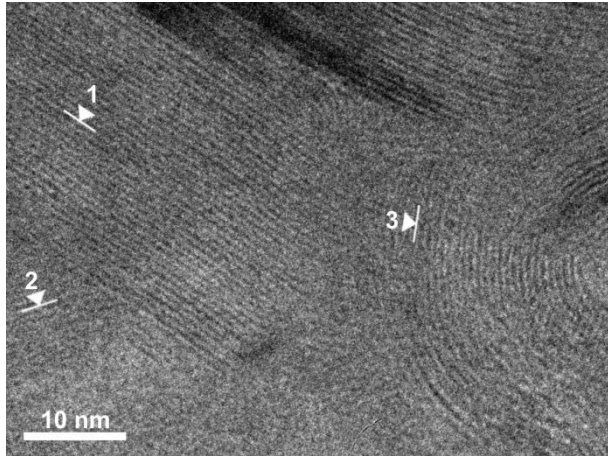


**Figure 4-3.** HRTEM image of ion-thinned lizardite with planar 1T crystallites (1 and 2) and curled lizardite (3).

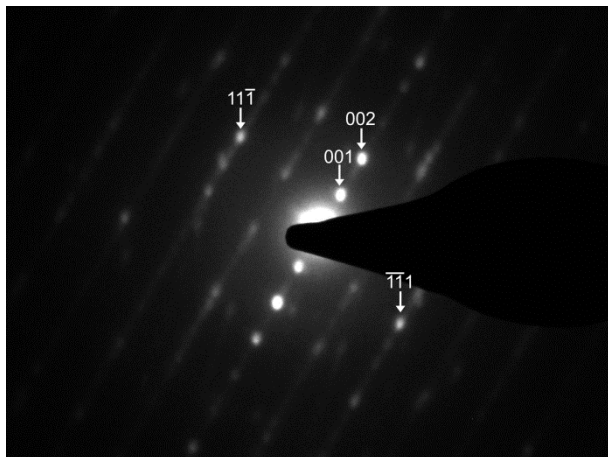


**Figure 4-4.** Representative [100] SAED pattern of lizardite. The strong reflections are compatible with the 1T polytype.

is 13.3 wt%, which fits the water content calculated on the base of TGA quite well.

#### 4.4.2 Decomposition of lizardite

The lizardite peaks in X-ray diffraction patterns decrease in intensity for annealing temperatures above 550 °C. After onset of the intensity reduction, a peak in the low-angle region of the diffractogram appears ( $\sim 7.4^\circ 2\theta$ ) as

previously observed by McKelvy *et al.* (2004). After a delay, the duration of which is a function of temperature, forsterite peaks appear (Fig. 4-5). Simultaneously with the formation of the so-called ‘ $\alpha$ ’ phase an increase in the background intensity is observed between 20 and 40 °2 $\theta$ . McKelvy *et al.* (2004) document the persistence of the increased background after disappearance of the ‘ $\alpha$ ’ phase related low-angle reflection and all lizardite peaks followed by a subsequent growth of forsterite. Unfortunately, such a stepwise phase transformation was not reproduced during this study.

The total weight loss measured by TG is between 12 and 13 wt%, which corresponds relatively well to the stoichiometric amount of water released by the reaction. The temperature range in which water is released and the corresponding reaction rate are not fixed during non-isothermal conditions, as suggested by Viti (2010), but controlled by the chosen heating rate  $\beta$ . The relationship between heating rate and the temperature of maximum reaction rate  $T_{\max}$  for the sieved and milled lizardite fractions is illustrated in Fig. 4-6 and were fitted by the general Hill equation (Seber and Wild 1989):

$$T_{\max}^{\text{sieved}} = 1410.155 \times \frac{\beta^{0.059}}{12.916^{0.059} + \beta^{0.059}} \quad (4.10)$$

with  $R^2 = 0.999$

$$T_{\max}^{\text{milled}} =$$

$$1886.542 \times \frac{\beta^{0.044}}{(2.242 \times 10^6)^{0.044} + \beta^{0.044}} \quad (4.11)$$

with  $R^2 = 0.999$

This dependency of water release rates and temperatures on heating rate has, therefore, to be considered when using non-isothermal TGA and equivalent data for unique discrimination of serpentine minerals.

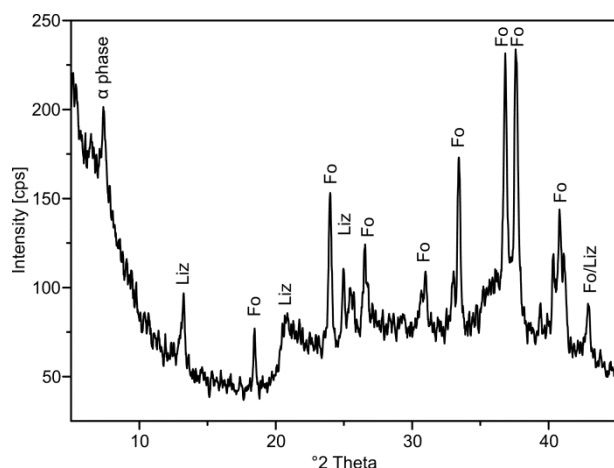


**Figure 4-5.** High-temperature X-ray diffractogram of LizZH1 after 35 hours at 600 °C showing the simultaneous occurrence of lizardite, forsterite and an intermediate 'α' phase.

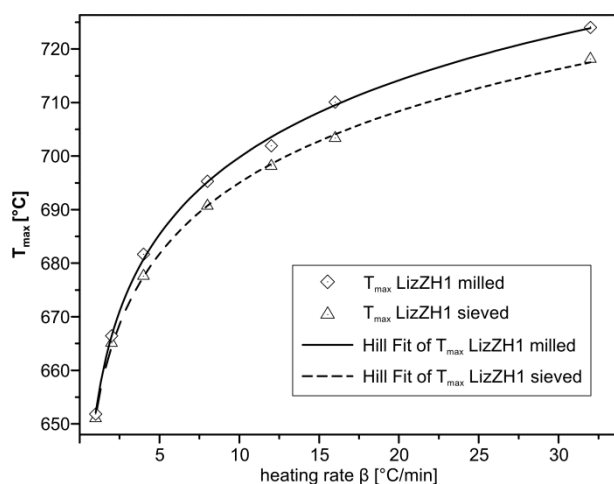


**Figure 4-6.**  $T_{max}$  as a function of the heating rate  $\beta$  of the lizardite subsamples based on non-linear curve fitting after the Hill equation.

FTIR data of thermally pre-treated and subsequently quenched powder samples show a general decrease of lizardite-related spectral features (Fuchs *et al.* 1998) i.e., of the O-H stretching bands (3600 - 3700  $\text{cm}^{-1}$ ), Si-O related bands (900 - 1100  $\text{cm}^{-1}$ ) and Mg-O respectively Mg-OH bands (Table 4-1, Fig. 4-7). The decrease in absorbance of the Si-O bands, however, seems to be lower than for the Mg-OH bands, although

quantitative results are not possible on the base of individually prepared quenched FTIR samples. Similar bands reappear after a certain time, but the position and shape of them correspond to spectral features given for forsterite (Jolicoeur and Duchesne 1981). The first evidence of forsterite can already be observed in the spectra Fig. 4-7d, although there hydroxyl groups remain present.

#### 4.4.3 Reaction kinetics

Although the TGF and the non-isothermal data show that dehydration of lizardite is not controlled by a single reaction step, it is still interesting to compare the activation energy  $E_a$  determined by the Avrami-Erofe'ev method with data available in the literature. Activation energies obtained by the Avrami-Erofe'ev method reach a value of  $347 \pm 16$  kJ/mol (milled sample, air atmosphere) and slightly lower values are found for experiments carried out under nitrogen atmosphere and with a slightly different particle size distribution (Table 4-2).

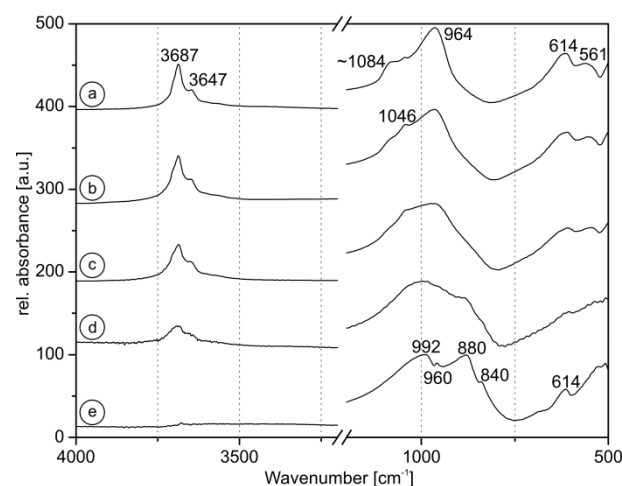


**Figure 4-7.** Phase transformation of lizardite LizZH1 observed on thermally pre-treated powder samples by FTIR (4000 to 500  $\text{cm}^{-1}$ ); a - 300 °C for 30 min, b - 500 °C for 30 min, c - 550 °C for 30 min, d - 600 °C for 30 min, e - 650 °C for 30 min.

Sample	OH stretching bands*†‡	symmetrical stretch of apical Si-O bonds‡	TO mode frequency - dipolar moment to a, b plane‡	degenerated Si-O stretching‡	in-plane displacement of hydrogen‡	further bands
LizZH1 RT	3700 3688 3648 3570 3420	1080	1045	964	614	560
	$\nu_3$ stretching of $\text{SiO}_4^\S$	$\nu_1$ stretching of $\text{SiO}_4^\S$	$\nu_4$ stretching of $\text{SiO}_4^\S$	corresponding to remaining hydroxyl groups†		
LizZH1 650 °C	992	883	615	673		
for 30 min	959	841				

Notes: ‡ Balan *et al.* (2002), † Farmer (1974a), \* Fuchs *et al.* (1998), § Jeanloz (1980)

RT - room temperature

**Table 4-1.** FTIR absorption bands [ $\text{cm}^{-1}$ ] in primary lizardite (LizZH1 RT) and resulting forsterite (LizZH1 650 °C).

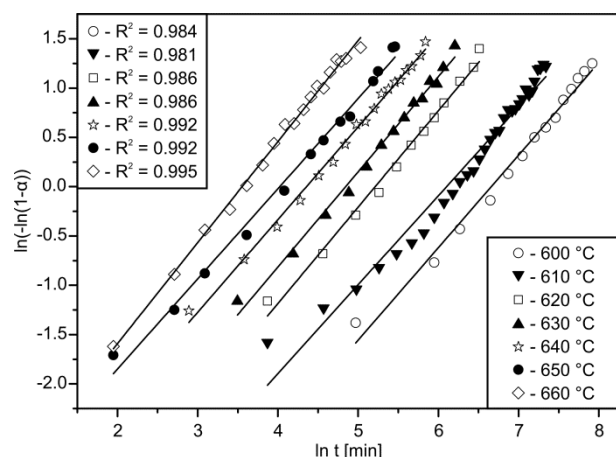


**Figure 4-8.** *ln-ln* plot of HT-XRD runs on LizZH1 milled.

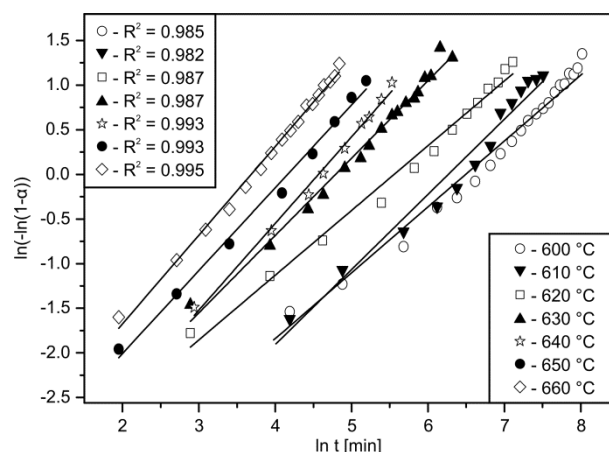


**Figure 4-9.** *ln-ln* plot of HT-XRD runs on LizZH1 sieved.

Two corresponding *ln-ln* plots (Figs. 4-8 and 4-9) showing the quality of the fitting procedure. The exponent  $n$  is between 0.6 and 1.0 and has tendency to increase with temperature (Table 4-2). These values are close to the results reported by Weber and Greer (1965).

Model-free kinetic data obtained from isothermal runs treated by the ‘time to a given fraction’ - method highlight a strong  $E_a$  versus reaction progress ( $\alpha$ ) dependency i.e., mechanistic interpretations cannot be made on the basis of the Avrami method. The values for small reaction progress ( $\alpha \leq 20\%$ ) are below 300

$\pm 16$  kJ/mol, which steadily increase to values between  $340$  and  $350 \pm 8$  kJ/mol for reaction progress  $\alpha > 60\%$ . The poor fits in the  $\ln t_a$  versus  $1/T$  [ $\text{K}^{-1}$ ] plots for small reaction progress reflect insufficient resolution in determination of the reaction progress with X-ray based methods (Fig. 4-10).

The activation energies as function of reaction progress for the milled particles obtained from a set of non-isothermal TGA experiments (Fig. 4-11) are characterised by an initial plateau with  $E_a \approx 240(3)$  kJ/mol, followed by an ascending part with small intermediate plateaus until a

Sample	$T$ [°C]	$n$	$R^2$	$k$	$A$ [s <sup>-1</sup> ]	$E_a$ [kJ/mol]
LizZH1 milled (air)	600	0.937(2)	0.9962	$1.28(1) \times 10^{-3}$	$8.9(4) \times 10^{17}$ $R^2 = 0.9836$	$347 \pm 16$
	610	0.903(4)	0.9922	$2.24(1) \times 10^{-3}$		
	620	0.978(2)	0.9956	$5.45(1) \times 10^{-3}$		
	630	0.970(4)	0.9918	$7.89(3) \times 10^{-3}$		
	640	0.941(4)	0.9908	$1.28(1) \times 10^{-2}$		
	650	0.91(1)	0.9713	$1.79(3) \times 10^{-2}$		
	660	1.025(7)	0.9866	$2.86(2) \times 10^{-2}$		
LizZH1 milled (N <sub>2</sub> )	600	0.634(1)	0.9961	$1.14(1) \times 10^{-3}$	$5.7(4) \times 10^{16}$ $R^2 = 0.9365$	$326 \pm 22$
	610	0.592(2)	0.9942	$4.07(1) \times 10^{-3}$		
	620	0.686(3)	0.9912	$4.39(2) \times 10^{-3}$		
	630	0.771(5)	0.9863	$9.64(6) \times 10^{-3}$		
	640	0.779(3)	0.9932	$1.38(1) \times 10^{-2}$		
	650	0.868(7)	0.9833	$1.49(1) \times 10^{-2}$		
	660	0.928(7)	0.9841	$2.91(2) \times 10^{-2}$		
LizZH1 sieved (air)	600	0.739(6)	0.9848	$1.51(1) \times 10^{-3}$	$3.1(2) \times 10^{16}$ $R^2 = 0.9877$	$323 \pm 14$
	610	0.862(8)	0.9825	$2.20(2) \times 10^{-3}$		
	620	0.726(5)	0.9873	$3.85(3) \times 10^{-3}$		
	630	0.867(6)	0.9866	$8.33(5) \times 10^{-3}$		
	640	0.974(3)	0.9929	$1.04(1) \times 10^{-2}$		
	650	0.927(3)	0.9929	$1.56(1) \times 10^{-2}$		
	660	0.992(3)	0.9947	$2.51(1) \times 10^{-2}$		

**Table 4-2.** Summary of calculated kinetic parameters for the dehydroxylation of lizardite (Avrami-Erofe'ev method).

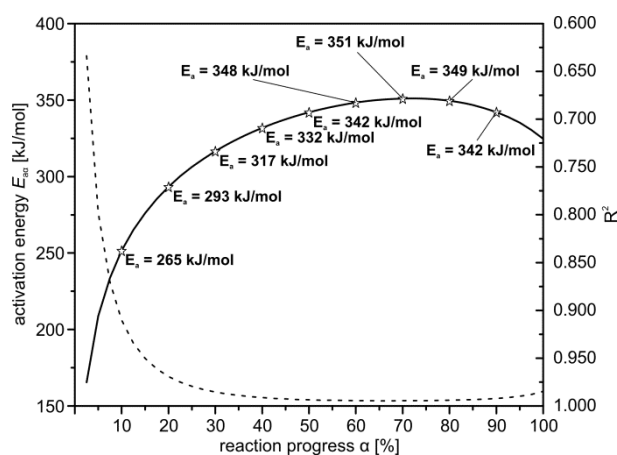


**Figure 4-10.** Results of the time to a given fraction method showing  $E_a$  as function of the reaction progress  $\alpha$ .

maximum of 370(4) kJ/mol is reached. At a more advanced stage of the reaction  $E_a$  decreases gently to a final value of around 340(3) kJ/mol (Fig. 4-12). These data are compatible with the model-free isothermal data obtained from the TGF data (Fig. 4-9). Generally, variations in the

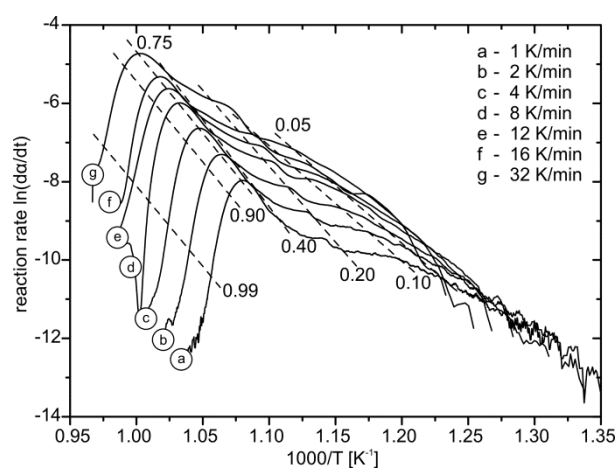


**Figure 4-11.** Reaction rate  $\ln(da/dt)$  as a function of the inverse absolute temperature for seven individual TGA runs.

pre-exponential factor  $A$  follow the course of  $E_a$  with  $\alpha$ . These results were reproduced in parallel experiments, although the local maxima in  $E_a$ , the intensity and position of stagnation plateaus are variable. Causes for such variations are slightly deviating starting conditions i.e., differences in

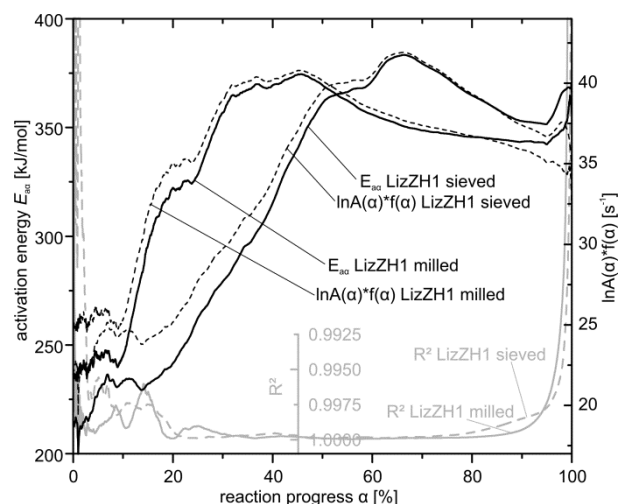


**Figure 4-12.** Calculated activation energy  $E_a$  as function of the reaction progress (isoconversional Friedman method), errors are smaller than the used line thickness.

the initial sample weights and differences in the particle size distribution (Roduit *et al.* 1996). In general, error estimations base on mathematical treatments by Cai and Chen (2009). The curve for the sieved sample is shifted to the right i.e., show a delayed increase but reaches the same maximum values. There are also no intermediate plateaus visible.

## 4.5 DISCUSSION

In a huge volume of literature on the kinetics of the dehydroxylation of phyllosilicates, data are typically treated by the Avrami or the TGF method and the activation energy and the ‘reaction order’ is interpreted in a mechanistic way (e.g., Redfern 1987; Bose and Ganguly 1994; Bellotto *et al.* 1995; Gualtieri *et al.* 1995; Bray and Redfern 1999; Mazzucato *et al.* 1999; Cattaneo *et al.* 2003; Tokiwai and Nakashima 2010). This procedure, however, is only strictly valid for reactions for which the rate-determining step does not change with reaction progress. The TGF and non-isothermal results clearly show that this is not the case for the dehydroxylation of lizardite. A similar

conclusion has probably to be drawn also for other phyllosilicates, and for most other solid state reactions (e.g., Vyazovkin and Wight 1997; Galwey and Brown 2002; Vyazovkin 2008). Non-isothermal experiments will readily show if the kinetic of a reaction is truly controlled by a single reaction step. Many authors present the kinetic derived mechanistic aspects of the reactions alone, without complementary support from spectroscopic or microscopic data (Raman, FTIR, X-ray based structural refinements, TEM) or from *ab initio* calculation to support their interpretations.

Classical isothermal and non-isothermal heating experiments of lizardite clearly reveal a multi-step dehydroxylation mechanism for which the activation energy and, therefore, also the rate-determining step changes with reaction progress (Fig. 4-12). To interpret mechanisms as a function of reaction progress we need to know how many parallel or sequential reaction steps are controlling the rate at any instant of the entire reaction duration. Afterwards, observed values could be compared with activation energies available for certain reaction steps. Such data have been obtained from *ab initio* quantum mechanical calculation (DFT models) for the dioctahedral phyllosilicate pyrophyllite (Molina-Montes *et al.* 2008a and b). The DFT models show that the reaction of adjacent hydroxyl groups to water molecules seem to be the rate-determining step in the initial stage of dehydroxylation of pyrophyllite (Molina-Montes *et al.* 2008a and b) and kaolinite (White *et al.* 2010). The reaction is favoured by reorientation of hydroxyl groups and direct transfer of the hydrogen to the adjacent hydroxyl without proton diffusion (Stackhouse *et al.* 2004). Because there are structurally different hydroxyl groups with different intermolecular distances it is not surprising that different rates and activation energies are obtained in the DFT calculations for the different recombination possibilities. Initially, the reaction between closest hydroxyl groups is predominant. With increasing reaction progress the recombinations involving more distant



hydroxyl groups become more important. For such a scenario, the activation energy obtained from non-isothermal heating experiments, which is an average of the weighted activation energies of the individual recombination reactions (Vyazovkin 2008), will change. As exemplarily outlined for lizardite such a change can result in increasing activation energies.

The decrease in absorbance of the Mg-OH infrared bands, which begins earlier and is faster than for the Si-O bands also indicate that the octahedral layer in lizardite is affected first and that most likely the recombination of OH groups and the formation of water molecules are dominant in the onset of the dehydroxylation reaction. According to McKelvy *et al.* (2006) the survival of the tetrahedral layer at the beginning of the reaction also explains the appearance of the  $7.4^\circ 2\theta$  XRD peak, which is an indicator for an intermediate phase similar to that observed during the thermal transformation of chrysotile (MacKenzie and Meinhold 1994). Assuming that the water-forming reaction is the initial rate-determining step, there are six nearest hydroxyl group pairs (Fig. 4-13). For the closest of them, the recombination is possible without an intervening diffusion step. It is obvious that all recombination possibilities may occur simultaneously, but the contributions of each step to the overall reaction rate will change with reaction progress leading to the observed increase of the activation energy. In pyrophyllite the activation energies for calculated individual steps range from around 150 to 250 kJ/mol (Stackhouse *et al.* 2004; Molina-Montes *et al.* 2008a and b), which match the minimum and maximum values observed in lizardite quite well considering the chemical and structural differences between both phyllosilicates.

In a recent paper, based on IR spectroscopic data Zhang *et al.* (2010) suggest, that the reaction between the hydroxyl groups in phyllosilicates does not inevitably lead to the formation of a water but of a  $H_2$  molecule, which diffuses to the surface where it reacts with oxygen. Although

not explored by the DFT calculations, such a reaction scenario would not change the fact that different recombinations are possible between hydrogen atoms, all with different probability of occurrence and activation energy. Already Martens *et al.* (1976) have successfully demonstrated the release of hydrogen and atomic oxygen during the dehydroxylation of brucite under controlled vacuum conditions. Therefore, similar reactions could also occur in complex phyllosilicates.

The recombination scheme presented in Fig. 4-13 does not take into account possible structural changes in the local structure due to the loss of a certain hydroxyl group. Such structural readjustments are to be expected and make a simple description of the individual reaction step difficult. Positive or negative ‘feedback loops’ initiated by local structural changes may affect the number of interaction possibilities of hydroxyl groups and may also be responsible for changes in the activation energy of individual rate-determining steps. Recent *ab initio* calculations concerning the dehydroxylation of phyllosilicates (e.g., Stackhouse *et al.* 2004; Molina-Montes *et al.* 2008; White *et al.* 2010) have not yet included such changes, as they used a rigid structure model except for the reacting atoms.

In non-isothermal experiments, both structural readjustments due to reaction progress and also structural changes due to the increase in temperature will affect reaction rates. Intramolecular distances  $H\cdots OH$  are not fixed but change with temperature (Gregorkiewicz *et al.* 1996; Guggenheim and Zhan 1998). Consequently, the temperature dependency of the activation energy of an individual reaction step will not only be controlled by vibrational, but also by geometrical factors.

A last assumption inherently made when applying Avrami or TGF type models to describe kinetic data is that the reaction progress is the same across the entire sample. For powdered samples this may be true as long as all particles

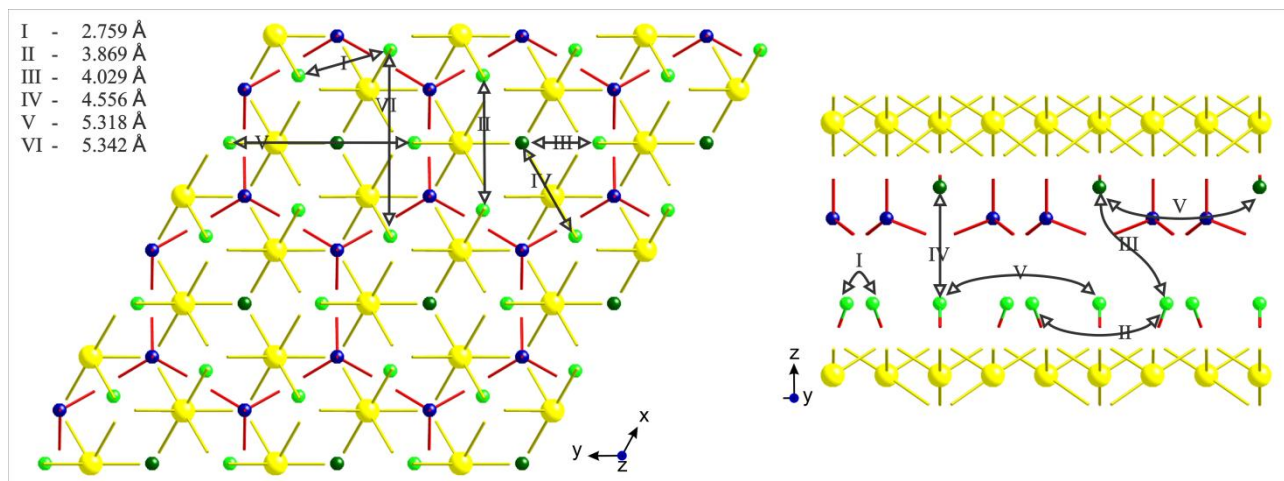


**Figure 4-13.** Six possible recombination possibilities of adjacent hydroxyl groups within the crystal structure of lizardite-1T (Mellini 1982) with respect to their proton distances ( $T = 25\text{ }^{\circ}\text{C}$ ); yellow - Mg, dark blue - Si, light green - H3, dark green - H4, red bonds - Si-O bonds, yellow bonds - Mg-O bonds, red-green bonds - OH groups, arrows representing hydroxyl group interactions.

have the same size. But, for polydisperse powders surface effects will significantly influence the decomposition kinetics (Vyazovkin and Wight 1997).

#### 4.6 CONCLUDING REMARKS

This study has shown that complex multi-step dehydroxylation processes in lizardite cannot adequately be described by the Avrami-Erofe'ev method, which is limited to homogeneous reactions. Solid-state transformations are characterised by multiple parallel and sequential

processes/ reaction steps and the control of the reaction rate may change in the course of the reaction. Neither isothermal kinetic experiments over a limited temperature range nor non-isothermal experiments alone are sufficient to extract physical information of complex reaction mechanisms. Thus, the interpretation of the physical meaning of rate parameters is very limited for such solid-state reactions. Therefore, kinetic dehydroxylation studies of complex solid-state phases should be accompanied and supported by data from the field of spectroscopy, electron microscopy and/ or *ab initio* calculations in order to make inferences on mechanisms.

## 5 - *IN SITU* HIGH-TEMPERATURE RAMAN AND FTIR SPECTROSCOPY OF THE PHASE TRANSFORMATION OF LIZARDITE

*Trittschack R, Grobéty B, Koch-Müller, M*

*published in American Mineralogist 97:1965-1976 (2012)*

---

### ABSTRACT

A temperature-dependent *in situ* micro-FTIR and micro-Raman spectroscopic investigation was performed on powdered (FTIR, Raman) and single-crystal (Raman) lizardite-1T samples between room temperature and 819 °C. Between room temperature and 665 °C, the OH stretching bands shift to lower wavenumbers, demonstrating a weak expansion of the O3-H3•••O2 interlayer distance. Band deconvolution of FTIR and Raman spectra at room temperature show differences in the number of bands in the OH stretching region with respect to group theory: four (FTIR) and six (Raman) OH stretching bands, respectively. This number reduces to four (Raman) at non-ambient temperatures either caused by LO-TO splitting, the presence of non-structural OH species or the presence of different lizardite polytypes and/ or serpentine polymorphs as well as defects. During dehydroxylation, the evolution of the integrated intensity of the OH bands suggests a transport of hydrogen and oxygen as individual ions/ molecule or OH<sup>-</sup>. A significant change in Raman spectra occurs between 639 and 665 °C with most lizardite peaks disappearing contemporaneously with the appearance of forsterite-related features and new, non-forsterite bands at 183, 350, and 670 cm<sup>-1</sup>. A further band appears at 1000 cm<sup>-1</sup> at 690 °C. The long stability of Si-O-related bands indicates a delayed decomposition of the tetrahedral sheet with respect to the dehydroxylation of the octahedral sheet. Moreover, evidence for a small change in the ditrigonal distortion angle during heating is given. In general, all appearing non-forsterite-related frequencies are similar to Raman data of talc and this indicates the presence of a talc-like intermediate.

### 5.1 INTRODUCTION

Lizardite Mg<sub>3</sub>Si<sub>2</sub>O<sub>5</sub>(OH)<sub>4</sub> is a member of the serpentine group. The 1:1 phyllosilicate consists of brucite-like octahedral sheets connected to SiO<sub>4</sub> tetrahedral sheets. The most common structures are the one-layer 1T and the two-layer 2H<sub>1</sub> polytype, although other polytypes are known. At ambient pressure and temperatures above 500 °C, lizardite breaks down to anhydrous phases, i.e., forsterite and enstatite. A probable mechanism for the liberation of the hydroxyl groups is a reaction of two adjacent hydroxyl groups which presumably recombine to a water molecule (e.g., Guggenheim *et al.* 1987). Theoretical studies have shown that the two symmetrically distinguishable hydroxyl

groups (Fig. 5-1) in each lizardite polytype can be recognised by their infrared (IR) and Raman active bands in the frequency range between 3500 and 3800 cm<sup>-1</sup> (Balan *et al.* 2002; Auzende *et al.* 2004). Temperature-dependent FTIR and Raman studies are therefore suitable to study the structural change of serpentine minerals, which is difficult to understand by X-ray techniques (XRD) alone (e.g., Guggenheim and Zhan 1998). In general, temperature-dependent peak shifts or intensity/ absorbance changes are caused by changes in the bond length, symmetry changes or short to large scaled structural rearrangements (e.g., Gillet 1996; Zhang *et al.* 2006). Intensity changes of the OH Raman bands and changes in absorbance of the OH IR bands can serve as a

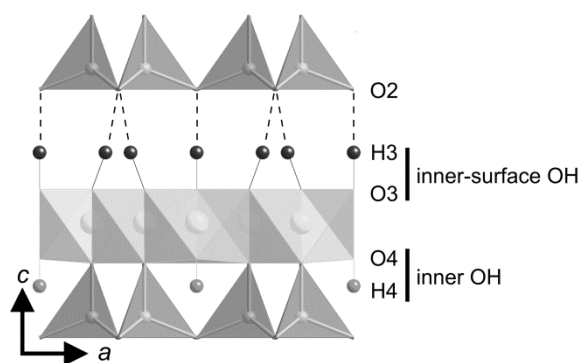


**Figure 5-1.** Crystal structure of lizardite-1T (Mellini 1982) projected along the *b* axis showing the positions of the inner and inner-surface hydroxyl groups. Some authors, e.g., Auzende *et al.* (2004), designate the ‘inner-surface’ OH also as ‘outer’ OH.

(semi)-quantitative information source to estimate the amount of OH or H<sub>2</sub>O within the crystal structure. Previous Raman and FTIR studies on serpentine minerals were mainly used as tools to distinguish serpentine polymorphs (e.g., Rinaudo *et al.* 2003) or to determine the structural behaviour at high-pressure/ high-temperature (HP/ HT) conditions within the stability region of lizardite (Auzende *et al.* 2004). To our knowledge, the ambient pressure breakdown of serpentine minerals to forsterite via an intermediate phase has not yet been studied by *in situ* HT Raman and HT FTIR techniques. This study focuses on *in situ* Raman and FTIR spectroscopy of a well characterised lizardite-1T from room temperature (RT) to 819 °C, i.e., well above the thermal breakdown interval (Trittschack and Grob  ty 2012).

## 5.2 EXPERIMENTAL PART

### 5.2.1 Sample material

The investigated lizardite sample, for which no origin is given, was taken from the ETH Zurich mineral collection. The electron microprobe based determination of the stoichiometry yields

(Mg<sub>2.84</sub>Fe<sub>0.04</sub>Al<sub>0.03</sub>)(Si<sub>2.02</sub>)O<sub>5</sub>(OH)<sub>4.09</sub> and a total water content of 13.3 wt%, which was estimated by thermogravimetry. The sample mainly consists of the 1T polytype, although there are intergrowths of curled 1:1-layers and regions with a high concentration of stacking faults based on Transmission Electron Microscopy (TEM) analyses (Trittschack and Grob  ty 2012).

As reference, a lizardite-1T single crystal from the Monte Fico quarries, Elba Island/ Italy, was used (private collection, Marcello Mellini). Comprehensive mineralogical and chemical data of this sample are provided by Mellini and Viti (1994) and Fuchs *et al.* (1998).

Powdered lizardite was gently pressed in a diamond-anvil cell (DAC) without gasket until a transparent film was generated. Single transparent pieces of this film were deposited in a sapphire crucible and used for all FTIR *in situ* dehydroxylation experiments. Raman experiments were performed on powdered samples and a Monte Fico single crystal, placed into a sapphire crucible.

### 5.2.2 FTIR and Raman spectroscopy

FTIR measurements were performed with a Bruker VERTEX 80v spectrometer attached to a Hyperion1000 IR microscope and a software-controlled Linkam TS1000 heating stage at the GeoForschungsZentrum Potsdam (GFZ Potsdam/ Germany). Spectra were collected in the 2500-4000 cm<sup>-1</sup> frequency range using a LN-INSB D413 detector, a KBr beamsplitter and a 6 mm aperture in transmission mode. Single spectra were measured with a resolution of 2 cm<sup>-1</sup> and averaged over 60 individual scans which results in a measurement interval of about 64 sec. A 20 x 20 µm sized area without visible cracks was chosen to collect FTIR spectra of the lizardite thin films. A constant flow of nitrogen was utilised to guarantee a rapid removal of the water generated during the dehydration. The thermocouple was calibrated using the melting points of different salts: NaNO<sub>3</sub> (*T*<sub>M</sub> - 306 °C), NaI (*T*<sub>M</sub> - 651 °C) and NaCl (*T*<sub>M</sub> -

801 °C). The zero degree Celsius point was included in the calibration line.

Micro-Raman investigations were performed with a HORIBA HR 800 UV spectrometer equipped with an Olympus BX41 microscope (20x objective) in backscattering configuration at the GFZ Potsdam. All examined spectra were measured with an argon laser (488 nm, 300 mW). The spectrometer was calibrated against the emission bands of a neon lamp. Spectra acquisition time was 10 sec and 4 spectra were cumulated for each temperature step. In general, spectra were measured in the frequency range of 100-1200  $\text{cm}^{-1}$  and 3500-3800  $\text{cm}^{-1}$ .

Non-isothermal runs were monitored to study the dehydroxylation of lizardite. The Raman experiments were obtained between 21 °C and 819 °C. An initial heating rate of 130 °C/min was used to heat the sample from 21 to 253 °C, afterwards the heating rate was fixed to 100 °C/min for 50 °C increments (to 459 °C) and 50 °C/min for 25 °C increments, starting with the 484 °C spectrum and ending with the 819 °C spectrum. Single measurements after each temperature increment required 5 min owing to the Raman set-up conditions. The FTIR data were collected between 21 °C and 665 °C. Initially, a heating rate of 100 °C/min was used for the following temperature intervals: 21-98 °C, 98-201 °C, 201-304 °C, 304-356 °C, 356-407 °C, 407-433 °C, 433-459 °C. FTIR spectra were recorded after each temperature interval. A linear heating rate of 1 °C/min and a continuous measurement was chosen from 459 °C to 665 °C.

### 5.2.3 Fitting procedure

Peak deconvolution and integration were performed with the PeakFit software package. The low-frequency range (100-1200  $\text{cm}^{-1}$ ) and high-frequency range (3500-3800  $\text{cm}^{-1}$ ) were treated independently. The Savitzky-Golay algorithm was used to smooth single spectra. After baseline subtraction, all spectra were deconvoluted using a

combined Gaussian-Lorentzian Amp function for which the width at the base and the full width at half maximum (FWHM) are refinable parameters. A minimum number of peaks was chosen to guarantee a best fit to allow the comparison between individual time and temperature resolved spectra as shown by Auzende *et al.* (2004).

## 5.3 RESULTS

### 5.3.1 Raman and FTIR spectra at ambient conditions

The low-frequency range of the Raman spectra obtained at RT is characterised by five well resolved strong bands which are accompanied by six weak bands (Fig. 5-2). Additional bands (Table 5-1) observable in the deconvoluted lizardite-1T spectrum of the Monte Fico sample are very weak or not present in spectra obtained from the powdered sample (Fig. 5-2). Precise peak positions and band assignments of both lizardite samples are summarised in Table 5-1 and 5-2. In general, the positions of the main peaks in the low-frequency range are identical with data summarised by Rinaudo *et al.* (2003). However, some bands were assigned to chrysotile by the latter (Table 5-1). We cannot unambiguously distinguish between purely lizardite-related or chrysotile containing, because these bands occur in the Monte Fico lizardite sample also, which contains up to 25 wt% chrysotile (Viti 2010). The 510  $\text{cm}^{-1}$  band assigned to deformation vibrations of  $\text{SiO}_4\text{-AlO}_4$  tetrahedra is visible in the spectrum of the Monte Fico crystal, but is missing in the powdered sample due to the low Al content of our sample. The antisymmetric Si-O stretching frequencies centred at around 1072  $\text{cm}^{-1}$  and 1099  $\text{cm}^{-1}$  are present but an accurate fitting in the *in situ* recorded spectra is difficult owing to their low intensity and large FWHM (Fig. 5-2).

For a deconvolution of the overlapping OH stretching frequencies at RT, four peaks were used for the FTIR spectra (Fig. 5-3a) and six for the related Raman spectra (Fig. 5-3b). Six bands were

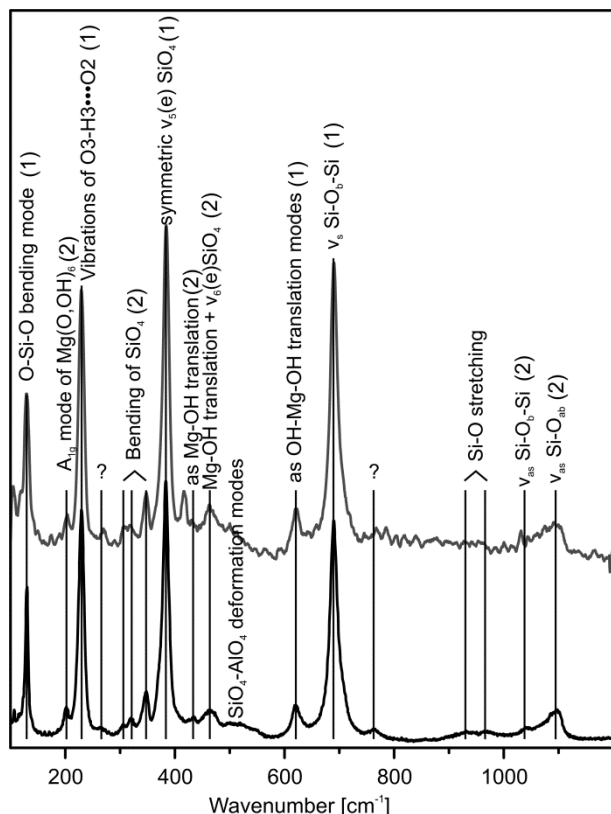


**Figure 5-2.** RT Raman spectra of lizardite-1T; the upper spectrum corresponds to the powdered ETH Zurich sample LizZH1, the lower spectrum to the single crystal lizardite-1T, Monte Fico quarry (Elba, Italy); (1) - indicates the five major bands and (2) the six minor bands of lizardite.

required also to fit OH bands in the Raman spectrum obtained from the Monte Fico single crystal (Table 5-1). This amount of bands is not compatible with theoretical data of the serpentine polymorph chrysotile by Kloprogge *et al.* (1999), who indicated the presence of just four Raman active OH stretching frequencies. Generally, the band assignments (Figs. 5-3a-b) follow the scheme of Balan *et al.* (2002), whereas close-set bands are interpreted as originating from the same mode.

Regarding the band multiplication, the possible role of longitudinal optical and transversal optical splitting modes and multiple OH bands originating from different polytypes/ polymorphes will be discussed in section 5.4. An increased number of OH stretching frequencies in the Raman spectra,

compared to the group theory predictions, were reported by Auzende *et al.* (2004).

### 5.3.2 Temperature-dependent Raman spectra in the low-frequency region

For an investigation of the phase transformation behaviour, six peaks of the RT spectra of the powdered sample were monitored through the entire temperature range. Smaller peaks, present in the RT spectrum, were omitted owing to the high background at elevated temperatures (Fig. 5-4). In general, the intensity of all lizardite-related bands decreases with increasing temperature and a steady frequency shift to lower wavenumbers is observed (Figs. 5-4, 5-5 and 5-6). Most shifts are linear functions of temperature, except for the  $A_{1g}$  mode of the  $Mg(O,OH)_6$  group and the symmetrical  $Si-O_b-Si$  vibration (Figs. 5-6b and 5-6f). There is no fundamental modification in Raman patterns of the powdered sample up to a temperature of 639 °C (Figs. 5-4 and 5-5b). A significant change is observed between the Raman spectrum at 639 °C and 665 °C (Figs. 5-5b-c). In the latter, most lizardite-related bands suffer an intensity decrease. In the spectrum of 639 °C, the formation of forsterite is documented with a broad band at around 848  $cm^{-1}$  (Fig. 5-5b). Initially, this band can be fitted adequately by one single peak. With increasing temperature, this broad band is split into two bands centred at 810  $cm^{-1}$  and 844  $cm^{-1}$  (Fig. 5-5c). Both are attributed to Si-O stretching vibrations (McKeown *et al.* 2010). The same bands are also present in a quenched sample, but shifted to 822  $cm^{-1}$  ( $\nu_1$ ) and 855  $cm^{-1}$  ( $\nu_3$ ) (Fig. 5-5f). Together with bands assigned to forsterite, a new peak at around 183  $cm^{-1}$  appears (gray shaded area in Fig. 5-4, marked by a rhomb in Figs. 5-5b-d). This band rapidly loses intensity at higher temperatures, which is in contrast to forsterite bands, which gain intensity. Simultaneously, a significant reduction in intensity and a frequency jump is observable for the  $\nu_6$   $Si-O_b-Si$  lizardite vibration (Fig. 5-6f). An additional feature appearing in the 665 °C spectrum is a 350  $cm^{-1}$  band and a band at 1000  $cm^{-1}$  at 690 °C

band assignment <sup>a,b</sup>	Lizardite-1T <sup>c</sup> (single crystal) Raman bands [cm <sup>-1</sup> ]	Lizardite-1T Raman bands [cm <sup>-1</sup> ]	Lizardite-1T FTIR bands [cm <sup>-1</sup> ]
Unknown		117.1	
O-Si-O bending mode <sup>1</sup>	129.4	129.5	
A <sub>1g</sub> mode of Mg(O,OH) <sub>6</sub>	201.9	202.4	
Vibrations of O3-H3•••O2 <sup>1</sup>	229.1	229.4	
Unknown		265.7	
Bending of SiO <sub>4</sub>	305.1		
	320.0		
	346.2	349.1	
s Mg-OH vibration <sup>chr</sup>	371.4		
s v <sub>5</sub> (e) bending of SiO <sub>4</sub> <sup>1</sup>	383.5	384.1	
Unknown artefact		416.9	
as Mg-OH tm <sup>chr</sup>	430.4		
Mg-OH translation + v <sub>6</sub> (e) SiO <sub>4</sub> <sup>chr</sup>	464.5	465.7	
SiO <sub>4</sub> -AlO <sub>4</sub> dm	517.5		
as OH-Mg-OH tm <sup>1</sup>	621.6	621.6	
Unknown	669.9		
s Si-O <sub>b</sub> -Si bridging/stretching mode <sup>1</sup>	689.8	690.1	
Mg-OH outer s tm	707.1		
Unknown	763.4		
Si-O sm	928.6		
	972.4		
as Si-O <sub>b</sub> -Si sm	1050.2	1072.4	
as Si-O <sub>nb</sub> sm	1094.3	1099.1	

Notes: as = antisymmetric, b = bridging, dm = deformation mode, nb = non-bridging, s = symmetric, sm = stretching mode, tm = translation mode, chr = attributed to chrysotile vibrations by Rinaudo et al. (2003)

<sup>1</sup>indicates the 5 major Raman bands of lizardite in the low-frequency range

<sup>a</sup>Rinaudo et al. (2003)

<sup>b</sup>Farmer (1974b)

<sup>c</sup>sample described by Mellini and Viti (1994), but measured individually for this study.

**Table 5-1.** Lizardite-1T related Raman and FTIR bands and their assignments at room temperature.

band assignment <sup>a,b</sup>	Lizardite-1T <sup>c</sup> (single crystal) Raman bands [cm <sup>-1</sup> ]	Lizardite-1T Raman bands [cm <sup>-1</sup> ]	Lizardite-1T FTIR bands [cm <sup>-1</sup> ]
OH stretching frequencies	3653.2	3649.9	3652
	3667.4	3670.2	3669
	3672.8	3684.0	3688
	3683.6	3690.6	3703
	3693.7	3698.1	
	3702.7	3704.0	

<sup>a</sup>Rinaudo et al. (2003)

<sup>b</sup>Farmer (1974b)

<sup>c</sup>sample described by Mellini and Viti (1994), but measured individually for this study.

**Table 5-2.** Lizardite-1T related Raman and FTIR OH bands.

(Figs. 5-5c-d). Only the latter persists up to 819 °C and is also present in spectra of the quenched sample (Fig. 5-5f). The various O-Si-O and SiO<sub>4</sub>-related lizardite stretching vibrations in the low-frequency range (Fig. 5-2, Table 5-1) and the 223 cm<sup>-1</sup> ( $\nu = 229$  cm<sup>-1</sup> at RT) band, characteristic for O3-H3•••O2 group vibrations (Fig. 5-1, Rinaudo *et al.* 2003), are present until the initial appearance of forsterite.

### 5.3.3 Temperature-dependent Raman- and FTIR-spectra in the OH stretching region

At temperatures higher than RT, the number of peaks necessary to deconvolute the OH bands adequately is four, both for the Raman (Fig. 5-7) and IR spectra (Fig. 5-8). There are no additional OH-related bands visible during heating. The frequency shifts of the four bands attributed to OH are illustrated in Fig. 5-9 (FTIR data) and Fig. 5-10 (Raman data) as a function of temperature. Following Balan *et al.* (2002), three bands (Fig. 5-3) are attributed to the out-of-phase stretching modes of the inner-surface OH groups (3652 cm<sup>-1</sup>), the in-phase stretching modes of the inner-surface OH groups (3688 cm<sup>-1</sup>) and the stretching modes of the inner OH groups (3703 cm<sup>-1</sup>). The fourth deconvoluted band at 3669 cm<sup>-1</sup> (RT) is not indicated among the 51 transverse optical modes

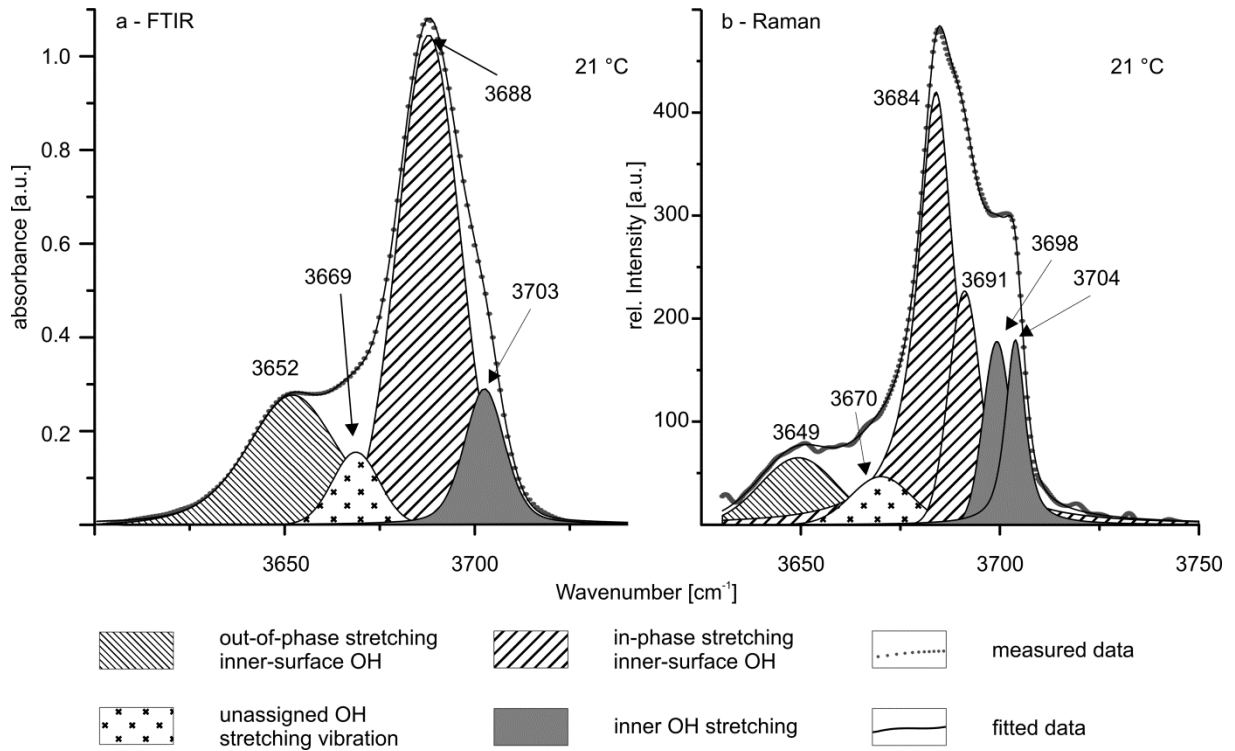


**Figure 5-3.** FTIR (a) and Raman (b) signals of the OH stretching region illustrating the peaks used for a signal deconvolution at RT.

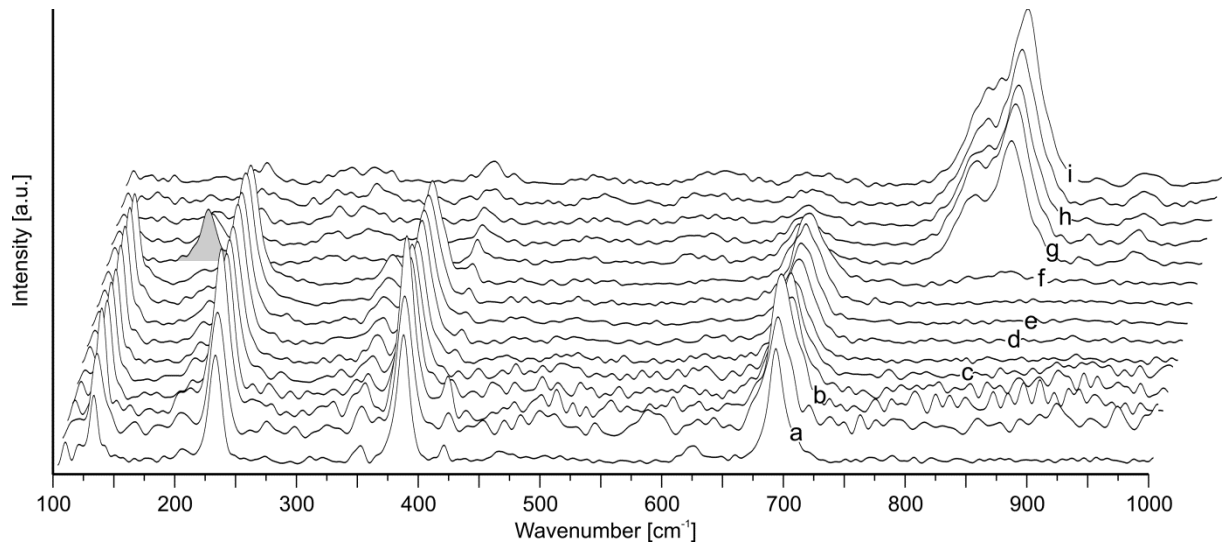


**Figure 5-4.** Temperature-dependent phase transformation behaviour of the low-frequency Raman bands of lizardite-1T between RT and 819 °C; grey shading marks the high-temperature 183  $\text{cm}^{-1}$  band at 665 °C simultaneously with a forsterite doublet between 800 and 900  $\text{cm}^{-1}$ ; a. RT, b. 253 °C, c. 407 °C, d. 510 °C, e. 587 °C, f. 639 °C, g. 665 °C, h. 742 °C, i. 819 °C.



indicated by Balan *et al.* (2002). The in-phase stretching modes of the inner-surface OH groups and the stretching vibrations of the inner OH groups show a linear temperature relationship, whereas two linear segments are necessary to describe the thermal frequency evolution of the out-of-phase vibration of the inner-surface OH

groups. The temperature at the intersection of the segments is indicated by an arrow in Fig. 5-9a. This temperature coincides roughly with the temperature of an enhanced dehydroxylation behaviour (Fig. 5-11a). The unassigned band shows a similar non-linear frequency evolution (Fig. 5-9b). The frequency of all Raman OH

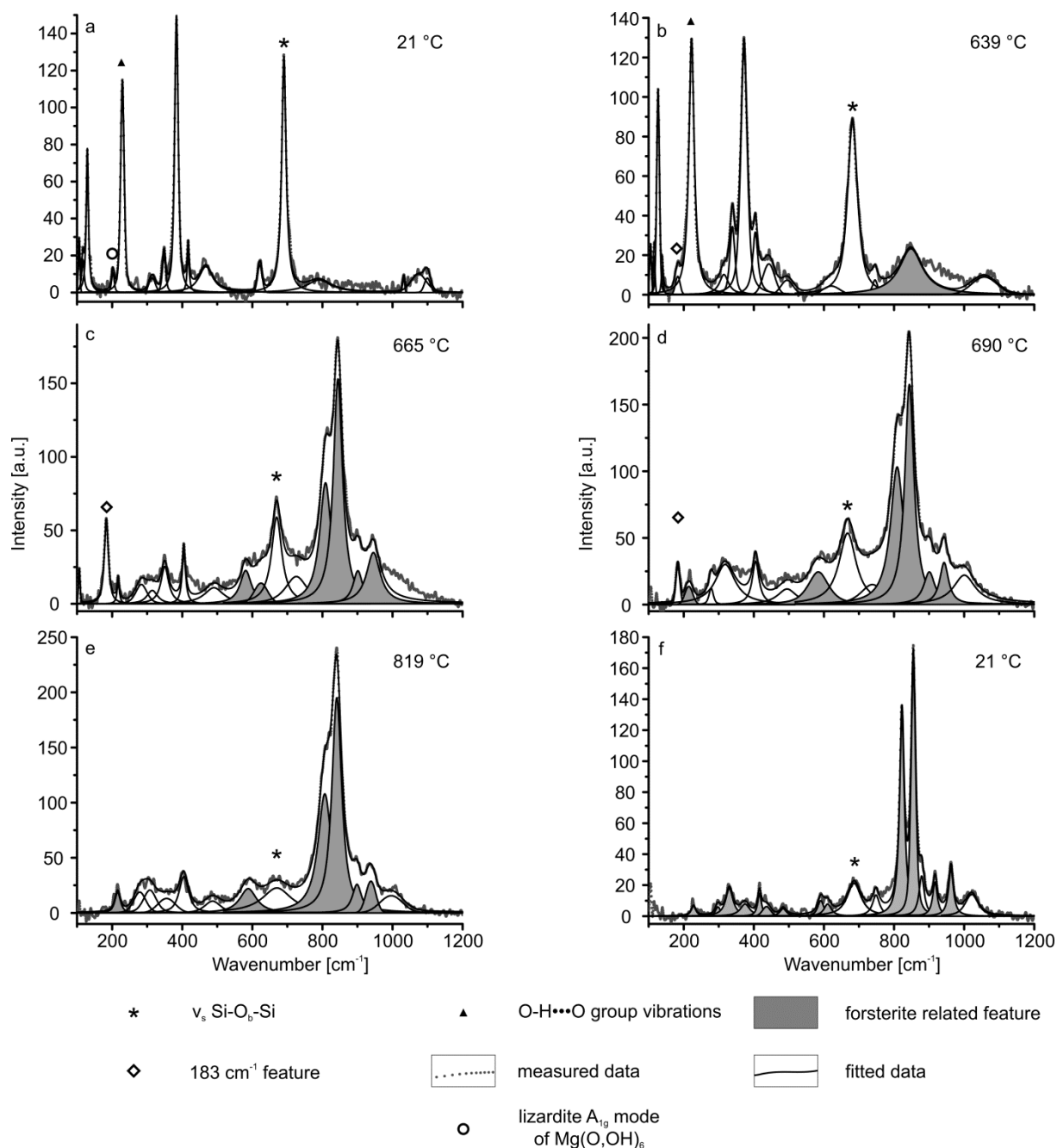


**Figure 5-5.** Low-frequency range of temperature-dependent Raman measurements representing the phase transformation of lizardite-1T to forsterite; f. sample was heated progressively to 819 °C and afterwards quenched and re-measured at RT (21 °C).

vibration modes decreases linearly with temperature (Fig. 5-10). A frequency jump in Raman data, characterised by an obvious deviation from the linear course and marked by the last two data points per Raman band, occurs between 639 °C and 665 °C. The latter spectrum is the last in which OH bands are still visible.

Libowitzky (1999) showed that the OH stretching frequencies can be used to calculate O•••O and H•••O distances in hydrous minerals, i.e., the lizardite interlayer distances (for comparison see Guggenheim and Zhan 1998) are determined from the OH stretching frequencies. Using this method, the interlayer distance (O2-O3 distance) derived from the FTIR data increases from  $2.89 \pm 0.06$  Å at RT to  $2.90 \pm 0.06$  Å at 582 °C. These distances correspond to an O2•••H3 distance of  $2.23 \pm 0.01$  Å at RT to  $2.27 \pm 0.01$  Å at 582 °C.

The evolution of the integrated absorbance with increasing temperature of the four OH bands extracted from the *in situ* FTIR experiments results in a sigmoidal shaped dehydroxylation curve. Initial dehydroxylation starts at  $450 \pm 20$  °C. The dehydroxylation maximum lies at 540 °C (Fig. 5-11a). The absorbance of the individual inner-surface and inner OH stretching modes also starts to decrease at around 450 °C (Fig. 5-11b). The average intensity of the unassigned band is picking up with beginning of the dehydroxylation reaction.

The sum curve of the four Raman OH stretching band intensities (including the unassigned band, for comparison see Figs. 5-3, 5-7 and 5-8), which occur at temperatures higher than RT, gently decreases between RT (Fig. 5-12a) and 450 °C. The minimum of the derivative, functionally related to the maximum in the OH release, occurs at around 640 °C. Above 665 °C the bands disappear completely. The inner-surface OH stretching bands start to decrease in intensity at around 550 °C to 600 °C (Fig. 5-12b). Similar to the behaviour observed in the FTIR spectra, the unassigned band has on average a higher intensity during the dehydroxylation than at lower temperatures.

## 5.4 DISCUSSION

### 5.4.1 OH bands and their assignments

Whereas RT low-frequency Raman spectra of lizardite are compatible with previous data (e.g., Rinaudo *et al.* 2003), OH stretching frequencies in both the Raman and FTIR data show unusual band multiplication compared to group theory considerations by Balan *et al.* (2002) and Prencipe *et al.* (2009). Additional bands to fit the spectrum for the OH stretching modes of lizardite at RT has been recognised previously (e.g., Auzende *et al.* 2004) and additional OH bands are also known from spectra of 2:1 phyllosilicates (Zhang *et al.* 2005). Three different causes are most likely responsible for the appearance of the extra OH band: 1) longitudinal optic-transverse optic (LO-TO) splitting, 2) additional OH groups such as non-structural OH groups, also related to disorder and 3) mixture of lizardite polytypes and/ or chrysotile-like layers. According to hybrid Hartree-Fock/ Density functional theory (HF/ DFT) calculations of the vibrational spectrum of lizardite, Prencipe *et al.* (2009) interpreted additional bands observed by Auzende *et al.* (2004) as originating from LO-TO splitting of the three OH vibrational modes. Additional OH bands in Raman spectra of kaolinite are also attributed to LO-TO splitting (Farmer 1998). Prencipe *et al.* (2009) and Farmer (1998) comprehensively presented the physical background of such additional band appearances related to LO-TO splittings. The key parameter for LO-TO splitting is the size of individual crystals compared to the Raman laser wavelength (Farmer 1998). IR data contain mostly TO modes, except for powdered samples with crystallite sizes greater than the IR wavelength, whereas Raman data are frequently affected by LO-TO splitting (Farmer 1998). Hence, a wavelength depending behaviour, i.e., band multiplication owing to sample size related parameters with respect to the IR and Raman laser wavelength, may result in additional bands in our RT FTIR and Raman datasets, with four observable IR bands, but six Raman bands. Thus, the transparent film used probably shows a less

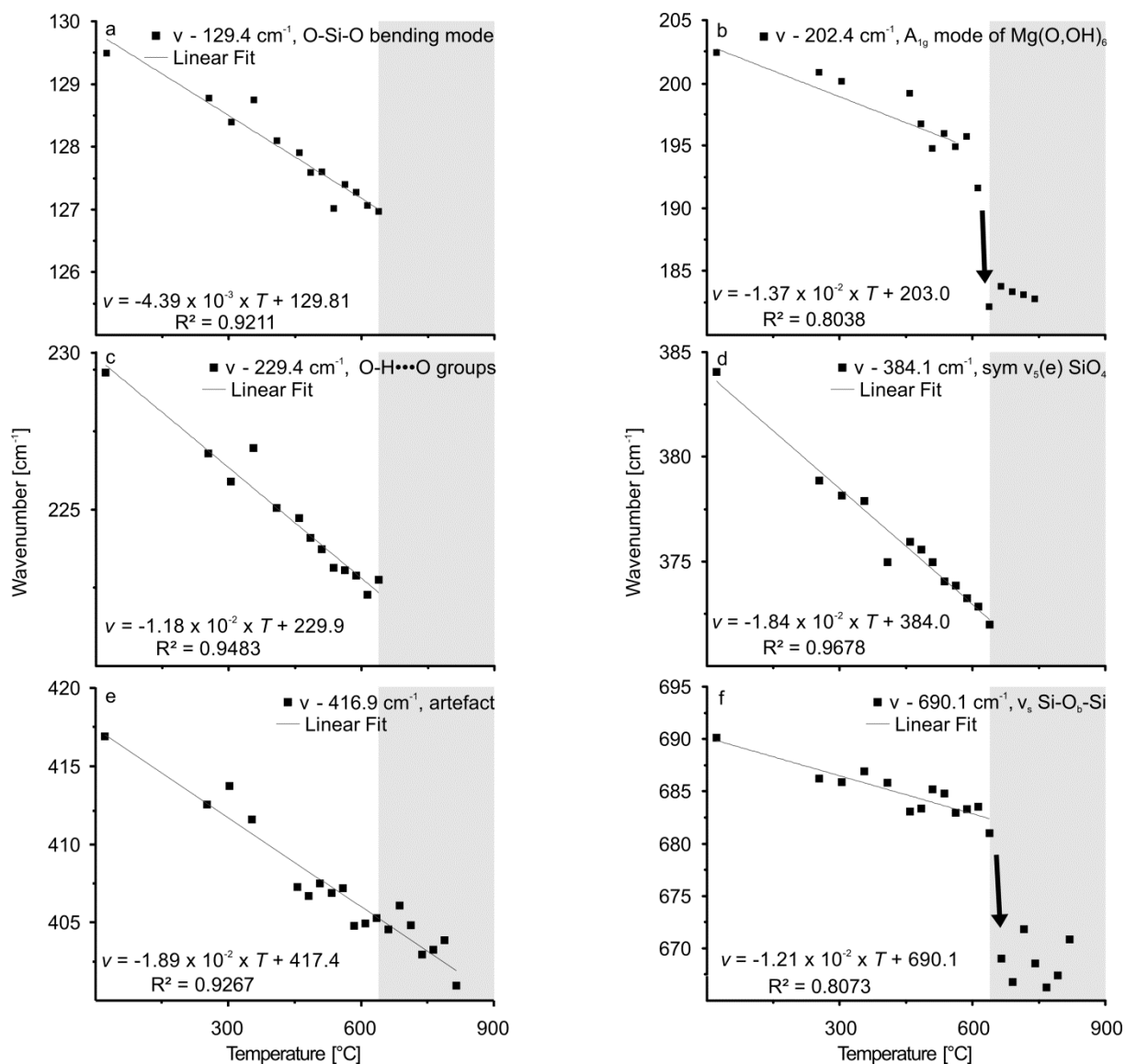


**Figure 5-6.** Temperature-dependent Raman band shifts in the low-frequency region of lizardite-1T; grey shading marks the presence of forsterite.

complex OH stretching band pattern (dominated by TO modes) than the resulting patterns of the single crystal and the loose powder used in the Raman experiments.

Non-structural OH species have been suggested as an alternative explanation for additional OH band(s) in vibrational spectra of phyllosilicates (Wang *et al.* 2002; Zhang *et al.* 2006; Zhang *et al.* 2010). However, most of these bands appear during the heat treatment and before significant dehydroxylation (e.g., Zhang *et al.* 2010). These bands are often situated at wavenumbers

significantly different from that of initial OH bands. In the case of talc, such extra bands occur within the range of the primary OH bands (Zhang *et al.* 2006). In our experiments, the band at 3669 cm<sup>-1</sup> (FTIR) and 3670 cm<sup>-1</sup> (Raman), respectively, labelled as the unassigned band in Fig. 5-3, can be interpreted as resulting from some non-structural OH species already present at RT, but increasing during dehydroxylation. A third possible cause for the additional bands may be the presence of different polytypes, turbostratic stacking faults or curved, chrysotile-like layers within the lizardite

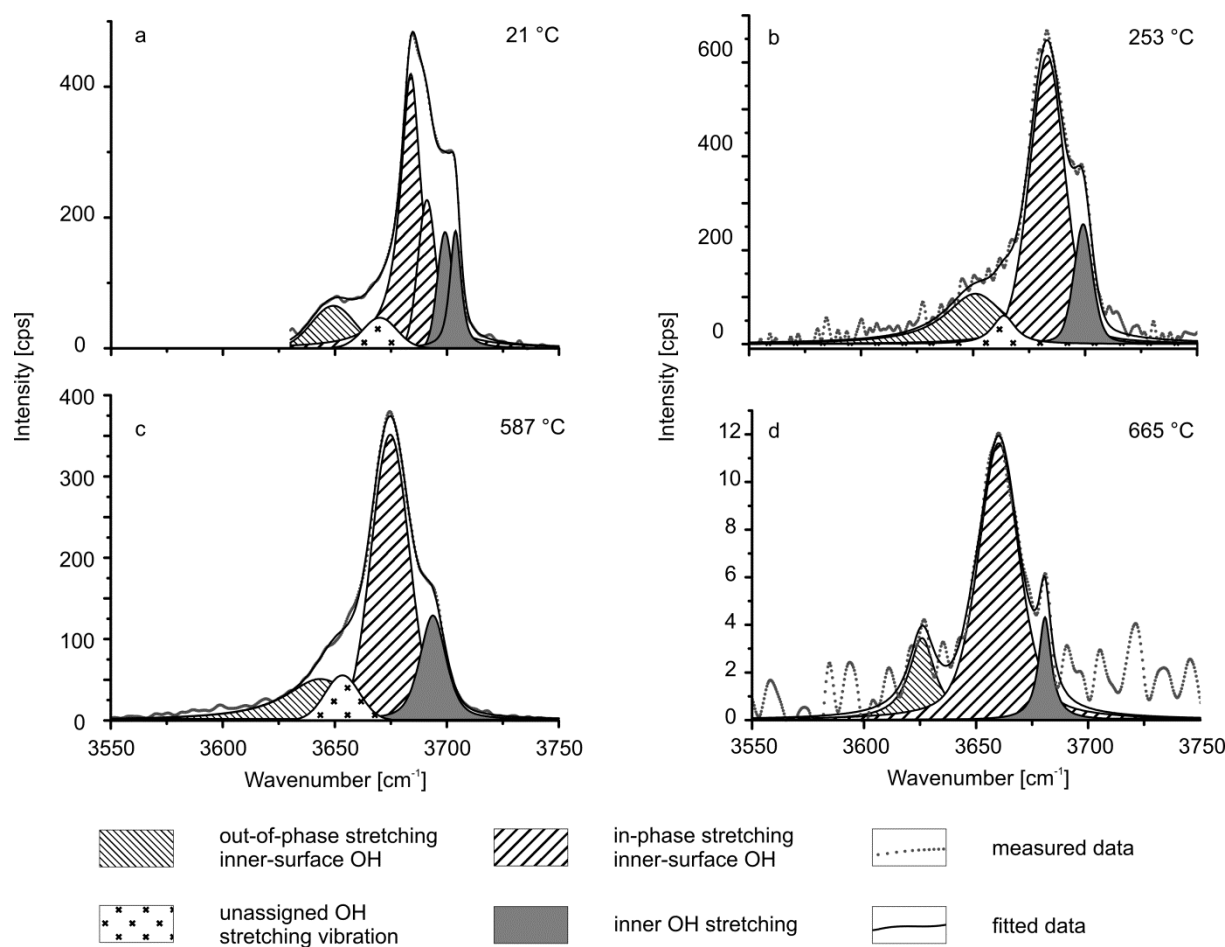


**Figure 5-7.** OH stretching frequency range of temperature-dependent Raman measurements representing significant intensity reduction between RT and 665 °C, the highest temperature where OH signals are still present.

sample (Trittschack and Grobéty 2012). Defects have been suggested as an explanation for additional hydroxyl bands in amphiboles (Burns and Strens 1966), micas (Beran 2002) and kaolinite and dickite (Brindley *et al.* 1986). For samples containing more than one polymorph of a phase, individual frequency shift rates ( $\delta\nu/\delta T$ ) for specific modes of individual polymorphs may change the degree of overlap. This changes the number of bands necessary for an accurate fit of the measured spectra. Brindley *et al.* (1986) document such temperature-dependent OH band specific shifts in kaolinite and dickite. However, taking the possibility of a LO-TO splitting into account, such a solution is simplistic.

#### 5.4.2 The lizardite dehydroxylation I: Comparison between FTIR, Raman and TGA data

The temperature at which the absorbance of the OH bands starts to decrease in the FTIR spectra is comparable with the dehydroxylation onset observed in TGA analysis of the same sample (Trittschack and Grobéty 2012). The rate of the intensity decrease (Fig. 5-11) is, however, more rapid than the TGA derived dehydroxylation rates in experiments with comparable heating rate (540 °C compared to  $\sim 650\text{ °C} \leq T_{\text{max}} \leq \sim 720\text{ °C}$ ) reported by Trittschack and Grobéty (2012). The explanation for the discrepancy may be that the two techniques monitor different steps of the dehydroxylation process. Whereas FTIR/ Raman

spectroscopy is sensitive to the primary hydrogen and hydroxyl liberation steps, TGA monitors the exit of the dehydroxylation products from the sample e.g., the weight loss after the products leaves the reactant grain and the powder. Thus, the TGA signal is initially delayed relative to the spectroscopic signal. The differences in dehydroxylation maxima observed in FTIR and Raman data are related to the different samples used. Also, the preparation of the samples used for the FTIR and Raman experiments were different, whereas for the Raman spectroscopy a gently pressed powder and a single crystal were used, the FTIR spectroscopy was obtained on a thin transparent film pressed in a DAC. The partial pressure (or activity) of the product species (water, hydroxyl, hydrogen and/ or oxygen molecules)

along the diffusion path decreases more rapidly in a thin film than in a loose powder and single crystal, respectively. This increases the absolute dehydroxylation reaction rate in the thin film, which may explain the accelerated intensity loss observed in the FTIR measurements. A similar explanation has been suggested for the differences in IR spectra between annealed pyrophyllite samples of a varying thickness (Wang *et al.* 2002).

### 5.4.3 The lizardite dehydroxylation II: Kinetic aspects and their spectroscopic indications

The activation energy  $E_a$  as function of the reaction progress estimated by TGA based dehydroxylation studies of lizardite shows an

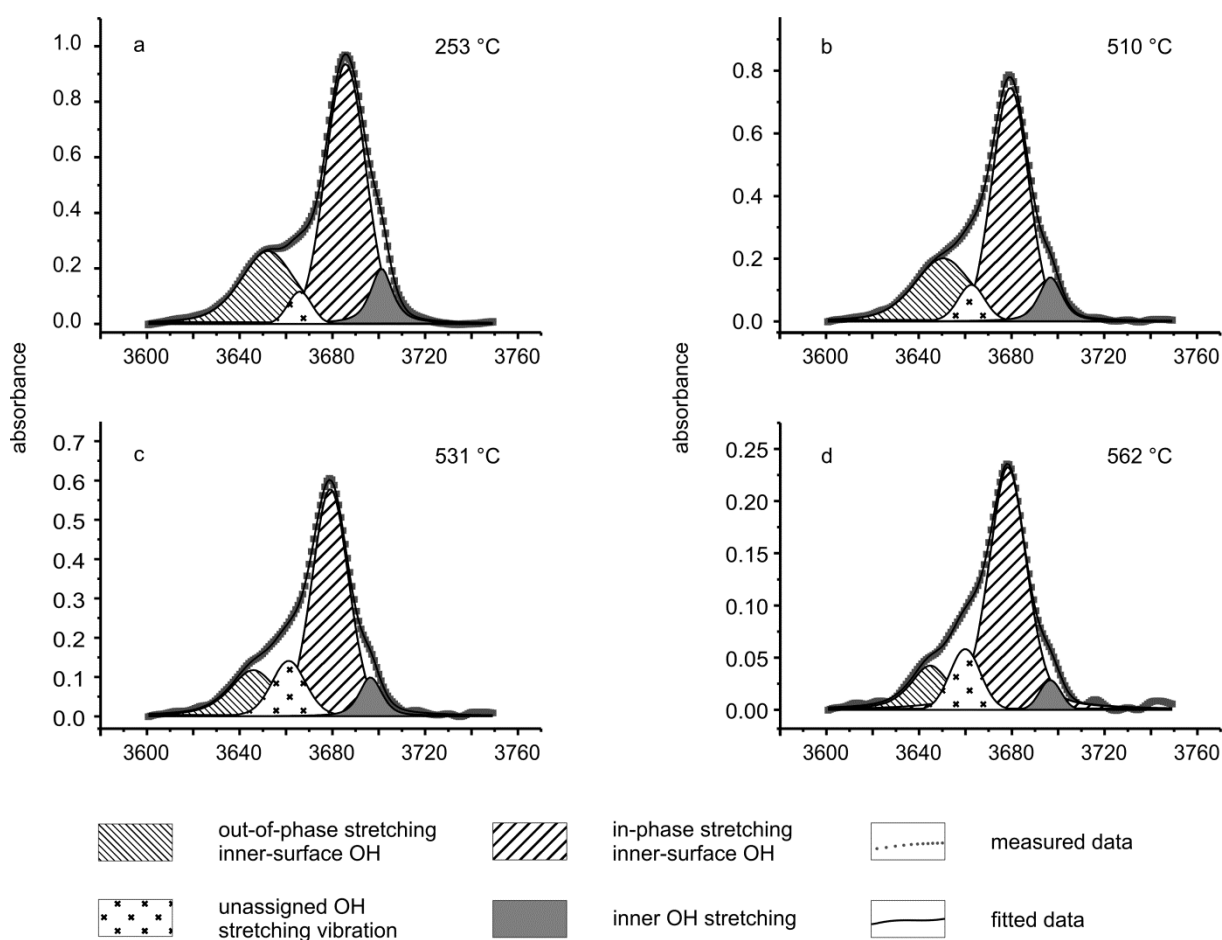


**Figure 5-8.** OH stretching frequency range of temperature-dependent FTIR measurements representing a significant reduction in absorbance between RT and 562 °C.

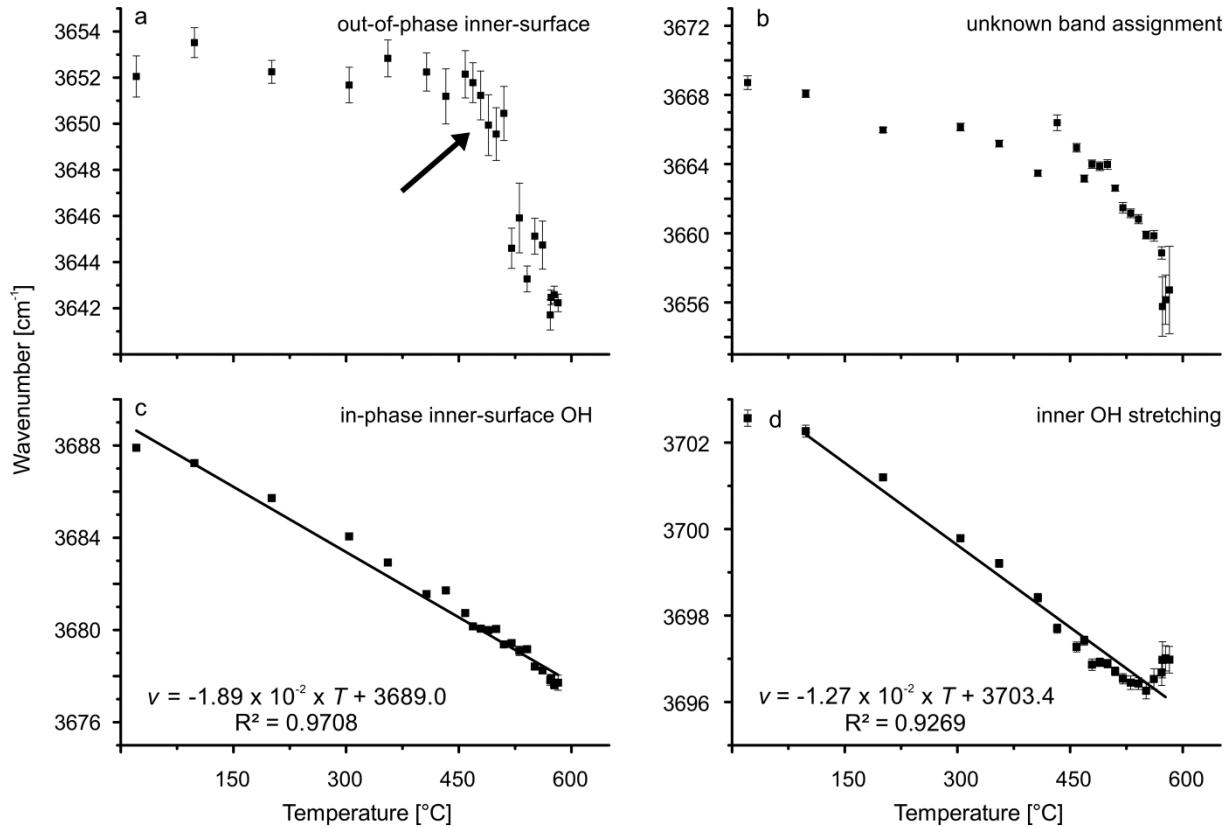


**Figure 5-9.** Development of the inner and inner-surface IR OH stretching frequencies during heat treatment; error bars are illustrated and may be smaller than the shown data points.

initial increase from 200 kJ/mol to over 350 kJ/mol followed by a plateau (Trittschack and Grob  ty 2012). For heating rates similar to the one used here, the activation energy plateau is reached at about 50   C below the temperature at which the OH bands have lost almost 60 % (at 639   C), respectively, 98 % (665   C) of their intensity in the Raman spectrum. DFT calculations and almost all previous works (e.g., Gualtieri and Ferrari 2006; Molina-Montes *et al.* 2008a and b; Sperinck *et al.* 2011) propose a recombination of neighbouring proton and hydroxyl ions to H  O molecules as the primary reaction step, followed by diffusion of the products (H  O molecules) along the interlayer to the surface. Several distinct recombination variants are possible, which differ by the distance between the reacting hydroxyls. Trittschack and Grob  ty (2012) interpreted the increasing  $E_a$  as a result of these parallel recombination steps, whereby the close distance, low  $E_a$  recombination reactions occur at the beginning of dehydroxylation. With

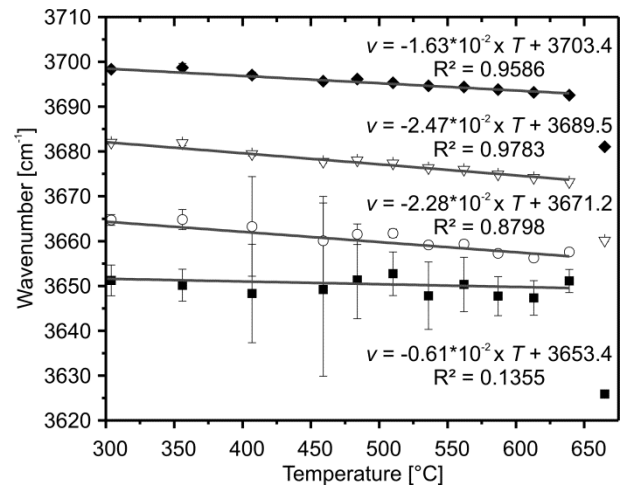


**Figure 5-10.** Development of the inner and inner-surface Raman OH stretching frequencies during heat treatment, error bars are illustrated and may be smaller than the shown data points; open circle - unassigned band, filled rhomb - inner OH band, filled square - out-of-phase inner-surface OH band, reverse triangle - in-phase inner-surface OH band.

increasing reaction progress, longer distance recombination variants with higher  $E_a$  become more frequent. The plateau  $E_a$  corresponds to the recombination variant with the highest  $E_a$  and the slight decrease indicates the increasing influence of transport in certain parts of the sample (large grains). This interpretation is compatible with DFT calculations (Molina-Montes *et al.* 2008a and b, Sperinck *et al.* 2011), but not with experimental work by Gualtieri and Ferrari (2006) and Gualtieri *et al.* (2012), who indicate one-dimensional diffusion of  $H_2O$  molecules through the six-membered silicate rings. In the latter case,  $H_2O$ -related modes should be visible in *in situ* Raman and FTIR spectra of partially dehydrated samples. Martin (1977) and Datta (1991) described a broad, infrared active band between  $3200\text{ cm}^{-1}$  and  $3500\text{ cm}^{-1}$  in thermally pre-treated chrysotile samples, which they assign to  $H_2O$  modes. Such bands were not present in our spectra. Also Zhang *et al.* (2010) did not find any  $H_2O$ -related bands in their FTIR spectra of partially dehydrated sericite, muscovite, pyrophyllite and talc. Zhang *et al.* (2005) prefer a hydrogen/ oxygen/ hydroxyl hopping mechanism over  $H_2O$  molecule diffusion as the transport mechanism for the dehydroxylation products. The transport by hopping requires similar bond breaking and formation steps as the initial liberation reactions. The transport mechanism would have similar  $E_a$  as the primary reactions, and could, therefore, also become rate-limiting. Thus, transport could also contribute to the  $E_a$  plateau. The increased intensity of the unassigned OH mode during dehydroxylation in both the FTIR and Raman spectra may be related to such transient hydroxyl groups formed during transport. This interpretation is tentative, because the unassigned hydroxyl band is the result of the deconvolution of strongly overlapping bands.

#### 5.4.4 Dehydroxylation products: A talc-like intermediate and forsterite

To approximately  $450\text{ }^{\circ}\text{C}$ , the spectra are only affected by a constant frequency shift of the Raman and IR bands, which relate to thermal

expansion of the structure. The intensity of all bands remains nearly constant to this temperature (Figs. 5-4 and 5-11a). Above this temperature, bands assigned to atom groups belonging to the octahedral sheet, i.e.,  $A_{1g}$  mode of lizardite (Fig. 5-6b) and OH stretching vibrations (Fig. 5-9a), show a strongly discontinuous behaviour (Figs. 5-6b and 5-6f). This is interpreted as resulting from changes in the atomic bonding environment. These changes occur at about the same temperature where the absorbances/ intensities of the OH bands start to decrease. Thus, the onset of dehydroxylation affects only the octahedral sheet. The different behaviour of the in-phase (Fig. 5-9a) and out-of-phase OH stretching mode frequencies (Fig. 5-9c) as function of temperature, however, is surprising. The in-phase stretching mode shows a break in the slope of  $\delta\nu/\delta T$  whereas the slope of the out-of-phase mode is characterised by a linear slope. Modes originating from the same atomic group should show the same frequency behaviour. A possible cause may be the deconvolution procedure.

The small temperature-dependent shift of the O-Si-O bending mode located at  $129\text{ cm}^{-1}$  (RT) to lower wavenumbers is related to the change in ditrigonal distortion of the tetrahedral sheet as demonstrated by X-ray diffraction (Guggenheim and Zhan 1998). The shifting rate  $\delta\nu/\delta T$  is one order of magnitude smaller than for all other bands ( $-0.439\text{ cm}^{-1}/100\text{ }^{\circ}\text{C}$ ). The first intensity changes in Si-O-related Raman modes occur above  $600\text{ }^{\circ}\text{C}$  (Fig. 5-4) where the hydroxyl modes have lost more than half of their initial intensity (Fig. 5-12a). The tetrahedral sheet is thus not affected by the initial changes in the octahedral sheet. The large jump in frequency of the  $A_{1g}$  mode of lizardite down to  $183\text{ cm}^{-1}$  and the jump in frequency of the  $\nu_s$  Si-O<sub>b</sub>-Si band is assigned to product phase(s) of the dehydroxylation. Under ambient, dry conditions the first recognisable dehydroxylation product is mainly amorphous, but crystallises upon further heating to forsterite, followed by enstatite (Brindley and Hayami 1963a). The stable products of the dehydroxylation reaction of pure magnesian lizardite under hydrothermal conditions are talc,

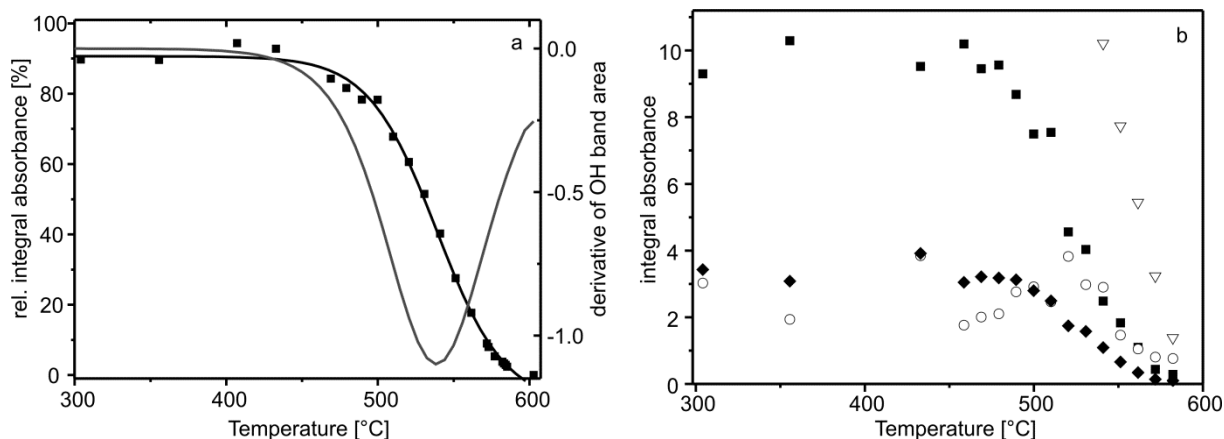


**Figure 5-11.** (a) Decrease of the integrated absorbance of all FTIR OH stretching bands as function of temperature and corresponding derivative curve and (b) for the individual inner-surface OH stretching bands and the unassigned band. The course of the inner OH stretching band behaves like the inner-surface OH bands and is just shown for temperatures higher than 500 °C. All symbols have the identical assignment as in Fig. 5-10.

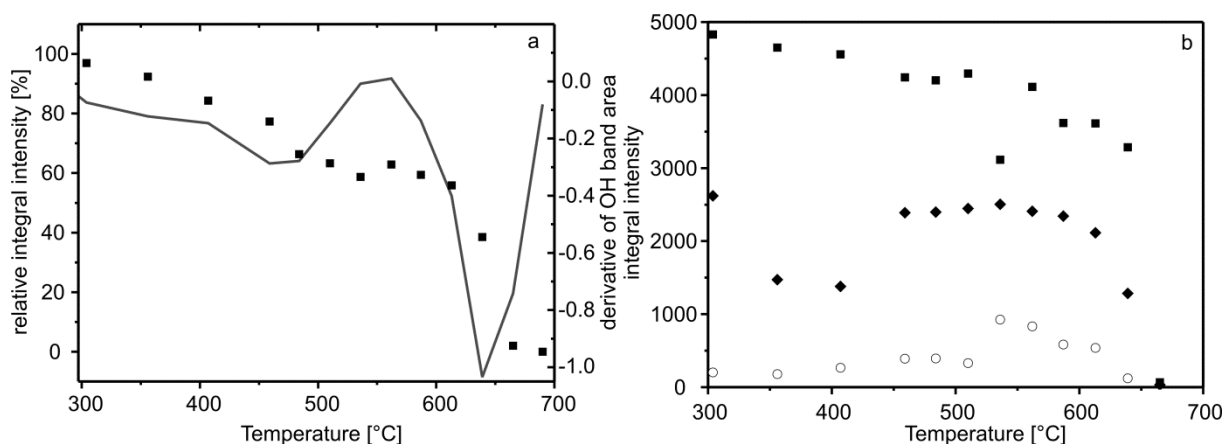


**Figure 5-12.** (a) Decrease of the integrated intensity of all Raman OH stretching bands as function of temperature and corresponding derivative curve and (b) for the individual inner-surface OH stretching bands and the unassigned band. All symbols have the identical assignment as in Fig. 5-10.

forsterite and water (O'Hanley *et al.* 1989). Various authors (e.g., Brindley and Zussman 1957; McKelvy *et al.* 2004) reported low-angle peaks in X-ray diffractograms of thermally treated serpentine phases, indicating that amorphisation is not complete and that dehydroxylation produces intermediate partially ordered structures. Although differing in detail, early studies by Ball and Taylor (1963) and Brindley and Hayami (1965) proposed reaction sequences with disordered dehydroxylated

intermediates. They infer the presence of a partially ordered structure from the topotactic relationship between forsterite and serpentine (Brindley and Hayami 1963a). Based on a peak corresponding to a  $d$ -spacing of 14 Å, McKelvy *et al.* (2006) proposed the formation of a lamellar oxyhydroxide meta-serpentine characterised by a doubled cell dimension along the  $c$  axis and a heterogeneous OH distribution. Their DFT calculations support the formation of such a 14 Å



structure, which is transformed to an amorphous phase with progressive dehydroxylation. Two different partially ordered, anhydrous intermediates, dehydroxylate I and II, are proposed by MacKenzie and Meinhold (1994) based on  $^{25}\text{Mg}$  and  $^{29}\text{Si}$  shifts in NMR spectra of heated chrysotile samples. According to these authors, dehydroxylate I has a structure similar to the parent phase, whereas the  $^{29}\text{Si}$  NMR position of dehydroxylate II is similar to talc. Viti (2010) suggests the formation of intermediate, partially ordered dehydroxylation products on the bases of DTG/DTA analyses of lizardite. Their weight-loss rate curves show two maxima, a feature also observable in DTG experiments of Trittschack and Grobéty (2012). The first maximum is attributed to the partial dehydroxylation of the initial lizardite leading to the intermediate phase. The dehydroxylation of the latter would be responsible for the second maximum.

Three new features at  $183\text{ cm}^{-1}$ ,  $350\text{ cm}^{-1}$  and  $670\text{ cm}^{-1}$  in the spectrum at  $665\text{ }^{\circ}\text{C}$ , which cannot be assigned to either lizardite or forsterite, are interpreted as originating from (a) intermediate phase(s). Supported by a band appearing at  $1000\text{ cm}^{-1}$  ( $690\text{ }^{\circ}\text{C}$ ) it is possible to assign them as

Raman bands related to talc as reported by Fumagalli *et al.* (2001). The bands located at  $670\text{ cm}^{-1}$  and  $1000\text{ cm}^{-1}$  are also observable in the spectrum of the quenched dehydroxylated sample, where they are shifted to  $686\text{ cm}^{-1}$  and  $1021\text{ cm}^{-1}$ , respectively. Referring to Fumagalli *et al.* (2001) these bands can be assigned to a  $\text{Mg}(\text{O},\text{OH})_6$  mode ( $183\text{ cm}^{-1}$ ), a symmetric  $\text{SiO}_4$  mode ( $350\text{ cm}^{-1}$ ), a  $\nu_s$  Si-O<sub>b</sub>-Si mode in case of the  $670\text{ cm}^{-1}$  ( $686\text{ cm}^{-1}$  at RT) feature (Fig. 5-5d) and one Si-O stretching mode represented by the  $1000\text{ cm}^{-1}$  feature at  $819\text{ }^{\circ}\text{C}$  and  $1021\text{ cm}^{-1}$ , respectively, in the spectra of the quenched sample. The strongest of three weak single bands in the OH stretching mode region (Fig. 5-7d) is also consistent with the spectrum of talc (Fumagalli *et al.* 2001). This interpretation supports NMR observations by MacKenzie and Meinhold (1994) who proposed a talc-like structure for their dehydroxylate II phase. During dehydroxylation, the partial pressure of the volatile products may be sufficiently high in certain regions of the sample to nucleate talc, a stable product of the lizardite dehydroxylation in the hydrous system (O'Hanley *et al.* 1989). The band at  $183\text{ cm}^{-1}$  appears also in the dehydroxylation of chrysotile (Trittschack and Grobéty 2013), where it is present for a much broader temperature range.

## 6 - THE DEHYDROXYLATION OF CHRYSOTILE: A COMBINED *IN SITU* MICRO-RAMAN AND MICRO-FTIR STUDY

*Trittschack R, Grobéty B*

*published in American Mineralogist 98:1133-1145 (2013)*

### ABSTRACT

The dehydroxylation of natural chrysotile and the subsequent phase change to forsterite was studied by *in situ* micro-Raman and micro-FTIR spectroscopy in the temperature range of 21 °C to 871 °C. Comparisons were made with previously published data of lizardite-1T. Micro-Raman spectra obtained in the low-frequency (100-1200 cm<sup>-1</sup>) and high-frequency range (3500-3800 cm<sup>-1</sup>) were complemented by micro-FTIR measurements between 2500 and 4000 cm<sup>-1</sup> in order to study changes in the chrysotile structure as function of dehydroxylation progress. In general, room-temperature chrysotile bands lie at higher wavenumbers than equivalent bands of lizardite-1T except of three bands positioned at 301.7 cm<sup>-1</sup>, 317.5 cm<sup>-1</sup> and 345.2 cm<sup>-1</sup>. Different band assignments of chrysotile and lizardite-1T Raman spectra from literature are compared. Most striking assignments concern the three aforementioned Raman bands and those lying between 620 cm<sup>-1</sup> and 635 cm<sup>-1</sup>. The herein presented data support a chrysotile-related or at least curved TO layer related origin of the latter. Deconvolution of overlapping OH stretching bands at room-temperature revealed the presence of five (FTIR) and four (Raman) bands, respectively. A slight change in the ditrigonal distortion angle  $\alpha$  during heating and the effects of a radius-dependent dehydroxylation progress can be shown. Furthermore, it was possible to identify a quenchable talc-like phase immediately after the onset of the dehydroxylation at 459 °C. Main bands of this phase are positioned at 184.7 cm<sup>-1</sup>, 359.2 cm<sup>-1</sup> and 669.1 cm<sup>-1</sup> and a single OH band at 3677 cm<sup>-1</sup>, and are thus quite similar to those reported for dehydroxylating lizardite-1T. Their appearance coincides with the formation of forsterite. A maximum in the integral intensity of the talc-like intermediate is reached at 716 °C. At higher temperatures the intermediate phase breaks down and supports the accelerated growth of forsterite. The lack of OH bands, but the appearance of broad chrysotile-related modes in the low-frequency range after heating the sample to 871 °C indicates the presence of a heavily disordered phase still resembling chrysotile. However, there are no spectral evidences for further Si- and/ or Mg-rich amorphous phases during the dehydroxylation and no indications for a relationship between the breakdown of the talc-like phase and the growth of enstatite as previously reported in literature.

### 6.1 INTRODUCTION

Chrysotile is a member of the serpentine group with an ideal formula Mg<sub>3</sub>Si<sub>2</sub>O<sub>5</sub>(OH)<sub>4</sub>. Common building blocks of this group are octahedrally-coordinated (O) brucite-like sheets linked with tetrahedrally-coordinated (T) sheets of SiO<sub>4</sub> which form a trioctahedral 1:1 (TO) layer phyllosilicate. The misfit between both sheets gives rise to a

variety of modulated polymorphs of the flat layered lizardite, such as antigorite with undulating layers and chrysotile with wrapped cylindrical layers, but also rare species like polygonal and polyhedral serpentine (Wicks and Whittaker 1975; Grobéty 2003; Dódonny and Buseck 2004; Cressey *et al.* 2008). X-ray diffraction (XRD) and high-resolution transmission electron microscopy (HRTEM) revealed the existence of different

chrysotile polytypes. Known polytypes are clino-, ortho- and parachrysotile, while clinochrysotile is the most abundant one (Wicks and O'Hanley 1988).

Physico-chemical properties of chrysotile, e.g., the dehydroxylation temperature, are likely to change with the radius of the fibre owing to slight changes of structural parameters (e.g., bond lengths and angles) with curvature (Evans 2004). This behaviour causes a continuous phase transformation starting on the chrysotile wall edges at approximately 450 °C and propagating to the inner wall, where the layers start to dehydroxylate only above 600 °C (Viti 2010). Literature on the thermal behaviour of chrysotile is extensive due to the peculiar structure, the excellent heat resistance and insulating properties of chrysotile (= white asbestos) compounds (e.g., Ball and Taylor 1963; Brindley and Hayami 1963a and b, Martin 1977; Datta *et al.* 1987; Candela *et al.* 2007). Early articles by Aruja (1943), Hey and Bannister (1948) and Brindley and Zussman (1957) have studied the phase transformation from chrysotile to forsterite. They observed an amorphous phase as primary product of dehydroxylation, followed by forsterite. Their results indicate a topotactic relationship between primary chrysotile and forsterite, despite the intervening amorphous phase. Among others, Brindley and Zussman (1957) also documented the presence of a potential poorly crystalline intermediate phase on the base of a low-angle XRD peak at around 14 Å, shifting to 10 Å with progressive heating. A series of studies also focused on the structure of (a) potential intermediate phase(s) without identifying such (a) phase(s) in detail (Ball and Taylor 1963; Brindley and Hayami 1963a and b; Martin 1977; Jolicoeur and Duchesne 1981; Datta *et al.* 1987; Datta 1991). Based on nuclear magnetic resonance (NMR) studies, MacKenzie and Meinhold (1994) suggested the occurrence of a talc-like intermediate during 'dry' dehydroxylation which they labelled as 'dehydroxylated II'. Talc is a stable product phase during the dehydroxylation of serpentine under hydrothermal conditions (Ball and Taylor 1963; O'Hanley *et al.* 1989). Among XRD and

FTIR results, McKelvy *et al.* (2004, 2006) made first principle simulations of the lizardite dehydroxylation process which gave as product phase an intermediate, 'meta-serpentine', ~ 14 Å phase, plus an amorphous phase. They explain the formation of the meta-serpentine phase with a lamellar nucleation and growth mechanism leading to a strong topotactic relationship between primary serpentine and the 14 Å phase. Recent studies on the dehydroxylation mechanisms and kinetics of chrysotile and serpentine minerals in general have gained growing interest (Cattaneo *et al.* 2003; Viti 2010; Gualtieri *et al.* 2012). This is caused by an enhanced interest in subduction zone seismicity, inertisation of asbestiform waste, CO<sub>2</sub> sequestration and the demand for a cost-efficient and simple way to distinguish serpentine polymorphs.

This study presents *in situ* micro-Raman and micro-FTIR investigations of the dehydroxylation of chrysotile, which will be compared with recently published data on the dehydroxylation of lizardite-1T (Trittschack *et al.* 2012).

## 6.2 EXPERIMENTAL METHODS

### 6.2.1 Sample material

The investigated chrysotile sample was taken from a chrysotile vein in a serpentinite of the mineral collection of the University of Fribourg/Switzerland without details of origin (internal reference chry 33/12). Transmission electron microscopy based energy-dispersive spectroscopy (TEM-EDS) studies yield 51.2 wt% MgO, 48.0 wt% SiO<sub>2</sub> and 0.1 wt% FeO<sup>tot</sup> which fits an almost pure Mg end-member. The resulting XRD spectrum is close to the ICDD reference patterns 25-0645 and 10-0381 of clinochrysotile and shows no additional peaks (Fig. 6-1). Selected area electron diffraction (SAED) patterns are compatible with XRD data and exclude the presence of parachrysotile (Fig. 6-2), although it is not possible to distinguish clearly between clino- and orthochrysotile. HRTEM based measurements

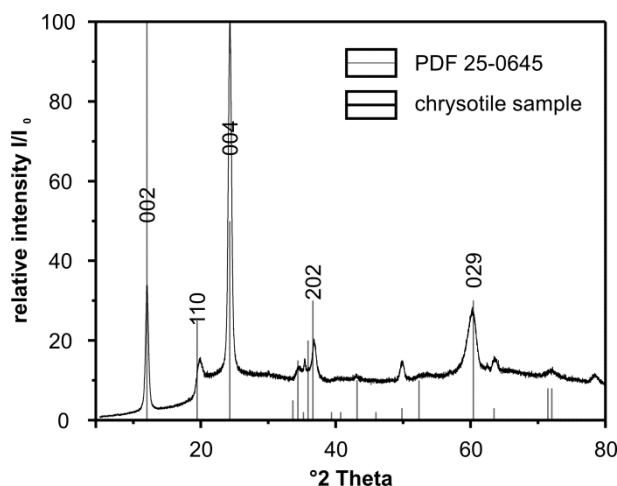


**Figure 6-1.** X-ray powder diffraction pattern of the studied chrysotile sample chry 33/12 compared with the ICDD entry 25-0645.

of the outer diameter give values between 23 nm and 85 nm, but more than 75 % of the measured fibres lie in the range between 30 nm and 60 nm.

As a reference for the interpretation of the chrysotile Raman measurements, spectra of a lizardite-1T single crystal from the Monte Fico quarries, Elba Island/ Italy, were used (private collection, Marcello Mellini). Mellini and Viti (1994) and Fuchs *et al.* (1998) provided comprehensive mineralogical and chemical data of this sample.

Raman and FTIR experiments were carried out on sub-parallel fibre bundles positioned in a heat-resistant sapphire crucible. The Monte Fico single crystal was independently measured in the same sapphire crucible with an orientation *c* parallel to the incident Raman laser beam.

### 6.2.2 FTIR and Raman spectroscopy

Micro-FTIR measurements were performed with a Bruker VERTEX 80v spectrometer attached to a Hyperion1000 FTIR microscope at the GeoForschungsZentrum Potsdam (GFZ Potsdam/ Germany). Spectra were collected in the 2500-4000  $\text{cm}^{-1}$  frequency range using a LN-INSB

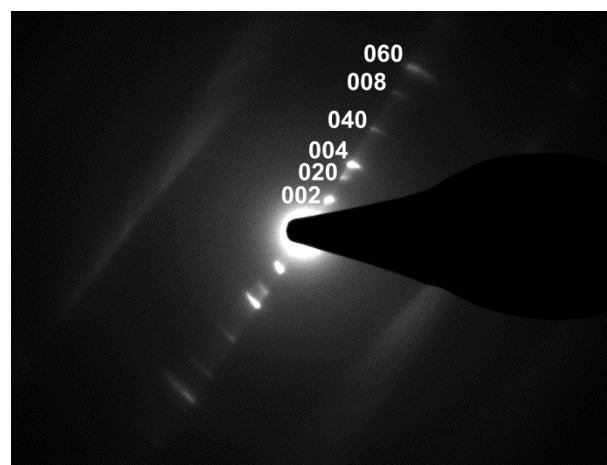


**Figure 6-2.** SAED pattern of chrysotile. Strong reflections are compatible with the clino- and orthochrysotile polytypes.

D413 detector, a KBr beamsplitter and a 6 mm aperture in transmission mode. Each spectrum was measured with a resolution of 2  $\text{cm}^{-1}$  and averaged over 60 individual scans resulting in a measurement interval of about 64 sec. A 10 x 40  $\mu\text{m}$  sized area of sub-parallel fibers was chosen to collect FTIR spectra of chrysotile.

Micro-Raman investigations were carried out with a HORIBA HR 800 UV spectrometer (grating 1800 grooves/mm, focal length 800 mm, 1024 x 256 pixel CCD detector) connected to a XY adjustable stage and an Olympus BX41 microscope (20x objective, backscattering configuration) at the GFZ Potsdam. A confocal pinhole of 100  $\mu\text{m}$  was used for all measurements. The Raman setup used offers a spectral resolution of about 1  $\text{cm}^{-1}$ . The Raman spectrometer was run with an argon laser (488 nm, 300 mW) and calibrated against the emission bands of a neon lamp. The illuminated diameter on the sample surface yields 4.4  $\mu\text{m}$  considering the used Raman setup. Spectra acquisition time was 40 sec and 3 spectra were cumulated for each temperature step. In general, spectra were measured in the frequency range of 100-1200  $\text{cm}^{-1}$  and 3500-3800  $\text{cm}^{-1}$ .

*In situ* high-temperature (HT) micro-FTIR and micro-Raman measurements were performed by

using a software-controlled Linkam TS1000 heating stage placed onto the FTIR and Raman microscope stage. The thermocouple was calibrated using the melting points of different salts:  $\text{NaNO}_3$  ( $T_M$  - 306 °C), NaI ( $T_M$  - 651 °C) and NaCl ( $T_M$  - 801 °C). The 0 °C point was included in the calibration line. To guarantee a rapid removal of the water generated during the dehydroxylation a constant flow of nitrogen was adjusted.

FTIR spectra of chrysotile were successively measured at 21 °C, 98 °C, 201 °C, 304 °C, 356 °C, 407 °C, 433 °C and 459 °C with a constant heating rate of 130 °C/min between the respective temperatures. For temperatures higher than 459 °C an automated measuring/ heating cycle was programmed up to a maximum temperature of 871 °C (heating rate  $\beta = 1$  °C/min, single acquisition time 64 sec). Raman data of one single fiber bundle were subsequently acquired at 21 °C, 47 °C, 98 °C\*, 150 °C\*, 201 °C\*, 253 °C\*, 304 °C\*, 356 °C\*, 407 °C\*, 459 °C\*, 484 °C, 510 °C\*, 562 °C, 587 °C, 613 °C\*, 639 °C, 665 °C\*, 690 °C, 716 °C, 768 °C\* and 871 °C\*. The dwell time amounts to around 8 minutes at the respective temperatures owing to the experimental conditions. The heating rate between each temperature level was fixed at  $\beta = 100$  °C/min. Additional low-temperature spectra, referred as ‘quenched’ data, were taken from samples heated to temperatures marked by a star and cooling them down to 47 °C. Afterwards the sample was heated up to the next higher temperature. Thus, the chrysotile bundle were cyclically heated and quenched down several times which result in total experiment duration of around 8.5 hours. The stability of the Raman shift was checked by an artificial, non-sample related band at 416.8  $\text{cm}^{-1}$  at RT (Fig. 6-3).

The Raman spectra were corrected for temperature- and frequency-dependent scattering intensity by the method provided by Long (1977). Afterwards, the Raman intensities were normalized to the temperature providing the greatest absolute intensity.

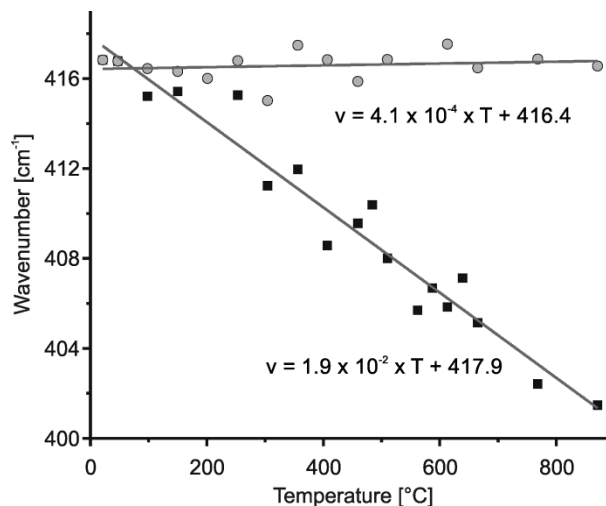


**Figure 6-3.** Temperature-dependent evolution of the Raman shift of an external, non-sample related artifact for observing the stability of the Raman setup with time and temperature.

### 6.2.3 Fitting procedure

PeakFit (v4.12) was used to perform peak deconvolution and integration of all FTIR and Raman spectra. The low-frequency range (100-1200  $\text{cm}^{-1}$ ) and high-frequency range (3500-3800  $\text{cm}^{-1}$ ) of the Raman data were treated independently. Spectra smoothing was done by the implemented Savitzky-Golay algorithm. After baseline subtraction (linear baseline), all spectra were fitted using a combined Gaussian-Lorentzian Amp function with the base and the full width at half maximum (FWHM) as refinable parameters. A minimum number of peaks were chosen to guarantee a best fit as shown by Auzende *et al.* (2004).

## 6.3 RESULTS

### 6.3.1 Raman and FTIR spectra at ambient conditions

The chrysotile sample was measured at ambient conditions in the low-frequency range (100-1200  $\text{cm}^{-1}$ ). A comparison with the Monte Fico lizardite-1T and a reference spectrum of chrysotile from the

RRUFF database (Downs 2006) is shown in Figure 6-4. Five major bands are located at  $129.3\text{ cm}^{-1}$ ,  $233.3\text{ cm}^{-1}$ ,  $389.4\text{ cm}^{-1}$ ,  $691.3\text{ cm}^{-1}$  and  $1105.4\text{ cm}^{-1}$ , which are accompanied by a series of less intense band (Fig. 6-4, Table 6-1). In general, all low-frequency bands are in good agreement with the RRUFF reference spectrum R070088 of chrysotile (Downs 2006) and data reported by Klopogge *et al.* 1999; Rinaudo *et al.* (2003) and Auzende *et al.* (2004). Compared to lizardite-1T (Trittschack *et al.* 2012), chrysotile bands lie at higher wavenumbers than equivalent lizardite modes (Fig. 6-4, Table 6-1).

Three bands at  $301.7\text{ cm}^{-1}$ ,  $317.5\text{ cm}^{-1}$  and  $345.2\text{ cm}^{-1}$  whose assignments are still under discussion (Farmer 1974a; Klopogge *et al.* 1999; Hofmeister and Bowey 2006) are an exception to this rule. They are located at lower wavenumbers with respect to the equivalent bands of lizardite-1T (Trittschack *et al.* 2012). Highly sensitive deformation modes of  $\text{SiO}_4\text{-AlO}_4$  as reported for the Monte Fico lizardite sample and antigorite (Rinaudo *et al.* 2003, Trittschack *et al.* 2012) are not present, which is compatible with the TEM-EDS based aluminium free composition of the analyzed chrysotile sample. The most significant difference between lizardite and chrysotile occurs in the region of the antisymmetric Si-O stretching modes. Whereas lizardite shows at least two bands belonging to  $\nu_{\text{as}}\text{ Si-O}_{\text{nb}}$  and  $\nu_{\text{as}}\text{ Si-O}_{\text{b-Si}}$ , chrysotile shows only one detectable band assigned to  $\nu_{\text{as}}\text{ Si-O}_{\text{nb}}$ , i.e., an antisymmetric stretching mode perpendicular to the tetrahedral sheet (Klopogge *et al.* 1999).

The high-frequency range ( $3500\text{-}3800\text{ cm}^{-1}$ ) is characterized by hydroxyl stretching vibrations which are listed and compared with that of lizardite-1T in Table 6-1. The RT band deconvolution (Fig. 6-5) gives five IR ( $3645\text{ cm}^{-1}$ ,  $3663\text{ cm}^{-1}$ ,  $3682\text{ cm}^{-1}$ ,  $3695\text{ cm}^{-1}$ ,  $3702\text{ cm}^{-1}$ ) and four Raman bands ( $3649\text{ cm}^{-1}$ ,  $3681\text{ cm}^{-1}$ ,  $3688\text{ cm}^{-1}$ ,  $3697\text{ cm}^{-1}$ ), respectively. The shape and the relative intensity/ absorbance of single OH stretching bands differ considerably between Raman and FTIR spectra. Thus, the Raman

spectrum contains four bands as proposed by Klopogge *et al.* (1999), but the two additional bands (six in total) reported by Auzende *et al.* (2004) were not observed. Contrary to that, there is a higher number of infrared (IR) active bands, i.e., five compared to two, as formerly reported (Farmer 1974a; Post and Borer 2000; Anbalagan *et al.* 2010). Similar observations were already made in spectroscopic investigation of lizardite-1T (Trittschack *et al.* 2012), i.e., there are more IR bands, but less Raman bands than reported in literature. Band assignments were made using the scheme of Balan *et al.* (2002) for lizardite and its application proposed for other serpentine polymorphs (Auzende *et al.* 2004). Adjacent bands are interpreted as originating from the same mode.

### 6.3.2 High-temperature FTIR and Raman spectroscopy of the dehydroxylation of chrysotile

The treatment and interpretation of the *in situ* HT spectra of chrysotile were done in similar manner as for lizardite-1T by Trittschack *et al.* (2012) in order to show differences related to the polymorphic character of both serpentine minerals. Only strong bands (Fig. 6-4) were followed in detail during the temperature treatment because of band broadening and a rapid decrease of the signal-to-noise ratio with increasing temperature. A major increase of the background intensity is present in the spectra measured at  $201\text{ }^{\circ}\text{C}$  to  $356\text{ }^{\circ}\text{C}$  (Fig. 6-6). In general, the frequency of all chrysotile modes in the low-frequency range shows a negative dependence on temperature in the HT as well as the quenched data. Individual Raman bands such as the  $\text{A}_{1\text{g}}$  mode ( $201.9\text{ cm}^{-1}$  at RT) and the symmetrical stretching mode of  $\text{Si-O}_{\text{b-Si}}$  ( $691.3\text{ cm}^{-1}$  at RT) are additionally characterized by band splitting at  $459\text{ }^{\circ}\text{C}$ , with a new band appearing at lower wavenumbers than that of the existing band (Figs. 6-6, 6-7a and 6-7b and 6-8). A common feature of all studied bands preventing a linear fit across the entire temperature range is a rapid shift down to a minimum in wavenumber position at  $356\text{ }^{\circ}\text{C}$  and  $407\text{ }^{\circ}\text{C}$  before going slightly up again

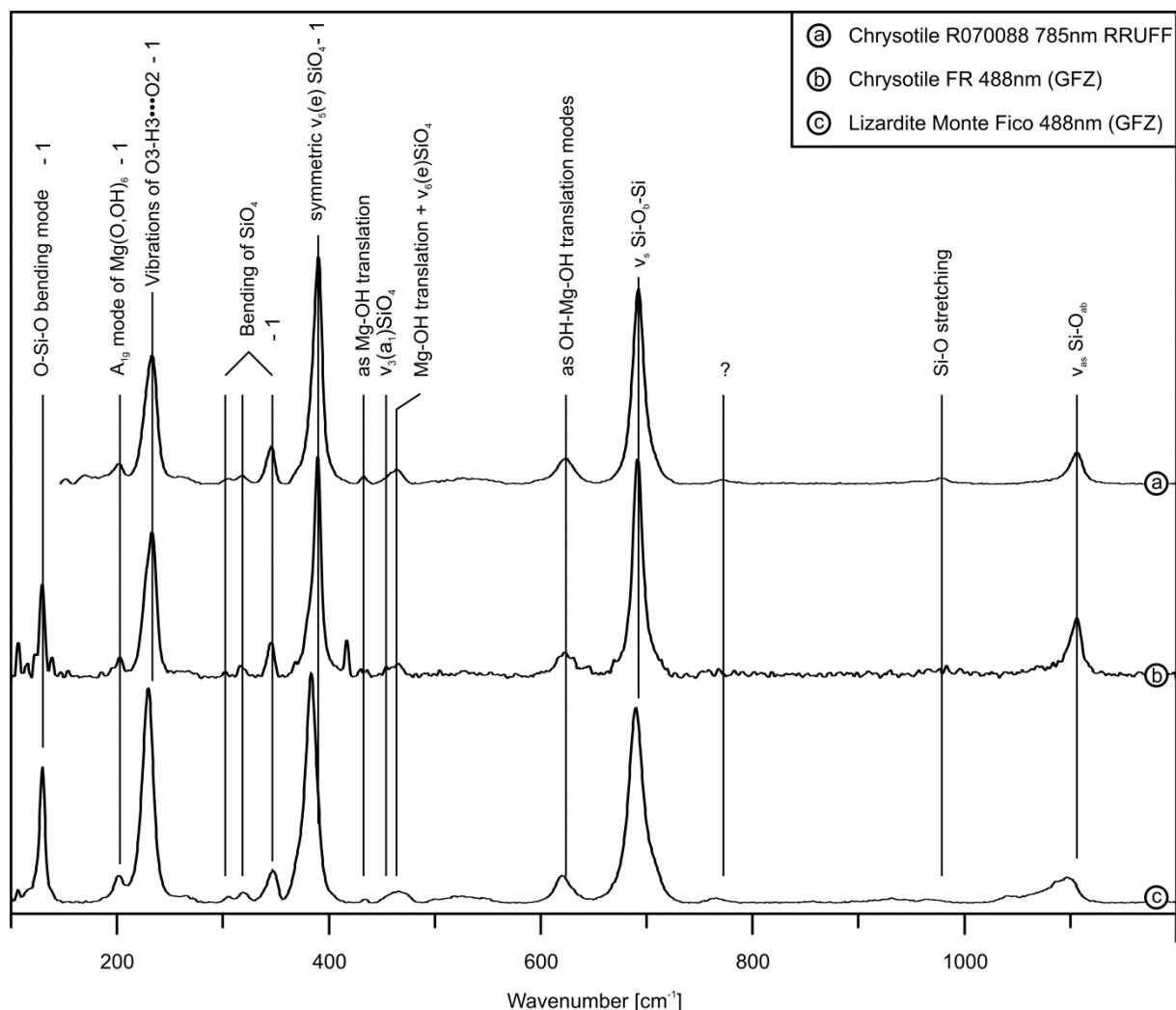


**Figure 6-4.** Comparison between the Raman spectrum of the chrysotile studied and the chrysotile reference spectrum R070088 (Downs 2006) as well as the Monte Fico lizardite-1T spectrum (Trittschack et al. 2012); 1 - marks those bands which were followed during heating to demonstrate the band shifting as shown in Fig. 6-7.

at  $T \geq 459$  °C, i.e., the temperature at which first forsterite bands are visible. Above this temperature there might be some kind of plateau or even a decelerated shift until  $T = 665$  °C, especially in data of the O3-H3•••O2 and the sym  $\nu_5(e)$  SiO<sub>4</sub> modes. Afterwards, individual bands shift again to lower wavenumbers and disappear almost completely due to a fast decrease in intensity. There is a considerable difference in the total amount of temperature-dependent frequency change when comparing the O-Si-O bending mode (Fig. 6-8a) with all other modes shown in Fig. 6-8.

The integral intensity/ absorbance of the chrysotile modes in the low-frequency range are characterized by a stepwise decrease. Major steps occur between 356 °C and 407 °C (Raman data) as well as 613 °C and 639 °C (Raman and FTIR data). The first intensity decrease is accompanied by a slightly delayed appearance of new bands initially located at around 182 cm<sup>-1</sup>, 668 cm<sup>-1</sup>, 815 cm<sup>-1</sup> and 849 cm<sup>-1</sup> at 459 °C, the intensity of which increase with temperature. Spectra taken at 716 °C contain further broad bands at around 351 cm<sup>-1</sup>, 598 cm<sup>-1</sup> and 951 cm<sup>-1</sup> (HT data, Fig. 6-7a). All newly formed bands survive up to 871 °C except

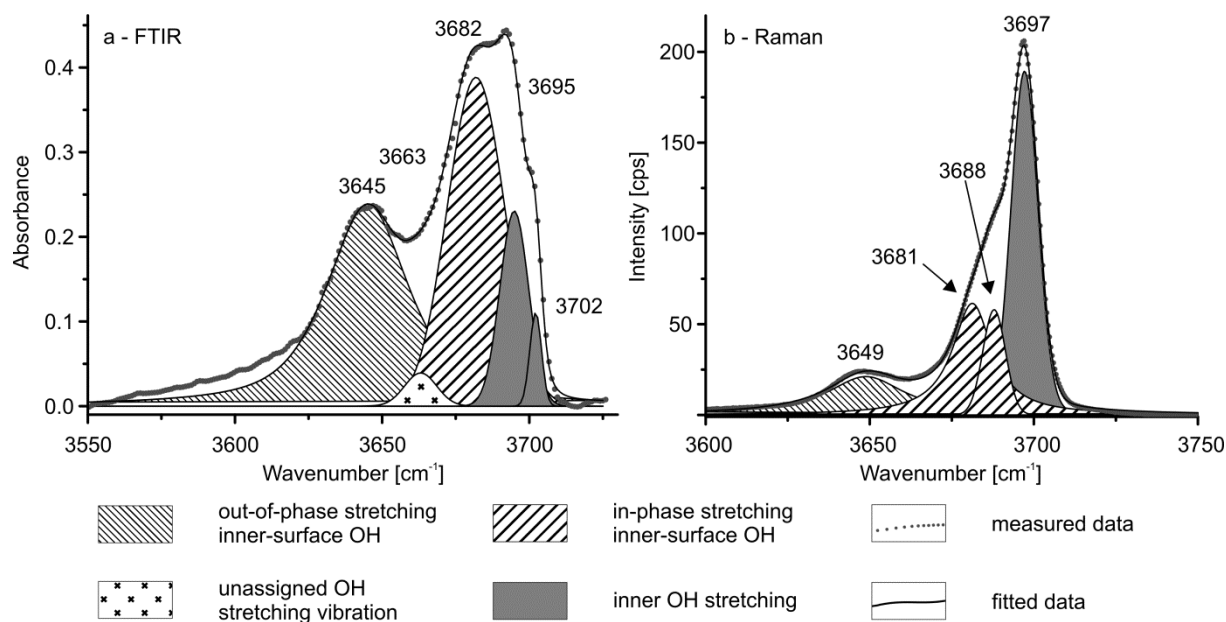


**Figure 6-5.** Band deconvolution of the OH stretching modes at RT and their assignments following Balan *et al.* (2002) and Auzende *et al.* (2004).

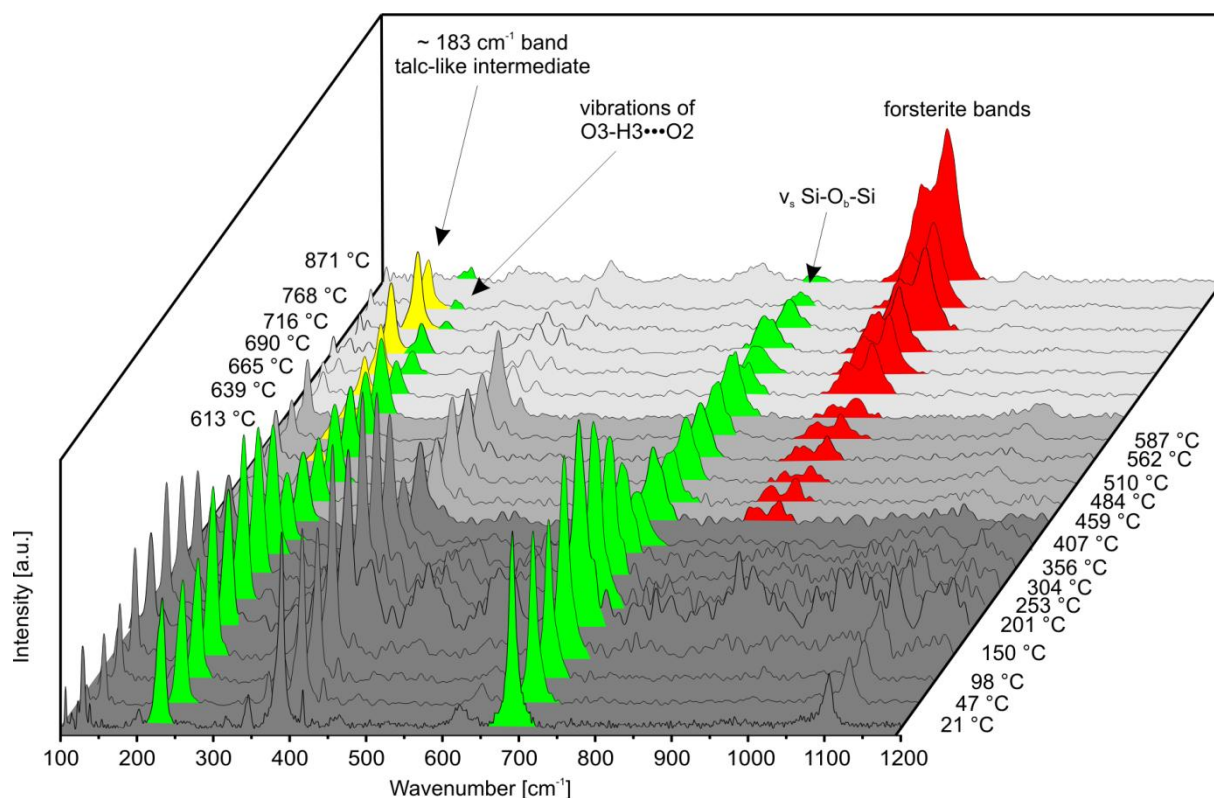


**Figure 6-6.** Temperature-dependent evolution of the low-frequency Raman bands between 21 °C and 871 °C; some bands are color-coded for clarity: green: chrysotile, yellow: transition phase and red: forsterite modes.



band assignment <sup>a,b,c</sup>	Chrysotile [cm <sup>-1</sup> ]	Chrysotile <sup>c</sup> [cm <sup>-1</sup> ]	Lizardite <sup>f</sup> [cm <sup>-1</sup> ]
O-Si-O bm	129.3		129.4
A <sub>1g</sub> mode of Mg(O,OH) <sub>6</sub>	201.9	199	201.9
Vibrations of O3-H3•••O2	233.3	231	229.1
SiO4 bm	301.7	304	305.1
	317.5	318	320.0
	345.2	345	346.2
s Mg-OH vibrations		374	371.4
s ν <sub>5</sub> (e)SiO <sub>4</sub>	389.4	388	383.5
unknown artefact	416.8		
as Mg-OH tm	432.4	432	430.4
ν <sub>3</sub> (a <sub>1</sub> )SiO <sub>4</sub>	455.1	458	
Mg-OH translation + ν <sub>6</sub> (e)SiO <sub>4</sub>	467.6	466	464.5
Libration of inner Mg-OH		607	
as OH-Mg-OH tm	623.3	622	621.6
		629	
ν <sub>s</sub> Si-O <sub>b</sub> -Si	691.3	692	689.8
Mg-OH outer s tm	706.5	705	707.1
		709	
Si-O sm			928.6
			972.4
ν <sub>as</sub> Si-O <sub>b</sub> -Si			1050.2
ν <sub>as</sub> Si-O <sub>nb</sub>	1105.4	1102	1094.3
<i>OH stretching frequencies<sup>d</sup></i>			
out-of-phase of inner surface OH unassigned OH band	3649	3643	3649
			3670
in-phase inner surface OH	3681	3678	3684
	3688	3686	3691
inner OH	3697	3696	3698
			3704

Notes: as = antisymmetric, b = bridging, bm = bending mode, nb = non-bridging, s = symmetric, sm = stretching mode, tm = translation mode

<sup>a</sup>Rinaudo *et al.* (2003), <sup>b</sup>Farmer (1974b), <sup>c</sup>Kloprogge *et al.* (1999), <sup>d</sup>Balan *et al.* (2002), <sup>e</sup>this work, <sup>f</sup>Tritschack *et al.* (2012)

**Table 6-1.** Raman bands of chrysotile and lizardite-1T and their assignments at room temperature.

of the bands at 182 cm<sup>-1</sup>, 351 cm<sup>-1</sup> and 668 cm<sup>-1</sup> which lose their intensity above 768 °C. Chrysotile-like features still observable *in situ* at 871 °C are the modes at 233.3 cm<sup>-1</sup> (RT) and 691.3 cm<sup>-1</sup> (RT), although there are more striking in the subsequently quenched spectrum measured at 47 °C (Fig. 6-7b).

*In situ* monitoring of the integral intensity of individual OH bands would be an elegant technique to obtain structural details of the dehydroxylation process. Unfortunately the resolution both in the HT FTIR and the Raman spectra does not allow proper deconvolution of the individual overlapping OH bands. Therefore, the dehydroxylation progress was monitored by changes in integral intensity/ absorbance of the entire OH band region only. The HT FTIR dataset shows a sharp decrease in the integral absorbance starting at around 580 °C (Fig. 6-9a) and going down to less than 10 % of the initial value (corresponds approximately to the detection limit for the entire OH bands) at 650 °C. This reduction coincides with the decrease in integral intensity of the Raman OH bands observed in both the HT and quenched spectra (Figs. 6-9b and 6-9c), although a first decrease in OH band intensity is already visible between 304 °C and 356 °C. The temperature range in the FTIR data between onset (at around 580 °C) and offset (at around 650 °C) of the dehydroxylation is much narrower than in DTG data (e.g., Viti 2010), which is typically separated by an interval of more than 200 K independent of the chosen heating rate. The loss of intensity/ absorbance is accompanied by a significant non-linear shift toward lower wavenumbers in both FTIR and Raman data. The total shift amounts to about 32 cm<sup>-1</sup> for the strongest OH Raman band at 3697 cm<sup>-1</sup>. Compared to the quenched dataset, HT data of the OH stretching region contain no clear indication for the appearance of a newly formed OH band.

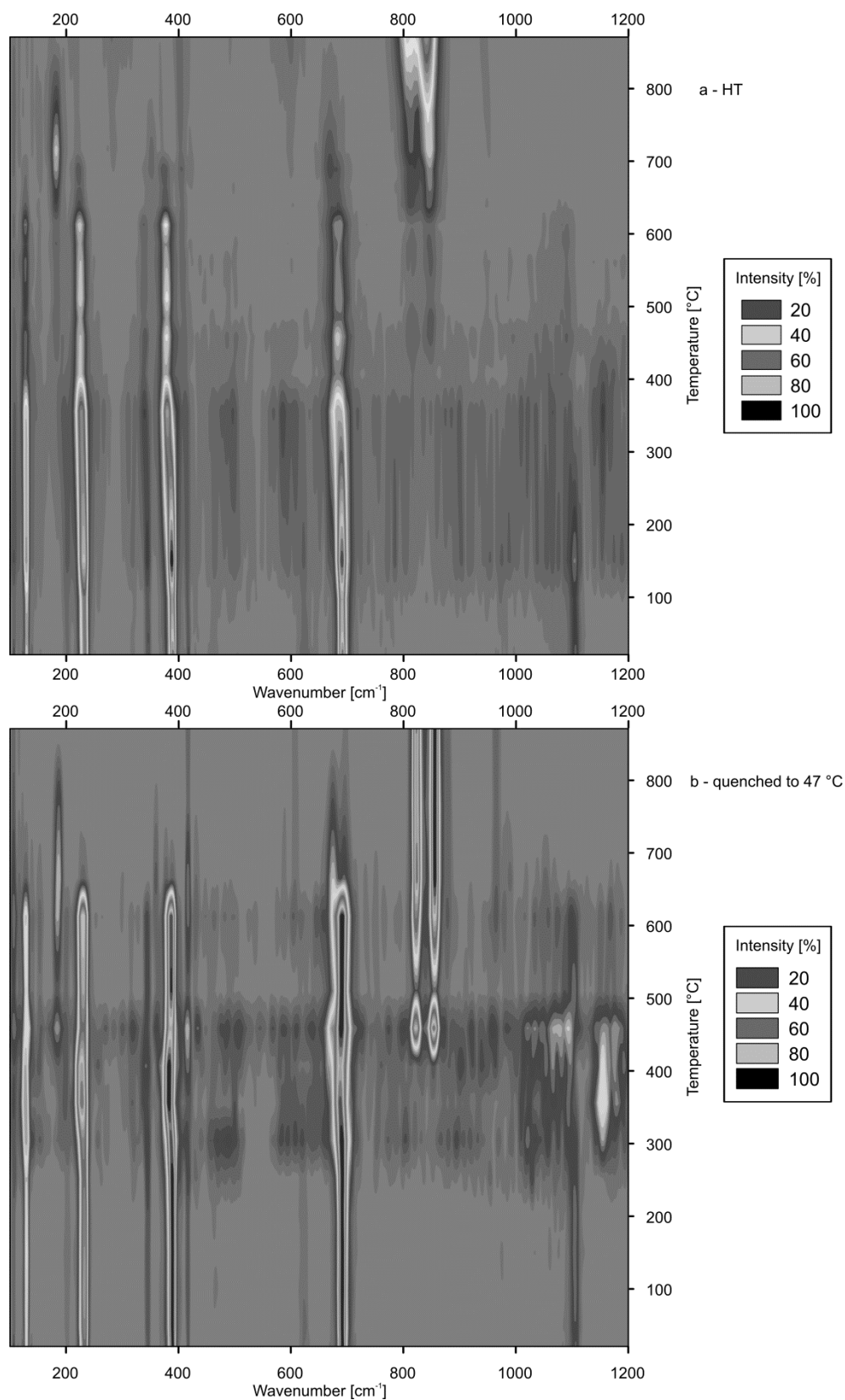


**Figure 6-7.** Temperature-dependent band evolution of Raman band intensity (a) measured at HT and (b) measured from samples quenched from the indicated temperatures to 47 °C.

### 6.3.3 FTIR and Raman spectroscopy of quenched samples

Spectra were also obtained from samples quenched to 47 °C after reaching the set temperature of the thermal treatment (see methods section) in order to improve the signal-to-noise ratio and the band resolution. Thus, it was possible to identify weak bands and band splitting much easier than at high temperatures. A comparison between the HT and quenched dataset can be done by using Figs. 6-7a and 6-7b. Here, weak bands of newly formed phases and remaining bands of a dehydroxylating chrysotile stand out much better (Table 6-2). Moreover, quenched spectra facilitate band assignments by comparison with Raman database entries (Fig. 6-10) and to deconvolute and to assign weak bands appearing as shoulders only.

Spectra of quenched samples confirm the appearance of new bands, e.g., at 182 cm<sup>-1</sup>, 669 cm<sup>-1</sup> and 822 cm<sup>-1</sup>. In spectra from quenched samples they already appear at lower temperatures than in HT spectra. The splitting of the Si-O<sub>b</sub>-Si is also better resolved. Inspection of the OH stretching vibrations reveals a band splitting or at least an increase in intensity at the low-frequency side of the major chrysotile OH band. Above 665 °C, the low frequency shoulder turns into a narrow single OH band centred at 3677 cm<sup>-1</sup> at the expense of primary chrysotile modes (Fig. 6-11a). This band is most striking in the quenched spectrum measured at 47 °C after reaching 768 °C, but is already visible at 665 °C.

## 6.4 DISCUSSION

### 6.4.1 Raman and FTIR spectra at ambient conditions

The number and frequency position of Raman bands in the low-frequency range (Table 6-1, Fig. 6-4) agrees well with literature data of chrysotile (e.g., Bard *et al.* 1997; Klopogge *et al.* 1999; Rinaudo *et al.* 2003; Auzende *et al.* 2004). However, Klopogge *et al.* (1999) list additional Raman bands at 374 cm<sup>-1</sup>, 607 cm<sup>-1</sup>, 629 cm<sup>-1</sup> and

709 cm<sup>-1</sup> originating from band deconvolution in the low-frequency range. Considering the degrees of freedom in choosing the parameters for band deconvolution as shown for chrysotile OH bands by Mizukami *et al.* (2007) it would also be possible to fit the 389.4 cm<sup>-1</sup> and 623.3 cm<sup>-1</sup> single bands in our data as potential double bands or even triplets, respectively. The Raman band doublet at 705 cm<sup>-1</sup> and 709 cm<sup>-1</sup> in the data of Klopogge *et al.* (1999) might be due to the measurement geometry. The spectra were obtained from crystallographically oriented samples. The chrysotile fibres in the present samples have arbitrary orientation and orientation dependent features were not considered in this study.

The assignments of the chrysotile low-frequency bands (Table 6-1) were taken from Klopogge *et al.* (1999) because of almost all recent papers dealing with Raman band assignments of serpentine minerals going back to this article or the paper of Rinaudo *et al.* (2003). The latter uses the assignments of Klopogge *et al.* (1999) for other serpentine minerals also. However, band assignments of serpentine minerals are not straightforward and have to be taken with care considering the considerable discrepancies between the assignment schemes presented in previous investigations (Luys *et al.* 1982; Klopogge *et al.* 1999; Rinaudo *et al.* 2003; Hofmeister and Bowey 2006; Šontevska *et al.* 2007; Prencipe *et al.* 2009). A good example for such discrepancies are the diagnostic Raman bands between 620 cm<sup>-1</sup> and 635 cm<sup>-1</sup> observed in experimental spectra of lizardite-1T and chrysotile. These are assigned as antisymmetric OH-Mg-OH translation modes of lizardite and chrysotile by Rinaudo *et al.* (2003). But, Luys *et al.* (1982) assigned these bands to in-plane Mg(O,OH)<sub>6</sub> stretching modes originating from curved TO layers. The fact that these bands do not appear in the calculated spectrum of lizardite-1T by Prencipe *et al.* (2009) is in favour of the latter interpretation. Therefore, the occurrence of 630 cm<sup>-1</sup> and 635 cm<sup>-1</sup> bands in Raman spectra of lizardite and antigorite presented by Rinaudo *et al.* (2003), is probably related to chrysotile impurities and/ or the presence

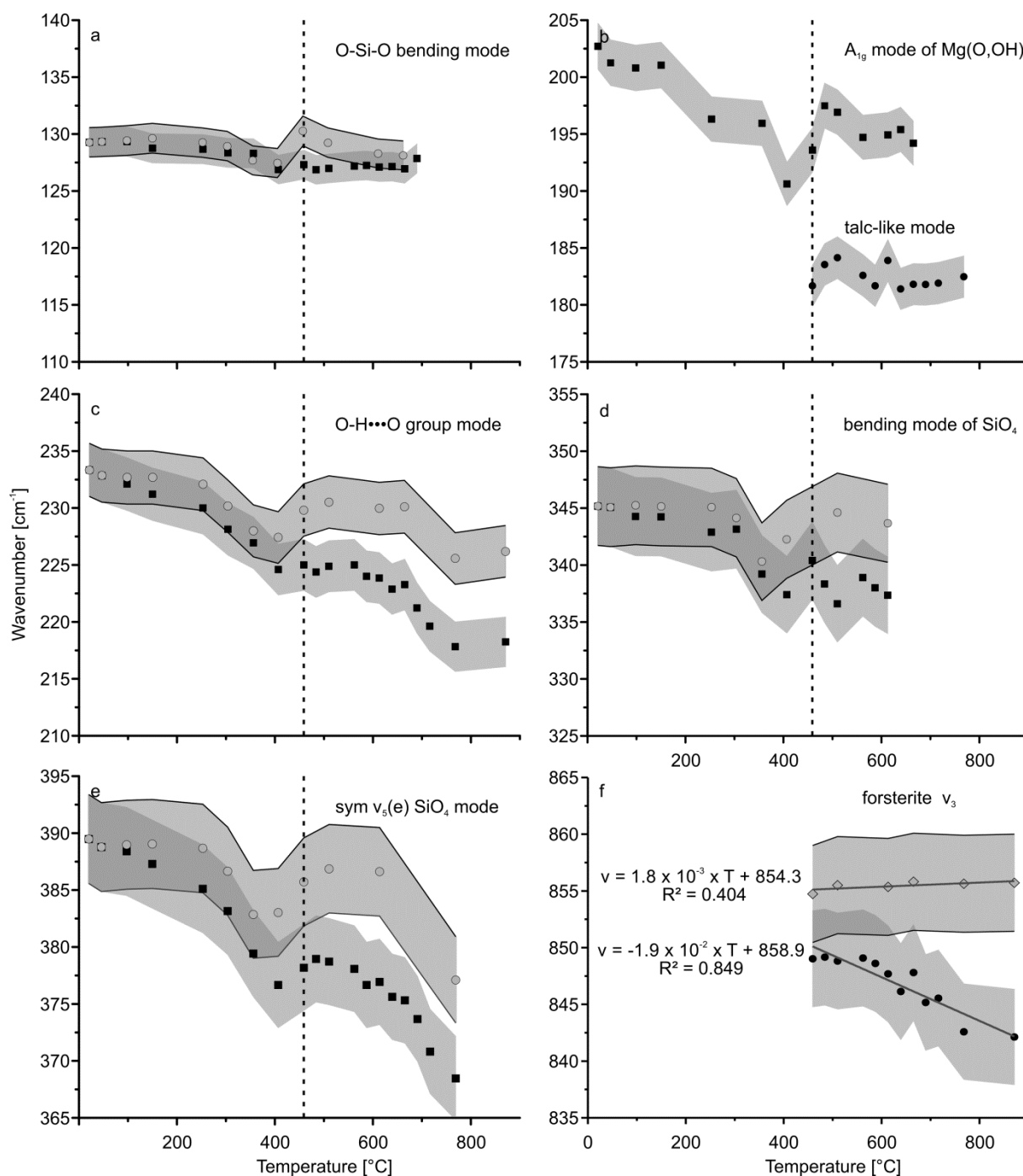


**Figure 6-8.** Frequency evolution of the major Raman bands during heating; the error envelope is grey shaded. Major error sources are band deconvolution and accuracy of the spectrometer calibration; the vertical dotted line marks the appearance of forsterite bands; reversible shifts as based on quenched data are indicated by the filled circles and their error range (grey shaded area with a black outline).

of curled lizardite as observed by Trittschack *et al.* (2012).

Wavenumber differences between the Raman bands of chrysotile and lizardite-1T are minor, especially when compared with the equivalent differences in the IR spectra of both polymorphs

(Yariv and Heller-Kallei 1975), which are more distinct. Differences  $\Delta \leq 1 \text{ cm}^{-1}$  are interpreted as related to measurement errors and/ or the band fitting procedure and thus only differences  $\Delta \geq 1 \text{ cm}^{-1}$  are considered. Band displacement resulting from different Raman laser wavelengths as suggested by Šontevska *et al.* (2007) can be excluded because of the same Raman system used for the previous analysis of lizardite (Trittschack *et al.* 2012) and the present chrysotile measurements. Differences  $\Delta \geq 1 \text{ cm}^{-1}$  may be caused either by substitution (Farmer 1974b; Yariv and Heller-Kallei 1975) or by the structural differences between lizardite and chrysotile. Structural differences are both long range scale, i.e., flat lizardite versus curved chrysotile, and short range scale, i.e., distortion of polyhedra (Blaha and Rosasco 1978). Considering the almost end-member stoichiometry of both the chrysotile used for this investigation and the lizardite-1T studied by Trittschack *et al.* (2012), we tend to associate the observed differences with the contrasting structures of both phases. It is interesting to note, that the largest differences are observed for bands representing tetrahedral units. In this context, the assignment of chrysotile bands at  $301.7 \text{ cm}^{-1}$ ,  $317.5 \text{ cm}^{-1}$  and  $345.2 \text{ cm}^{-1}$  is disputed. Klopogge *et al.* (1999) attribute these bands to bending modes of  $\text{SiO}_4$ , whereas Hofmeister and Bowey (2006) assign them to Mg-O stretching modes. Their common negative shift compared to the frequencies observed in lizardite speaks for a common structural origin, i.e., all are either tetrahedral or octahedral modes. The large shift is rather in favour of modes in the tetrahedral sheet.

There are also discrepancies in the number, frequencies and assignments of OH stretching modes presented in previous FTIR and Raman investigations of serpentine minerals (Klopogge *et al.* 1999; Balan *et al.* 2002; Auzende *et al.* 2004; Mizukami *et al.* 2007; Prencipe *et al.* 2009; Trittschack *et al.* 2012). In general, older literature document just two IR active bands at  $3651 \text{ cm}^{-1}$  and  $3697 \text{ cm}^{-1}$  (Farmer 1974a) and two Raman active bands at around  $3685 \text{ cm}^{-1}$  and  $3700 \text{ cm}^{-1}$  (Bard *et al.* 1997), respectively. These findings are

mostly caused by the lack of band deconvolution. In recent literature, more bands in chrysotile spectra were reported and assignments were done using the schemes established for lizardite (Balan *et al.* 2002). Group theory considerations give four Raman active OH stretching vibrations for lizardite-1T ( $C_{3v}$  factor group). First-principle calculations of Balan *et al.* (2002) and Prencipe *et al.* (2009) result in three IR active OH stretching modes and three Raman active modes plus a contribution of one longitudinal-optical (LO) mode of lizardite-1T, respectively. A higher number of modes than in lizardite are to be expected due to the curved layers and a higher degree of disorder in chrysotile (Devouard and Baronnet 1995; Auzende *et al.* 2004). The OH stretching band assignments used in this work are in accordance with the scheme proposed for lizardite by Balan *et al.* (2002). This scheme was already used for high-pressure Raman spectra of chrysotile (Auzende *et al.* 2004; Mizukami *et al.* 2007), the ambient spectra of which are comparable to the present ones. Narrow bands in the high frequency side of the Raman OH bands, i.e., at  $3681 \text{ cm}^{-1}$  and  $3688 \text{ cm}^{-1}$ , are attributed to LO-TO splitting of the in-phase stretching mode of the inner-surface OH groups as proposed by Prencipe *et al.* (2009). The same splitting was experimentally documented for lizardite-1T by Trittschack *et al.* (2012). However, as already mentioned, there is a high degree of freedom when applying band deconvolution techniques (see Mizukami *et al.* 2007). Thus, only state-of-the-art *ab initio* techniques are suited to unravel the exact number of vibrational bands considering the influence of substitution, crystal defects or such physical influences like LO-TO splitting. The two adjacent IR bands at  $3695 \text{ cm}^{-1}$  and  $3702 \text{ cm}^{-1}$  are probably caused by a minor substitutional exchange of Mg by Fe (Yariv and Heller-Kallei 1975) or a distortion of the  $\text{SiO}_4$  tetrahedra (Blaha and Rosasco 1978). LO-TO splitting as cause for an OH band multiplication in FTIR data can be excluded due to the size of individual chrysotile fibres with respect to the IR wavelength range. A band occurring between the out-of-phase stretching and the in-phase stretching mode of the inner-surface OH, which is not present

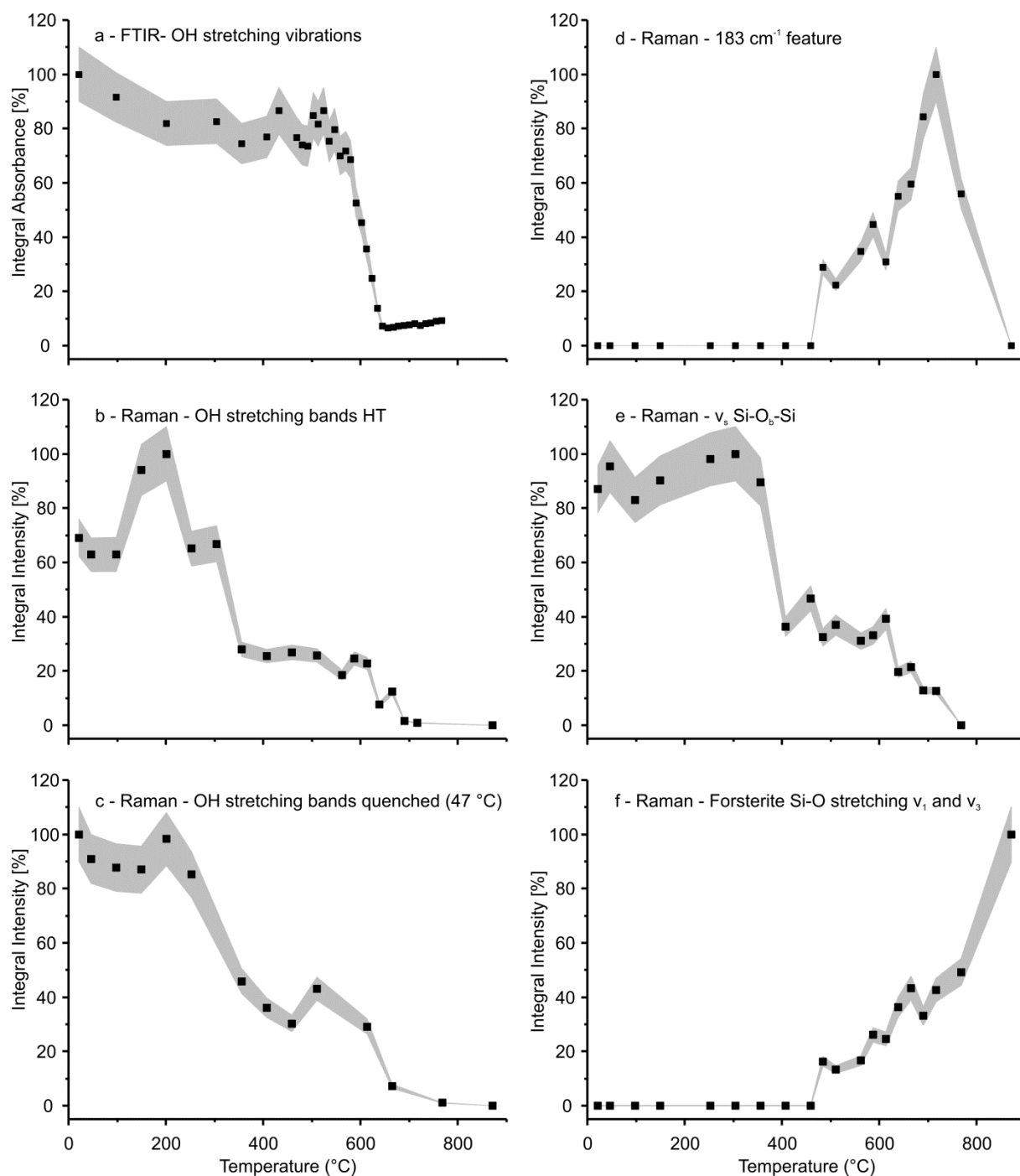


**Figure 6-9.** Temperature-dependent development of the OH IR band absorbance and integral intensities of some selected Raman bands (grey shading: error envelope).

in the Balan *et al.* (2002) scheme, was already observed in spectra of lizardite-1T (Trittschack *et al.* 2012). This band has been attributed to non-

structural OH in the case of lizardite, although a deconvolution artefact cannot be excluded (Trittschack *et al.* 2012).

### 6.4.2 The chrysotile phase transformation as seen in the OH stretching band range

The dehydroxylation of chrysotile as deduced from the decrease in integral absorbance/ intensity of OH stretching modes (Figs. 6-9a and 6-9c) starts approximately at the same temperature as the onset of the weight loss in published differential thermogravimetric (DTG) data of chrysotile (Viti 2010). However, the total dehydroxylation interval in spectroscopic data is much narrower than that recorded by DTG, a fact already observed in the dehydroxylation of lizardite (Trittschack *et al.* 2012). This difference is related to the nature of the measured signals, i.e., debonding of hydroxyl groups lead to the signal decrease in FTIR/ Raman data, whereas the diffusion of reaction products out of the sample is responsible for the weight loss in the solid sample, which is monitored by DTG. The latter is delayed relative to the hydroxyl debonding reactions. The stepwise decrease in Raman intensity as recognizable from the OH Raman bands (Figs. 6-9b and 6-9c) demonstrates a more complex reaction path than observable by FTIR alone. Thus, we suggest two interpretation models for the herein documented Raman band changes which are linked to each other: 1) A decrease in the integral OH Raman intensity at temperatures lower than 400 °C could be caused by temperature-induced reorientation of single chrysotile fibres within the fibre bundle as the intensity of OH Raman bands is also a function of the fibre orientation (Kloprogge *et al.* 1999); 2) An early order/ disorder phase transition in the outer, less temperature resistant chrysotile layers is also possible. Such an interpretation would partly support the interpretation of Candela *et al.* (2007) who suggest an increase in the degree of order at temperatures between 400 °C and 450 °C. Interestingly, Cattaneo *et al.* (2002) also document a slight increase in their summed integrated XRD peak intensity between 400 °C and 500 °C which can also be interpreted as an indication for increased order. However, in any case such a transition would also cause reorientation of OH and therefore a change in the Raman intensity. Moreover, Malkov *et al.* (2009) document an early

release of OH in the temperature range of 20 °C to 400 °C. Their calculations yield a loss in OH of almost 2 mmol/g which is equal to around 12.7 % of the initial amount of OH.

Generally, the chrysotile structure and in particular the average curvature change during dehydroxylation. The dehydroxylation temperature of the individual chrysotile layers is radius-dependent, i.e., the outer, less curved layers, dehydroxylate at lower temperatures than the inner ones (Evans 2004). As long as the maximum experimental temperature is lower than the onset of the dehydroxylation in the outermost layer, the average curvature in the quenched samples is equal to the value in the starting sample. This assumption is fulfilled as shown in Fig. 6-11. Accordingly, a broadening of the OH stretching region in HT and quenched data is expected after the onset of the dehydroxylation resulting from progressive disorder moving inwards. Then, the resulting OH mode pattern would consist of OH modes coming from the primary chrysotile and a disordered one. This assumption can also be verified by the presented OH band development in Fig. 6-11 showing a comparable OH band pattern up to 253 °C with respect to the initial sample. Although diminishing in intensity, the position of the main OH band at 3697 cm<sup>-1</sup> keeps fixed (in quenched data) as long as the inner chrysotile layers are not affected by dehydroxylation. Afterwards a significant broadening can be detected in both HT and quenched data (Fig. 6-11), respectively.

A rather simple model of chrysotile as shown by D'Arco *et al.* (2009) enables us to use a compatible dehydroxylation model as for lizardite-1T (Trittschack and Grobéty 2012). There, the distance between adjacent OH groups in lizardite-1T counts as a trigger for a preferential loss of protons and finally causing disorder and creating a host for a potential intermediate phase. The appearance of a new OH band at 3677 cm<sup>-1</sup> (quenched sample), which is the only visible OH stretching band after heating the sample to 768 °C, is an indication for the formation of an

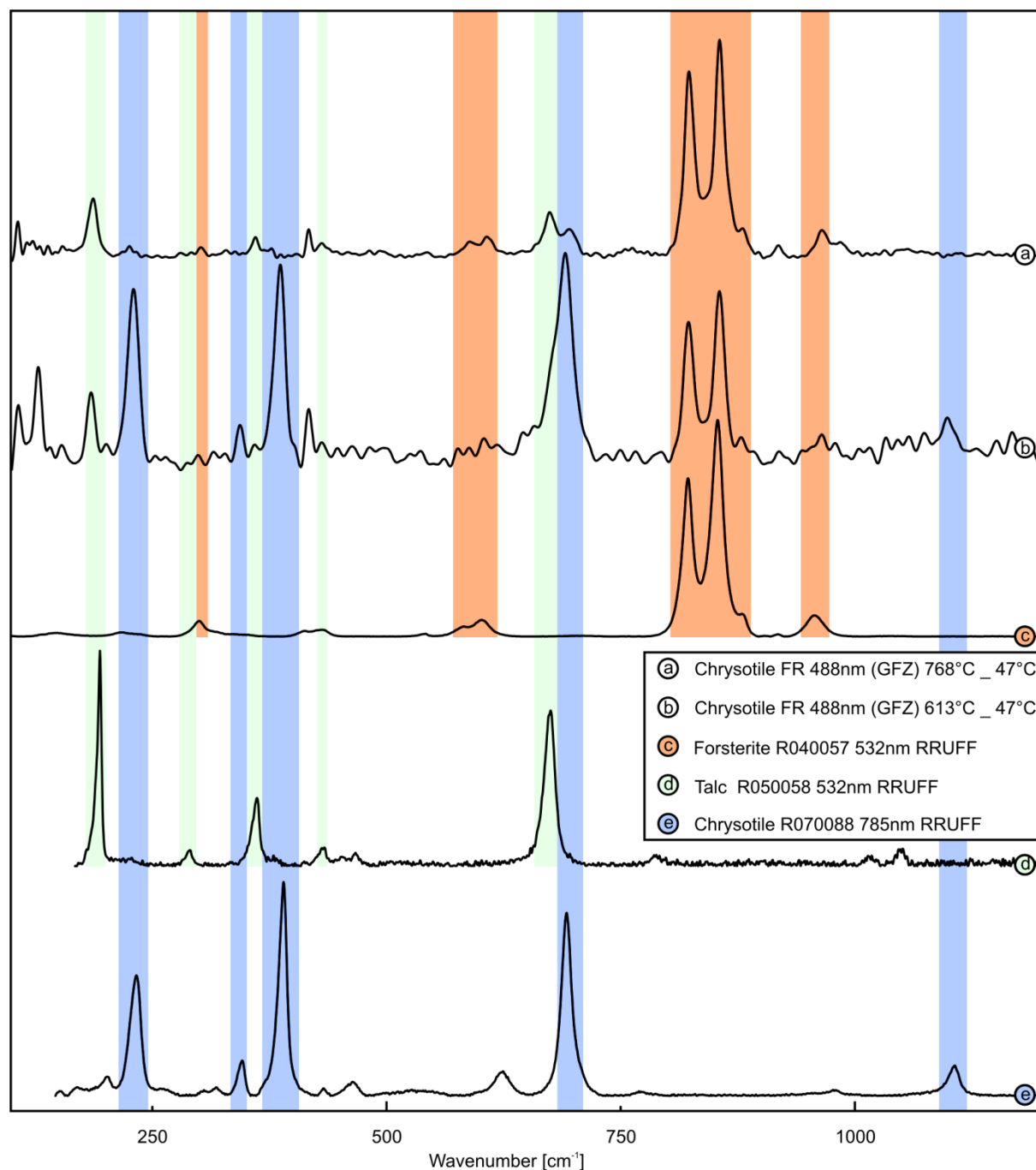


**Figure 6-10.** Raman spectra of quenched samples after being heated to 613 °C and 768 °C, respectively, as well as reference spectra of forsterite, talc and chrysotile from the RRUFF database (Downs 2006).

intermediate phase other than the ill crystallized primary product and forsterite. This single OH band is compatible with the OH band position of talc at RT (Fumagalli *et al.* 2001), an interpretation strongly supported by newly formed bands in the

low-frequency range and discussed in detail in the following section. The lack of this OH band at 871 °C and in the spectrum of the subsequently quenched sample indicates that this intermediate breaks down between 768 °C and 871 °C.



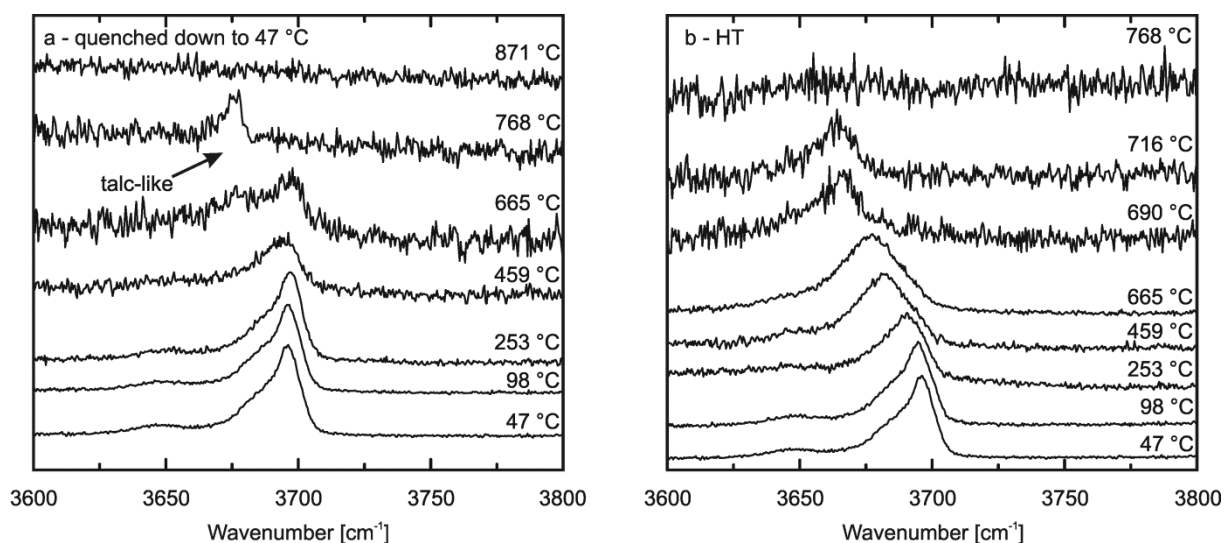


**Figure 6-11.** Temperature-dependent changes in the Raman OH stretching band region; (a) measured on samples quenched from the indicated temperature and (b) HT spectra measured at the indicated temperatures.

### 6.4.3 The chrysotile phase transformation as seen in the low-frequency range (100-1200 cm<sup>-1</sup>)

Frequency shifts, intensity loss and appearance of new bands also characterize the low-frequency range of both quenched samples and HT spectra independent of the temperature of the heat treatment (Figs. 6-6 to 6-9). Considering the small difference between the frequencies observed in chrysotile compared to lizardite (Fig. 6-4, Table 6-1), the influence of the curvature on the frequency of individual bands seems to be small. The measurement errors related to sample refocusing due to the thermal expansion of the sample holder and the chrysotile itself are not helping in determining small permanent frequency shifts. The layer volume corresponding to a certain curvature decreases with increasing curvature, e.g., the overall impact on the spectra of the outer, less curved layers is larger than that of the inner layers.

The local frequency minima at 356 °C and 407 °C and the following plateau are interpreted as a first step in the phase transformation which takes place in the outer, less curved layers. This is again in favour with the findings of Candela *et al.* (2007). But, comparable experiments by Gualtieri *et al.* (2012) have not confirmed such behaviour.

Nevertheless, the local minima observable in the low-frequency Raman bands are supported by the first significant decrease in the integral intensities of OH Raman bands between 304 °C and 356 °C (Figs. 6-6, 6-7 and 6-9). The apparent loss of OH and the significant step to lower wavenumbers might be interpretable as a loss of primary chrysotile features. But, a recrystallization to a chrysotile with different radii at higher temperatures as proposed by Candela *et al.* (2007) seems to be problematic due to the loss of primary OH. Unfortunately, there is no further literature on the phase transformation and dehydroxylation behaviour of chrysotile supporting such low-temperature ( $T < \sim 450$  °C) recrystallization effects which could also support a better understanding of our own data.

The overall phase change is not restricted to a narrow temperature interval like in lizardite, but a broad temperature range with a 'transition' zone between 407 °C and 768 °C (Figs. 6-6, 6-7a and 6-7b). The maximum stability temperature of chrysotile is in accordance with recently published data (Gualtieri *et al.* 2012). This transition zone is characterized by the coexistence of chrysotile, a 'disordered chrysotile' plus a quenchable talc-like

phase and forsterite as interpreted from the wavenumber positions of quenched samples at 47 °C (Table 6-2, Fig. 6-10). The 'disordered chrysotile' is an almost OH free phase containing remnants of the primary structure as interpreted from missing hydroxyl bands, but still appearing chrysotile-compatible bands in the low-frequency range (Figs. 6-6, 6-7b, 6-8c and 6-10). Such an OH poor, amorphous phase occurred also during the dehydroxylation of lizardite (McKelvy *et al.* 2006; Trittschack *et al.* 2012). The most striking band of the talc-like intermediate lies at  $184.7\text{ cm}^{-1}$  followed by less intense bands at  $359.2\text{ cm}^{-1}$  and  $669.1\text{ cm}^{-1}$  (Figs. 6-7a and 6-7b and 6-10). It is labelled as 'talc-like' due to the deviations of measured Raman modes when comparing them with those reported for talc in literature (Table 6-2, Downs 2006). Moreover, there are no clear evidences in previous XRD based literature for the presence of talc, but the appearance of a talc-like and rapidly changing  $10+\text{ Å}$  peak. Forsterite can easily be identified by the remarkable doublet at  $823\text{ cm}^{-1}$  and  $856\text{ cm}^{-1}$  and a smaller doublet at  $589\text{ cm}^{-1}$  and  $607\text{ cm}^{-1}$  (Figs. 6-7a and 6-7b and 6-10). The appearance of an intermediate phase during the 'dry' dehydroxylation of chrysotile is compatible with existing reaction schemes (Ball and Taylor 1963; Brindley and Hayami 1965; Martin 1977; Datta 1991). The talc-like character was firstly proposed by MacKenzie and Meinhold (1994) based on NMR analysis. Gualtieri *et al.* (2012) and Trittschack *et al.* (2012) have also found evidence of a talc-like phase in *in situ* HT X-ray powder diffraction and Raman spectra of partially dehydroxylated lizardite. The presence of a talc-like intermediate is not surprising as talc is a stable product during the breakdown of chrysotile and lizardite under hydrothermal conditions (Ball and Taylor 1963; O'Hanley *et al.* 1989). MacKenzie and Meinhold (1994) explained the appearance of a talc-like intermediate with the possibility of quasi-hydrothermal conditions in the innermost layers of chrysotile. Such conditions might not be limited to the innermost layers as demonstrated by the first appearance of talc-like features at 459 °C (Figs. 6-7a and 6-7b and 6-9d), i.e., early after the Raman/ FTIR detectable onset

of dehydroxylation (Figs. 6-9a to 6-9c) and the DTG detectable onset of dehydration (Viti 2010). What can be stated at this point is that hydrothermal conditions have to be achieved in certain parts of the changing host-structure during the dehydroxylation of chrysotile and lizardite. The formation of a disordered, OH free chrysotile intermediate inhibiting the diffusion of  $\text{H}_2\text{O}$  or OH might be the reason for a locally enrichment of volatile dehydroxylation products.

The accelerated growth of the talc-like intermediate at temperatures  $\geq 613\text{ °C}$  is mirrored by a strong decrease in the intensity of chrysotile bands (Figs. 6-9d and 6-9e). This behaviour implies an immediate nucleation and growth of the talc-like phase during the dehydroxylation. Owing to the contemporaneous appearance of the talc-like phase and forsterite at 459 °C it is not possible to state whether the intermediate is necessary or not to form forsterite. However, the accelerated increase in intensity of the Si-O stretching mode doublet of forsterite after the maximum intensity of the talc-like phase at 716 °C suggest a strong interrelation. The fact that forsterite shows the largest integral intensity at 871 °C point to an unfinished growth. The breakdown of the talc-like intermediate is not accompanied by the formation of enstatite as proposed for antigorite by Gualtieri *et al.* (2012). The absence of enstatite is either related to an unfinished breakdown of the chrysotile structure preventing a formation of the inosilicate or kinetic effects in general. However, both possibilities are linked to each other as the chrysotile breakdown itself is a time-dependent, i.e., kinetic-controlled, reaction (Candela *et al.* 2007). The exposure time at  $T \geq 800\text{ °C}$  is less than 10 min which is also not favourable for a formation of enstatite. The formation of a Si-rich amorphous phase as dehydroxylation product as inferred from *in situ* X-ray diffraction (Ball and Taylor 1963; Martin 1977; MacKenzie and Meinhold 1994; Gualtieri *et al.* 2012) is difficult to prove by the present spectroscopic data, as all Raman bands in the HT and quenched spectra can be assigned to known crystalline phases, i.e., talc-, chrysotile- and forsterite-related modes. The

broadened chrysotile bands point to a decrease in crystallinity and what was called amorphous phase by previous authors is rather a heavily disordered phase still resembling chrysotile. Such a disordered chrysotile phase might be similar to the dehydroxylate II using the nomenclature of MacKenzie and Meinhold (1994). The latter argue that the NMR shift of this dehydroxylated II is compatible with a 1:1 layer structure of chrysotile in general, i.e., dehydroxylated II is still containing elements of the primary chrysotile structure, although disordered. They also demonstrate its presence above 800 °C which is compatible with the herein documented data. However, MacKenzie and Meinhold (1994) suggest either a phase similar to talc or a phase still containing structural elements of chrysotile for their dehydroxylated II. Their phrases exclude therefore an unambiguous assignment.

The frequency change of the O-Si-O bending mode ( $\sim 129 \text{ cm}^{-1}$  at RT) which is a measure of the change in ditrigonal distortion  $\alpha$  (Mookherjee and Redfern 2002) is nearly one order of magnitude smaller than the rest of the chrysotile bands. Weak dependency of  $\alpha$  on temperature was already observed for lizardite-1T upon heating as shown by HT Raman (Tritschack *et al.* 2012) and XRD studies (Guggenheim and Zhan 1998). The possibility to fit the O-Si-O bending mode with just one band with nearly constant FWHM upon the entire temperature range suggests no or minor influence of the layer curvature on  $\alpha$ .

Chrysotile fibres are characterized by an inward migrating dehydroxylation surface according to the proposed chrysotile structures of Yada (1971), thermodynamic considerations given by Evans (2004). This surface generates a 'chrysotile' fibre consisting of three or four different phases, respectively (Fig. 6-12). However, the variability in the fibre diameter of the studied chrysotile causes a more complex situation. Nevertheless, the principle scheme maintains.

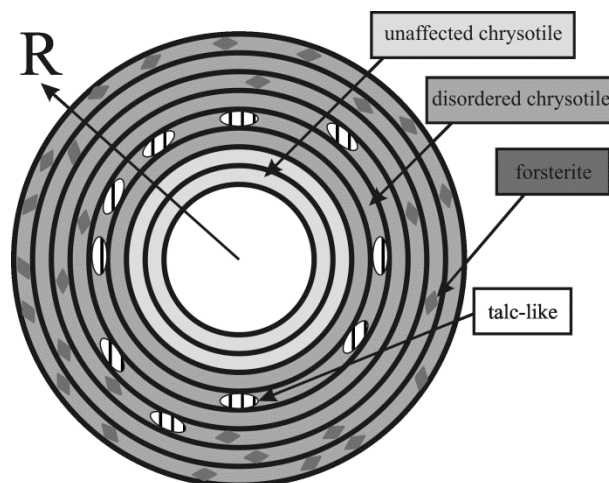


**Figure 6-12.** Schematic representation of a dehydroxylating chrysotile fiber (concentric type) with a multiphase assemblage of unaffected chrysotile, disordered chrysotile, the talc-like phase and forsterite; the talc-like phase is shown as formed on certain areas of the disordered chrysotile only,  $R$ : fiber radius.

It is necessary to underline that the talc-like intermediate is quenchable during the breakdown of chrysotile. Thus, the intermediate is an important carrier of  $\text{H}_2\text{O}$  and  $\text{OH}$ , respectively. This has to be considered when interpreting the kinetics of the chrysotile dehydroxylation by DTG, a statement also valid for all other phyllosilicates creating an  $\text{H}_2\text{O}/\text{OH}$  containing intermediate phase during dehydroxylation. In any case, the chrysotile dehydroxylation is not that linear as assumed in the past which has already been demonstrated by experiments of Viti (2010) indicating a multistage dehydration process. The FTIR and Raman data of this article clearly show a multistage dehydroxylation and phase transformation scenario with an early onset of a possible order/ disorder phase transition at temperatures between around 350 °C and 450 °C, followed by the main dehydroxylation reaction and phase change later on. However, the low temperature of the first appearance of the talc-like phase and forsterite compared to the temperatures of the first release of water in data of Viti (2010) demonstrate that one has to be careful with a direct

comparison of both datasets. It has to be emphasized that a multistage dehydration is not inevitably caused by a multistage dehydroxylation reaction.

The occurrence of a talc-like intermediate stable under ambient pressure conditions and the presence of a disordered chrysotile also have an impact on the understanding of subduction zone dehydration processes and the storage of CO<sub>2</sub> in serpentine bearing rocks. The presence of a talc-like phase rather than talc offers the possibility for a transport, storage and release of H<sub>2</sub>O at low-pressure conditions, but after the onset of the temperature-dependent dehydroxylation reaction of chrysotile and lizardite. Much work has been devoted to high-pressure experiments studying the breakdown reaction of antigorite (e.g., Perillat *et al.* 2005; Chollet *et al.* 2009). But, less is

documented about the relation of the lizardite and chrysotile breakdown including the formation of a talc-like intermediate. Additional studies are important to unravel the complex association between primary serpentine minerals, the talc-like phase, talc and the 10 Å phase (Fumagalli *et al.* 2001; Chollet *et al.* 2009) in the MSH system. Moreover, a talc-like phase offers potential nucleation sites of carbonate bearing phases in carbon capture and sequestration experiments. Some of our work in progress indicates a delayed decomposition and a shift of the chrysotile breakdown towards higher temperature when not using a purging gas. Thus, the activity/  $p_{\text{H}_2\text{O}}$  has a major impact on the breakdown and formation conditions of all occurring phases, a fact already demonstrated for high-pressure decomposition reactions of antigorite (Perillat *et al.* 2005).

## 7 - KINETICS OF THE CHRYSOTILE AND BRUCITE DEHYDROXYLATION REACTION: A COMBINED NON-ISOTHERMAL/ ISOTHERMAL THERMOGRAVIMETRIC ANALYSIS AND HIGH-TEMPERATURE X-RAY DIFFRACTION STUDY

*Trittschack R, Grobéty B, Brodard P*

*submitted to Physics and Chemistry of Minerals*

---

### ABSTRACT

The dehydroxylation reactions of chrysotile  $\text{Mg}_3\text{Si}_2\text{O}_5(\text{OH})_4$  and brucite  $\text{Mg}(\text{OH})_2$  were studied under inert nitrogen atmosphere using isothermal and non-isothermal approaches. The brucite decomposition was additionally studied under  $\text{CO}_2$  in order to check the influence of a competing dehydroxylation/ carbonation/ decarbonisation reaction on the reaction kinetics. Isothermal experiments were realised by using *in situ* high-temperature X-ray diffraction, whereas non-isothermal experiments were performed by thermogravimetric analyses. All data were treated by model-free, isoconversional approaches ('time to a given fraction' and Friedman method) to avoid the influence of kinetic misinterpretation caused by model-fitting techniques. All examined reactions are characterised by a dynamic, non-constant reaction progress-resolved ( $\alpha$ -resolved) course of the apparent activation energy  $E_a$  and indicate, therefore, multi-step reaction scenarios in case of the three studied reactions. The dehydroxylation kinetics of chrysotile can be subdivided into three different stages characterised by a steadily increasing  $E_a$  ( $\alpha \leq 15\%$ , 240 - 300 kJ/mol), before coming down and forming a plateau ( $15\% \leq \alpha \leq 60\%$ , 300 - 260 kJ/mol). The reaction ends with an increasing  $E_a$  ( $\alpha \geq 60\%$ , 260 - 290 kJ/mol). The dehydroxylation of brucite under nitrogen shows a less dynamic, but generally decreasing trend in  $E_a$  versus  $\alpha$  (160 - 110 kJ/mol). In contrast to that, the decomposition of brucite under  $\text{CO}_2$  delivers a dynamic course with a much higher apparent  $E_a$  characterised by an initial stage of around 290 kJ/mol. Afterwards, the apparent  $E_a$  comes down to around 250 kJ/mol at  $\alpha \sim 65\%$  before rising up to around 400 kJ/mol. The delivered kinetic data has been investigated by the  $z(\alpha)$  master plot and generalised time master plot methods in order to discriminate the reaction mechanism. Resulting data verify the multi-step reaction scenarios (reactions governed by more than one rate-determining step) already visible in  $E_a$  versus  $\alpha$  plots.

### 7.1 INTRODUCTION

Kinetic analyses of solid state reactions have been studied in Material and Earth sciences since more than 100 years. Kinetics are important in the fields of magmatic (crystal and/ or bubble growth in magmas) and metamorphic petrology (mineral transformations), and they are an important (limiting) factor for many dating tools used in Earth sciences (e.g., geospeedometry based on diffusion, Ar-Ar dating of micas, etc.)

(Zhang 2008). In Material Sciences, kinetics are not only of scientific interest, but also of economic importance. In material synthesis, the rate of processes often influence the texture and therefore also the properties of materials (e.g., Salehi *et al.* 2011; Cheong *et al.* 2009).

The theoretical background on the principles of solid state reaction kinetics evolved considerably during this time period. Experimental techniques and models to extract

kinetic parameters for similar reactions differ widely between individual branches of science (e.g., chemistry *versus* geosciences). Even different research groups within the same field are using quite different experimental and mathematical approaches to extract kinetic information from a reaction. Results are, therefore, often not directly comparable with each other. During the last three decades, some people active in the field of thermal analysis and kinetics started to question the validity of the theoretical models used to describe rates of solid state reactions (Brown 1987; Maciejewski 1992; Vyazovkin and Wight 1997; Vyazovkin 2000b; Galwey 2004). In addition, Galwey and Brown (2002) initiated a new discussion on the validity of the Arrhenius equation in the field of solid state kinetics. In the chemistry community a joint effort was undertaken to clarify some doubtful practices and to propose general procedures for performing experiments and data evaluation. A series of guideline/ review papers are available in literature to provide a comprehensive base for 'users' of solid state kinetics (e.g., Vyazovkin and Wight 1997; Brown *et al.* 2000; Burnham 2000; Maciejewski 2000; Roduit 2000; Vyazovkin 2000b; Galwey 2004; Vyazovkin 2008; Vyazovkin *et al.* 2011). However, none of these articles were published in geosciences literature. This absence may explain the low number of geoscientific papers dealing with modern solid state kinetic concepts such as isoconversional kinetics, variable activation energies, multi-step reaction mechanisms, etc. In fact, most of the papers written since the millennium are still using the Avrami-Erofe'ev reaction model and isothermal model-fitting functions (Bamford and Tipper 1980; Hancock and Sharp 1972) to describe the experimental data. The Avrami-Erofe'ev model describes reactions whose rates are determined by nucleation and growth steps as well as diffusion steps (e.g., Bamford and Tipper 1980). Models for one-, two-, three-dimensional nucleation and growth as well as diffusion models are included therein. The (force) fitted data are then used to determine the dimensionality of the single 'rate-

determining step' (e.g., Bray and Redfern 2000; Cattaneo *et al.* 2003; Perrillat *et al.* 2005; Ferrage *et al.* 2007; Carbone *et al.* 2008; Ballirano and Melis 2009; Chollet *et al.* 2009; Inoue *et al.* 2009; Tokiwai and Nagashima 2010; Gualtieri *et al.* 2012). Most of these authors, however, did not check independently that the Avrami-Erofe'ev model is correctly describing the kinetics of the reaction they analysed.

The two master plot approaches presented herein, combine the model-free methods with model-based ones to decipher possible rate-limiting steps. Prior to the use of master plots it is necessary to determine reaction progress-resolved data of the apparent activation energy ( $E_a$ ). This is commonly done by the help of model-free methods such as the used integral (e.g., Ozawa 1965; Flynn and Wall 1966, Vyazovkin 1996, 1997, 2001) and differential isoconversional (Friedman 1964) approaches which allow to determine the kinetic parameters ( $E_a$ ,  $A$ ) independent of a discrete assumption on either an integral  $g(\alpha)$  or differential  $f(\alpha)$  model function. In case of an almost constant apparent  $E_{aa}$  it is possible to use the  $z(\alpha)$  master plot method to determine the rate-limiting mechanism provided that the same step controls the rate over the entire reaction progress. If the latter 'prerequisite' is not fulfilled, the generalised time master plot is more suitable as it allows determining a reaction progress-resolved change in the rate-limiting step. In both master plot approaches, the experimentally determined data are compared to a set of curves corresponding to theoretical models (Table 7-1). Then, the best fit between the experimental and theoretical curve is taken as the most appropriate reaction model.

The paper presents and discusses kinetic data of the dehydroxylation and subsequent phase transformation of chrysotile  $\text{Mg}_3\text{Si}_2\text{O}_5(\text{OH})_4$  to forsterite  $\text{Mg}_2\text{SiO}_4$  and brucite  $\text{Mg}(\text{OH})_2$  to periclase  $\text{MgO}$ . Apart from the dehydroxylation in inert nitrogen atmosphere, brucite was additionally studied under a constant flux of  $\text{CO}_2$  to examine the influence of secondary formed

carbonates on the dehydroxylation reaction. Ongoing reactions were investigated by non-isothermal thermogravimetry (TGA) and treated with model-free techniques. Resulting kinetics will be compared with that of isothermal high-temperature X-ray diffraction (HT-XRD). Both reactions have been studied comprehensively in the past (e.g., Martin 1977; Datta *et al.* 1987; Datta 1991; MacKenzie and Meinhold 1994; Butt *et al.* 1996; Halikia *et al.* 1998; McKelvy *et al.* 2001; Bearat *et al.* 2002; Cattaneo *et al.* 2003; Yue *et al.* 2005; McKelvy *et al.* 2006; Nahdi *et al.* 2009; Viti 2010; Gualtieri *et al.* 2012; Trittschack and Grobéty 2013) and offer, therefore, good possibilities to compare assessed data. Mechanistic interpretations are performed by comparing model-free and reaction progress-resolved values of the apparent activation energy ( $E_{\text{app}}$ ) with the ones plotted into the two independent master plot graphs. The results are compared with literature data.

## 7.2 EXPERIMENTAL METHODS

### 7.2.1 Sample materials

The investigated chrysotile sample, a vein crosscutting an antigorite serpentinite, is from the mineralogical collection of the Department of Geosciences at the University of Fribourg/Switzerland (internal reference chry 33/12). The material for chemical and phase analysis as well as kinetic investigations was extracted mechanically from the vein. Transmission electron microscopy based energy-dispersive spectroscopy (TEM-EDS) analysis gave an almost pure Mg end-member composition with 48.0 wt% SiO<sub>2</sub>, 51.2 wt% MgO and 0.1 wt% FeO<sub>tot</sub>. X-ray powder diffractograms point towards the dominance of the polytype clinochrysotile as the resulting pattern is close to that of the ICDD references 25-0645 and 10-0381. The outer diameter of the chrysotile fibres were determined from high-resolution TEM images and gave values ranging between 23 nm and 85 nm, more than 75 % were between 30 nm

and 60 nm. A detailed description of the dehydroxylation reaction is provided by Trittschack and Grobéty (2013).

The analysed brucite is a synthetic Mg(OH)<sub>2</sub> sample obtained from Sigma-Aldrich (M5421-, SigmaUltra, minimum 95%). X-ray fluorescence analysis (XRF) yield a composition of 0.07 wt% SiO<sub>2</sub>, 0.01 wt% Al<sub>2</sub>O<sub>3</sub>, 69.63 wt% MgO, 0.15 wt% CaO, 0.02 wt% BaO and 0.10 wt% Cl, corresponding to 30.02 wt% H<sub>2</sub>O which is close to the theoretical value of 30.89 wt% H<sub>2</sub>O for Mg(OH)<sub>2</sub>.

### 7.2.2 X-ray fluorescence

X-ray fluorescence was carried out with a Philips PW2400 X-ray fluorescence wavelength-dispersive spectrometer (XRF-WDS) using a voltage of 60 kV and a current of 30 mA. The analysis was done on a pressed Mg(OH)<sub>2</sub> powder disc with a diameter of 32 mm. Calculations were realised with the UniQuant5 software package by Thermo Fisher Scientific.

### 7.2.3 X-ray powder diffraction

X-ray powder diffraction for qualitative phase analysis was performed with a Philips PW1800 diffractometer (Bragg-Brentano geometry, Cu K $\alpha$  radiation generated at 40 kV and 40 mA, variable divergence slit and a receiving slit size of 1 mm). The diffractograms were measured in the 5-100 °2 $\theta$  range using a step size of 0.02 °2 $\theta$  with a scanning rate of 5 sec/step for brucite and a step size of 0.01 °2 $\theta$  with a scanning rate of 2.5 sec/step for chrysotile, respectively.

### 7.2.4 Thermogravimetric analyses

Thermogravimetric analyses were realised with a Mettler-Toledo TGA/SDTA 851e device at the College of Engineering and Architecture Fribourg/ Switzerland. In general, all analyses

were run under a constant flux of nitrogen (100 ml/min N<sub>2</sub>) to reduce possible oxidation effects due to FeO<sub>tot</sub> and other oxidisable impurities of the sample material. An additional experiment with brucite was run under a constant flux of CO<sub>2</sub> (100 ml/min) to study dehydroxylation under simultaneous carbonatisation. The weight loss of the powdered sample material was measured for seven different linear heating rates (1, 2, 4, 8, 12, 16 and 32 K/min). The variation of the sample mass was kept as small as possible and reached a maximum of 0.5 mg within a single thermoanalytical dataset consisting of data of seven different heating rates.

### 7.3 KINETIC APPROACH

Our kinetic investigations are based on time (isothermal and non-isothermal data) and temperature (non-isothermal data) resolved datasets of the reaction progress  $\alpha$ . For *in situ* high-temperature X-ray experiments,  $\alpha$  is proportional to the reduction of the integral XRD peak intensity of the reactant, e.g. chrysotile and brucite with time:

$$\alpha = 1 - \frac{I_t}{I_0} \quad (7.1)$$

Where  $I_t$  is the integral peak intensity of a respective peak at time  $t$  and  $I_0$  the initial peak intensity. In our case,  $I_0$  corresponds to the strongest, i.e., first peak intensity measured after the heating up of the sample. Kinetic data of chrysotile were acquired by measuring the (002) XRD peak, whereas for brucite the (001) peak was monitored. In TG data, the reaction progress  $\alpha$  is defined as:

$$\alpha = \frac{m_0 - m_t}{m_0 - m_f} \quad (7.2)$$

or

$$\alpha = \frac{m_0 - m_T}{m_0 - m_f} \quad (7.3)$$

where  $m_0$ ,  $m_t$ ,  $m_T$  and  $m_f$  are initial mass, the mass at time  $t$  or at temperature  $T$  and the final mass of the sample.

#### 7.3.1 Avrami-Erofe'ev method

The general rate-equation is given by:

$$\frac{d\alpha}{dt} = k(T)f(\alpha) \quad (7.4)$$

The function  $f(\alpha)$ , called the reaction model, describes the dependency of the rate on reaction progress. Functions for many rate-limiting reaction steps have been derived (e.g. Bamford and Tipper 1980; Vyazovkin *et al.* 2011). An often used model is the classical Avrami-Erofe'ev equation (Bamford and Tipper 1980), for which the integrated form is given by:

$$\alpha = 1 - e^{-(kt)^n} \quad (7.5)$$

where  $k(T)$  corresponds to the rate constant and  $n$  to a respective rate-determining step. The Avrami-Erofe'ev approach describes the rate of reactions in which nucleation and growth steps (or diffusion) are rate-limiting. The parameter  $n$  changes with the morphology (dimension) of the nucleating phase or with the dimension in which diffusion occurs (one-, two- or three-dimensional diffusion). Equation 7.5 can be linearised after taking the logarithm two times which gives:

$$\ln(-\ln(1-\alpha)) = n \ln k + n \ln t \quad (7.6)$$

which then can be used to extract  $n$  and  $k$  from a  $\ln(-\ln(1-\alpha))$  versus  $\ln t$  plot. Using the Arrhenius relationship:

$$k = Ae^{-\frac{E_a}{RT}} \quad (7.7)$$

allows the calculation of the apparent activation energy  $E_a$  and the pre-exponential factor  $A$  from the slope of a corresponding Arrhenius plot. In many studies, the Avrami-Erofe'ev model is taken *a priori* i.e., without independent control if the latter is really describing the rate-limiting step. The coefficient  $n$  is then extracted from the



best fit and the corresponding mechanism is presented as the rate-limiting step (Hancock & Sharp 1972).

### 7.3.2 Time to a given fraction method (TGF method)

The TGF method is an isothermal isoconversional technique enabling the calculation of reaction progress-resolved apparent activation energies  $E_{aa}$  without using a specific reaction model  $f(\alpha)$  (Burke 1965; Putnis 1992). For this, equation 7.4 has to be rewritten as follows:

$$dt = k^{-1} f^{-1}(\alpha) d\alpha \quad (7.8)$$

Thus, the time  $t_{\alpha(i)}$ , i.e., the time  $t$  necessary to reach a certain reaction progress  $\alpha_i$ , can be calculated by integrating 7.8:

$$t_{\alpha_i} = k^{-1} \int_{\alpha=0}^{\alpha=\alpha_i} f^{-1}(\alpha) d\alpha \quad (7.9)$$

Under the assumption that the reaction model  $f(\alpha)$  will not change during the course of the reaction and is also independent of temperature, the integral in equation 7.9 is constant.

Values for  $E_{aa}$  can then be calculated from the Arrhenius plot  $\ln(t_{\alpha})$  versus  $1/T$  [K<sup>-1</sup>].

### 7.3.3 Friedman method

With non-isothermal experiments the error introduced by having to heat up the sample inherent to isothermal experiments are avoided. The following relationship holds for non-isothermal experiments:

$$\frac{d\alpha}{dT} = \frac{d\alpha}{dt} \cdot \frac{dt}{dT} \quad (7.10)$$

The general non-isothermal rate equation with  $\beta = dT/dt$  reads:

$$\frac{d\alpha}{dT} = \frac{A}{\beta} e^{-\frac{E_a}{RT}} f(\alpha) \quad (7.11)$$

Friedman (1964) proposed a method to extract model-free values of  $E_{aa}$  from the logarithmic form of 7.11

$$\begin{aligned} \ln\left(\beta \frac{d\alpha}{dT}\right) &= \ln\left(\frac{d\alpha}{dt}\right)_{\alpha,i} \\ &= -\frac{E_a}{RT} + \ln[A f(\alpha)] \quad (7.12) \end{aligned}$$

An experimental series of different heating rates  $\beta$  can then be used to plot the linear relationship between  $\ln(d\alpha/dt)_{\alpha,i}$  and  $1/T_{\alpha}$  at the same value of  $\alpha$  reached at  $i$  different heating rates  $\beta$  to calculate model-free values of  $E_{aa}$ .

### 7.3.4 ASTM E 698

Following this international standard routine (N.N. 1979), the maximum reaction rate of single step reactions (non-isothermal conditions) are reached at the same degree of conversion independent of the heating rate  $\beta$ . Accordingly, it is possible to calculate the overall apparent activation energy from the slope of the logarithm of the heating rate *versus* the reciprocal absolute temperature of the maximum.

### 7.3.5 Master Plots

Non-isothermal and isothermal data obtained in the present experiments were analysed with the help of two independent master plot approaches, the  $z(\alpha)$  master plots (Vyazovkin *et al.* 2011) and the generalised time master plots (Sánchez-Jiménez *et al.* 2013), in order to make inferences on possible reaction mechanisms and rate-limiting steps. Master plots are calculated and normalised reference curves for all possible reaction models, which do not depend on the numerical values of the kinetic parameters (Gotor *et al.* 2000). Comparison between these master plots and the normalised experimental data allows selecting the most appropriate reaction

Mechanistic model	Symbol	$f(\alpha)$	$g(\alpha)$
<i>Nucleation models</i>			
(Random nucleation and growth of nuclei through different nucleation and nucleus growth)			
Avrami-Erofeev eq., n=2	A2	$2(1-\alpha)[- \ln(1-\alpha)]^{1/2}$	$[- \ln(1-\alpha)]^{1/2}$
Avrami-Erofeev eq., n=2.5	A2.5	$2.5(1-\alpha)[- \ln(1-\alpha)]^{3/5}$	$[- \ln(1-\alpha)]^{1/2.5}$
Avrami-Erofeev eq., n=3	A3	$3(1-\alpha)[- \ln(1-\alpha)]^{2/3}$	$[- \ln(1-\alpha)]^{1/3}$
Avrami-Erofeev eq., n=4	A4	$4(1-\alpha)[- \ln(1-\alpha)]^{3/4}$	$[- \ln(1-\alpha)]^{1/4}$
<i>Geometrical contraction models</i>			
Phase boundary controlled reaction (contracting area)	R2	$2(1-\alpha)^{1/2}$	$[1 - (1-\alpha)^{1/2}]$
Phase boundary controlled reaction (contracting volume)	R3	$3(1-\alpha)^{2/3}$	$[1 - (1-\alpha)^{1/3}]$
<i>Diffusion models</i>			
One-dimensional diffusion (Parabola law)	D1	$1/(2\alpha)$	$\alpha^2$
Two-dimensional diffusion (Valensi equation)	D2	$[- \ln(1-\alpha)]^{-1}$	$(1-\alpha)\ln(1-\alpha) + \alpha$
Three-dimensional diffusion (Jander equation)	D3	$[3(1-\alpha)^{2/3}]/[2(1 - (1-\alpha)^{1/3})]$	$[1 - (1-\alpha)^{1/3}]^2$
<i>Reaction order model</i>			
First order (Mampel) (Random nucleation followed by instantaneous growth of nuclei) Avrami-Erofeev eq., n=1	F1, A1	$(1-\alpha)$	$-\ln(1-\alpha)$

<sup>a</sup>Vyazovkin *et al.* (2011), <sup>b</sup>Sánchez-Jiménez *et al.* (2013)

**Table 7-1.** Differential  $f(\alpha)$  and integral  $g(\alpha)$  functions of some widely used kinetic models in solid-state kinetics<sup>a,b</sup>.

model. The functions used to obtain these master plots should be independent of temperature (isothermal conditions) or heating rates (non-isothermal conditions). The use of  $z(\alpha)$  master plots has limitations when applied to reactions with a highly dynamic evolution of the apparent activation energy with reaction progress (Vyazovkin *et al.* 2011). The master plot approach using the generalised time allows to cross-check the influence of a variable apparent  $E_{aa}$  (Ozawa 1986; Sánchez-Jiménez *et al.* 2013). An isoconversional data treatment to determine  $E_{aa}$  is a prerequisite for both master plot approaches.

The function for the  $z(\alpha)$  master plots has been derived using the generalised time defined by Ozawa (1986). Integrating the general rate equations gives:

$$\begin{aligned}
 g(\alpha) &= \int_0^\alpha \frac{d\alpha}{f(\alpha)} \\
 &= A \int_0^t \exp\left(\frac{-E}{RT}\right) dt \\
 &= A\theta \quad (7.13)
 \end{aligned}$$

Ozawa called the integral on the right hand side generalised time  $\theta$ . The first derivative of generalised time is given by:

$$\frac{d\theta}{dt} = \exp\left(\frac{-E}{RT}\right) \quad (7.14)$$

The following master plot functions using the generalised time are proposed (e.g., Vyzovkin *et al.* 2011):

$$y(\alpha) = \frac{d\alpha/dt}{d\theta/dt} = \frac{d\alpha}{d\theta} = \frac{A\left(\frac{-E}{RT}\right)f(\alpha)}{\left(\frac{-E}{RT}\right)} = Af(\alpha) \quad (7.15)$$

$$z(\alpha) = \frac{d\alpha}{d\theta}\theta = \theta Af(\alpha) = g(\alpha)f(\alpha) \quad (7.16)$$

The master curve of a model  $f(\alpha)$  is given by the values of the right hand product as function of  $\alpha$ . In the following, only the  $z(\alpha)$  master plot approach will be used. The position of the maxima  $z(\alpha)$  are characteristic for the reaction model:

$$z'(\alpha_{\max}) = g(\alpha_{\max})f'(\alpha_{\max}) = -1 \quad (7.17)$$

$\alpha_{\max}$  is the reaction progress for which the maximum is observed. The curve derived from the experimental data is obtained by introducing the corresponding differential and integral general rate equations for  $f(\alpha)$  and  $g(\alpha)$ , respectively. The resulting equation for non-isothermal conditions is:

$$z(\alpha) = g(\alpha)f(\alpha) = \left(\frac{d\alpha}{dt}\right)_{\alpha} T_{\alpha}^2 \left[\frac{\pi(x)}{\beta T_{\alpha}}\right] \quad (7.17)$$

where  $\pi(x)$  is an approximation of the temperature integral and  $\beta$  the heating rate. Eq. (7.17) has to be normalised to the reaction rate at  $\alpha = 50\%$  and can be simplified by removing the term in brackets as it has a negligible effect of the shape of the  $z(\alpha)$  function (Al-Mulla *et al.* 2011; Vyazovkin *et al.* 2011). The normalised, simplified function is given by:

$$z(\alpha) \cong \frac{\left(\frac{d\alpha}{dt}\right)_{\alpha}}{\left(\frac{d\alpha}{dt}\right)_{0.5}} \left(\frac{T_{\alpha}}{T_{0.5}}\right)^2 \quad (7.18)$$

To draw the (normalised) experimental curve, the temperature and the rate as a function of reaction progress have to be extracted from the DTG curves.

The second master plot approach is also based on the generalised time  $\theta$  (Ozawa 1986; Gotor *et al.* 2000; Sánchez-Jiménez *et al.* 2010) and the generalised reaction rate given by:

$$\frac{d\alpha}{d\theta} = \frac{d\alpha}{dt} \exp\left(\frac{-E_a}{RT}\right) \quad (7.19)$$

Normalising to a reaction progress of 50 % gives following relationship between the generalised reaction rate and the experimental data for the non-isothermal case (Sánchez-Jiménez *et al.* 2013):

$$\frac{\left(\frac{d\alpha}{d\theta}\right)}{\left(\frac{d\alpha}{d\theta}\right)_{0.5}} = \frac{\left(\frac{d\alpha}{dt}\right)}{\left(\frac{d\alpha}{dt}\right)_{0.5}} \frac{\exp\left(\frac{E_{aa}}{RT}\right)}{\exp\left(\frac{E_{aa}}{RT_{0.5}}\right)} \quad (7.20)$$

which simplifies to:

$$\frac{\left(\frac{d\alpha}{d\theta}\right)}{\left(\frac{d\alpha}{d\theta}\right)_{0.5}} = \frac{\left(\frac{d\alpha}{dt}\right)}{\left(\frac{d\alpha}{dt}\right)_{0.5}} \quad (7.21)$$

for isothermal conditions. Experimental data are then simply compared to a set of theoretical curves (Table 7-1).

## 7.4. RESULTS AND DISCUSSION

### 7.4.1 The dehydroxylation reaction as seen from thermogravimetry

A comparison of the first derivative graphs (DTG) of chrysotile (Fig. 7-1) and brucite (Fig. 7-2) illustrates different degrees in the complexity of the investigated reactions under an inert  $N_2$  atmosphere. The DTG plots of brucite are dominated by just one peak, whereas the curves for chrysotile have multiple shoulders on the flanks of the primary maximum, i.e., the dehydroxylation rate has several secondary maxima. A summary of the onsets, peak maxima and offsets of the TG analyses of both minerals are given in Table 7-2. The temperatures of all peak maxima listed in Table 7-2 are a function of the heating rate, i.e., an increase of the heating

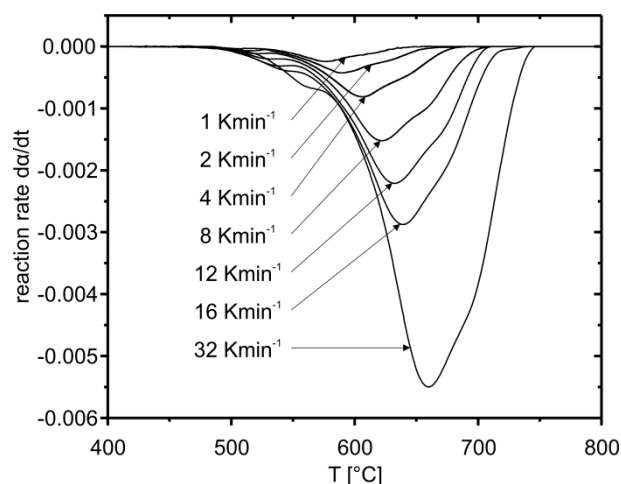


**Figure 7-1.** Reaction rates of the dehydroxylation reaction of chrysotile under a constant flux of  $N_2$  (100 ml/min) determined from TG data.

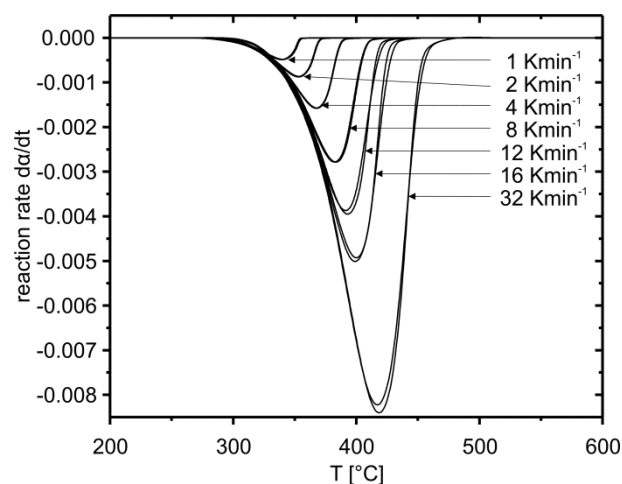


**Figure 7-2.** Reaction rates of the dehydroxylation reaction of brucite under a constant flux of  $N_2$  (100 ml/min) determined from TG data.

rate shifts the respective maxima towards higher temperatures. A broadening tendency of the DTG features is evident in both samples. The DTG curve of chrysotile corresponding to a heating rate of 32 Kmin<sup>-1</sup> is additionally characterised by an evident shoulder at the low temperature side. The total release of  $H_2O$  calculated from the TG data yields 13.1 wt% in case of chrysotile and 29.6 wt% in case of brucite, respectively. In both cases, the estimated mass release deviates slightly from the theoretical value (chrysotile 13.0 wt%, brucite 30.9 wt%), which is most probably due to the presence of impurities or defects.

All DTG maxima of chrysotile and brucite are similar to previously published data (e.g., Nahdi *et al.* 2009; Viti 2010). However, the shapes of the DTG curves for chrysotile vary considerably between authors (e.g., Naumann and Drescher 1966; Viti 2010; Zaremba *et al.* 2010), which makes it difficult to compare the different datasets. In general, such a variability in thermoanalytical data of phyllosilicates are common and caused by physical and chemical properties specific to each sample, e.g., particle size distribution, presence of different polytypes and/ or polymorphs within the sample, chemical heterogeneities, etc. (Bish and Duffy 1990). In

case of chrysotile, the particular crystal structure contributes to the variation in the dehydroxylation behaviour. The dehydroxylation temperature in nanotube-like chrysotile is radius-dependent and will be higher in the innermost layers compared to the less curved outer parts of the chrysotile fibres.

The multiple nature of peak maxima in DTG curves of chrysotile are typical for a reaction scenario with (metastable) reaction intermediates as inferred by Viti (2010) and experimentally demonstrated by MacKenzie and Meinhold (1994), Gualtieri *et al.* (2012) and Tritschack and Grobéty (2013). The broad temperature range in which chrysotile dehydroxylates is related to the radius-dependent dehydroxylation temperature and the appearance of an  $H_2O$  containing talc-like intermediate phase, which breaks down at even higher temperatures (Tritschack and Grobéty 2013). The much simpler DTG graphs of brucite seem to be indicative for a direct dehydroxylation and subsequent formation of periclase MgO without intervening (metastable) phases as demonstrated by XRD studies (Bearat *et al.* 2002; Nahdi *et al.* 2009). An obvious change in the shape of the chrysotile DTG curves with heating rate is an indication for a change of the kinetic equation

(Šesták 1984), i.e., the rate-limiting step does not only depend on reaction progress but also on the heating rate. This point has to be considered in kinetic analysis as all isoconversional methods are based on the isoconversional principle which states that the reaction rate at a constant reaction progress depends only on temperature (Vyazovkin and Wight 1997), and not on the heating rate.

The TG curves for the brucite  $\text{Mg}(\text{OH})_2$  breakdown reaction under  $\text{CO}_2$  atmosphere show an interval of mass gain before the main decomposition event (Fig. 7-3). The gain itself is related to the formation of magnesite  $\text{MgCO}_3$  as shown by Bearat *et al.* (2002) and/ or a series of crystal-water bearing Mg-carbonates (Hänchen *et al.* 2008). The main weight loss is due to a combination of dehydroxylation of remaining brucite and decarbonisation of magnesite (Fig. 7-4). This combined breakdown event is shifted towards higher temperatures relative to the pure dehydroxylation reaction under  $\text{N}_2$ . The total difference between  $\text{N}_2$  and  $\text{CO}_2$  runs decreases at higher heating rates (Fig. 7-4). Despite the mass gain as a result of the formation of carbonate bearing species and two different breakdown reactions, there are no multiple decomposition peaks observable in the DTG curves. The total mass loss under  $\text{CO}_2$  relative to the maximum weight reached after the initial mass gain is 34 to 35 wt% which is up to 7 wt% more than observed under a constant flux of  $\text{N}_2$ . This corresponds to a formation of about 15 wt% carbonate under the chosen experimental conditions. The lack of multiple peaks might be related to a competitive reaction sequence, i.e., the formation of carbonate is directly linked with the breakdown of brucite.

#### 7.4.2 The course of the apparent activation energies

The isoconversional treatment (Friedman method) of the non-isothermal DTG data gave a strongly reaction progress-dependent evolution of

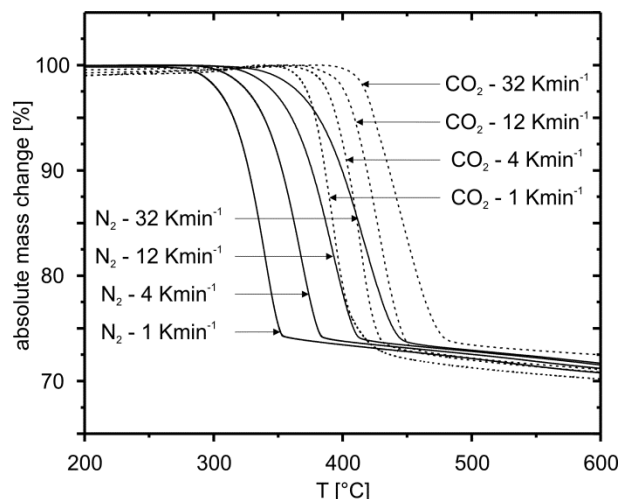


**Figure 7-3.** TG curves for the decomposition of brucite under  $\text{N}_2$  (100 ml/min) and  $\text{CO}_2$  (100 ml/min).

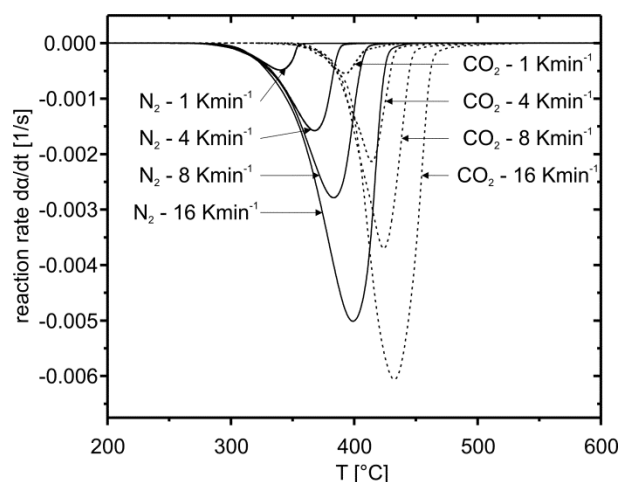


**Figure 7-4.** Resulting DTG curves of the decomposition of brucite under  $\text{N}_2$  (100 ml/min) and  $\text{CO}_2$  (100 ml/min).

the apparent activation energy in case of chrysotile (Fig. 7-5). The evolution is characterised by a first  $E_a$  maximum for  $\alpha \approx 0.15$ , followed by a decreasing trend up to  $\alpha \approx 0.5$  and a final increase. The corresponding graph for brucite shows a weaker and generally decreasing evolution of the apparent activation energy with  $\alpha$  (Fig. 7-6). Several runs under identical experimental conditions with the same sample material show a much poorer reproducibility of

	onset [°C]	chrysotile maxima [°C]	offset [°C]	onset [°C]	brucite maximum [°C]	offset [°C]
1 K/min	445.2	522.5, 585.6, ~ 625	662.3	249.3	340.2	407.4
2 K/min	455.4	527.5, 599.9, ~ 632	682.4	253.0	353.1	420.9
4 K/min	464.5	538.8, 615.6, ~ 651	687.7	257.0	367.9	435.7
8 K/min	473.2	546.3, 631.3, ~ 667	706.7	260.5	383.4	448.8
12 K/min	481.3	556.1, 641.4, ~ 677	707.5	262.1	393.0	455.2
16 K/min	488.4	563.2, 649.0, ~ 680	710.4	263.3	399.0	459.1
32 K/min	532.9	577.5, 673.5, ~ 708	746.1	274.8	418.8	506.8

**Table 7-2.** Corresponding maxima in DTG curves for chrysotile and brucite dehydroxylation experiments carried out under 100 ml/min  $N_2$ .

the  $E_a$  evolution among the different runs than for brucite decomposition. However, the general trends remain the same in both cases.

A variable apparent  $E_{aa}$  of chrysotile can also be shown when using the ASTM E 698 method. The  $E_{aa}$  values which correspond to the dehydroxylation rate maxima listed in Table 7-2 yield around 343 kJ/mol for the first, 272 kJ/mol for the main and 303 kJ/mol for the high-temperature maxima. The rate maxima match with a reaction progress of around 20 %, 50 % and 90 %. All values calculated by this method are similar with those achieved by the Friedman treatment. HT-XRD data of chrysotile treated by the TGF method (Fig. 7-7) are compatible with data obtained by the Friedman approach applied to the TG data (Fig. 7-5). But, TGF derived reaction progress-resolved  $E_a$  do not correspond to the activation energy determining the rate at  $\alpha$ , but to the gliding average  $E_a$  up to that respective  $\alpha$ . Thus, TGF derived values cannot be compared directly with TG derived data treated with the Friedman method. In addition, TGF data obtained for large  $\alpha$  ( $\alpha > 70$  %) are also less reliable. The evolution of the average  $E_a$ , however, is similar as of the actual  $\alpha$  resolved  $E_a$  but the changes are dampened.

The evolution of the average  $E_a$  extracted by the TGF method from the brucite HT-XRD runs (Fig. 7-8) show an opposite trend to the data obtained from the isoconversional treatment of the TG data. Nevertheless, the absolute values of the gliding average  $E_a$ , i.e., 120-140 kJ/mol ( $20 \% \leq \alpha \leq 80 \%$ ), are quite similar to those derived

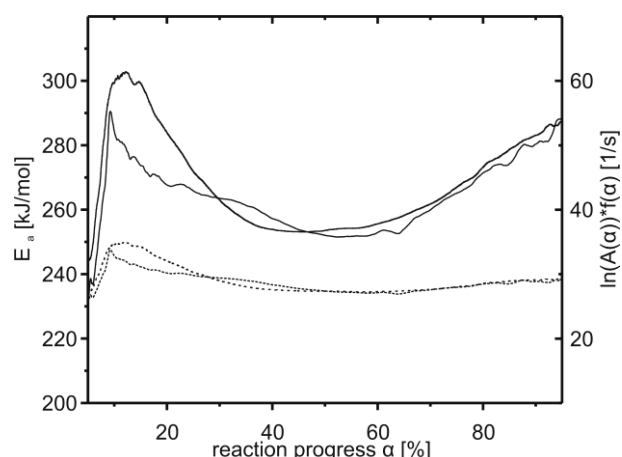


**Figure 7-5.** Apparent  $E_{aa}$  as calculated from the isoconversional Friedman analysis of TG data of the chrysotile dehydroxylation; solid lines =  $E_{aa}$  for two separate runs; dashed lines = corresponding  $\ln(A(\alpha)) \cdot f(\alpha)$  values.

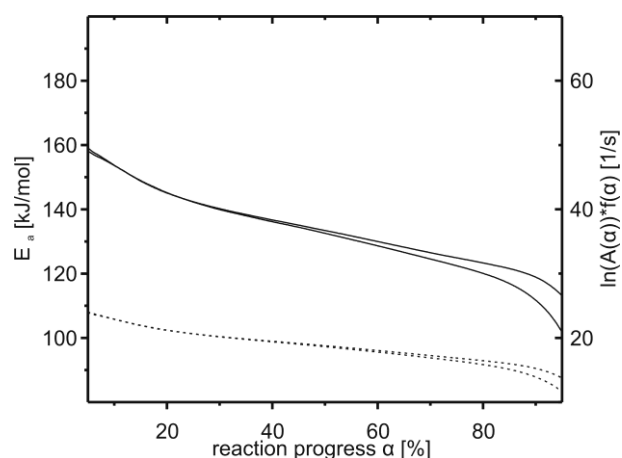


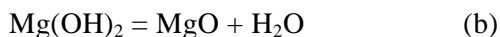
**Figure 7-6.** Apparent  $E_{aa}$  as calculated from the isoconversional Friedman analysis of TG data of the brucite dehydroxylation under a constant flux of  $N_2$ ; solid lines =  $E_{aa}$  for two separate runs; dashed lines = corresponding  $\ln(A(\alpha)) \cdot f(\alpha)$  values.

from the Friedman treatment of the TG data in the equivalent  $\alpha$  range. The differences between both datasets might be related to the isothermal technique, where the sample undergoes a heating up stage prior to the real measurement. All reactions occurring during the heating up stage are virtually lost and, therefore, not included within data derived from a subsequent mathematical treatment, e.g., the TGF method.

The reproducibility between individual HT-XRD runs is worse than for TG derived data. This is most likely caused by the geometry of the sample holder, i.e., a glass platelet positioned on a platinum stripe with the thermocouple below. The contact between the glass platelet and the platinum stripe is not totally flat. Thus, the exact position of the sample may vary between individual experimental runs. This may explain the higher variability/ poor reproducibility of data obtained from HT-XRD.

Compared to experiments conducted under inert  $N_2$  atmosphere, the influence of  $CO_2$  on the apparent activation energies of the breakdown of brucite in TG and HT-XRD data is quite distinct as all values are almost doubled in case of TG data and increased by around a quarter in XRD data, respectively (Figs. 7-9 and 7-10).

At least three different reactions take place in presence of  $CO_2$ :



Brucite is always metastable in a pure  $CO_2$  atmosphere, i.e., as soon as the temperature and therefore the activation energy is high enough, brucite will either transform through reaction (a) or a combination of reaction (b) and (c). This is confirmed by the initial weight gain, i.e., a weight gain below the onset of the brucite dehydroxylation under inert  $N_2$  atmosphere. A reaction involving hydrated carbonate species is also possible and would complicate the reaction

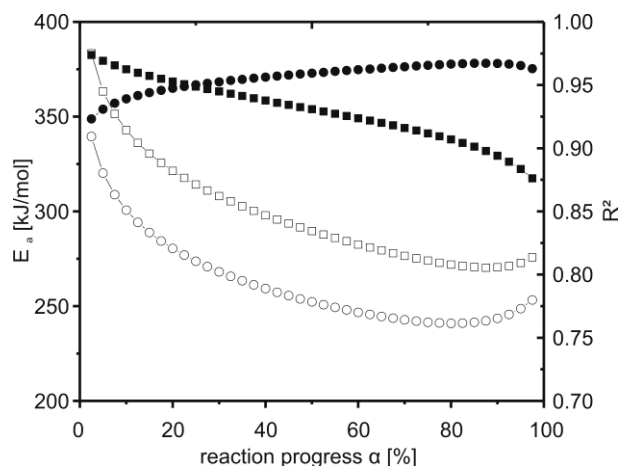


**Figure 7-7.** Apparent  $E_{aa}$  for the chrysotile dehydroxylation obtained from the isoconversional TGF treatment of HT-XRD data; filled symbols =  $R^2$ , open symbols =  $E_a$ .

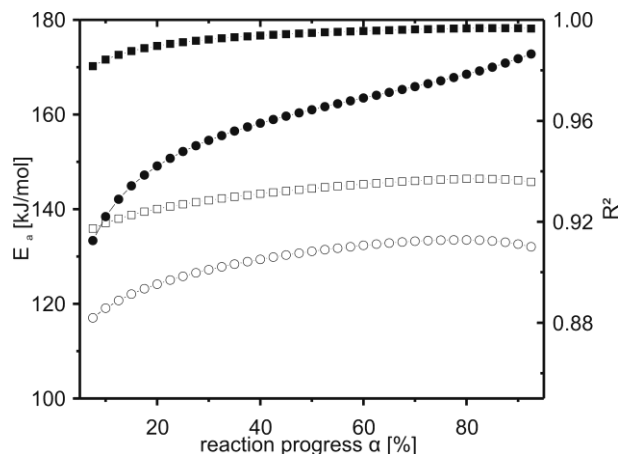


**Figure 7-8.** Apparent  $E_{aa}$  for the brucite dehydroxylation obtained from the isoconversional TGF treatment of HT-XRD data; filled symbols =  $R^2$ , open symbols =  $E_a$ .

sequence (Hänchen *et al.* 2008). For the chosen heating rates, it is impossible to achieve a completion of the carbonation reaction (Bearat *et al.* 2002). Thus, the onset of the main weight loss is due to the presence of metastable brucite and magnesite. As values derived from XRD measurement are taken from specific reflections of brucite only, all activation energies extracted from the TGF analyses can be attributed to the decomposition reactions (a) and (b) of brucite only. The activation energy calculated for the

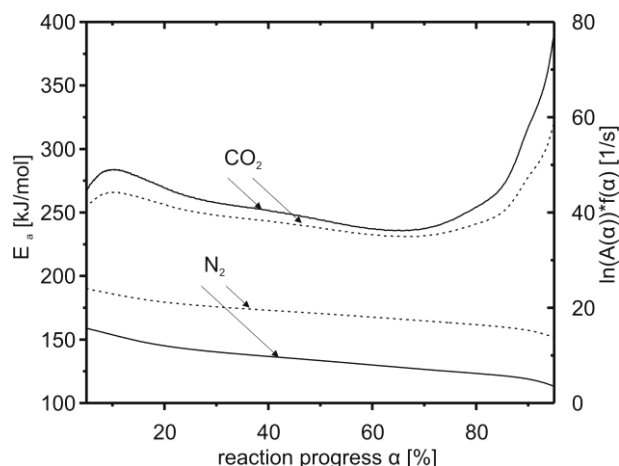


**Figure 7-9.** Dependency of the apparent  $E_a$  on the extent of conversion determined from TG data of the brucite dehydroxylation under  $\text{CO}_2$  and  $\text{N}_2$ ; solid lines =  $E_a$ ; dashed lines = corresponding  $\ln(A(\alpha) \cdot f(\alpha))$ .

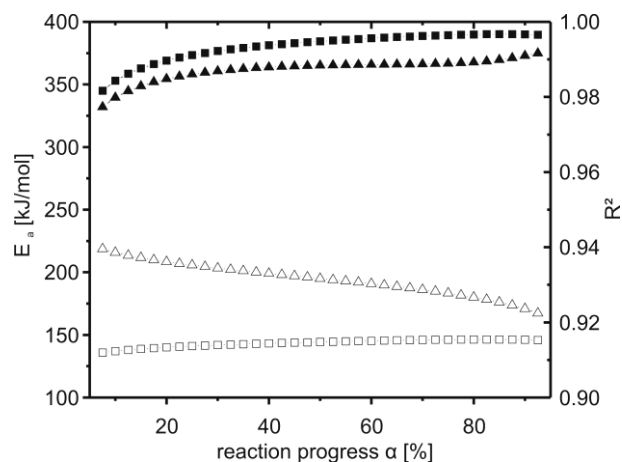


**Figure 7-10.** Dependency of the apparent  $E_a$  on the extent of conversion determined from HT-XRD data of brucite dehydroxylation under  $\text{CO}_2$  (triangles) and  $\text{N}_2$  (squares); filled symbols =  $R^2$ , open symbols =  $E_a$ .

onset of the brucite peak decrease ( $\text{CO}_2$ , low  $\alpha$ ) is considerably higher than the initial activation energy of reaction (b) under  $\text{N}_2$  (Fig. 7-10). To explain these differences, two possibilities are favoured:

(i) The higher values of  $E_a$  are due to a weighted average of reactions (a) and (b)

(ii) There is a change in the rate-limiting step of reaction (b), i.e., the presence of a carbonate layer on the surface of brucite crystallites as inferred by Butt *et al.* (1996) causes a change of the reaction mechanism.

Experimental, model-free values for  $E_a$  of reaction (b) under  $\text{N}_2$  atmosphere reported in literature vary between 45 and 188 kJ/mol (Halikia *et al.* 1998; Nahdi *et al.* 2009). *Ab initio* calculation gave a value of 180 kJ/mol for reaction (b) and values of around 226 kJ/mol for the carbonation reaction (Churakov *et al.* 2004). Because the weight change observed by TG in the same temperature interval as in HT-XRD experiments is negative, the contribution of reaction (b) to the overall decomposition reaction must be more important than reaction (a) as the carbonation is increasing the weight of the

sample. Even when taking the reported  $E_a$  value for reaction (a), the contribution of reaction (a) would have to be almost 100 % to explain the observed  $E_a$ . But, this would cause a weight gain instead of a loss as observable in our data. Thus, a change of the rate-limiting step in reaction (b) due to presence of a carbonate layer is more likely and might be causal for the increase to much higher  $E_a$  under  $\text{CO}_2$  atmosphere when compared to the  $\text{N}_2$  runs. The steep increase of  $E_a$  determined from the TG data beyond  $\alpha > 0.8$  is probably related to the breakdown of magnesite, which in a pure  $\text{CO}_2$  atmosphere with  $p_{\text{CO}_2} = 1 \text{ bar}$  is stable to approximately  $500^\circ\text{C}$  (Bearat *et al.* 2002). Therefore, the initial weight loss seems to have no contribution of reaction (a). The final  $E_a$  values of the brucite decomposition experiments under  $\text{CO}_2$  are considerably higher than reported values for the magnesite decomposition in literature (156 kJ/mol  $\text{N}_2$  flux, Liu *et al.* 2012) and the values of reaction (b) under nitrogen. Unfortunately, there are no kinetic data on the magnesite decomposition under a  $\text{CO}_2$  atmosphere in literature. As magnesite starts to decarbonise only at approximately  $500^\circ\text{C}$  under a  $\text{CO}_2$  atmosphere (Stone 1954), which corresponds to a reaction progress beyond 50 %



in our TG data, the decarbonisation reaction must have a much higher contribution towards the end of the studied decomposition reaction. Thus, we suppose that the final increase is caused by a coupled reaction composed of the breakdown of magnesite and remnants of brucite.

### 7.4.3 Towards a mechanistic interpretation

#### 7.4.3.1 Brucite

As mentioned earlier, the DTG data of brucite shown in Fig. 7-2 suggest a reaction sequence governed by a single rate-determining step as there are no indications for shoulders or a heating rate dependent change in the shape of DTG curves. The continuously decreasing value of the apparent  $E_a$  with  $\alpha$  (TG dataset) is, however, not compatible with such a simple scenario. The change in  $E_a$  seems to indicate a change in the rate-limiting step (reaction model(s)) or a change in the contribution of rate-limiting reaction steps (Vyazovkin 2000b). If parallel reaction steps are rate-limiting, each contributes to the apparent activation energy (Vyazovkin 2000b):

$$E_{aa} = -R \left[ \frac{d \ln \left( \frac{d\alpha}{dt} \right)}{dT^{-1}} \right]_{\alpha}$$

$$= \frac{E_1 k_1 f_1(\alpha) + \dots + E_i k_i f_i(\alpha)}{k_1 f_1(\alpha) + \dots + k_i f_i(\alpha)} \quad (7.22)$$

Given that non-isothermal TG data are more reliable than isothermal HT-XRD data with respect to the course of the apparent activation energy and the dehydroxylation rate, it is useful to check if the resulting data can be described by one of the master plot techniques outlined in the experimental section. Fig. 7-11 and 7-12 show a comparison of experimental data with theoretical curves calculated for a number of commonly used reaction models presented in Table 7-1. It is evident from Fig. 7-11 that the dehydroxylation reaction mechanism of brucite under nitrogen atmosphere is only slightly affected by the heating rate. This is in contradiction with earlier

findings of Yue *et al.* (2005) who claim a heating rate dependent change of the reaction mechanism. They suggest an A1.5 or A2 mechanism for the entire reaction progress with a trend to the A1.5 model when increasing the heating rate.

In general, data presented here support an An mechanism with a good agreement with the A3 model up to  $\alpha \leq 60$  %, but changing to an A4 model in the range  $90 \% \leq \alpha \leq 100$  %. However, the maxima  $z_{\max}(\alpha)$  of individual experimental curves in Fig. 7-11 are not close enough to the theoretical values of  $\alpha_p = 0.632$  and  $63.2$  %, respectively, indicative for an An mechanism (Vyazovkin *et al.* 2011). This is not surprising when considering the variation in  $E_a$ . The method presented by Sánchez-Jiménez *et al.* (2013) does not depend on a constant apparent  $E_{aa}$  and uses, therefore, the generalised time directly. Thus, it is much better suited than the  $z(\alpha)$  master plot approach to analyse complex reaction mechanism. Corresponding curves of experimental data in Fig. 7-12 point towards a phase-boundary controlled mechanism (R2, R3) between  $15 \% \leq \alpha \leq 60$  % before following the paths of A2 - A3 models without a possibility to distinguish clearly between the respective mechanisms. The obvious mismatch at  $0 \leq \alpha \leq \sim 10$  % might be related to artefacts in the calculation of  $E_{aa}$ .

The best-fitting mechanistic models for the second part of the dehydroxylation reaction ( $\alpha \geq 60$  %) agree well with Controlled Rate Thermal Analysis (CRTA) data of the brucite decomposition of Nahdi *et al.* (2009) who suggest an A2 and/ or A3 model for the entire reaction. The R-type model suggested by the master plots for the first part of the reaction are supported by kinetic, microscopic and diffraction studies by Gordon and Kingery (1966, 1967) who proposed a nucleation and growth governed mechanism accompanied by extensive cracking of the primary phase (R3 mechanism). A R3 model was also proposed by Hancock and Sharp (1972) in the range  $15 \leq \alpha \leq 50$  %. However, their mechanistic interpretation might be

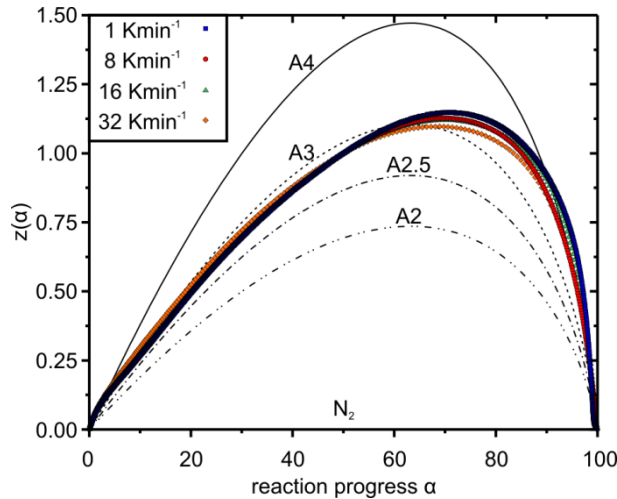


**Figure 7-11.** Comparison between theoretical  $z(\alpha)$  master plots and experimental non-isothermal TG data of the brucite dehydroxylation under  $N_2$ .

influenced by the isothermal approach. Van Aken and Langenhorst (2001) verified former findings of Hancock and Sharp (1972) and Gordon and Kingery (1966, 1967) concerning a R3 mechanism by transmission electron microscopy. They demonstrated a complex multi-step reaction mechanism including at least two stages of an interface-controlled process, one at the reaction onset and one towards the end. Both R3 dominated stages are interrupted by a diffusion-controlled stage, which cannot be seen in our data. There are no further hints regarding a specific diffusion model within the article of Van Aken and Langenhorst (2001).

The use of  $CO_2$  as reactive gas instead of an inert  $N_2$  atmosphere complicates the decomposition reaction by the simultaneously occurring carbonatisation reaction. The decarbonisation of magnesite will overlap with the dehydroxylation towards the end of the reaction progress. Resulting master plots of this reaction are presented in Figs. 7-13 and 7-14.

Fig. 7-13 clearly illustrates a heating rate dependent reaction mechanism scenario compared to the dehydroxylation under a constant flux of  $N_2$  (Fig. 7-11). The experimental curves are lacking the smooth shape expected for

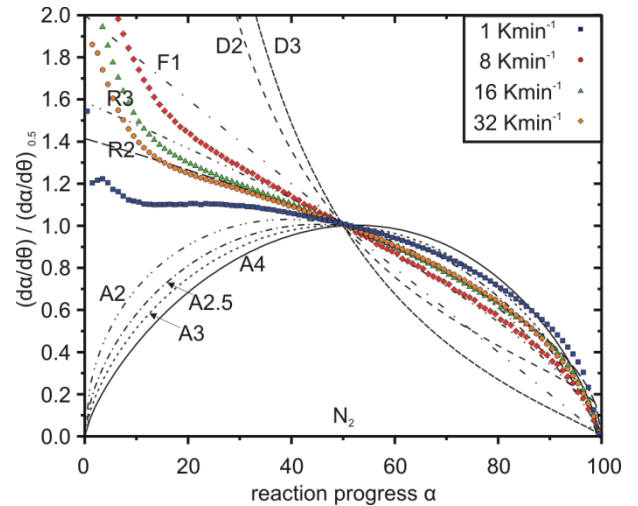


**Figure 7-12.** Comparison between generalised time master plots and experimental non-isothermal TG data of the brucite dehydroxylation under  $N_2$ .

a reaction controlled by a single step. The generalised time master plots (Fig. 7-14) clearly show that also under  $CO_2$  atmosphere the rate-limiting reactions are dependent on the heating rate. An unambiguous identification of the rate-limiting mechanisms is not possible. At a low reaction progress there is no fit with any master curve, but for  $30\% < \alpha < 80\%$  the rate-limiting steps are R-type for the two intermediate heating rates and between F- and D-type for the highest heating rate. At  $\alpha = 80-90\%$  the curves change their curvature with a trend towards a diffusion model (D3). At this reaction progress a fast increase of  $E_{a\alpha}$  is observed (Fig. 7-9). All published data for decarbonisation of magnesite are for experiments using nitrogen or another inert gas atmosphere. The reported mechanisms range from three-dimensional (D3) diffusion (Liu *et al.* 2012), first order reaction (F1) (Demir *et al.* 2003) and contracting sphere model (R3) (Hurst 1991). The activation energies for the decomposition under nitrogen are lower than the values observed here (160 -300 kJ/mol).

The large influence of the heating rate on the reaction mechanism is compatible with former studies of Butt *et al.* (1996) and Bearat *et al.* (2002). They observed that the amount of

carbonates formed during the decomposition reaction of brucite ( $\text{CO}_2$  atmosphere) is both a function of temperature and  $\text{CO}_2$  pressure. However, the influence of the latter was not a field of interest in this study. Slow heating rates are more favourable for the formation of carbonates than fast heating rates as the dwell time in a certain temperature range is an inverse function of the heating rate itself. Thus, the rate-determining mechanisms must be a function of the heating rate, too. This hypothesis can be verified by the non-isothermal dataset of this study, which can best be seen in Figs. 7-13 and 7-14. A reaction governed by a contracting sphere model (R3) and three-dimensional diffusion is also compatible with findings of Butt *et al.* (1996). They use the R3 model for the main dehydroxylation interval (350 - 400 °C) only. At the highest temperature reached, i.e., an advanced reaction progress far beyond 50 % they justify a reaction complicated by diffusion with the formation of a nanocrystalline carbonate barrier around brucite crystallites which inhibit the outward diffusion of  $\text{H}_2\text{O}$  and the inward diffusion of  $\text{CO}_2$ . This process might be compatible with the latest stage seen in our data (Fig. 7-14 at  $\alpha \geq 80$  %).

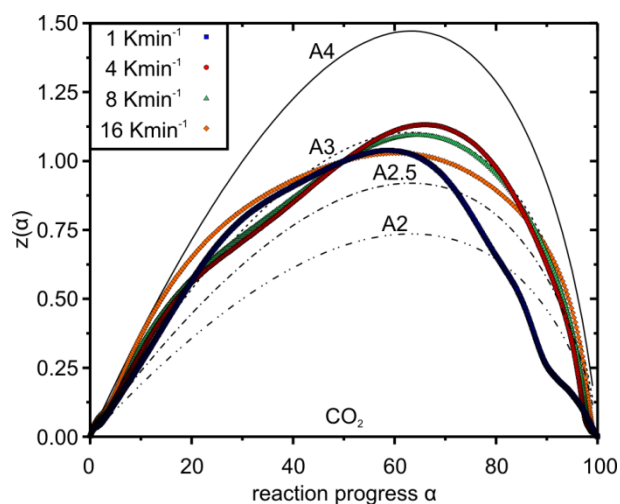


**Figure 7-13.** Comparison between theoretical  $z(\alpha)$  master plots and experimental curves obtained from non-isothermal TG data of the brucite dehydroxylation under  $\text{CO}_2$ .

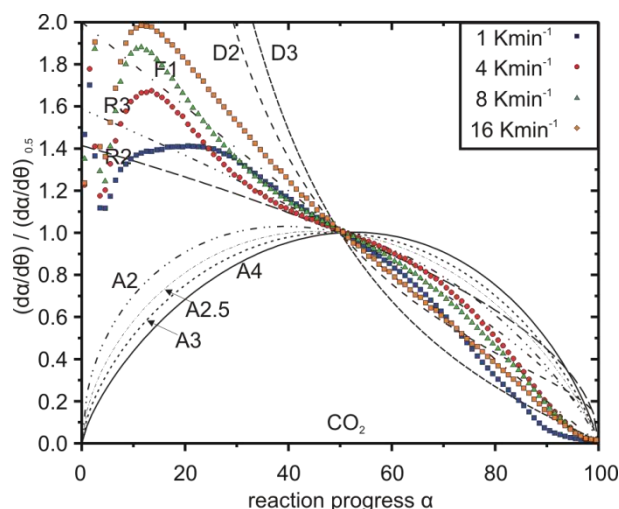


**Figure 7-14.** Comparison between generalised time master plots and experimental curves obtained from non-isothermal TG data of the brucite dehydroxylation under  $\text{CO}_2$ .

#### 7.4.3.2 Chrysotile

Multiple maxima in the reaction rate (Fig. 7-1) and the variation of  $E_a$  with  $\alpha$  (Fig. 7-5) are obvious signs, for a multi-step reaction dehydroxylation reaction of chrysotile, i.e., the rate-limiting step(s) changes with  $\alpha$ . The nature of possible rate-limiting steps have been identified by *in situ* HT XRD, Raman and FTIR spectroscopy as well as *ex situ* TEM analyses (Gualtieri *et al.* 2012; Trittschack and Grob ty 2013). The nanotube structure of chrysotile dehydroxylates from the outer, less curved sheets inwards. The first reaction products are a strongly disordered chrysotile-like phase plus a talc-like phase (Trittschack and Grob ty 2013).

The storage of OH groups within a talc-like intermediate phase might be causal for the multiple dehydroxylation peaks observable in TGA. The metastable talc-like phase starts to dehydroxylate towards the end of the overall dehydroxylation reaction (Trittschack and Grob ty 2013).

Figs. 7-15 and 7-16 demonstrate a heating rate dependent change in the reaction mechanism of the dehydroxylation, especially between the

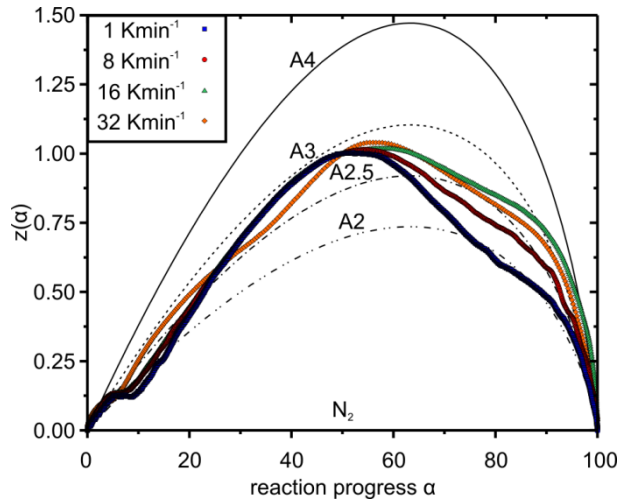


**Figure 7-15.** Comparison between theoretical  $z(\alpha)$  master plots and curves obtained from experimental non-isothermal TG data of the chrysotile dehydroxylation.

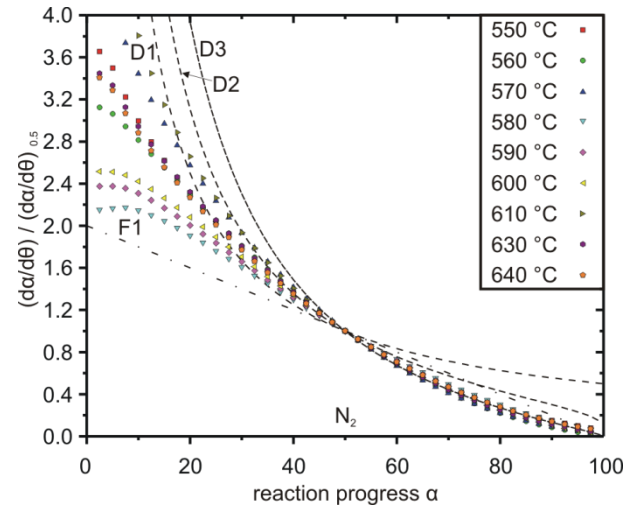


**Figure 7-17.** Comparison between generalised time master plots and curves obtained from experimental isothermal HT-XRD data of the chrysotile dehydroxylation.

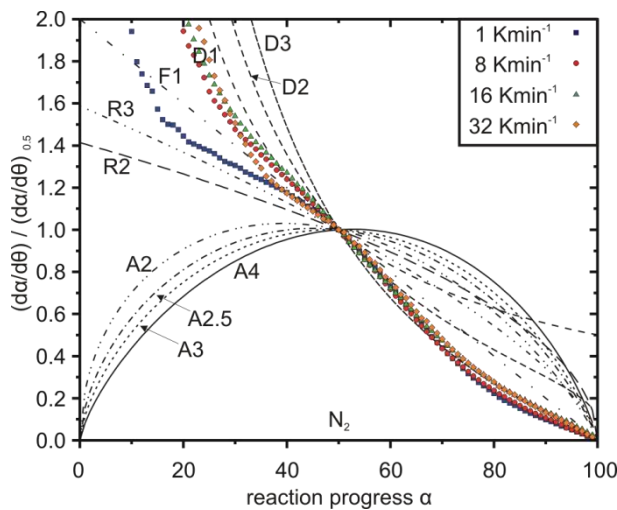


**Figure 7-16.** Comparison between generalised time master plots with curves obtained from experimental non-isothermal TG data of the chrysotile dehydroxylation.

reaction measured at the lowest heating rate and all other curves. This dependency primarily results from a variable amount of OH stored in the talc-like intermediate phase which is a function of temperature and heating rate, respectively. Such behaviour is similar to that observed during the brucite decomposition under  $\text{CO}_2$ . Thus, the

slower the heating rate the higher the amount of OH preserved during the primary dehydroxylation step of chrysotile which afterwards has to be released by the breakdown of the talc-like intermediate itself. This interpretation is sustained by compatible reaction sequences of lizardite and antigorite (Gualtieri *et al.* 2012).

The curve corresponding to a heating rate of 1 K/min is close to the R3 master curve ( $\alpha \leq 50\%$ ) and indicates, therefore, a reaction whose rate is controlled by an interface reaction. For all other heating rates (Fig. 7-16) the experimental curves at  $\alpha \leq 50\%$  are close for the master curve indicating a reaction controlled by one-dimensional diffusion. At a more advanced reaction progress ( $\alpha \geq 50\%$ ), non-isothermal (Fig. 7-16) and isothermal data (Fig. 7-17) point towards two- and three-dimensional diffusion models (D2 followed by D3), respectively. Thus, the evacuation of the (gaseous)  $\text{H}_2\text{O}$  products by diffusion seems to control the reaction rate. Such findings are consistent with former scenarios presented by Cattaneo *et al.* (2003) and Alizadehhesari *et al.* (2012). However, both investigations present some pit falls which

should be kept in mind when compared with our data. Alizadehhesari *et al.* (2012) studied a serpentine mixture without identifying the mineral composition in detail. As the crystal structure of serpentine minerals is quite different between the different polymorphs, e.g., flat lying lizardite, cylindrical chrysotile and wavy antigorite, kinetic data obtained from serpentine mixture will represent averages of the polymorphs present. Results of Cattaneo *et al.* (2003) are based on the Avrami-Erofe'ev approach applied to isothermal data only. Thus, similar to our own HT-XRD experiments, the kinetic parameters, especially those derived from high temperature runs, are extracted from a few data points only. The data are also extracted from a narrow temperature range, which disregards all processes occurring during the heating up cycle of the experiment. These outlined disadvantages might also be the reason for the scatter of the data at  $\alpha \leq \sim 30\%$  in Fig. 7-17 which do not fit any of the most commonly used kinetic models. Master plots using isothermal data often depict less (complex) reaction mechanisms than those of non-isothermal experiments. A potential nucleation and growth mechanism (An model) related to the appearance of disordered chrysotile or the talc-like intermediate phase might be invisible as long as such a rate controlling mechanism acts during the initial dehydroxylation and therefore the heating up of an isothermal run. Some indications for an An mechanism acting at an early stage ( $\alpha \leq \sim 10\%$ ) of the dehydroxylation are visible in the the  $z(\alpha)$  master plot (Fig. 7-15).

Three trends in the  $E_a$ - $\alpha$  plot (Fig. 7-5), i.e., decreasing  $E_a$  ( $15 \leq \alpha \leq 30\%$ ), almost constant  $E_a$  ( $30 \leq \alpha \leq 60/70\%$ ) and increasing  $E_a$  ( $60/70 \leq \alpha \leq 100\%$ ), coincide roughly with a matching of a D1, D2 and D3 mechanism in Fig. 7-16. As (in the present case) TG data mainly reflect the behaviour of  $H_2O$  and  $OH$ , respectively, one can derive a progressively more complex dehydroxylation reaction whose rate is determined by diffusion. Different parallel recombination reactions of adjacent hydroxyl

groups to form a water molecule have been proposed as first rate-determining steps in case of lizardite (Trittschack and Grob  ty 2012). Such a mechanism is affecting the octahedral sheet only (McKelvy *et al.* 2006; Trittschack and Grob  ty 2012). The local environment is, except the curvature of the layer, very similar in lizardite and chrysotile. Therefore, similarities in the reaction mechanisms are not surprising. Hydroxyl combination to form a  $H_2O$  molecule is also favoured as the first step of dehydroxylation of kaolinite (Sperinck *et al.* 2010; White *et al.* 2010), pyrophyllite (Molina-Montes *et al.* 2008) and muscovite (Guggenheim *et al.* 1987; Mazzucato *et al.* 1999).

The dehydroxylation mechanisms of phyllosilicates are generally described as (e.g., Redfern 1987; Belloto *et al.* 1995; Mazzucato *et al.* 1999; Cattaneo *et al.* 2003; Gualtieri and Ferrari 2006; Gridi-Bennadji and Blanchart 2007; Tokiwai and Nakashima 2010): 1) reaction of two adjacent hydroxyl groups to form one  $H_2O$  molecule or the formation of  $OH^-$  and/ or  $H^+$  species (D1, one-dimensional diffusion) plus an  $O^-$  vacancy which becomes structurally bounded; 2) diffusion of the resulting species to the interlayer, if necessary (D1 or D2, one- or two-dimensional diffusion); 3) diffusion along the interlayer or along (001) to the edges of a crystallite (D2, two-dimensional diffusion). The nature of the diffusing species is still disputed. Already Rouxhet (1970) stressed the possibility for a proton hopping mechanism instead of  $H_2O$  bulk diffusion during the dehydroxylation of mica. The spectroscopic attempt of Zhang *et al.* (2010) to identify  $H_2O$  as transport medium during dehydroxylation of a series of phyllosilicates failed. They suggest, therefore, a transport of hydroxyl and/ or protons to the sample surface where water molecules are finally formed. Nevertheless, first product species, whatever they are, have to leave the reaction site to keep on running the dehydroxylation progress

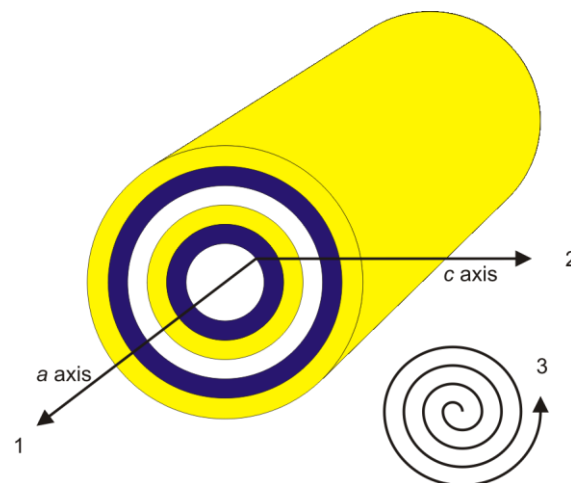
Possible/ theoretical diffusion paths in the peculiar structure of chrysotile are illustrated in



Fig. 7-18. In general, there are two possible directions along the interlayer, i.e., along the crystallographic  $a$  and  $b$  axes or a combination of both. A third possibility, usually labelled as radial diffusion, is across the TO-layers towards the inner tube channel or towards the outer wall of the nanotube/ edge of the chrysotile crystal. A radial diffusion towards the tube channel requires a subsequent diffusion along the tube channel towards the end of a chrysotile nanotube. But, these theoretical diffusion paths do not take into account the formation of a metastable talc-like intermediate and forsterite.

There are few examples in the literature showing the influence of product species on the dehydroxylation kinetics of phyllosilicates. Ortega *et al.* (2010) mentioned that the formation of metakaolinite during the dehydroxylation of kaolinite closes the interlamellar space initially used for the outward diffusion of  $H_2O$  molecules. They subsequently conclude that the change of diffusion paths after the closure is responsible for the change of the rate-determining step and the increase in  $E_a$ . However, they do not discuss details of such a change in the rate-determining step.

Caused by the appearance of an  $H_2O$  containing intermediate phase, we propose an alternative dehydroxylation scenario which is also explainable by the herein documented findings. A scheme summarising the model is illustrated in Fig. 7-19. At first, the dehydroxylation starts with a condensation of adjacent hydroxyl groups to form a  $H_2O$  molecule or the liberation of  $OH^-$  and/ or  $H^+$  to diffuse along the interlayer (one-dimensional diffusion). This process starts along the outer sheets as proposed by the chrysotile structure (Evans 2004). An inward migrating dehydroxylation front causes a predominantly amorphous outer layer (disordered chrysotile) which inhibits a bulk diffusion/ radial diffusion. This process is accompanied by a fast increase in  $E_a$  (until  $E_a = \max$  at  $\alpha = 10 - 20 \%$ ). Later on, the formation of a talc-like phase and forsterite take



**Figure 7-18.** Theoretical diffusion pathways for the crystal structure of normal chrysotile/ clinochrysotile; 1 - along the interlayer and the tube channel, respectively; 2 - radial diffusion parallel to the crystallographic  $c$  axis, i.e., vertical to the TO layers; 3 - 'circular' diffusion along the interlayer ( $b$  axis or a mixture between  $a$  and  $b$  axis).

place within the inward moving amorphous layer (Trittschack and Grob ty 2013). The formation of first product phases enables one-dimensional diffusion along interlayer remnants of chrysotile and two-dimensional diffusion along newly formed grain boundaries. The increase in the relative amount of nucleation sites of forsterite and the talc-like phase increase the amount of grain boundaries. This process accelerates the diffusion and causes therefore a decreasing tendency in  $E_a$ . The final increase in  $E_a$  ( $\alpha \geq 60 \%$ ) and the simultaneous change from a two-dimensional mechanism to a three-dimensional diffusion (Figs. 7-16 and 7-17) might be caused by the final dehydroxylation of the inner sheets and the breakdown of the talc-like intermediate itself. The proposed multi-step dehydroxylation mechanisms do not exclude the theoretical diffusion pathways in primary chrysotile, but focus on interface/ grain boundary related diffusion pathways between the primary host structure and newly formed phases (talc-like intermediate and forsterite).

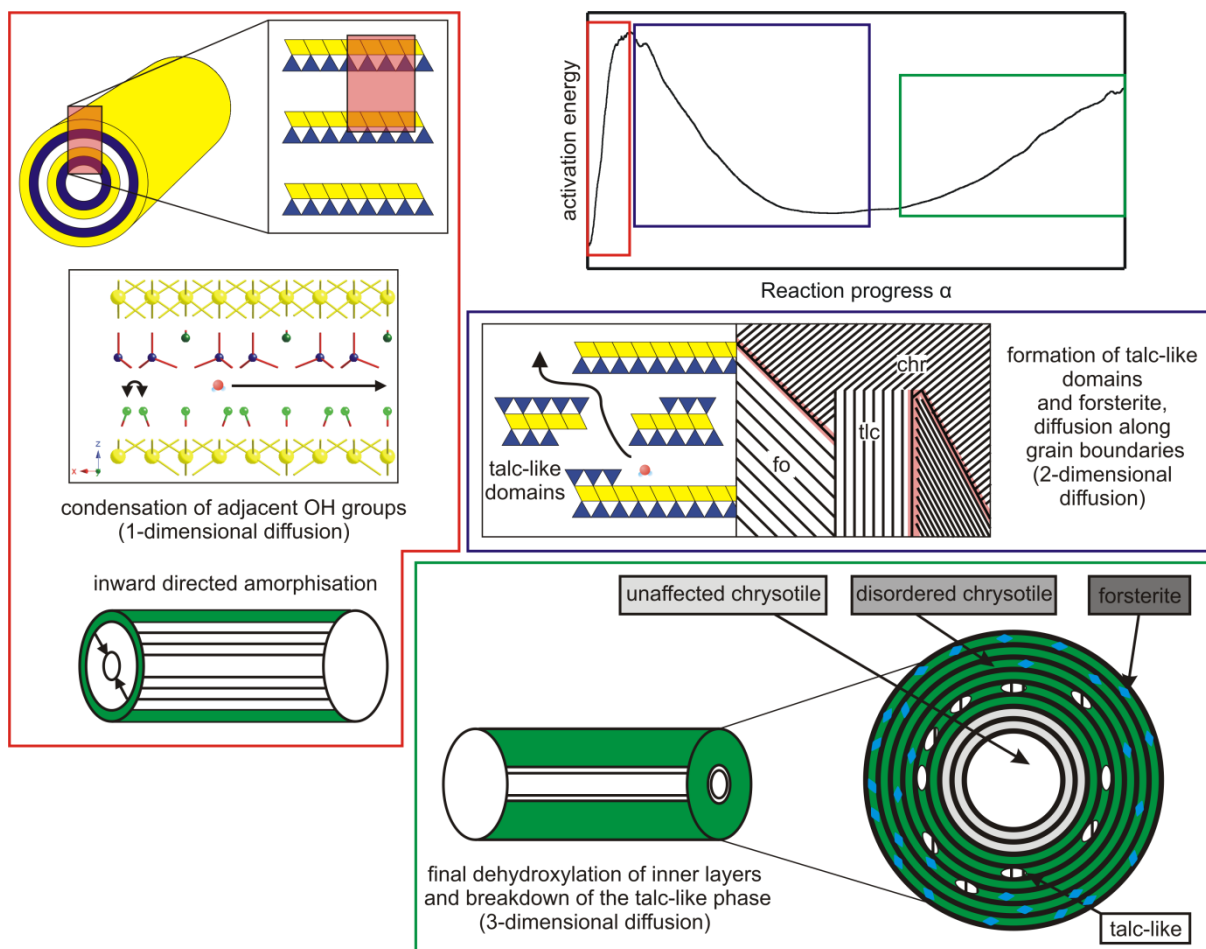


**Figure 7-19.** Schematic sketch summarising the proposed multi-step reaction mechanism scenario of the chrysotile dehydroxylation. The colour-coded windows correspond to three different stages of the  $E_a$  versus reaction progress graph. Although they are acting simultaneously, the proposed mechanisms are interpreted as the rate-determining mechanism for the respective stage of the reaction.

High-temperature dehydroxylation experiments of lizardite examined by infrared spectroscopy have shown that some of the liberated OH groups are trapped in nominally anhydrous forsterite (Tritschack unpublished work). Similar observations were made during dehydroxylation experiments of kaolinite where more than 10 % persist within the structure (MacKenzie *et al.* 1985; Watanabe *et al.* 1987). Those OH remnants are difficult to remove within the temperature range of the primary dehydroxylation reaction and may also contribute to a significant increase in  $E_a$ .

## 7.5 CONCLUDING REMARKS

Reaction kinetics of the thermally induced decomposition/ dehydroxylation of chrysotile and brucite were investigated by non-isothermal TG and isothermal HT-XRD analyses. The kinetic data obtained from the two analytical techniques are compatible to each other, i.e., the evolution of  $E_{aa}$ , with  $\alpha$ , and the rate-limiting steps derived from master plots are similar, for both chrysotile and brucite, respectively. Chrysotile dehydroxylation experiments gave variable  $E_{aa}$  values in the range of around 250 – 300 kJ/mol (TG data) and 250 – 380 kJ/mol (HT-XRD). This evolution is compatible with a change of the rate-limiting step with  $\alpha$ . Brucite decomposition

under nitrogen shows a decreasing trend for  $E_a$  with  $\alpha$  in TG data, while HT-XRD data point to a slightly increasing trend with activation energies in the range of 110 - 160 kJ/mol. A larger variation in  $E_a$  versus  $\alpha$  is seen in data obtained from brucite dehydroxylation experiments under  $\text{CO}_2$  atmosphere. There, activation energies are significantly increased with values of around 270 kJ/mol at an early stage of the reaction ( $\alpha = 10$  %) which slowly decrease to around 250 kJ/mol ( $\alpha = 50$  %) before rising up again to values larger than 350 kJ/mol ( $\alpha = 90$  %). Contrary to that, HT-XRD derived kinetic data illustrate a linearly decreasing trend of  $E_a$  versus  $\alpha$  with  $E_a = 220$  kJ/mol ( $\alpha = 10$  %) to 180 kJ/mol ( $\alpha = 90$  %). Differences between TG and HT-XRD data are interpreted as resulting from different processes studied, i.e., brucite dehydroxylation in HT-XRD data versus brucite-Mg-carbonate bulk decomposition in TG data.

The attempt to compare acquired kinetic data with theoretical reaction models in  $z(\alpha)$  master

plots failed in case of multi-step reaction sequences as observed during chrysotile dehydroxylation and brucite decomposition under  $\text{CO}_2$ . The  $z(\alpha)$  master plot approach of the brucite dehydroxylation under  $\text{N}_2$  yields a good fit with A-type master curves, although the reaction is not controlled by one and the same step across the entire reaction progress range. This is a strong caveat against using  $z(\alpha)$  master plots in cases of variable  $E_a$  versus  $\alpha$ , even in case of brucite whose reaction progress resolved  $E_a$  is less dynamic than that of chrysotile. The method may yield good fits, which are, however, pure coincidence. In contrast to that, master plots using the generalised time are better suited to unravel multiple reaction mechanisms in case of the dehydroxylation of chrysotile and brucite under nitrogen atmosphere. Mechanistic information taken from these plots are also compatible with former literature studies. However, corresponding data of the brucite decomposition under  $\text{CO}_2$  are less consistent and difficult to interpret.



## CONCLUSIONS AND PERSPECTIVES

---

The scientific articles compiled in this PhD thesis brought some light into the controversial debate about the dehydroxylation of lizardite and chrysotile and the way to interpret the results of kinetic analyses of these reactions. The two FTIR and Raman studies in Chapters 5 and 6 have focussed on the identification of reaction intermediates, such as the talc-like phase, and final reaction products, i.e., forsterite. Although the idea of an intermediate phase with talc-like character occurring during the dehydroxylation of serpentine minerals is not totally new, this thesis delivered first unambiguous results of such a phase by studying the phase transformations *in situ* and with the help of vibrational spectroscopy. Most of the former investigations on this topic have been realised with X-ray diffraction based techniques alone (see references in Chapters 5 and 6), which gave only very limited (one) peak information on the nature of this phase. The present spectroscopic results decipher much better possible candidates. By the chosen *in situ* spectroscopy methods it was possible to study the evolution of H<sub>2</sub>O/ OH related modes of the present crystal structure(s) in detail. The identification of OH in the framework of the talc-like phase, which is best seen during the dehydroxylation of chrysotile (Chapter 6), but probably present during the lizardite dehydroxylation also (Chapter 5), is of major importance for kinetic studies, especially for those performed with thermogravimetric techniques (Chapter 4 and 7).

The kinetic studies presented in this thesis (Chapters 4 and 7) are dealing with dehydroxylation reactions of lizardite, chrysotile and brucite. All reactions were studied by X-ray powder diffraction and thermogravimetry in

order to treat resulting data with the classical Avrami-Erofe'ev approach and more advanced, isoconversional approaches. The latter revealed the weakness of the Avrami-Erofe'ev approach by showing the complexity of ongoing reactions (e.g., variable  $E_a$ , multiple rate-determining steps) even in case of brucite. Moreover, it was possible to demonstrate that the Avrami-Erofe'ev approach is an improper method when trying to decipher complex and multi-step reaction mechanisms. The results presented in Chapters 4 to 7 clearly show that the dehydroxylation of lizardite and chrysotile are multi-step reactions/ reactions with more than one rate-determining step.

The study on dehydroxylation kinetics of brucite was added to Chapter 7 in order to use a 'standard' material, i.e., a comprehensively studied phase regarding the phase transformation reactions and reaction kinetics. This was done to test the application of master plot techniques when trying to unravel the change of rate-limiting steps/ mechanisms in multi-step dehydroxylation reactions.

The final outcome of the herein presented kinetic and phase transformation studies is promising in respect of further work devoted to the dehydroxylation of phyllosilicates in general and the deciphering of reaction mechanisms in particular. There is some hope that the geoscientific community will recognize the importance of using model free methods, that most reaction kinetics are controlled by more than one rate-limiting step and that, therefore, single-step force-fitting methods are an unsuitable tool to make general statements about the rate control of complex reactions.

## APPENDIX I

The thermocouple of the PW1830 diffractometer was regularly calibrated by using the melting points of four different salts:  $\text{NaNO}_3$  ( $T_m = 306^\circ\text{C}$ ),  $\text{Ba}(\text{NO}_3)_2$  ( $T_m = 592^\circ\text{C}$ ),  $\text{KCl}$  ( $T_m = 790^\circ\text{C}$ ) and  $\text{NaCl}$  ( $T_m = 801^\circ\text{C}$ ). Per definition, the complete loss of the strongest XRD peak of the respective salt was set as the melting point  $T_m$ . For this, the temperature of the thermocouple was stepwise increased by 2 K increments until finishing the melting process. The results of this standard calibration routine are presented in Figures A1-1 to A1-6 and Tables A1-1 to A1-6.

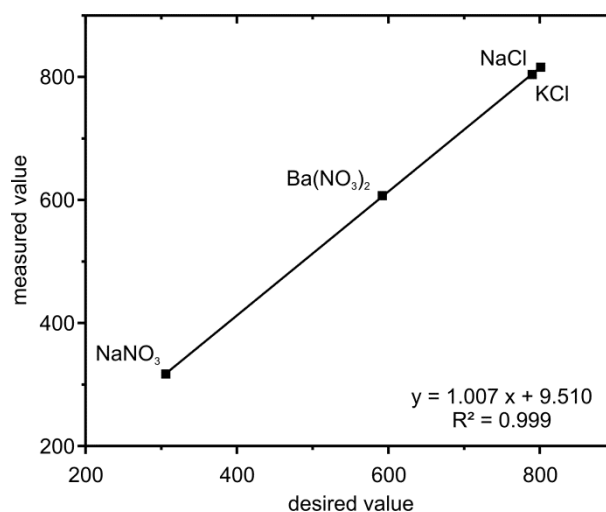


**Figure A1-2.** Resulting linear correlation chart of the temperature calibration; scale units:  $[\text{°C}]$  (October 2009).

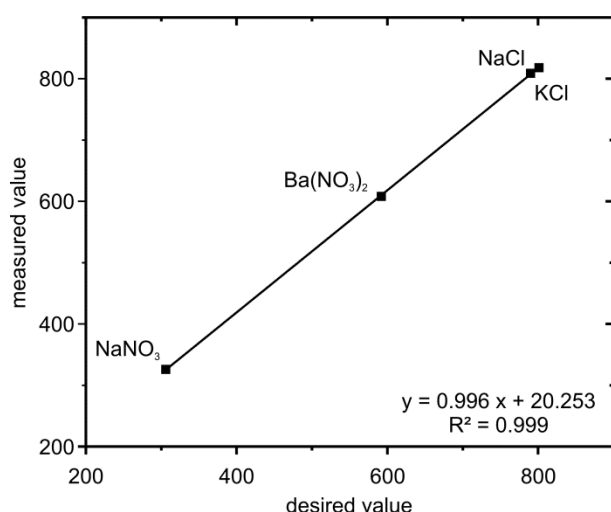


**Figure A1-1.** Resulting linear correlation chart of the temperature calibration; scale units:  $[\text{°C}]$  (July 2009).

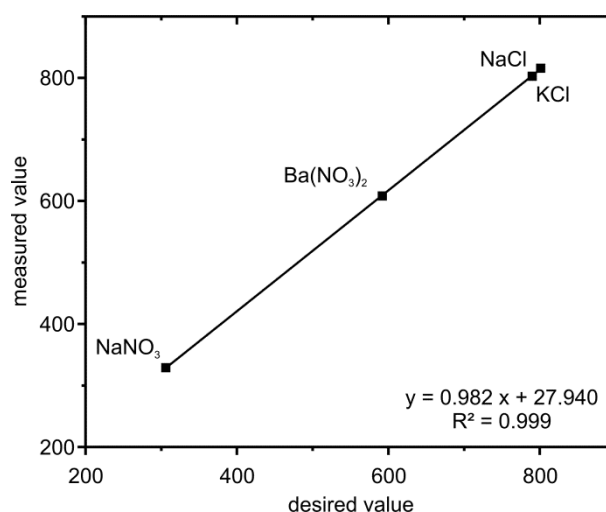


**Figure A1-3.** Resulting linear correlation chart of the temperature calibration; scale units:  $[\text{°C}]$  (January 2010).

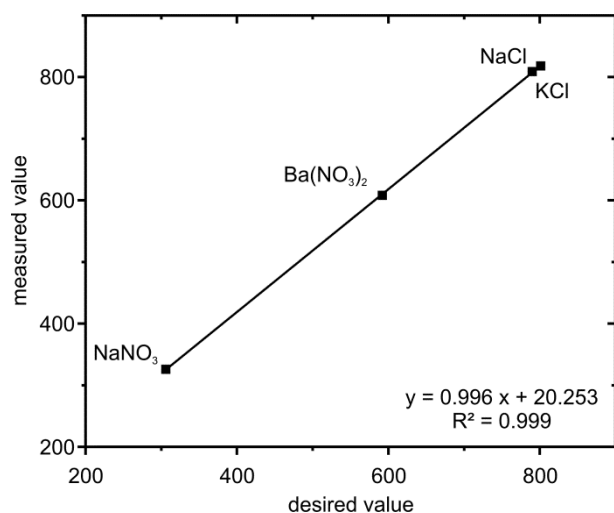


**Figure A1-4.** Resulting linear correlation chart of the temperature calibration; scale units: [°C] (May 2010).

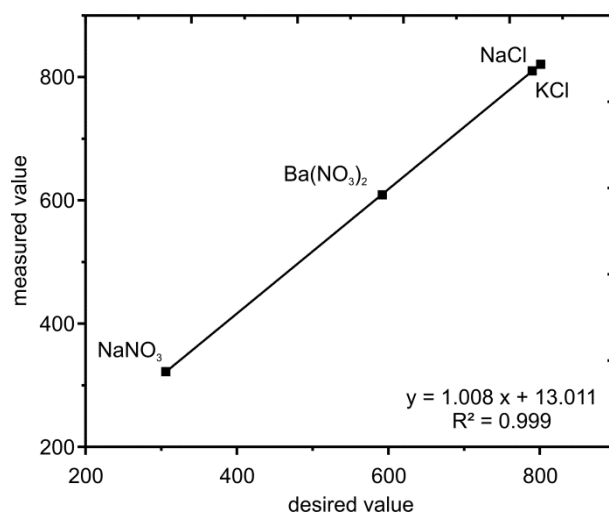


**Figure A1-6.** Resulting linear correlation chart of the temperature calibration; scale units: [°C] (October 2011).

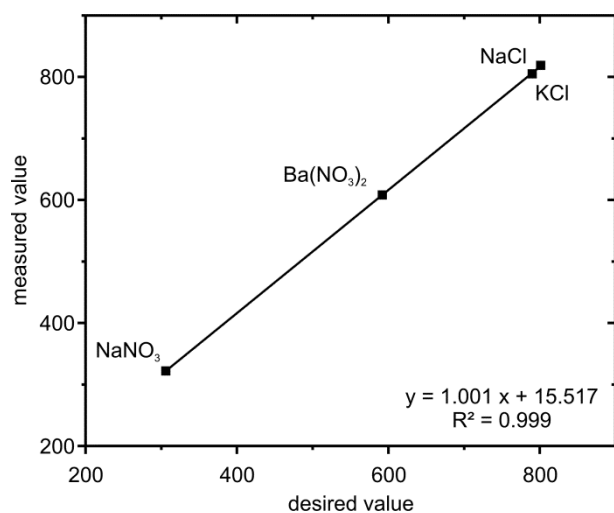


**Figure A1-5.** Resulting linear correlation chart of the temperature calibration; scale units: [°C] (January 2011).

calibration substance	$T_m$ [°C] desired	$T_m$ [°C] measured 1 <sup>st</sup>	$T_m$ [°C] measured 2 <sup>nd</sup>	$T_m$ [°C] measured 3 <sup>rd</sup>	$\emptyset$ [°C] measured
NaNO <sub>3</sub>	306	325	324	324	324
Ba(NO <sub>3</sub> ) <sub>2</sub>	592	609	607	604	607
KCl	790	803	803	804	803
NaCl	801	816	814	815	815

**Table A1-1.** Temperature calibration data of the Pt-10%RhPt thermocouple attached to the HTK10 (Anton Paar/ Austria) of the PW1830 diffractometer, July 2009.

calibration substance	$T_m$ [°C] desired	$T_m$ [°C] measured 1 <sup>st</sup>	$T_m$ [°C] measured 2 <sup>nd</sup>	$T_m$ [°C] measured 3 <sup>rd</sup>	$\emptyset$ [°C] measured
NaNO <sub>3</sub>	306	318	316	316	317
Ba(NO <sub>3</sub> ) <sub>2</sub>	592	608	606	608	607
KCl	790	806	805	802	804
NaCl	801	815	817	815	816

**Table A1-2.** Temperature calibration data of the Pt-10%RhPt thermocouple attached to the HTK10 (Anton Paar/ Austria) of the PW1830 diffractometer, October 2009.

calibration substance	$T_m$ [°C] desired	$T_m$ [°C] measured 1 <sup>st</sup>	$T_m$ [°C] measured 2 <sup>nd</sup>	$T_m$ [°C] measured 3 <sup>rd</sup>	$\emptyset$ [°C] measured
NaNO <sub>3</sub>	306	328	330	328	329
Ba(NO <sub>3</sub> ) <sub>2</sub>	592	606	609	608	608
KCl	790	802	800	806	803
NaCl	801	816	815	816	816

**Table A1-3.** Temperature calibration data of the Pt-10%RhPt thermocouple attached to the HTK10 (Anton Paar/ Austria) of the PW1830 diffractometer, January 2010.

calibration substance	$T_m$ [°C] desired	$T_m$ [°C] measured 1 <sup>st</sup>	$T_m$ [°C] measured 2 <sup>nd</sup>	$T_m$ [°C] measured 3 <sup>rd</sup>	$T_m$ [°C] measured 4 <sup>th</sup>	$\emptyset$ [°C] measured
NaNO <sub>3</sub>	306	321	329	325	327	326
Ba(NO <sub>3</sub> ) <sub>2</sub>	592	609	609	607		608
KCl	790	809	809	807	809	809
NaCl	801	815	819	819		818

**Table A1-4.** Temperature calibration data of the Pt-10%RhPt thermocouple attached to the HTK10 (Anton Paar/ Austria) of the PW1830 diffractometer, May 2010.

calibration substance	$T_m$ [°C] desired	$T_m$ [°C] measured 1 <sup>st</sup>	$T_m$ [°C] measured 2 <sup>nd</sup>	$T_m$ [°C] measured 3 <sup>rd</sup>	$\emptyset$ [°C] measured
NaNO <sub>3</sub>	306	322	324	320	322
Ba(NO <sub>3</sub> ) <sub>2</sub>	592	609	608	606	608
KCl	790	806	802	806	805
NaCl	801	818	820	818	819

**Table A1-5.** Temperature calibration data of the Pt-10%RhPt thermocouple attached to the HTK10 (Anton Paar/ Austria) of the PW1830 diffractometer, January 2011.

calibration substance	$T_m$ [°C] desired	$T_m$ [°C] measured 1 <sup>st</sup>	$T_m$ [°C] measured 2 <sup>nd</sup>	$T_m$ [°C] measured 3 <sup>rd</sup>	$\emptyset$ [°C] measured
NaNO <sub>3</sub>	306	320	324	322	322
Ba(NO <sub>3</sub> ) <sub>2</sub>	592	610	610	608	609
KCl	790	810	810	810	810
NaCl	801	822	822	820	821

**Table A1-6.** Temperature calibration data of the Pt-10%RhPt thermocouple attached to the HTK10 (Anton Paar/ Austria) of the PW1830 diffractometer, October 2011.

## APPENDIX II

A summary of the outcome of serpentine dehydroxylation experiments performed with the PW1830 high-temperature X-ray diffractometer and treated by the Avrami-Erofe'ev approach are presented in Tables A2-1 to A2-15 and Figures A2-1 to A2-15. Milled and sieved lizardite samples correspond to two different subsamples which are comprehensively described in Chapter 4.

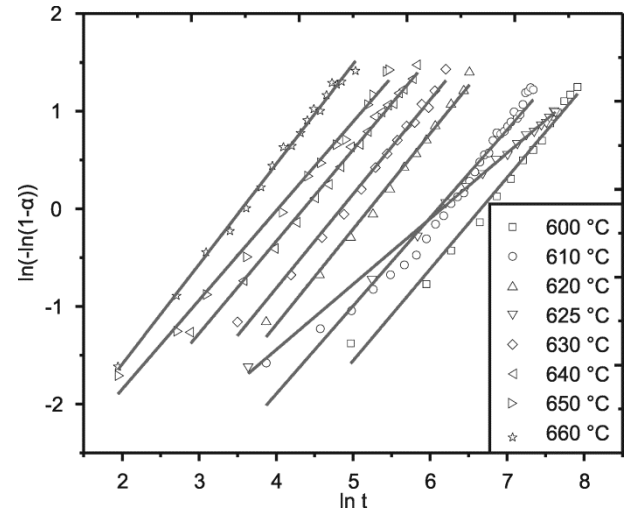


**Figure A2-2.** Arrhenius plot (ln-ln plot) of the 2<sup>nd</sup> lizardite dehydroxylation experiment used for the calculation of kinetic parameters (Avrami-Erofe'ev method) listed in Table A2-2; milled lizardite, no purging gas.

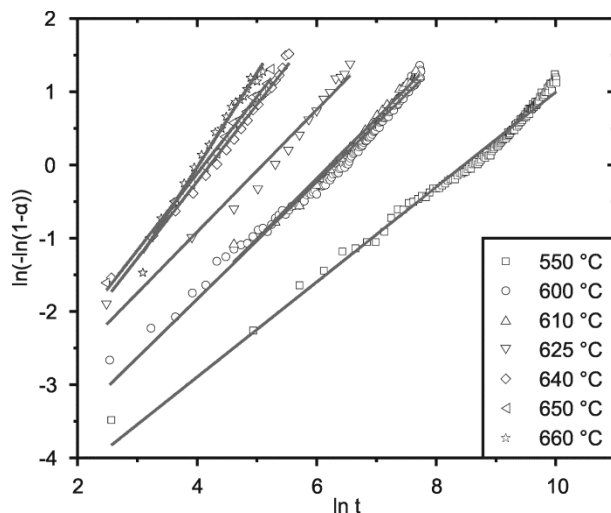


**Figure A2-1.** Arrhenius plot (ln-ln plot) of the 1<sup>st</sup> lizardite dehydroxylation experiment used for the calculation of kinetic parameters (Avrami-Erofe'ev method) listed in Table A2-1; milled lizardite, no purging gas.

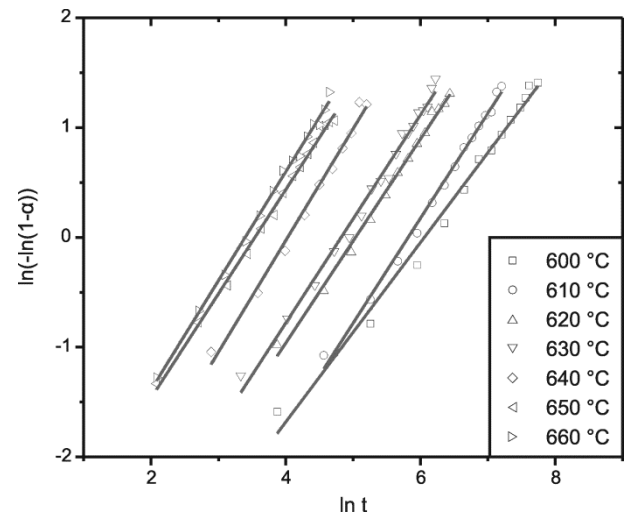


**Figure A2-3.** Arrhenius plot (ln-ln plot) of the 3<sup>rd</sup> lizardite dehydroxylation experiment used for the calculation of kinetic parameters (Avrami-Erofe'ev method) listed in Table A2-3; sieved lizardite, no purging gas.

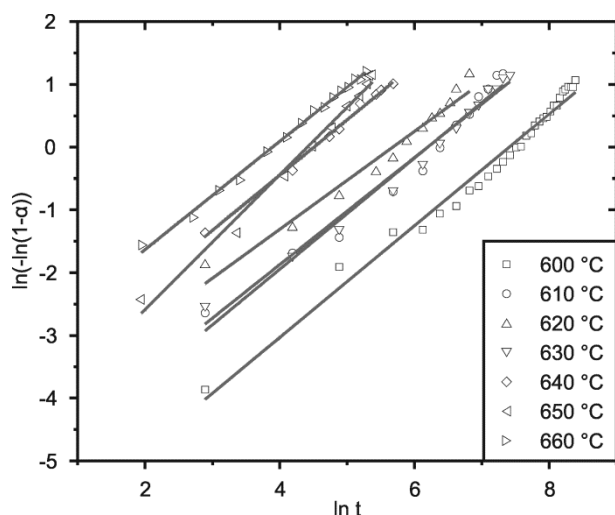


**Figure A2-4.** Arrhenius plot (ln-ln plot) of the 4<sup>th</sup> lizardite dehydroxylation experiment used for the calculation of kinetic parameters (Avrami-Erofe'ev method) listed in Table A2-4; milled lizardite, no purging gas.

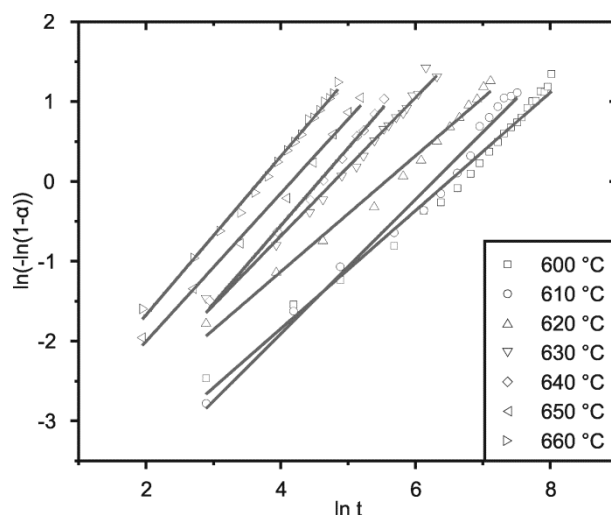


**Figure A2-6.** Arrhenius plot (ln-ln plot) of the 6<sup>th</sup> lizardite dehydroxylation experiment used for the calculation of kinetic parameters (Avrami-Erofe'ev method) listed in Table A2-6; sieved lizardite, no purging gas.

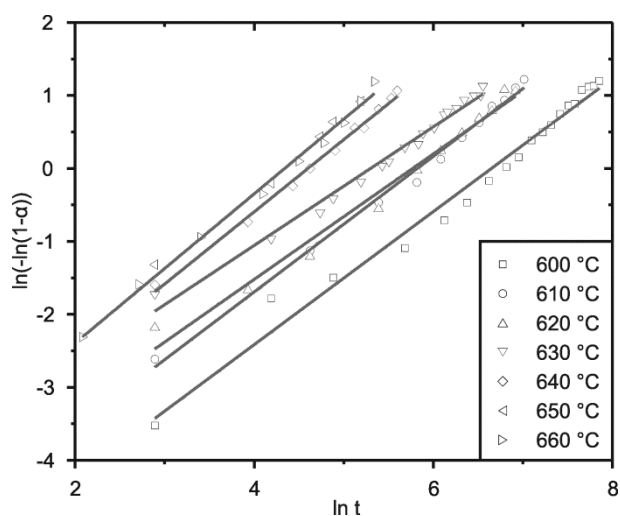


**Figure A2-5.** Arrhenius plot (ln-ln plot) of the 5<sup>th</sup> lizardite dehydroxylation experiment used for the calculation of kinetic parameters (Avrami-Erofe'ev method) listed in Table A2-5; milled lizardite, no purging gas.

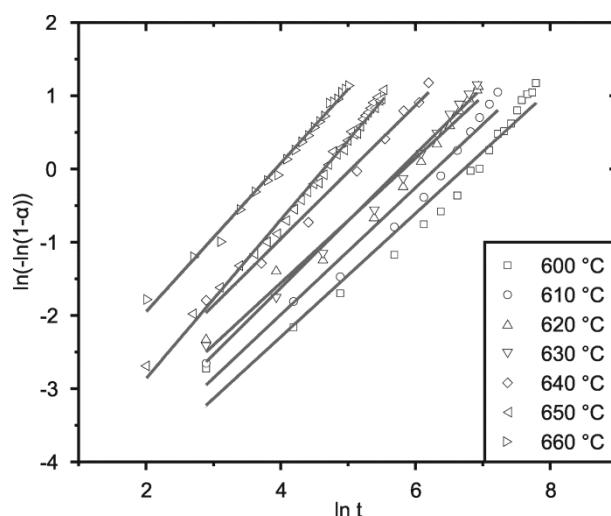


**Figure A2-7.** Arrhenius plot (ln-ln plot) of the 7<sup>th</sup> lizardite dehydroxylation experiment used for the calculation of kinetic parameters (Avrami-Erofe'ev method) listed in Table A2-7; milled lizardite, no purging gas.

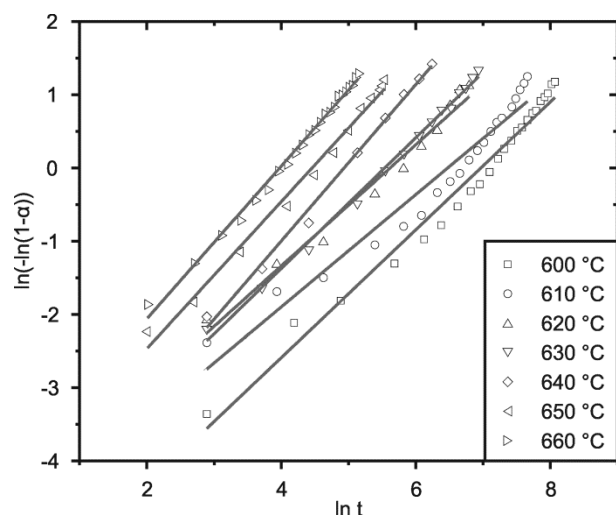


**Figure A2-8.** Arrhenius plot (ln-ln plot) of the 8<sup>th</sup> lizardite dehydroxylation experiment used for the calculation of kinetic parameters (Avrami-Erofe'ev method) listed in Table A2-8; milled lizardite, no purging gas.

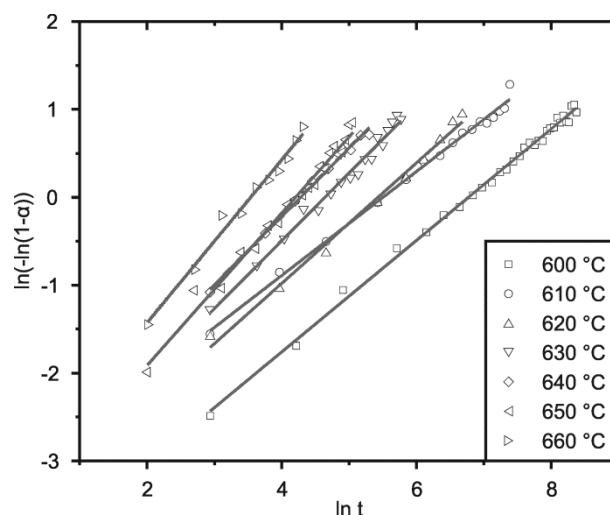


**Figure A2-10.** Arrhenius plot (ln-ln plot) of the 10<sup>th</sup> lizardite dehydroxylation experiment used for the calculation of kinetic parameters (Avrami-Erofe'ev method) listed in Table A2-10; milled lizardite, 200 ml/min N<sub>2</sub>.

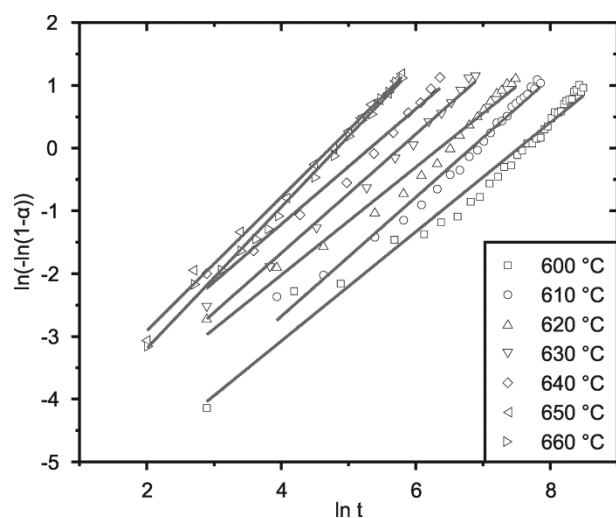


**Figure A2-9.** Arrhenius plot (ln-ln plot) of the 9<sup>th</sup> lizardite dehydroxylation experiment used for the calculation of kinetic parameters (Avrami-Erofe'ev method) listed in Table A2-9; milled lizardite, no purging gas.

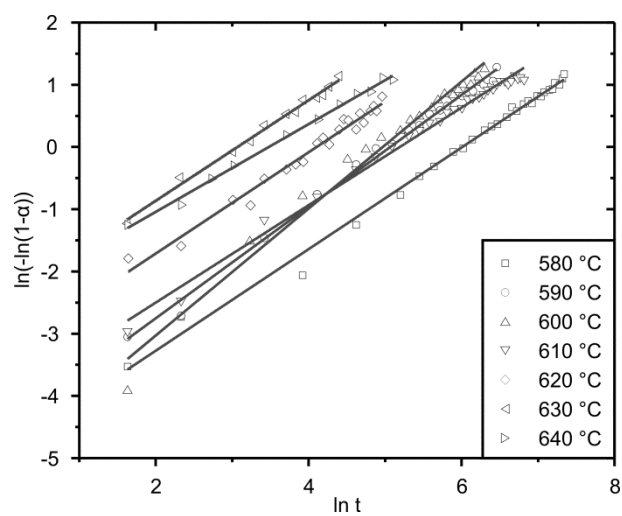


**Figure A2-11.** Arrhenius plot (ln-ln plot) of the 1<sup>st</sup> chrysotile dehydroxylation experiment used for the calculation of kinetic parameters (Avrami-Erofe'ev method) listed in Table A2-11; no purging gas.



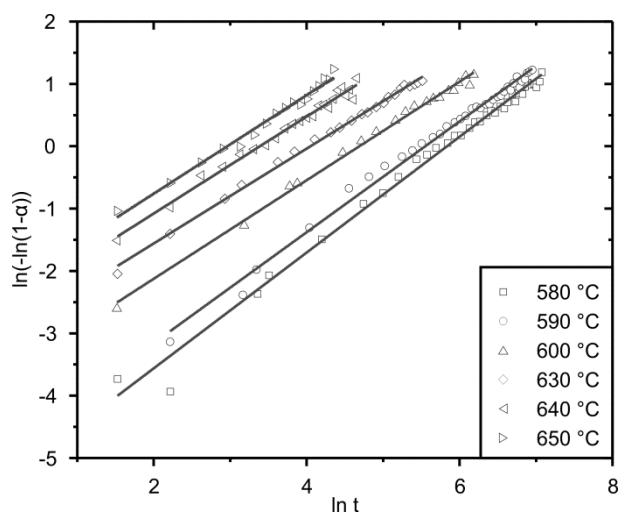


**Figure A2-12.** Arrhenius plot ( $\ln\text{-}\ln$  plot) of the 2<sup>nd</sup> chrysotile dehydroxylation experiment used for the calculation of kinetic parameters (Avrami-Erofe'ev method) listed in Table A2-12; no purging gas

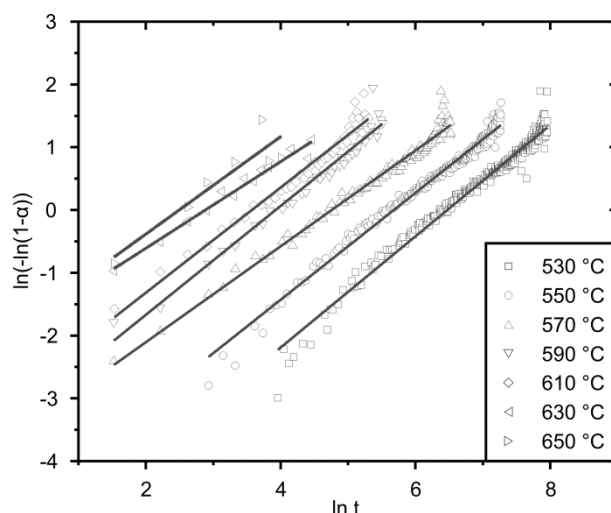


**Figure A2-14.** Arrhenius plot ( $\ln\text{-}\ln$  plot) of the 4<sup>th</sup> chrysotile dehydroxylation experiment used for the calculation of kinetic parameters (Avrami-Erofe'ev method) listed in Table A2-14; 200 ml/min  $\text{N}_2$ .

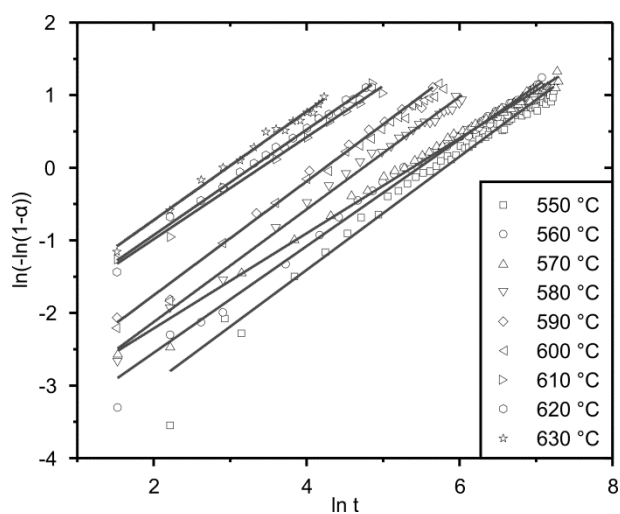


**Figure A2-13.** Arrhenius plot ( $\ln\text{-}\ln$  plot) of the 3<sup>rd</sup> chrysotile dehydroxylation experiment used for the calculation of kinetic parameters (Avrami-Erofe'ev method) listed in Table A2-13; 200 ml/min  $\text{N}_2$ .

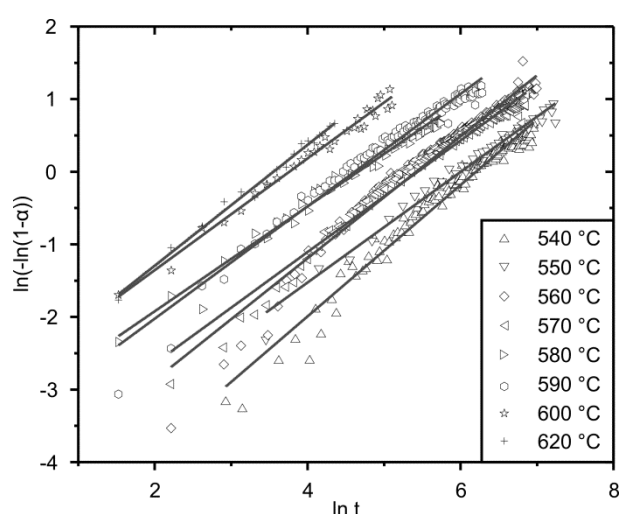


**Figure A2-15.** Arrhenius plot ( $\ln\text{-}\ln$  plot) of the 5<sup>th</sup> chrysotile dehydroxylation experiment used for the calculation of kinetic parameters (Avrami-Erofe'ev method) listed in Table A2-15; 200 ml/min  $\text{N}_2$ .

$T$ [°C]	$1/T$ [K <sup>-1</sup> ]	$n$	$k$	$\ln k$	$E_a$ [kJ/mol]
550	1.21E-03	0.65	2.11E-04	-8.46	281 $R^2 = 0.945$
600	1.15E-03	0.80	1.85E-03	-6.29	
610	1.13E-03	0.82	1.98E-03	-6.23	
625	1.11E-03	1.17	1.26E-02	-4.37	
640	1.10E-03	1.05	1.48E-02	-4.21	
650	1.08E-03	1.05	1.64E-02	-4.11	
660	1.07E-03	1.20	1.87E-02	-3.98	

**Table A2-1.** Summary of kinetic parameters of the first high-temperature X-ray diffraction dehydroxylation experiment of lizardite (milled) realised without using a purging gas.

$T$ [°C]	$1/T$ [K <sup>-1</sup> ]	$n$	$k$	$\ln k$	$E_a$ [kJ/mol]
600	1.15E-03	0.94	1.28E-03	-6.66	347 $R^2 = 0.984$
610	1.13E-03	0.90	2.24E-03	-6.10	
620	1.12E-03	0.98	5.45E-03	-5.21	
625	1.11E-03	0.67	2.55E-03	-5.97	
630	1.11E-03	0.97	7.89E-03	-4.84	
640	1.10E-03	0.94	1.28E-02	-4.36	
650	1.08E-03	0.91	1.79E-02	-4.02	
660	1.07E-03	1.02	2.86E-02	-3.55	

**Table A2-2.** Summary of kinetic parameters of the second high-temperature X-ray diffraction dehydroxylation experiment of lizardite (milled) realised without using a purging gas.

$T$ [°C]	$1/T$ [K <sup>-1</sup> ]	$n$	$k$	$\ln k$	$E_a$ [kJ/mol]
600	1.15E-03	0.91	2.10E-03	-6.17	336 $R^2 = 0.981$
610	1.13E-03	0.96	2.98E-03	-5.82	
620	1.12E-03	0.93	6.50E-03	-5.04	
630	1.11E-03	0.95	8.05E-03	-4.82	
640	1.10E-03	0.99	1.77E-02	-4.04	
650	1.08E-03	0.95	2.90E-02	-3.54	
660	1.07E-03	0.99	3.35E-02	-3.40	

**Table A2-3.** Summary of kinetic parameters of the third high-temperature X-ray diffraction dehydroxylation experiment of lizardite (sieved) realised without using a purging gas.

$T$ [°C]	$1/T$ [K <sup>-1</sup> ]	$n$	$k$	$\ln k$	$E_a$ [kJ/mol]
600	1.15E-03	0.89	6.06E-04	-7.41	370 $R^2 = 0.890$
610	1.13E-03	0.89	2.03E-03	-6.20	
620	1.12E-03	0.78	3.42E-03	-5.68	
630	1.11E-03	0.85	2.04E-03	-6.20	
640	1.10E-03	0.88	1.10E-02	-4.51	
650	1.08E-03	1.07	1.22E-02	-4.41	
660	1.07E-03	0.86	2.04E-02	-3.89	

**Table A2-4.** Summary of kinetic parameters of the fourth high-temperature X-ray diffraction dehydroxylation experiment of lizardite (milled) realised without using a purging gas.

$T$ [°C]	$1/T$ [K <sup>-1</sup> ]	$n$	$k$	$\ln k$	$E_a$ [kJ/mol]
600	1.15E-03	0.91	1.30E-03	-6.65	271 $R^2 = 0.945$
610	1.13E-03	0.93	2.96E-03	-5.82	
620	1.12E-03	0.86	3.12E-03	-5.77	
630	1.11E-03	0.81	5.00E-03	-5.30	
640	1.10E-03	1.00	1.01E-02	-4.59	
650	1.08E-03	0.98	1.38E-02	-4.28	
660	1.07E-03	1.02	1.30E-02	-4.34	

**Table A2-5.** Summary of kinetic parameters of the fifth high-temperature X-ray diffraction dehydroxylation experiment of lizardite (milled) realised without using a purging gas.

$T$ [°C]	$1/T$ [K <sup>-1</sup> ]	$n$	$k$	$\ln k$	$E_a$ [kJ/mol]
600	1.15E-03	0.74	1.51E-03	-6.49	323 $R^2 = 0.988$
610	1.13E-03	0.86	2.20E-03	-6.12	
620	1.12E-03	0.73	3.85E-03	-5.56	
630	1.11E-03	0.87	8.33E-03	-4.79	
640	1.10E-03	0.97	1.04E-02	-4.57	
650	1.08E-03	0.93	1.56E-02	-4.16	
660	1.07E-03	0.99	2.51E-02	-3.68	

**Table A2-6.** Summary of kinetic parameters of the sixth high-temperature X-ray diffraction dehydroxylation experiment of lizardite (sieved) realised without using a purging gas.

$T$ [°C]	$1/T$ [K <sup>-1</sup> ]	$n$	$k$	$\ln k$	$E_a$ [kJ/mol]
600	1.15E-03	0.84	1.20E-03	-6.72	325 $R^2 = 0.943$
610	1.13E-03	0.87	1.85E-03	-6.29	
620	1.12E-03	0.85	2.94E-03	-5.83	
630	1.11E-03	0.91	3.10E-03	-5.78	
640	1.10E-03	0.91	6.44E-03	-5.04	
650	1.08E-03	1.08	9.66E-03	-4.64	
660	1.07E-03	1.10	2.73E-02	-3.60	

**Table A2-7.** Summary of kinetic parameters of the seventh high-temperature X-ray diffraction dehydroxylation experiment of lizardite (milled) realised without using a purging gas.

$T$ [°C]	$1/T$ [K <sup>-1</sup> ]	$n$	$k$	$\ln k$	$E_a$ [kJ/mol]
600	1.15E-03	0.87	9.43E-04	-6.97	331 $R^2 = 0.985$
610	1.13E-03	0.77	1.56E-03	-6.46	
620	1.12E-03	0.83	3.64E-03	-5.61	
630	1.11E-03	0.89	3.94E-03	-5.54	
640	1.10E-03	1.07	7.21E-03	-4.93	
650	1.08E-03	1.01	1.16E-02	-4.46	
660	1.07E-03	1.04	1.88E-02	-3.97	

**Table A2-8.** Summary of kinetic parameters of the eighth high-temperature X-ray diffraction dehydroxylation experiment of lizardite (milled) realised without using a purging gas.

$T$ [°C]	$1/T$ [K <sup>-1</sup> ]	$n$	$k$	$\ln k$	$E_a$ [kJ/mol]
600	1.15E-03	0.87	5.36E-04	-7.53	324 $R^2 = 0.968$
610	1.13E-03	1.06	1.06E-03	-6.85	
620	1.12E-03	0.86	1.74E-03	-6.35	
630	1.11E-03	0.95	3.14E-03	-5.77	
640	1.10E-03	0.92	4.89E-03	-5.32	
650	1.08E-03	1.07	8.82E-03	-4.73	
660	1.07E-03	1.13	7.96E-03	-4.83	

**Table A2-9.** Summary of kinetic parameters of the ninth high-temperature X-ray diffraction dehydroxylation experiment of lizardite (milled) realised without using a purging gas.

$T$ [°C]	$1/T$ [K <sup>-1</sup> ]	$n$	$k$	$\ln k$	$E_a$ [kJ/mol]
600	1.15E-03	0.63	1.14E-03	-6.77	326 $R^2 = 0.937$
610	1.13E-03	0.59	4.08E-03	-5.50	
620	1.12E-03	0.69	4.39E-03	-5.43	
630	1.11E-03	0.77	9.64E-03	-4.64	
640	1.10E-03	0.78	1.39E-02	-4.28	
650	1.08E-03	0.87	1.49E-02	-4.21	
660	1.07E-03	0.93	2.91E-02	-3.54	

**Table A2-10.** Summary of kinetic parameters of the tenth high-temperature X-ray diffraction dehydroxylation experiment of lizardite (milled) realised with a purging flux of 200 ml/min N<sub>2</sub>.

$T$ [°C]	$1/T$ [K <sup>-1</sup> ]	$n$	$k$	$\ln k$	$E_a$ [kJ/mol]
580	1.17E-03	0.82	2.45E-03	-6.01	288 $R^2 = 0.848$
590	1.16E-03	0.90	6.30E-03	-5.07	
600	1.15E-03	1.02	6.94E-03	-4.97	
610	1.13E-03	0.78	5.55E-03	-5.19	
620	1.12E-03	0.81	1.65E-02	-4.10	
630	1.11E-03	0.81	4.63E-02	-3.07	
640	1.10E-03	0.70	3.09E-02	-3.48	

**Table A2-11.** Summary of kinetic parameters of the first high-temperature X-ray diffraction dehydroxylation experiment of chrysotile realised without using a purging gas.

$T$ [°C]	$1/T$ [K <sup>-1</sup> ]	$n$	$k$	$\ln k$	$E_a$ [kJ/mol]
580	1.17E-03	0.89	2.99E-03	-5.81	259 $R^2 = 0.972$
590	1.16E-03	0.92	3.83E-03	-5.56	
600	1.15E-03	0.79	9.19E-03	-4.69	
630	1.11E-03	0.76	1.74E-02	-4.05	
640	1.10E-03	0.80	3.41E-02	-3.38	
650	1.08E-03	0.79	5.17E-02	-2.96	

**Table A2-12.** Summary of kinetic parameters of the second high-temperature X-ray diffraction dehydroxylation experiment of chrysotile realised without using a purging gas.

$T$ [°C]	$1/T$ [K <sup>-1</sup> ]	$n$	$k$	$\ln k$	$E_a$ [kJ/mol]
550	1.21E-03	0.78	3.02E-03	-5.80	230 $R^2 = 0.969$
560	1.20E-03	0.73	4.21E-03	-5.47	
570	1.19E-03	0.66	4.61E-03	-5.38	
580	1.17E-03	0.78	8.75E-03	-4.74	
590	1.16E-03	0.78	1.44E-02	-4.24	
600	1.15E-03	0.78	1.32E-02	-4.33	
610	1.13E-03	0.70	3.34E-02	-3.40	
620	1.12E-03	0.73	3.77E-02	-3.28	
630	1.11E-03	0.75	5.16E-02	-2.96	

**Table A2-13.** Summary of kinetic parameters of the third high-temperature X-ray diffraction dehydroxylation experiment of chrysotile realised with a purging flux of 200 ml/min  $N_2$ .

$T$ [°C]	$1/T$ [K <sup>-1</sup> ]	$n$	$k$	$\ln k$	$E_a$ [kJ/mol]
530	1.25E-03	0.84	1.57E-03	-6.46	204 $R^2 = 0.987$
550	1.21E-03	0.85	3.41E-03	-5.68	
570	1.19E-03	0.73	8.49E-03	-4.77	
590	1.16E-03	0.82	1.93E-02	-3.95	
610	1.13E-03	0.77	2.77E-02	-3.59	
630	1.11E-03	0.73	5.64E-02	-2.87	
650	1.08E-03	1.15	7.59E-02	-2.58	

**Table A2-14.** Summary of kinetic parameters of the fourth high-temperature X-ray diffraction dehydroxylation experiment of chrysotile realised with a purging flux of 200 ml/min  $N_2$ .

$T$ [°C]	$1/T$ [K <sup>-1</sup> ]	$n$	$k$	$\ln k$	$E_a$ [kJ/mol]
540	1.23E-03	0.86	1.70E-03	-6.38	229 $R^2 = 0.981$
550	1.21E-03	0.76	2.34E-03	-6.06	
560	1.20E-03	0.89	4.00E-03	-5.52	
570	1.19E-03	0.93	7.39E-03	-4.91	
580	1.17E-03	0.72	9.82E-03	-4.62	
590	1.16E-03	0.81	9.38E-03	-4.67	
600	1.15E-03	0.76	2.33E-02	-3.76	
620	1.12E-03	0.79	4.70E-02	-3.06	

**Table A2-15.** Summary of kinetic parameters of the fifth high-temperature X-ray diffraction dehydroxylation experiment of chrysotile realised with a purging flux of 200 ml/min  $N_2$ .

## APPENDIX III

Summary of LECO (IR Spectrometry) derived dehydroxylation data of which thermally pre-treated samples were afterwards used for FTIR measurements presented in Chapter 4, Fig. 4-7. The 10 selected graphs illustrate major problems arising from the LECO measurements itself, i.e., significant overheating when changing from non-isothermal to isothermal conditions and insufficient data resolution when trying to set the offset of the dehydroxylation reaction. The latter causes major errors in the automated calculation routine.

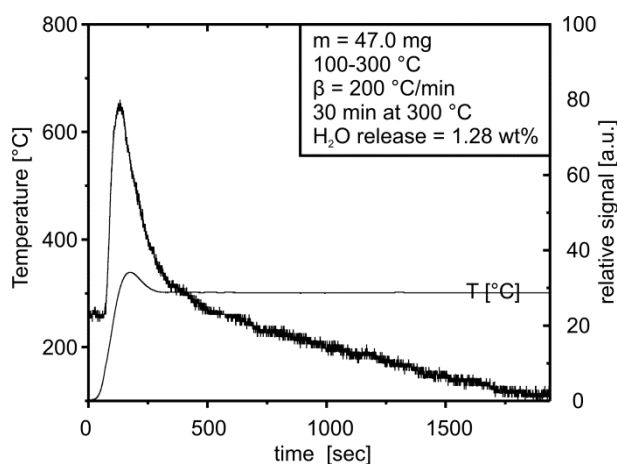


**Figure A3-1.** LECO derived dehydroxylation experiment corresponding to the lizardite subsample LizZH1\_IR1. As the relative dehydroxylation signal reaches values lower than the initial one, the calculated value of the H<sub>2</sub>O release is rather unlikely.

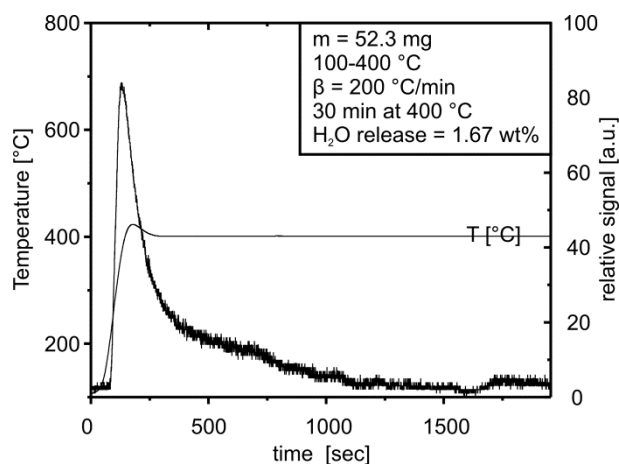


**Figure A3-2.** LECO derived dehydroxylation experiment corresponding to the lizardite subsample LizZH1\_IR2. Although the maximum temperature is 100 °C higher as in the IR1 experiment, the relative dehydroxylation signal reaches a similar value.

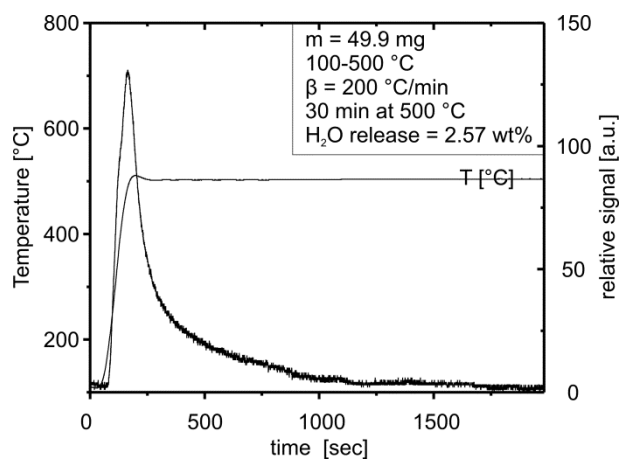


**Figure A3-3.** LECO derived dehydroxylation experiment corresponding to the lizardite subsample LizZH1\_IR3. There are no clear indications for a multiple dehydroxylation event as visible in TGA derived data (Chapter 4).

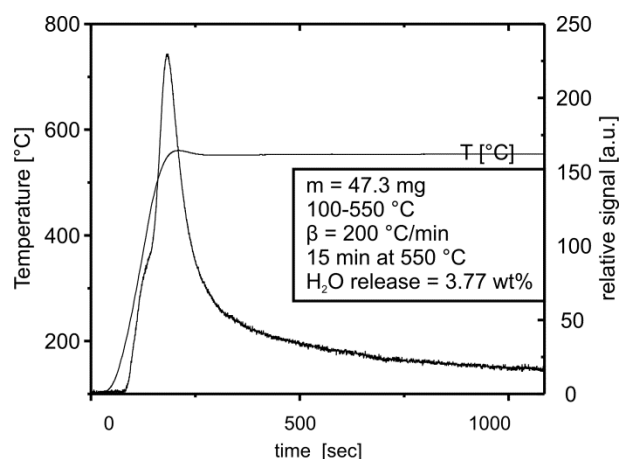


**Figure A3-4.** LECO derived dehydroxylation experiment corresponding to the lizardite subsample LizZH1\_IR4. Here, there are first signs for a multiple dehydroxylation event as also shown in TGA derived data of the same sample material (Chapter 4).

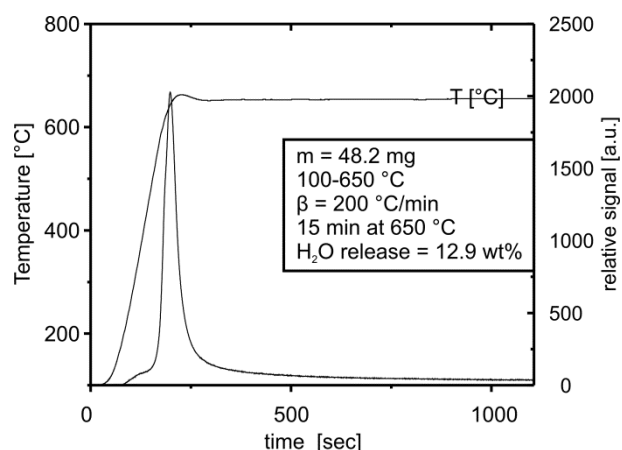


**Figure A3-6.** LECO derived dehydroxylation experiment corresponding to the lizardite subsample LizZH1\_IR6. The total amount of water release is close to the theoretical value. This indicates an almost complete dehydroxylation at 650 °C.

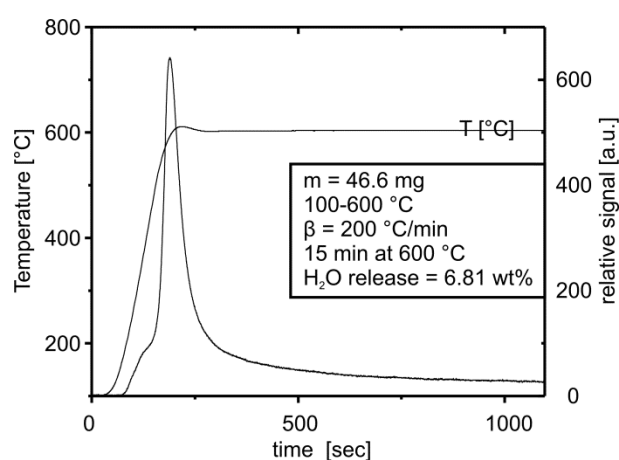


**Figure A3-5.** LECO derived dehydroxylation experiment corresponding to the lizardite subsample LizZH1\_IR5. Again, there are indications for a multiple dehydroxylation event with a significant shoulder on the low-temperature side. As the total water release is almost half of the theoretical value, the main dehydroxylation (as inferred from this technique) takes place between 600 °C and 650 °C.

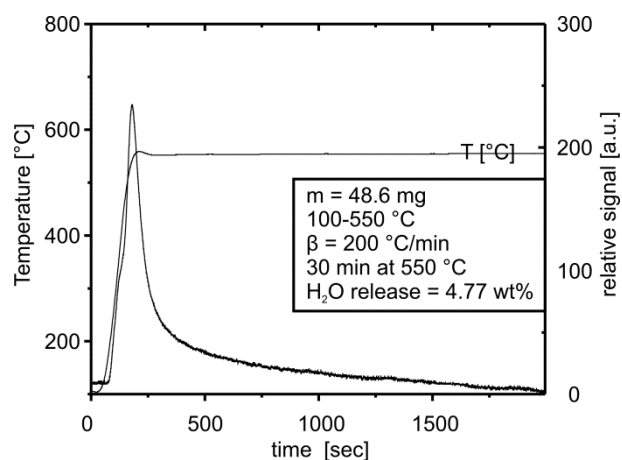


**Figure A3-7.** LECO derived dehydroxylation experiment corresponding to the lizardite subsample LizZH1\_IR7. There is no large difference between this experiment and those shown in Fig. A3-4. Therefore, the longer duration has only a marginal effect on the dehydroxylation behaviour at 550 °C.



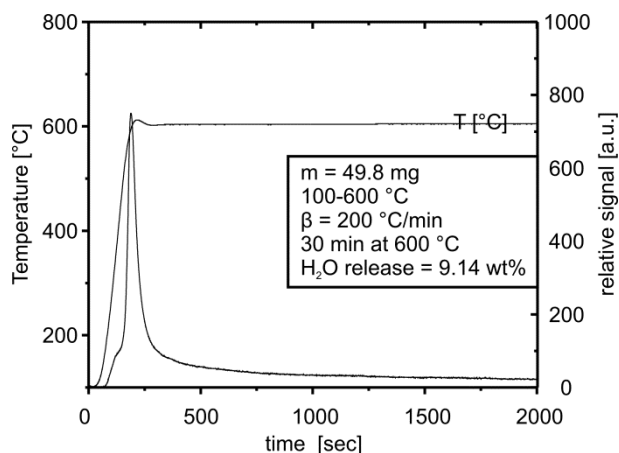


**Figure A3-8.** LECO derived dehydroxylation experiment corresponding to the lizardite subsample LizZH1\_IR8. Here, the longer duration at 600 °C causes a more advanced reaction progress compared to the IR5 experiment.

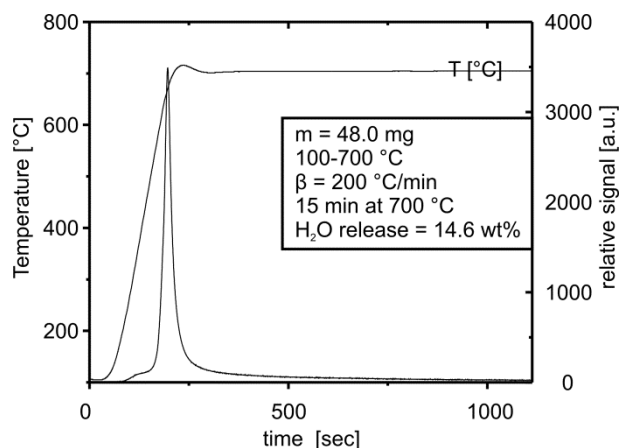


**Figure A3-10.** LECO derived dehydroxylation experiment corresponding to the lizardite subsample LizZH1\_IR10. The high temperature causes a fast release of H<sub>2</sub>O from the crystal structure as seen in the narrow, but strong relative signal.

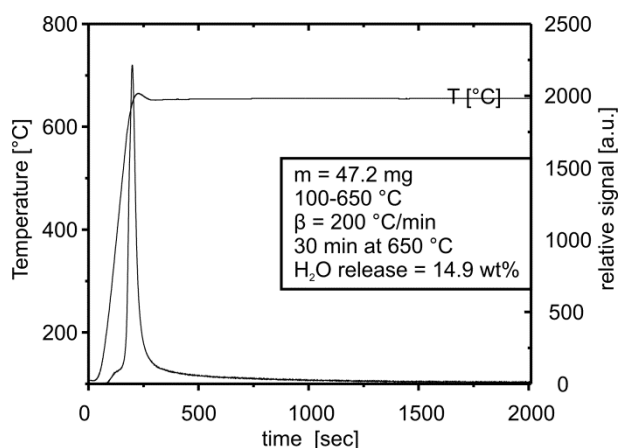


**Figure A3-9.** LECO derived dehydroxylation experiment corresponding to the lizardite subsample LizZH1\_IR9. The high temperature causes a fast release of H<sub>2</sub>O from the crystal structure as seen in the narrow, but strong relative signal.

## APPENDIX IV

A series of multi-cycle heating and cooling experiments were conducted by using the TG technique in order to check the applicability of a kinetic method presented for the dehydroxylation of dioctahedral 2:1 clay minerals (Drits *et al.* 2011, 2012). A calculation of reaction progress resolved,  $\alpha$ ,  $E_a$  compatible to those published by Drits *et al.* (2011, 2012) failed as the dehydroxylation kinetics of chrysotile cannot be treated as a single step reaction. Although such behaviour was already known from TG based dehydroxylation experiments using linear heating rates (Chapter 7), it can also be shown by the data treatment provided by Drits *et al.* (2011, 2012). Unambiguous results for appearing reaction mechanisms cannot be drawn by this method.

Altogether, three different experiments were run using a multi-cycle heating and cooling temperature program. The temperature programs are summarized in Table A4-1. Every run contains a pre-treatment stage to remove adsorbed water from the sample. This temperature, 250 °C, is far beyond the onset of the dehydroxylation, but high enough to remove adsorbed water in an adequate timeframe. The sample was cooled down by a controlled cooling rate after reaching the maximum temperature of each cycle. This is in difference to the method provided by Drits *et al.* (2011, 2012), but without any influence on the kinetic properties studied.

In contrast to analyses of Drits *et al.* (2011, 2012), there are no rehydroxylation effects which require a special handling of the cooling and heating cycle. Thus, usable data for a kinetic treatment derive from the heating periods only.

Information/ Cycle	T <sub>programmed</sub> [°C] 1 <sup>st</sup> , 2 <sup>nd</sup> , 3 <sup>rd</sup> run
heating rate $\beta_h$	10 K/min
cooling rate $\beta_c$	20 K/min
pre-treatment	30 min at 250 °C
1	250-300
2	300-350
3	350-400
4	400-450
5	450-500
6	500-550
7	550-600
8	600-650
9	650-700
10	700-750
11	750-800
12	800-850
13	850-900

**Table A4-1.** Chosen multi-cycle heating and cooling program for three different experimental runs in order to provide data base for the ‘Drits treatment’.

First, multi-cycle heating and cooling data were subdivided into data corresponding to each of the cycles. The mass loss of each cycle observable during heating was transformed to values of  $\alpha$  as follows:

$$\alpha_i = \frac{m_{0,i} - m_{t,i}}{m_{0,i} - m_{f,i}} \quad (\text{A2.1})$$

with  $1 \leq i \leq 13$ , i.e., the maximum number of cycles defined in one experiment. All other variables have the same meaning as outlined in Chapter 2. The resulting values were afterwards

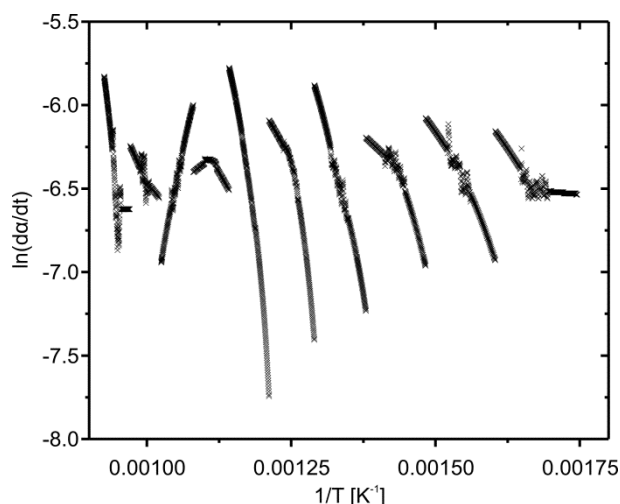


**Figure A4-1.** Dehydroxylation rates of chrysotile for a series of different heating rates (2<sup>nd</sup> run).

differentiated to get pairs of  $d\alpha/dt$  vs.  $1/T$  [K] which were then plotted into a  $\ln(d\alpha/dt)$  vs.  $1/T$  Arrhenius diagram. Corresponding data of two runs are shown in Figs. A4-1 and A4-2.

The scatter in Figs. A4-1 and A4-2 are a result of measurement artefacts due to the multi-cycle heating and cooling procedure. All cycles are characterised by overheating and undercooling after reaching the highest and lowest temperature of each corresponding cycle, respectively. This artefact has not been eliminated although a TG calibration with an empty crucible has been undertaken before each measurement. The remaining artefacts are related to differences

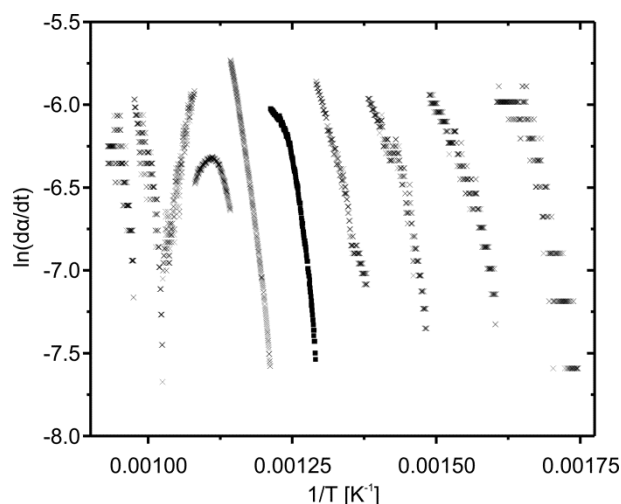


**Figure A4-2.** Dehydroxylation rates of chrysotile for a series of different heating rates (3<sup>rd</sup> run).

in the thermal behaviour between an empty and a sample loaded crucible which cannot be avoided by the TG device used.

In contrast to data presented by Drits *et al.* (2011, 2012), chrysotile dehydroxylation is not characterised by almost straight lines with positive slopes. It is rather a mixture of positive and negative slopes indicating a change of the reaction mechanisms. Moreover, it is possible to exclude a zero-order reaction mechanism for the whole dehydroxylation path. A calculation of  $E_a$  was not realized as an extraction of  $E_a$  values would only be possible by force-fitting a series of probable reaction models.

## REFERENCES

- Agranier A, Lee CTA, Li ZXA, Leeman WP (2007) Fluid-mobile element budgets in serpentinized oceanic lithospheric mantle: Insights from B, As, Li, Pb, PGEs and Os isotopes in the feather river Ophiolite, California. *Chemical Geology* 245:230-241.
- Alizadehhesari K, Golding SD, Bhatia SK (2012) Kinetics of the dehydroxylation of serpentine. *Energy Fuels* 26:783-790.
- Al-Mulla A, Mathew J, Al-Omairi L, Bhattacharya S (2011) Thermal decomposition kinetics of tricomponent polyester/polycarbonate systems. *Polymer Engineering and Science* 51:2335-2344.
- Anbalagan G, Sivakumar G, Prabakaran AR, Gunasekaran S (2010) Spectroscopy characterization of natural chrysotile. *Vibrational Spectroscopy* 52:122-127.
- Aruja E (1943) An X-ray study of silicates, chrysotile, antigorite, gumbelite. Ph.D. thesis, University of Cambridge, England.
- Auzende A-L, Daniel I, Reynard B, Lemaire C, Guyot F (2004) High-pressure behaviour of serpentine minerals: a Raman spectroscopic study. *Physics and Chemistry of Minerals* 31:269-277.
- Avrami M (1939) Kinetics of phase change I - General theory. *Journal of Chemical Physics* 7:1103-1112.
- Avrami M (1940) Kinetics of phase change II - Transformation-time relations from random distribution of nuclei. *Journal of Chemical Physics* 8:212-224.
- Avrami M (1941) Granulation, phase change, and microstructure - Kinetics of phase change III. *Journal of Chemical Physics* 9:177-184.
- Balan E, Saitta AM, Mauri F, Lemaire C, Guyot F (2002) First-principles calculation of the infrared spectrum of lizardite. *American Mineralogist* 87:1286-1290.
- Ball MC, Taylor HFW (1963) The dehydration of chrysotile in air and under hydrothermal conditions. *Mineralogical Magazine* 33:467-482.
- Ballirano P, Melis E (2009) Thermal behaviour and kinetics of dehydroxylation of gypsum in air from in situ real-time laboratory parallel-beam X-ray powder diffraction. *Physics and Chemistry of Minerals* 36:391-402.
- Bamford CH and Tipper CFH Eds. (1980) *Comprehensive chemical kinetics Vol. 22 - Reactions in the solid state*. Elsevier, Amsterdam, Oxford, New York, 340 p.
- Bard D, Yarwoord J, Tylee B (1997) Asbestos fibre identification by Raman microspectroscopy. *Journal of Raman spectroscopy* 28:803-809.
- Bearat H, McKelvy MJ, Chizmeshya AVG, Sharma R, Carpenter RW (2002) Magnesium hydroxide dehydroxylation/carbonation reaction process: implications for carbon dioxide mineral sequestration. *Journal of the American Ceramic Society* 85:742-748.
- Bellotto M, Gualtieri A, Artioli G, Clark SM (1995) Study of the kaolinite-mullite

- reaction sequence. Part I: kaolinite dehydroxylation. *Physics and Chemistry of Minerals* 22:207-214.
- Beran A (2002) Infrared spectroscopy of micas. *Reviews in Mineralogy and Geochemistry* 46:351-369.
- Bish DL, Duffy CJ (1990) Thermogravimetric analysis of minerals. In: Mumpton FA (ed), *cms workshop lectures*, Vol. 3. Thermal analysis in clay sciences. The Clay Minerals Society, Boulder.
- Blaha JJ, Rosasco GJ (1978) Raman microprobe spectra of individual microcrystals and fibers of talc, tremolite, and related silicates minerals. *Analytical Chemistry* 50:892-896.
- Bose K, Ganguly J (1994) Thermogravimetric study of the dehydration kinetics of talc. *American Mineralogist* 79:692-699.
- Bray HJ, Redfern SAT (2000) Influence of counterion species on the dehydroxylation of  $\text{Ca}^{2+}$ -,  $\text{Mg}^{2+}$ -,  $\text{Na}^+$ - and  $\text{K}^+$ -exchanged Wyoming montmorillonite. *Mineralogical Magazine* 64:337-346.
- Bray HJ, Redfern SAT (1999) Kinetics of dehydration of Ca-montmorillonite. *Physics and Chemistry of Minerals* 26:591-600.
- Brigatti MF, Galli E, Medici L, Poppi L (1997) Crystal structure refinement of aluminian lizardite- $2H_2$ . *American Mineralogist* 82:931-935.
- Brindley GW, Hayami R (1965) Mechanism of formation of forsterite and enstatite from serpentine. *Mineralogical Magazine* 35:189-195.
- Brindley GW, Hayami R (1963a) Kinetics and mechanisms of dehydration and recrystallization of serpentine-I. *Clays and Clay Minerals* 12:35-47.
- Brindley GW, Hayami R (1963b) Kinetics and mechanisms of dehydration and recrystallization of serpentine-II, spectrum of activation energies for recrystallization. *Clays and Clay Minerals* 12:49-54.
- Brindley GW, Chih-Chun K, Harrison JL, Lipsicas M, Raythatha R (1986) Relation between structural disorder and other characteristics of kaolinites and dickites. *Clays and Clay Minerals* 34:239-249.
- Brindley GW, Zussman J (1957) A structural study of the thermal transformation of serpentine minerals to forsterite. *American Mineralogist* 42:461-474.
- Brown ME (1987) Quantitative thermoanalytical studies of the kinetics and mechanisms of the thermal decomposition of inorganic solids. *Thermochimica Acta* 110:153-158.
- Brown ME, Maciejewski M, Vyazovkin S, Nomen R, Sempere J, Burnham A, Opferman J, Strej R, Anderson HL, Kemmler A, Keuleers A, Janssens J, Desseyn HO, Li C-R, Tang TB, Roduit B, Malek J, Mitsuhashi T (2000) Computational aspects of kinetic analysis Part A: The ICTAC kinetics project-data, methods and results. *Thermochimica Acta* 355:125-143.
- Burke J (1965) The kinetics of phase transformation in metals. Pergamon Press Inc., Oxford, 226 p.
- Burnham AK (2000) Computational aspects of kinetic analysis Part A: The ICTAC kinetics project – multi-thermal-history model-fitting methods and their relation to isoconversional methods. *Thermochimica Acta* 355:165-170.
- Burns RG, Strens RGJ (1966) Infrared study of the hydroxyl bands in clinoamphiboles. *Science* 153:890-892.
- Butt DP, Lackner KS, Wendt CH, Conzone SD, Kung H, Lu YC, Bremser JK (1996)

- Kinetics of thermal dehydroxylation and carbonation of magnesium hydroxide. *Journal of the American Ceramic Society* 79:1892-1898.
- Cai J, Chen S (2009) A new iterative linear integral isoconversional method for the determination of the activation energy varying with the conversion degree. *Journal of Computational Chemistry* 30:1986-1991.
- Candela PA, Crummet CD, Earnest DJ, Frank MR, Wylie AG (2007) Low-pressure decomposition of chrysotile as a function of time and temperature. *American Mineralogist* 92:1704-1713.
- Carbone M, Ballirano P, Caminiti R (2008) Kinetics of gypsum dehydration at reduced pressure: an energy dispersive X-ray diffraction study. *European Journal of Mineralogy* 20:621-627.
- Caruso LJ, Chernosky JV (1979) The stability of lizardite. *Canadian Mineralogist* 17:757-769.
- Cattaneo A, Gualtieri AF, Artioli G (2003) Kinetic study of the dehydroxylation of chrysotile asbestos with temperature by in situ XRPD. *Physics and Chemistry of Minerals* 30:177-183.
- Cheong S, Watt J, Ingham B, Toney MF, Tilley RD (2009) In situ and ex situ studies of platinum nanocrystals: growth and evolution in solution. *Journal of the American Ceramic Society* 131:14590-14595.
- Chollet M, Daniel I, Koga KT, Petitgirard S, Morard G (2009) Dehydration kinetics of talc and 10 Å phase: consequences for subduction zone seismicity. *Earth and Planetary Science Letters* 284:57-64.
- Churakov SV, Iannuzzi M, Parrinello M (2004) Ab initio study of dehydroxylation-carbonation reaction on brucite surface. *Journal of Physical Chemistry B* 108:11567-11574.
- Cressey G, Cressey BA, Wicks FJ (2008) Polyhedral serpentine: a spherical analogue of polygonal serpentine? *Mineralogical Magazine* 72:1229-1242.
- D'Arco P, Noel Y, Demichelis R, Dovesi R (2009) Single-layered chrysotile nanotubes: A quantum mechanical ab initio simulation. *Journal of Chemical Physics* 131:204701-1-7.
- Datta AK (1991) Dehydration of chrysotile asbestos: an infrared absorption study. *Journal of Materials Science Letters* 10:870-871.
- Datta AK, Mathur BK, Samantaray BK, Bhattacharjee S (1987) Dehydration and phase transformation on chrysotile asbestos-a radial distribution analysis study. *Bulletin of Material Science* 9:103-110.
- Deer WA, Howie RA, Zussman J (2009) *Serpentine In: "Rock-forming minerals 3B: Layered silicates excluding micas and clay minerals"*, Deer WA, Howie RA, Zussman J, The Geological Society, London, 157-229.
- Demir F, Dönmez B, Okur H, Sevim F (2003) Calcination kinetic of magnesite from thermogravimetric data. *Chemical Engineering Research and Design* 81:618-622.
- Devouard B, Baronnet A (1995) Axial diffraction of curved lattices: geometrical and numerical modeling. Application to chrysotile. *European Journal of Mineralogy* 7:835-846.
- Dódy I, Buseck PR (2004) Serpentine close-up and intimate: an HRTEM view. *International Geology Review* 46:507-527.

- Downs RT (2006) The RRUFF Project: an integrated study of the chemistry, crystallography, Raman and infrared spectroscopy of minerals. Program and Abstracts of the 19th General Meeting of the International Mineralogical Association in Kobe, Japan. O03-13.
- Drits VA, Derkowski A, McCarty DK (2012) Kinetics of partial dehydroxylation of dioctahedral 2:1 layer clay minerals. *American Mineralogist* 97:930-950.
- Drits VA, Derkowski A, McCarty DK (2011) Kinetics of thermal transformation of partially dehydroxylated pyrophyllite. *American Mineralogist* 96:1054-1069.
- Dungan MA (1979) A microprobe study of antigorite and some serpentine pseudomorphs. *Canadian Mineralogist* 17:771-784.
- Erofe'ev BV (1946) Generalized equation of chemical kinetics and its application in reactions involving solids. *Doklady Akademii Nauk SSSR* 52:511-514.
- Evans BW (2004) The serpentinite multisystem revisited: chrysotile is metastable. *International Geology Review* 46:479-506.
- Farjas J, Roura P (2011) Isoconversional analysis of solid state transformations. A critical review. Part II. Complex transformations. *Journal of Thermal Analysis and Calorimetry* 105:767-773.
- Farmer VC (1998) Differing effects of particle size and shape in the infrared and Raman spectra of kaolinite. *Clay Minerals* 33:601-604.
- Farmer VC (1974a) The layer silicates. In: "The infra-red spectra of minerals", Farmer VC, ed. Mineralogical Society, London, 331-363.
- Farmer VC Ed. (1974b) The infra-red spectra of minerals. Mineralogical Society, London.
- Ferrage E, Kirk CA, Cressey G, Cuadros J (2007) Dehydration of Ca-montmorillonite at the crystal scale. Part 2. Mechanisms and kinetics. *American Mineralogist* 92:1007-1017.
- Flynn JH, Wall LA (1966) A quick direct method for determination of activation energy from thermogravimetric data. *Journal of Polymer Science Part B-Polymer Letters* 4:323-328.
- Friedman HL (1964) Kinetics of thermal degradation of char-forming plastics from thermogravimetry. Application to phenolic plastic. *Journal of Polymer Science Part C-Polymer Symposium* 6:183-195.
- Früh-Green GL, Connolly JAD, Plas A, Kelley DS, Grobéty B (2004) Serpentinization of oceanic peridotites: Implications for geochemical cycles and biological activity. *The Subseafloor Biosphere at Mid-Ocean Ridges* 144:119-136.
- Fuchs Y, Linares J, Mellini M (1998) Mössbauer and infrared spectrometry of lizardite-1T from Monte Fico, Elba. *Physics and Chemistry of Minerals* 26:111-115.
- Fuller EL, Yoos TR (1987) Surface properties of limestones and their calcinations products. *Langmuir* 3:753-760.
- Fumagalli P, Stixrude L, Poli S, Snyder D (2001) The 10Å phase: a high-pressure expandable sheet silicate stable during subduction of hydrated lithosphere. *Earth and Planetary Science Letters* 186:125-141.
- Galwey AK (2004) Is the science of thermal analysis kinetics based on solid foundations? A literature appraisal. *Thermochimica Acta* 413:139-183.
- Galwey AK (2003) What is meant by the term 'variable activation energy' when applied in the kinetic analyses of solid state

- decompositions (crystolysis reactions)? *Thermochimica Acta* 397:249-268.
- Galwey AK, Brown ME (2002) Application of the Arrhenius equation to solid state kinetics: can this be justified? *Thermochimica Acta* 386:91-98.
- Gillet P (1996) Raman spectroscopy at high pressure and high temperature. Phase transitions and thermodynamic properties of minerals. *Physics and Chemistry of Minerals* 23:263-275.
- Goff F, Lackner KS (1998) Carbon dioxide sequestering using ultramafic rocks. *Environmental Geosciences* 5:89-101.
- Gordon RS, Kingery WD (1967) Thermal decomposition of brucite: II, kinetics of decomposition in vacuum. *Journal of the American Ceramic Society* 50:8-14.
- Gordon RS, Kingery WD (1966) Thermal decomposition of brucite: I, electron and optical microscope studies. *Journal of the American Ceramic Society* 49:654-660.
- Gotor FJ, Criado JM, Malek J, Koga N (2000) Kinetic analysis of solid-state reactions: the universality of master plots for analyzing isothermal and nonisothermal experiments. *Journal of Physical Chemistry A* 104:10777-10782.
- Gregorkiewicz M, Lebech B, Mellini M, Viti C (1996) Hydrogen positions and thermal expansion in lizardite-1T from Elba: a low-temperature study using Rietveld refinement of neutron diffraction data. *American Mineralogist* 81:1111-1116.
- Gridi-Bennadji F, Blanchart P (2007) Dehydroxylation kinetic and exfoliation of large muscovite flakes. *Journal of Thermal Analysis and Calorimetry* 90:747-753.
- Grobéty B (2003) Polytypes and higher-order structures of antigorite: a TEM study. *American Mineralogist* 88:27-36.
- Gualtieri A, Bellotto M, Artioli G, Clark SM (1995) Kinetic study of the kaolinite-mullite reaction sequence. Part II: Mullite formation. *Physics and Chemistry of Minerals* 22:215-222.
- Gualtieri AF, Ferrari S (2006) Kinetics of illite dehydroxylation. *Physics and Chemistry of Minerals* 33:490-501.
- Gualtieri AF, Giacobbe C, Viti C (2012) The dehydroxylation of serpentine group minerals. *American Mineralogist* 97:666-680.
- Gualtieri AF, Tartaglia A (2000) Thermal decomposition of asbestos and recycling in traditional ceramics. *Journal of the European Ceramic Society* 20:1409-1418.
- Guggenheim S, Chang Y-H, Koster van Gross AF (1987) Muscovite dehydroxylation: high-temperature studies. *American Mineralogist* 72:537-550.
- Guggenheim S, Zhan W (1998) Effect of temperature on the structures of lizardite-1T and lizardite-2H<sub>1</sub>. *Canadian Mineralogist* 36:1587-1594.
- Guillot S, Hattori K (2012) Introduction to serpentinites. *Elements* 8:405.
- Hacker BR, Peacock SM, Abers GA, Holloway SD (2003) Subduction factory 2. Are intermediate-depth earthquakes in subducting slabs linked to metamorphic dehydration reactions? *Journal of Geophysical Research-Solid Earth* 108:11-1 – 11-8.
- Halikia I, Economacou A (1993) Application of various methods of nonisothermal kinetic-analysis to magnesium-hydroxide decomposition. *International Journal of Chemical Kinetics* 25:609-631.
- Halikia I, Neou-Syngouna P, Kolitsa D (1998) Isothermal kinetic analysis of the thermal decomposition of magnesium hydroxide



- using thermogravimetric data. *Thermochimica Acta* 320:75-88.
- Hancock JD, Sharp JH (1972) Method of comparing solid-state kinetic data and its application to decomposition of kaolinite, brucite, and BaCO<sub>3</sub>. *Journal of the American Ceramic Society* 55:74-77.
- Hänchen M, Prigione V, Baciocchi R, Mazzotti M (2008) Precipitation in the Mg-carbonate system-effects of temperature and CO<sub>2</sub> pressure. *Chemical Engineering Science* 63:1012-1028.
- Hey MH, Bannister FA (1948) A note on the thermal decomposition of chrysotile. *Mineralogical Magazine* 28:333-337.
- Hofmeister AM, Bowey JE (2006) Quantitative infrared spectra of hydrosilicates and related minerals. *Monthly Notices of the Royal Astronomical Society* 367:577-591.
- Hurst HJ (1991) The thermal decomposition of magnesite in nitrogen. *Thermochimica Acta* 189:91-96.
- Hyndman RD, Peacock SM (2003) Serpentinization of the forearc mantle. *Earth and Planetary Science Letters* 212:417-432.
- Inoue T, Yoshimi I, Yamada A, Kikegawa T (2009) Time-resolved X-ray analysis of the experimental dehydration of serpentine at high pressure. *Journal of Mineralogical and Petrological Sciences* 104:105-109.
- Jeanloz R (1980) Infrared spectra of olivine polymorphs:  $\alpha$ ,  $\beta$  phase and spinel. *Physics and Chemistry of Minerals* 5:327-341.
- Johnson WA, Mehl RF (1939) Reaction kinetics in processes of nucleation and growth. *Transactions of the American Institute of Mining and Metallurgical Engineers* 135:416-458.
- Jolicoeur C, Duchesne D (1981) Infrared and thermogravimetric studies of the thermal-degradation of chrysotile asbestos fibers: evidence for matrix effects. *Canadian Journal of Chemistry* 59:1521-1526.
- Kalousek GL, Muttart LE (1957) Studies on the chrysotile and antigorite components of serpentine. *American Mineralogist* 42:1-22.
- Kerrick D (2002) Serpentine seduction. *Science* 298:1344-1345.
- Khawam A (2007) Application of solid-state kinetics to desolvation reactions. Ph.D. thesis, University of Iowa, U.S.A.
- Kloprogge JT, Frost RL, Rintoul L (1999) Single crystal Raman microscopic study of the asbestos mineral chrysotile. *Physical Chemistry Chemical Physics* 1:2559-2564.
- Kunze G (1961) Antigorit. Strukturtheoretische Grundlagen und ihre praktische Bedeutung für die weitere Serpentin-Forschung. *Fortschritte der Mineralogie* 39:206-324.
- Landsberg G, Mandelstam L (1928) Eine neue Erscheinung bei der Lichtstreuung in Kristallen. *Naturwissenschaften* 16:557-558.
- Lasaga AC (1998) Kinetic theory in Earth science. Princeton University Press, Princeton, New Jersey.
- Lepora A (2002) Gas-mixing techniques for the synthesis and characterization of iron-based minerals and catalysts. Ph.D. thesis, University of Fribourg, Switzerland.
- Libowitzky E (1999) Correlation of O-H stretching frequencies and O-H...O hydrogen bond lengths in minerals. *Monatshefte für Chemie* 130:1047-1059.
- Liu XW, Feng YL, Li HR, Zhang P, Wang P (2012) Thermal decomposition of magnesite from thermogravimetric data.

- Journal of Thermal Analysis and Calorimetry 107:407-412.
- Long DA (1977) Raman spectroscopy. McGraw-Hill, New York.
- Luys M-J, De Roy G, Vansant EF, Adams F (1982) Characteristics of asbestos minerals. Journal of the Chemical Society, Faraday Transactions I 78:3561-3571.
- L'vov BV, Ugolkov VL (2004) Kinetics and mechanism of free-surface decomposition of Group IIA and IIB hydroxides analyzed thermogravimetrically by the third-law method. Thermochimica Acta 413:7-15.
- Maciejewski M (2000) Computational aspects of kinetic analysis Part A: The ICTAC kinetics project – the decomposition kinetics of calcium carbonate revisited, or some tips on survival in the kinetic minefield. Thermochimica Acta 355:145-154.
- Maciejewski M (1992) Somewhere between fiction and reality. The usefulness of kinetic data of solid-state reactions. Journal of Thermal Analysis 38:51-70.
- MacKenzie KJD, Meinhold RH (1994) Thermal reactions of chrysotile revisited: A  $^{29}\text{Si}$  and  $^{25}\text{Mg}$  MAS NMR study. American Mineralogist 79:43-50.
- MacKenzie KJD, Brown IWM, Meinhold RH, Bowden ME (1985) Outstanding problems in the kaolinite-mullite reaction sequence investigated by  $^{29}\text{Si}$  and  $^{27}\text{Al}$  solid-state nuclear magnetic resonance: I, metakaolinite. Journal of the American Ceramic Society 68:293-297.
- Malkov AA, Korytkova EN, Maslennikova TP, Shtykhova AM, Gusarov VV (2009) Effect of heat treatment on structural-chemical transformations in magnesium hydrosilicate  $[\text{Mg}_3\text{Si}_2\text{O}_5(\text{OH})_4]$  nanotubes. Russian Journal of Applied Chemistry 82:2079-2086.
- Martens R, Gentsch H, Freund F (1976) Hydrogen release during thermal decomposition of magnesium hydroxide to magnesium oxide. Journal of Catalysis 44:366-372.
- Martin CJ (1977) The thermal decomposition of chrysotile. Mineralogical Magazine 41:453-459.
- Mazzucato E, Artioli G, Gualtieri A (1999) High temperature dehydroxylation of muscovite- $2M_1$ : a kinetic study by in situ XRPD. Physics and Chemistry of Minerals 26:375-381.
- McKelvy MJ, Chizmeshya AVG, Diefenbacher J, Béarat H, Wolf G (2004) Exploration of the role of heat activation in enhancing serpentine carbon sequestration reactions. Environmental Science and Technology 38:6897-6903.
- McKelvy MJ, Sharma R, Chizmeshya AVG (2006) Lamellar reaction phenomena: from intercalation to nanomaterials formation. Journal of Physics and Chemistry of Solids 67:888-895.
- McKelvy MJ, Sharma R, Chizmeshya AVG, Carpenter RW, Streib K (2001) Magnesium hydroxide dehydroxylation: in situ nanoscale observations of lamellar nucleation and growth. Chemistry of Materials 13:921-926.
- McKeown DA, Bell MI, Caracas R (2010) Theoretical determination of the Raman spectra of single-crystal forsterite ( $\text{Mg}_2\text{SiO}_4$ ). American Mineralogist 95:980-986.
- Mellini M (1982) The crystal structure of lizardite 1T: hydrogen bonds and polytypism. American Mineralogist 67:587-598.

- Mellini M, Viti C (1994) Crystal-structure of lizardite-1T from Elba, Italy. *American Mineralogist* 79:1194-1198.
- Mellini M, Trommsdorff V, Compagnoni R (1987) Antigorite polysomatism: behavior during progressive metamorphism. *Contributions to Mineralogy and Petrography* 97:147-155.
- Mellini M, Zanazzi PF (1987) Crystal structures of lizardite-1T and lizardite-2H<sub>1</sub> from Coli, Italy. *American Mineralogist* 72:943-948.
- Mizukami T, Kagi T, Wallis SR, Fukura S (2007) Pressure-induced change in the compressional behavior of the O-H bond in chrysotile: A Raman high-pressure study up to 4.5 GPa. *American Mineralogist* 92:1456-1463.
- Molina-Montes E, Donadio D, Hernández-Laguna A, Sainz-Díaz CI, Parrinello M (2008a) DFT research on the dehydroxylation reaction of pyrophyllite 1. First-principle molecular dynamics simulations. *Journal of Physical Chemistry B* 112:7051-7060.
- Molina-Montes E, Donadio D, Hernández-Laguna A, Sainz-Díaz CI (2008b) DFT research on the dehydroxylation reaction of pyrophyllite 2. Characterization of reactants, intermediates, and transition states along the reaction path. *Journal of Physical Chemistry A* 112:6373-6383.
- Mookherjee M, Redfern SAT (2002) A high-temperature Fourier transform infrared study of the interlayer and Si-O-stretching region in phengite-2M<sub>1</sub>. *Clay Minerals* 37:323-336.
- Nahdi K, Rouquerol F, Ayadi MT (2009) Mg(OH)<sub>2</sub> dehydroxylation: a kinetic study controlled by controlled rate thermal analysis (CRTA). *Solid State Sciences* 11:1028-1034.
- Nasdala L, Smith DC, Kaindl R, Ziemann MA (2004) Raman spectroscopy: analytical perspectives in mineralogical research. In: "Spectroscopic Methods in Mineralogy" Beran A and Libowitzky E, eds., *EMU Notes in Mineralogy* Vol. 6:281-343.
- Naumann AW, Dresher WH (1966) The influence of sample texture on chrysotile dehydroxylation. *American Mineralogist* 51:1200-1211.
- N.N. (1990) Instruction Manual RC-412 Multiphase carbon/hydrogen/moisture determinator model 787-900-300. LECO® corporation.
- N.N. (1979) Arrhenius kinetic constants for thermally unstable materials. American Society for Testing and Materials (ASTM) standard, E698-79.
- O'Hanley DS, Chernosky JV, Wicks FJ (1989) The stability of lizardite and chrysotile. *Canadian Mineralogist* 27:483-493.
- Ortega A, Macías M, Gotor, FJ (2010) The multistep nature of the kaolinite dehydroxylation: kinetics and mechanism. *Journal of the American Ceramic Society* 93:197-203.
- Ozawa T (1986) Nonisothermal kinetics and the generalized time. *Thermochimica Acta* 100:109-118.
- Ozawa T (1965) Initial kinetic parameters from thermogravimetric rate and conversion data. *Bulletin of the Chemical Society of Japan* 38:1881-1886.
- Padron-Navarta JA, Tommasi A, Garrido CJ, Sanchez-Vizcaino VL, Gomez-Pugnaire MT, Jabaloy A, Vauchez A (2010) Fluid transfer into the wedge controlled by high-pressure hydrofracturing in the cold top-slab mantle. *Earth and Planetary Science Letters* 297:271-286.

- Peacock SM (2001) Are the lower planes of double seismic zones caused by serpentine dehydration in subducting oceanic mantle? *Geology* 29:299-302.
- Pelletier MJ Ed. (1999) Analytical applications of Raman spectroscopy. Blackwell Science, 492 p.
- Perrillat J-P, Daniel I, Koga KT, Reynard B, Cardon H, Crichton WA (2005) Kinetics of antigorite dehydration: a real-time X-ray diffraction. *Earth and Planetary Science Letters* 236:899-913.
- Post JL, Borer L (2000) High-resolution infrared spectra, physical properties, and micromorphology of serpentines. *Applied Clay Sciences* 16:73-85.
- Prencipe M, Noel Y, Bruno M, Dovesi R (2009) The vibrational spectrum of lizardite-1T [ $\text{Mg}_3\text{Si}_2\text{O}_5(\text{OH})_4$ ] at the  $\Gamma$  point: a contribution from an ab initio periodic B3LYP calculation. *American Mineralogist* 94:986-994.
- Putnis A (1992) An introduction to mineral sciences. Cambridge University Press, 457 p.
- Redfern SAT (1987) The kinetics of dehydroxylation of kaolinite. *Clay Minerals* 22:447-456.
- Raman CV, Krishnan KS (1928) A new type of secondary radiation. *Nature* 121:501-502.
- Rinaudo C, Gastaldi D, Belluso E (2003) Characterization of chrysotile, antigorite and lizardite by FT-Raman spectroscopy. *Canadian Mineralogist* 41:883-890.
- Rodriguez-Navarro C, Ruiz-Agudo E, Luque A, Rodriguez-Navarro AB, Ortega-Huertas M (2009) Thermal decomposition of calcite: mechanisms of formation and textural evolution of CaO nanocrystals. *American Mineralogist* 94:578-593.
- Roduit B (2000) Computational aspects of kinetic analysis Part A: The ICTAC kinetics project-numerical techniques and kinetics of solid state processes. *Thermochimica Acta* 355:171-180.
- Roduit, B, Maciejewski M, Baiker A (1996) Influence of experimental conditions on the kinetic parameters of gas-solid reactions - Parametric sensitivity of thermal analysis. *Thermochimica Acta* 283:101-119.
- Rouxhet PG (1970) Kinetics of dehydroxylation and OH-OD exchange in macrocrystalline micas. *American Mineralogist* 55:841-853.
- Rüpke LH, Morgan JP, Hort M, Connolly JAD (2004) Serpentine and the subduction zone water cycle. *Earth and Planetary Science Letters* 223:17-34.
- Salehi M, Clemens F, Pfaff EM, Diethelm S, Leach C, Graule T, Grob  ty B (2011) A case study of the effect of grain size on the oxygen permeation flux of BSCF disk-shaped membrane fabricated by thermoplastic processing. *Journal of Membrane Science* 382:186-193.
- S  nchez-Jim  nez PE, P  rez-Maqueda LA, Perej  n A, Criado JM (2013) Generalized master plots as a straightforward approach for determining the kinetic model: the case of cellulose pyrolysis. *Thermochimica Acta* 552:54-59.
- S  nchez-Jim  nez PE, P  rez-Maqueda LA, Perej  n A, Criado JM (2010) Generalized kinetic master plots for the thermal degradation of polymers following a random scission mechanism. *Journal of Physical Chemistry A* 114:7868-7876.
- Seber GAF and Wild CJ (1989) Nonlinear regression. John Wiley & Sons, New York, 768 p.

- Senum GI, Yang RT (1977) Rational approximations of the integral of the Arrhenius function. *Journal of Thermal Analysis* 11:445-447.
- Šesták J (1984) Thermal analysis. Part D: Thermophysical properties of solids: their measurements and theoretical thermal analysis. Elsevier, New York, U.S.A.
- Šimon P (2004) Isoconversional methods. Fundamentals, meaning and application. *Journal of Thermal Analysis and Calorimetry* 76:123-132.
- Smekal A (1923) Zur Quantentheorie der Dispersion. *Naturwissenschaften* 11:873-875.
- Šontevska V, Jovanovski G, Makreski P (2007) Minerals from Macedonia. Part XIX. Vibrational spectroscopy as identificational tool for some sheet silicate minerals. *Journal of Molecular Structure* 834:318-327.
- Sperinck S, Raiteri P, Marks N, Wright K (2011) Dehydroxylation of kaolinite to metakaolin-a molecular dynamics study. *Journal of Materials Chemistry* 21:2118-2125.
- Stackhouse S, Coveney PV, Benoit DM (2004) Density-Functional-Theory-based study of the dehydroxylation behavior of aluminous dioctahedral 2:1 layer-type clay minerals. *Journal of Physical Chemistry B* 108:9685-9694.
- Steinfeld JJ, Francisco JS, Hase WL (1999) Chemical kinetics and dynamics. 2<sup>nd</sup> edition. Prentice Hall, Upper Saddle River, New Jersey, U.S.A.
- Stone RL (1954) Thermal analysis of magnesite at CO<sub>2</sub> pressured up to six atmospheres. *Journal of the American Ceramic Society* 37:46-48.
- Taylor HFW (1962) Homogeneous and inhomogeneous mechanisms in the dehydroxylation of minerals. *Clay Minerals Bulletin* 5:45-55.
- Thomas S (2013) [http://serc.carleton.edu/NAGTWorkshops/mineralogy/mineral\\_physics/raman\\_ir.html](http://serc.carleton.edu/NAGTWorkshops/mineralogy/mineral_physics/raman_ir.html) visited on 11th March 2013.
- Tokiwai K, Nakashima S (2010) Dehydration kinetics of muscovite by in situ infrared microspectroscopy. *Physics and Chemistry of Minerals* 37:91-101.
- Trittschack R, Grobéty B (2013) The dehydroxylation of chrysotile: a combined in situ micro-Raman and micro-FTIR study. *American Mineralogist* 98:1133-1145.
- Trittschack R, Grobéty B (2012) Dehydroxylation kinetics of lizardite. *European Journal of Mineralogy* 24:47-57.
- Trittschack R, Grobéty B, Koch-Müller M (2012) In situ high-temperature Raman and FTIR spectroscopy of the phase transformation of lizardite. *American Mineralogist* 97:1965-1976.
- Ulmer P, Trommsdorff V (1995) Serpentine stability to mantle depths and subduction-related magmatism. *Science* 268:858-861.
- van Aken PA, Langenhorst F (2001) Nanocrystalline, porous periclase aggregates as product of brucite dehydration. *European Journal of Mineralogy* 13:329-341.
- Viti C (2010) Serpentine minerals discrimination by thermal analysis. *American Mineralogist* 95:631-638.
- Viti C, Mellini M (1997) Contrasting chemical compositions in associated lizardite and chrysotile in veins from Elba, Italy. *European Journal of Mineralogy* 9:585-596.

- Vyazovkin S (2008) Isoconversional kinetics. In: "Handbook of thermal analysis and calorimetry", Brown ME and Gallagher PK, eds., Elsevier, Amsterdam, Oxford, New York, 503-538.
- Vyazovkin S (2003) Reply to "What is meant by the term 'variable activation energy' when applied in the kinetics analyses of solid state decompositions (crystolysis reactions)?" *Thermochimica Acta* 397:269-271.
- Vyazovkin S (2001) Modification of the integral isoconversional method to account for variation in the activation energy. *Journal of Computational Chemistry* 22:178-183.
- Vyazovkin S (2000a) Computational aspects of kinetic analysis. Part C. The ICTAC kinetics project-the light at the end of the tunnel? *Thermochimica Acta* 355:155-163.
- Vyazovkin S (2000b) Kinetic concepts of thermally stimulated reactions in solids: a view from a historical perspective. *International Reviews in Physical Chemistry* 19:45-60.
- Vyazovkin S (1997) Evaluation of activation energy of thermally stimulated solid-state reactions under arbitrary variation of temperature. *Journal of Computational Chemistry* 18:393-402.
- Vyazovkin S (1996) A unified approach to kinetic processing of nonisothermal data. *International Journal of Chemical Kinetics* 28:95-101.
- Vyazovkin S, Burnham AK, Criado JM, Pérez-Maqueda LA, Popescu C, Sbirrazzuoli N (2011) ICTAC Kinetics committee recommendations for performing kinetic computations on thermal analysis data. *Thermochimica Acta* 520:1-19.
- Vyazovkin S, Wight CA (1997) Kinetics in solids. *Annual Review of Physical Chemistry* 48:125-149.
- Wang L, Zhang M, Redfern SAT, Zhang Z (2002) Dehydroxylation and transformation of the 2:1 phyllosilicate pyrophyllite at elevated temperatures: an infrared spectroscopic study. *Clays and Clay Minerals* 50:272-283.
- Watanabe T, Shimizu H, Nagasaka K, Masuda A, Saito H (1987)  $^{29}\text{Si}$ - and  $^{27}\text{Al}$ -MAS/NMR study of the thermal transformations of kaolinite. *Clay Minerals* 22:37-48.
- Weber JN, Greer RT (1965) Dehydration of serpentine: heat of reaction and reaction kinetics at  $P_{\text{H}_2\text{O}} = 1$  Atm. *American Mineralogist* 50:450-464.
- White CE, Provis JL, Proffen T, Riley DP, van Deventer JSJ (2010) Density functional modeling of the local structure of kaolinite subjected to thermal dehydroxylation. *Journal of Physical Chemistry A* 114:4988-4996.
- Whittaker EJW, Zussman J (1956) The characterization of serpentine minerals by X-ray diffraction. *Mineralogical Magazine* 31:107-126.
- Wicks FJ, O'Hanley DS (1988) Serpentine minerals: structures and petrology. In: "Hydrous phyllosilicates (Exclusive of Micas)". Bailey SW, ed., *Reviews in Mineralogy* 19:91-167.
- Wicks FJ, Whittaker EJW (1975) A reappraisal of the structures of the serpentine minerals. *Canadian Mineralogist* 13:227-243.
- Wiebe RA (1988) Structural and magmatic evolution of a magma chamber: the Newark Island layers intrusion, Nain, Labrador. *Journal of Petrology* 29:383-411.

- Wunder B, Deschamps F, Watenphul A, Guillot S, Meixner A, Romer RL, Wirth R (2010) The effect of chrysotile nanotubes on the serpentine-fluid Li-isotopic fractionation. *Contributions to Mineralogy and Petrology* 159:781-790.
- Yada K (1979) Microstructures of chrysotile and antigorite by high-resolution electron microscopy. *Canadian Mineralogist* 17:679-691.
- Yada K (1971) Study of microstructure of chrysotile asbestos by high resolution electron microscopy. *Acta Crystallographica A* 27:659-664.
- Yariv S, Heller-Kallei L (1975) The relationship between the I.R. spectra of serpentines and their structures. *Clays and Clay Minerals* 23:142-152.
- Yue LH, Jin DL, Lu DY, Xu ZD (2005) The non-isothermal kinetic analysis of thermal decomposition of  $\text{Mg}(\text{OH})_2$ . *Acta Physico-Chimica Sinica* 21:752-757.
- Zaremba T, Krzakala A, Piotrowski J, Garczorz D (2010) Study on the thermal decomposition of chrysotile asbestos. *Journal of Thermal Analysis and Calorimetry* 101:479-485.
- Zema M, Ventruti G, Lacalamita M, Scordari F (2010) Kinetics of Fe-oxidation/deprotonation process in Fe-rich phlogopite under isothermal conditions. *American Mineralogist* 95:1458-1466.
- Zhang M, Hui Q, Lou X-J, Redfern SAT, Salje EKH, Tarantino SC (2006) Dehydroxylation, proton migration, and structural changes in heated talc: An infrared spectroscopy study. *American Mineralogist* 91:816-825.
- Zhang M, Redfern SAT, Salje EKH, Carpenter MA, Wang L (2010)  $\text{H}_2\text{O}$  and the dehydroxylation of phyllosilicates: An infrared spectroscopic study. *American Mineralogist* 95:1686-1693.
- Zhang M, Wang L, Hirai S, Redfern SAT, Salje EKH (2005) Dehydroxylation and  $\text{CO}_2$  incorporation in annealed mica (sericite): An infrared spectroscopic study. *American Mineralogist* 90:173-180.
- Zhang Y (2008) *Geochemical kinetics*. Princeton University Press. Princeton and Oxford, 631 p.
- Zussman J (1954) Investigation of the crystal structure of antigorite. *Mineralogical Magazine* 30:498-512.
- Zussman J, Brindely GW, Comer JJ (1957) Electron diffraction studies of serpentine minerals. *American Mineralogist* 42:133-153.

## CURRICULUM VITAE

---

Roy Trittschack

Birth: 11<sup>th</sup> March 1984, Leipzig, Germany



## WORK EXPERIENCE

---

- 2009 – present*      **University of Fribourg**, Fribourg, Switzerland  
Teaching assistant for undergraduate courses  
e.g., General Geology, Mineralogy, Geological Mapping Courses and Field Trips
- 2008*                **Martin-Luther-University Halle-Wittenberg** (Prof. Gregor Borg), Halle (Saale), Germany  
Student assistant: Practical training with an ASD Terraspec (SWIR) handheld device and production of a user manual for laboratory assistants and students
- 2007 – 2008*      **Deutsche Rohstoff AG**, Heidelberg & Chemnitz, Germany  
Student assistant: Prospection of ore mineral deposits in Germany
- 2007*                **Federal Institute for Geosciences and Natural Resources**, Hannover, Germany  
Internship: Petrographic and mineralogical description of Pt-bearing ultramafic pipes
- 2006*                **VTs Koop GmbH & Co. Thüringen KG**, Schmiedebach & Unterloquitz, Germany  
Internship: Drill core logging and documentation, geological mapping, open pit planning
- 2005 – 2007*      **University of Leipzig** (Prof. Werner Ehrmann), Leipzig, Germany  
Student assistant: Clay mineral analysis of marine sediment cores



## EDUCATION

---

- 2009 – 2013      **University of Fribourg**, Fribourg, Switzerland  
 PhD candidate under the supervision of Prof. Bernard Grobéty  
 Thesis title: Dehydroxylation kinetics of the serpentine group minerals
- 2007 – 2008      **Martin-Luther-University Halle-Wittenberg**, Halle (Saale), Germany  
 Diploma (M.Sc.) candidate under the supervision of Prof. Gregor Borg  
 Thesis title: Geological identification and mineralogical characterisation of palaeosurfaces and channel fills at the Langer Heinrich uranium deposit, Namibia
- 2002 – 2007      **University of Leipzig, Leipzig**, Germany  
 study of Geology-Palaeontology
- 2002              **Dr. Max Näder Gymnasium**, Königsee, Germany  
 Graduation of grammar school (A-level)

## PUBLICATIONS

---

- Trittschack R, Grobéty B, Brodard P (submitted) Kinetics of the chrysotile and brucite dehydroxylation reaction: a combined non-isothermal/ isothermal thermogravimetric analysis and high-temperature X-ray diffraction study. *Physics and Chemistry of Minerals*.
- Trittschack R, Grobéty B (2013) The dehydroxylation of chrysotile: a combined *in situ* micro-Raman and micro FTIR study. *American Mineralogist* 98:1133-1145.
- Trittschack R, Grobéty B, Koch-Müller M (2012) *In situ* high-temperature Raman and FTIR spectroscopy of the lizardite phase transformation. *American Mineralogist* 97:1965-1976.
- Trittschack R, Grobéty B (2012) Dehydroxylation kinetics of lizardite. *European Journal of Mineralogy* 24:47-57.
- Trittschack R, Borg G (2009) Lithostratigraphie und Sedimentologie der Uran-führenden Langer-Heinrich Formation/ Namibia. *Zentralblatt für Geologie und Paläontologie* Jg. 2008 1/2:127-138.
- Trittschack R (2007) Platin führende ultramafische Pipes des östlichen Bushveld-Komplexes, Südafrika: Dünnschliffuntersuchungen, BGR Referenz 0127034, 37 p.